SYNTHESIS AND DEVELOPMENT OF HARD AND TOUGH NANOCRYSTALLINE METAL NITRIDE COATINGS

Ph.D. THESIS

by

PARITOSH DUBEY

DEPARTMENT OF METALLURGICAL & MATERIALS ENGINEERING
INDIAN INSTITUTE OF TECHNOLOGY ROORKEE
ROORKEE-247667 INDIA
DECEMBER, 2014

SYNTHESIS AND DEVELOPMENT OF HARD AND TOUGH NANOCRYSTALLINE METAL NITRIDE COATINGS

A THESIS
submitted in partial fulfilment of the
requirements for the award of the Degree
of
DOCTOR OF PHILOSOPHY
in
METALLURGICAL & MATERIALS ENGINEERING

by

PARITOSH DUBEY

DEPARTMENT OF METALLURGICAL & MATERIALS ENGINEERING
INDIAN INSTITUTE OF TECHNOLOGY ROORKEE
ROORKEE-247667 INDIA
DECEMBER, 2014

INDIAN INSTITUTE OF TECHNOLOGY ROORKEE
ROORKEE

CANDIDATE'S DECLARATION

I hereby certify that the work which is being presented in the thesis "**Synthesis and Development of Hard and Tough Nanocrystalline Metal Nitride Coatings**" in partial fulfilment of the requirement for the award of the Degree of Doctor of Philosophy and submitted in the Department of Metallurgical & Materials Engineering of the Indian Institute of Technology Roorkee, Roorkee is an authentic record of my own work carried out during a period from December, 2009 to December, 2014 under the supervision of **Dr. Devendra Singh** Associate Professor, Department of Metallurgical and Materials Engineering and **Dr. Ramesh Chandra** Professor, Institute Instrumentation Centre, Indian Institute of Technology Roorkee, Roorkee.

The matter presented in this thesis has not been submitted by me for the award of any other degree of this or any other Institute.

(PARITOSH DUBEY)

This is to certify that the above statement made by the candidate is correct to the best of our knowledge.

(Devendra Singh)
Supervisor

(Ramesh Chandra)
Supervisor

Date:_____

ABSTRACT

Nanocrystalline metal nitrides coatings have been successfully applied on various industrial components since the 1970's, for the protection and particularly to enhance the life of components. The metal nitrides coatings studied for tribological application are mainly based on transition metal nitrides includes TiN, CrN, TaN, ZrN, W_2N and their alloys like TiAlN, TiCrN, HfON, ZrON, TiAlBN, WSiN, nc-TiN/a-Si_3N_4 and so on. Most of them are commonly referred to as refractory hard metals. But, the hardness alone may not provide the level of protection against wear damage. In addition to high hardness, high toughness of a coating also has equal importance especially for tribological applications where high normal and shear forces are present. A coating with high toughness has high resistance to propagation and formation of cracks under stress. Moreover, high energy absorbance capability of tough coatings prevents catastrophic failure.

Hard nanocrystalline coatings with enhanced toughness exhibit a high elasticity (resilience), an enhanced resistance to cracking and low plastic deformation. Multicomponent refractory material systems can provide opportunities for the synthesis of hard and tough coatings. The development nanocrystalline metal nitride coatings by various physical deposition techniques is ever growing to achieve their superior performance in the actual engineering applications. The literature on the optimized process variables using magnetron sputtering technique for the deposition of hard and tough metal nitride coating with the desirable microstructural characteristics is very limited. The control of the microstructural characteristics in terms of grain size, lattice defects, crystallographic orientation (texture) and surface morphology as well as phase compositions of these coatings are very important in realizing the aforementioned properties so as to extend the performance and life time of the coated products.

The main objectives of present research work are to synthesize hard and tough nanocrystalline transition metal nitride coatings such as Zirconium Tungsten Nitride (Zr-W-N), and Zirconium Tungsten Boron Nitride (Zr-W-B-N) coatings using DC/RF magnetron sputtering technique and to investigate the effect of sputtering process parameters on microstructure, thermal stability and mechanical properties of these coatings for obtaining high quality films. A chapter-vise summary of the thesis is given below:

Chapter 1 The potential application of present research work is centered on prevention of wear damages like cavitation and silt erosion in hydro turbine components using hard and tough nanocrystalline metal nitride coatings. Hence this chapter discusses about hydropower generation in India, erosion problems facing in electricity generation by hydro turbines and approaches used to encounter silting problems. This chapter also gives an overview of metal nitride coatings in which background, synthesis techniques and applications are discussed. A role of hardness and toughness to control wear damages has been discussed briefly. The structural, thermal stability and mechanical properties of zirconium nitride, tungsten nitride, zirconium tungsten nitride and zirconium tungsten boron nitride coatings and their applications are discussed in this chapter. The motivations, research gaps and objectives for the development of hard and tough nanocrystalline zirconium tungsten nitride and zirconium tungsten boron nitride coatings are also discuss in **Chapter 1**.

Chapter 2 deals with the synthesis and characterization of "thin films" and describes the process of DC/RF magnetron sputtering used for the fabrication of thin films in the present work. Process and mechanism of thin films growth have been explained to understand how a film actually grows on a substrate. Three different modes of thin film growth (layer, island and layer + island) have been explained in detail. A description of working principles of different characterization techniques such as X-Ray Diffraction (XRD), Field Emission Scanning Electron Microscopy (FESEM), Atomic Force Microscopy (AFM), Transmission Electron Microscopy (TEM), Wavelength dispersive spectroscopy (EDS), Energy dispersive spectroscopy (EDS), Nanoindentation and Microindentation used for the analyses of elemental composition, phase, textures, grain size, surface morphology and mechanical performance of the deposited films have been given in detail.

Chapter 3 describes the effect of nitrogen partial pressure (pN_2) (0.07 to 0.67 Pa) on structural, composition and mechanical properties of $Zr_xW_{1-x}N_y$ thin films. It has been observed that the structure and elemental composition of the deposited $Zr_xW_{1-x}N_y$ thin films strongly depend on pN_2. XRD analysis shows that for 0.07 Pa $\leq pN_2 \leq$ 0.17 Pa, $Zr_xW_{1-x}N_y$ films exhibit single (fcc) phase, for 0.20 Pa $\leq pN_2 \leq$ 0.27 Pa, an amorphous phase is obtained and for 0.33 Pa $\leq pN_2 \leq$ 0.67 Pa reflections corresponding to fcc phase Zr-W-N and hcp phase ZrN have been observed. The phase formation has been confirmed by TEM diffraction patterns (SAED). The diffuse rings in SAED pattern of film deposited at pN_2 = 0.27 Pa confirm that nanocrystalline grains were not grown during deposition. The film deposited at pN_2 = 0.47 Pa exhibit maximum

(6.8 nm) roughness because the XRD peaks of ZrN are relatively prong with the XRD peaks of Zr-W-N phase which indicate that ZrN phase is well established along with Zr-W-N phase and hence roughness increases. Results of nano-indentation analysis confirm moderate hardness, high wear resistance, high resistance to plastic deformation and high adhesiveness of $Zr_xW_{1-x}N_y$ films. Among all the phases, maximum hardness (~ 24 GPa) and maximum reduced elastic modulus (135 GPa) have been obtained for dual phase (fcc+hcp) film while resistance to fatigue fracture (H^3/E_r^2 ~ 0.87 GPa), wear resistance (H/E_r ~ 0.2) and ductility for single phase (fcc) film were found to be maximum. All the films were found to exhibit high adhesion with the substrate surface.

Chapter 4 discusses about the structure, thermal stability and mechanical properties of crystalline (fcc) phase and amorphous phase Zr-W-N thin films. This chapter divided into two sections. **Section 4.1** describes the effect of substrate temperatures T_s (100º-600ºC) and post annealing temperature T_n (100º-600ºC) on thermal stability and mechanical properties of amorphous phase $Zr_{19}W_{18}N_{63}$ thin films. For 100ºC ≤ T_s≤ 300ºC, XRD patterns show an amorphous structure of the films and for 400ºC ≤ T_s≤ 600ºC, a crystalline fcc phase with (111) and (200) orientation has been observed. The XRD findings are further confirmed by TEM and SAED patterns. Maximum wear resistance (H/E_r ~ 0.22) and maximum resistance to fatigue fracture (H^3/E_r^2 ~ 1.1 GPa) have been obtained for the amorphous films deposited at T_s = 200ºC. Post annealing of films deposited at 200ºC have been carried out in air from 100º-600ºC. Oxygen starts to be incorporated in the films at T_n = 300ºC and its content increases with increasing T_n. No crystalline oxide phases are observed up to T_n = 600ºC. The hardness of the annealed films decreases with increasing oxygen incorporation. Indentation and scratch tests for as deposited and annealed films show that no cracks propagate in the films even at a high load of 50 mN and all the films exhibit high adhesion with the substrate. **Section 4.1** describes the effect of substrate temperatures T_s (100º-600ºC) and post annealing temperature T_n (100º-600ºC) on thermal stability and mechanical properties of crystalline fcc phase $Zr_{22}W_{19}N_{58}$ thin films. For 100ºC ≤ T_s ≤ 600ºC, X-ray diffraction patterns of the deposited films show a crystalline fcc phase with (111) and (200) preferred crystallographic orientations of grains. A close analysis of the diffraction pattern shows that for low T_s (< 400ºC) the coating structure is not simply fcc but probably contains some amorphous parts along with the fcc phase. It can be clearly seen that the contribution of amorphous part is maximum for T_s =100ºC, decreases with increasing T_s and disappears for T_s ≥ 400ºC. The XRD findings are further

confirmed by TEM and SAED patterns. Maximum wear resistance ($H/E_r \sim 0.22$) and maximum resistance to plastic deformation ($H^3/E_r^2 \sim 1.0$ GPa) have been obtained for the film deposited at T_s = 400ºC. Post annealing of the films deposited at 400ºC have been carried out in open atmosphere at 100º-600ºC. For the annealed films, no crystalline oxide phase has been detected for 100ºC ≤ T_n ≤ 600ºC, even though oxygen incorporation in the films starts at $T_n \geq$ 300ºC. The films start peeling off at 500ºC and got completely peeled off at 600ºC. The crystallite size increases with increasing T_n and reaches a maximum value of ~10 nm at T_n = 400ºC. Hardness and elastic modulus of annealed films found to be increasing with increasing strain. For practical applicability, the film deposited at 400ºC is found to be most suitable for application in the temperature range below 300ºC. But the deposition of wear protective coatings at low substrate temperature (≤ 200ºC) is more feasible for commercial aspects.

Mechanical properties of amorphous phase Zr-W-N coatings are found superior to crystalline phase Zr-W-N coatings. But Zr-W-N coatings exhibit amorphous phase at low $T_s \leq$ 300ºC which restricts the further enhancement of physical and mechanical properties of Zr-W-N coatings either by varying other sputtering parameter likes negative biasing (**chapter 5**) or by changing the architecture of coatings through substitution of amorphous non-metal nitride phases (**chapter 6**). Hence, crystalline (fcc) phase Zr-W-N coatings has been selected for further study in the present research work.

In Chapter 5 effect of negative substrate bias voltage V_s (-20 V to -120 V) on structure and mechanical properties of fcc phase Zr-W-N coatings deposited at 200ºC substrate temperature has been studied in details. The application of negative bias voltage to the substrate leads to impingement of energetic ions on the coating surface is an effectual way to grow dense and void-free microstructure of coating at low deposition temperatures. The deposition rate and substrate ion current density vary non-monotonically with increasing V_s. XRD patterns of the Zr-W-N coatings revealing one group of peaks of fcc structure, indicating that this coating tends to form a single solid-solution nitride phase rather than the co-existence of separated nitrides. FESEM analysis shows that the morphology evolves from columnar structure to dense and then glassy structure with increasing negative bias voltages. Nanoindentation hardness H and effective elastic modulus E_r of the coating increases as the negative substrate bias goes up. Maximum wear resistance ($H/E_r \sim 0.23$) and fracture toughness ($K_{IC} \sim 2.25$ MPa.$m^{1/2}$) have been obtained for the film deposited at -100 V bias voltage. This indicates that the simultaneous increment of wear resistance and toughness is achievable if the negative bias voltage is

properly controlled. Therefore, for the deposition of Zr-W-N system done at low substrate temperature (200ºC) and at -100V bias voltage, pronounced mechanical properties (H~ 34 GPa, $H/E_r > 0.1$, $W_e > 60\%$, $H^3/E_r^2 > 0.1$, $K_{IC} \sim 2.25$ MPa.m$^{1/2}$) has been achieved.

Chapter 6 discusses about the effect of microstructure on thermal stability and mechanical properties of Zr-W-B-N nanocomposite coatings. The Zr-W-B-N nanocomposite coatings have been co-sputtered deposited on Si (100) substrates by varying power density (0.1 to 7.5 watt/cm^2) to boron target to obtain films of various compositions and microstructure. It has been observed that the Zr-W-B-N films with boron contents ≤ 2.3 at.% exhibited (200) preferred crystallographic orientation of grains and columnar structure. For the boron content ≥ 7.5 at.%, non-columnar films with the crystal phase grain size less than 7 nm and films of crystalline (Zr-W-B-N)-amorphous structure (BN) or high amorphous component are produced. Owing to synergetic contribution of solid solution strengthening and grain boundary hardening, film with boron content ~7.5 at.% exhibits maximum hardness (~ 37 GPa), wear resistance ($H/E_r \sim 0.24$) and fracture toughness (2.9 MPa.m$^{1/2}$). Due to the superior mechanical performance of Zr-W-B(7.5 at.%)-N film over other deposited films of varying B content, post annealing of the this films has been carried out at 300º-900ºC in vacuum (T_v) and in air (T_n). Zr-W-B(7.5 at.%)-N film retains the fcc structure after vacuum annealing at T_v = 900ºC. However, film retains the fcc structure during air annealing at $T_n \leq 700$ºC and at T_n = 900ºC, full degradation of the Zr-W-B(7.5 at.%)-N film in crystalline phases of ZrO_2 and WO_3 was observed. The oxygen starts to be incorporated in the film at T_n = 500ºC and its content increases substantially with increasing T_n. The film got completely peeled off at T_n = 900ºC. Hardness H and elastic modulus E_r of the films remains unaffected by vacuum annealing while increased with increasing oxygen concentration in to the films.

Chapter 7 summarizes the results and findings of the present work discussed in this thesis. The future directions in which these studies can be extended have been suggested at the end.

ACKNOWLEDGEMENTS

The research presented in this doctoral thesis has been carried out at the Department of Metallurgical and Materials Engineering, Indian Institute of Technology Roorkee, India. The completion of my thesis has been due to enormous support and encouragement of numerous people including my supervisors, my family, my friends, colleagues and my institute. At this stage I would also like to express my thanks to all those who contributed in many ways to the success of this study and made it an unforgettable experience for me. Although the completion of my doctoral thesis has been a long journey of five years, but still I feel that it is only a few days back story.

At this moment of accomplishment, first of all I pay my sincere appreciation to my supervisor, Prof. Ramesh Chandra, who assisted and guided me throughout the entire study. I am heartily thankful to him for picking me up as a student and was fortunate to be one of the members of his nano science research group. His smiling face persona, frank and friendly temperament provided a stimulating and fun filled environment in the laboratory for pursuing the research work. I thank him for allowing me to have hands on experience on all the equipments that I used for my work. His invaluable guidance, support, encouragement and suggestions from the initial to the final level of my work helped me to improve the quality of work and enabled me to develop an understanding of the subject. His gracious approach and motivation were the major strength in successfully overcoming tough times during my research work. He not only boosted my moral in tough conditions but also injected a fair degree of self confidence in me. His enthusiasm and dedication towards developing new state of the art facilities in his lab will always inspire me to do the same in my career.

I am grateful to my supervisor Dr. Devendra Singh for his motivation and help throughout this work. It would have been completely impossible for me to accomplish this mammoth work without his valuable advices and discussions. His punctuality and habit of setting a deadline for every small and big task are always motivating me to complete my work on time. Without his comments and suggestions it would have been extremely difficult to bring this thesis in final form. He has always been very generous and forthcoming in allowing me to

have a discussion with him any time. His patience, flexibility, genuine caring and concern, and faith in me enabled to successfully complete my research work.

I express my sincere thanks to Prof. S.K. Nath, Head of Department of Metallurgical and Materials engineering, and all other faculty members of the Metallurgy and Materials Engineering Department for their keen interest in this work. I take this opportunity to thank all the members of my SRC committee, Dr. Devendra Puri (Chairman), Metallurgy and Materials engineering Department, Prof. B.S.S. Daniel (Internal member), Metallurgy and Materials engineering Department and Prof. Pravindra Kumar (External Member), Department of Biotechnology, IIT Roorkee for their invaluable suggestions and encouragement to carry out this work.

I am highly obliged and express my sincere thanks to the official & technical staff of Metallurgical and Materials Engineering Department and Institute Instrumentation Centre, IIT Roorkee. I wish to acknowledge Mr. Kamal Singh Gotyan, Mr. R.K. Sharma, Mr. Rajneesh, Mr. Ashok kumar, Mr. Birendar Dutt, Mr. S.D.Sharma, Mr. D.R.S. Pundir, Mr. Mr. Mahavir Singh, Mr. Yashpal and Mr. Shiv Kumar in our lab for their cooperation and affection.

I wish to give my heartiest thanks to Mr. Subhash Pai, CTO, Excel Instrument, Mumbai and India, for not only designing and manufacturing the experimental equipments as per our need but also being helpful and forthcoming in discussing technical difficulties with the work.

I am also extremely grateful to Dr. S.K. Srivastava for his support and motivation. He has always been a great source of inspiration since my Ph.D days. Despite of his busy schedule, he used to review my research papers, give his valuable suggestions and made corrections. I have learnt a lot from him both in academics and otherwise. I greatly enjoyed working with all my lab mates Dr. Amit Kumar Chawla, Dr. Vipin Chawla, Dr. Y.K. Gautam, Dr. Mukesh Kumar, Dr. Sushant Rawal, Dr. Rajan Walia, Dr. Sonal Singhal, Dr. Atikur Rahman, Archana Mishra, Vivek Arya, Ravish Jain, Vikramaditya Dave, Samta Chauhan, Sunil Tanwar, Monu Verma, Pradeep Mishra, Akshey Kaushal, Ashwani Kumar, Amit Sanger, Amit Rajput, Jyoti, Anuj Upadhyay, Mukesh Tripathi, Arvind Choudhary, Gaurav Malik and Radhe Krishna. I thank them all for their full cooperation and ever needed help throughout to carry out this work

and also for being around all the time. During my research work in lab I greatly enjoyed my interaction with M.Tech students Shreya Goel, Pallavi Gupta, Vivek Surana, Anuj Kumar, Gurjinder Kaur, Vinay Chauhan, Sandhya , Amit Singh, Sonam Jain and Guru Prakash.

I have been blessed with a friendly and cheerful group of buddies like Ashish Selokar, Vineet Bharti, Shveta Dubey, Nidhi Rana, Rashmi Mittal, Deepa Mudgal, Rashmi Rani, Rajeev Sehrawat, Devasri Fuloria, Kiran Deep, Sunkulp Goel, Himanshu Panjiar, Nikhil, Ravikant and all others who shared their valuable time with me.. I enjoyed every single moment spent with them. Their friendly behavior helped me to feel home away from home.

The financial support provided by Ministry of Human Resource Development (MHRD), Govt. of India as a fellowship for this work is gratefully acknowledged. The financial assistance obtained from Indian National Science Academy (INSA) India and IIT Roorkee Alumni fund for attending a conference "International Conference on Metallurgical Coatings and Thin Films-April 2014" San Diego, CA, USA is duly acknowledged.

I would be failing my emotion if I do not mention the name of my elder brother in fact my best friend, Mr. Ashutosh Dubey, who has always been a great source of inspiration since my childhood. He always taught me to have self confidence and never give up in tough time of my research work. A special thanks to my family (*Maa, Papa & Bhabhi*). Words cannot express how grateful I am to my family for all of the sacrifices that they've made on my behalf. Their prayer for me was what sustained me thus far. It would be impossible what I am today without my family.

At the outset, let me thank the almighty God (*Sai Maharaj*), who is the most graceful and generous for his blessing that has given me courage, strength to face any adverse situation, wisdom to make wise decisions and pleasant, memorable moments of my life. Our work greatly improved thanks to the comments of the anonymous reviewers and editors of the articles published with contributions of this thesis. I would like to thanks everybody who was important to the successful realization of thesis, as well as expressing my apology that I could not mention personally one by one.

(Paritosh Dubey)

CONTENTS

LIST OF FIGURES

LIST OF TABLES

LIST OF PUBLICATIONS

Paper Published in journals

1. **P. Dubey**, V. Dave, S. Srivastava, D. Singh, R. Chandra, "Study of thermal stability and mechanical properties of amorphous $Zr_{19}W_{18}N_{63}$ coatings deposited by DC/RF reactive magnetron sputtering, **Surface and coating Technology 237 205-211 (2013)**.

2. **P. Dubey**, V. Arya, S. Srivastava, D. Singh, R. Chandra, "Effect of nitrogen flow rate on structural and mechanical properties of Zirconium Tungsten Nitride (Zr-W-N) coatings deposited by magnetron sputtering", **Surface and coating Technology 236 182-187 (2013).**

3. **P. Dubey**, V. Arya, S. Srivastava, D. Singh, R. Chandra, "Study of thermal stability and mechanical properties of fcc phase $Zr_{22}W_{19}N_{58}$ thin films deposited by reactive magnetron sputtering", **Surface and coating Technology 245 34-39 (2014)**.

4. **P. Dubey,** V. Chauhan, S. Verma, R. Jayaganthan, D. Singh, R. Chandra, "Adhesive and Abrasive Wear Behavior of Nanostructure Zr-W-N Coating", **Transaction of Indian Institute of Metals (partially accepted).**

5. **P. Dubey**, V. Arya, M. Kumar, D. Singh, R. Chandra, "Study on thermal stability and mechanical properties of nanocomposite Zr-W-B-N thin films" **Surface and coating Technology (under review).**

6. **P. Dubey,** S. Chauhan, V. Arya, S. Srivastava, D. Singh, R. Chandra, "Bias Effect on Structure and Mechanical Properties of Magnetron Sputtered Nanocrystalline Zirconium Tungsten Nitride Coatings", **Surface and coating Technology (under review).**

7. V. Dave, **P. Dubey**, H.O. Gupta, R. Chandra, "Effect of sputtering gas on structural, optical and hydrophobic properties of DC-sputtered hafnium oxide thin films", **Surface and Coatings Technology, 232 425–431 (2013).**

8. V. Dave, **P. Dubey**, H.O. Gupta, R. Chandra, "Influence of sputtering pressure on the structural, optical and hydrophobic properties of sputtered deposited HfO2 coatings", **Thin Solid Films 549 2-7 (2013).**

9. V. Dave, **P. Dubey**, H.O. Gupta, R. Chandra, "Nanotechnology for outdoor High voltage insulator: An experimental investigation", **International Journal of ChemTech Research 5 (2) 666-670 (2013).**

10. G. Das, Mousumi Das, Sabita Ghosh, **Paritosh Dubey** and A. K. Ray, "Effect of Aging on Mechanical Properties of 6063 Al-Alloy Using Instrumented Indentation Technique", **Materials Science and Engineering: A 527(6) 1590-1594 (2010).**

Paper Published in proceedings

1. V. Dave**, P. Dubey,** H. O. Gupta and R. Chandra**, "**Temperature dependent structural, optical and hydrophobic properties of sputtered deposited HfO2 films". **AIP Conference Proceeding 29 1576 (2014)**; **http://dx.doi.org/10.1063/1.486197**.

2. V. Dave, **P. Dubey**, H.O. Gupta, R. Chandra, "Microstructural and optical properties of Sputter deposited Hafnium oxynitride films on glass substrate", **International Conference on Energy Efficient Technologies for Sustainability, ICEETS -2013, Article number 6533528 1031-1035 (2013).**

Patent File

1. Vivek Arya, **Paritosh Dubey**, Ramesh Chandra, "A method of producing erosion resistant hard layer for hydro turbine components" application no. **932/KOL/214**.

Paper Presented in conferences

1. **Paritosh Dubey**, Devendra Singh, Ramesh Chandra; "Effect deposition parameter on nanocrystalline single phase Zirconium Tungsten Nitride (Zr-W-N) coating" Indian Vacuum Society Symposium on Thin film: Science and technology, november 9-12, 2011, Bhabha Atomic Research Centre, Trombay, Mumbai-400085 and India.

2. **Paritosh Dubey**, Vivek Arya, Devendra Singh, Ramesh Chandra, "Development of Nanocrystalline Zirconium Tungsten Nitride (Zr-W-N) coating by magnetron sputtering" International conference on nanoscience and technology, ICONSAT, January 20-23, 2012, Hotel Taj Krishna, Hyderabad, Banjara Hills, Hyderabad, AP - 500034 and India.

3. **Paritosh Dubey**, Vivek Arya, Ravish Jain, Devendra Singh, Ramesh Chandra, "Synthesis and Development of thermally stable nanocrystalline single phase Zirconium Tungsten Nitride (Zr-W-N) coating", International Conference on Advance Materials and Processing (AMPCO), November 2-4, 2012, Department of Metallurgical and Materials Engineering, Indian Institute of Technology Roorkee, Roorkee-247667, India.

4. **P. Dubey**, V. Arya, D. Singh, R. Chandra, "Effect of In-situ and Ex-situ heat treatments on practical applicability of nanocrystalline single phase Zirconium Tungsten Nitride (Zr-W-N) coatings" National Seminar on Metallurgical Problems in Power Projects in India, February 22-23, 2013, Seminar Hall, Design Centre, Malaviya National Institute of Technology Jaipur, Jaipur, Rajasthan 302001 and India.

5. **P. Dubey**, V. Dave, S. Srivastava, D. Singh, R. Chandra, "Study of thermal stability and mechanical properties of amorphous $Zr_{19}W_{18}N_{63}$ coatings deposited by DC/RF reactive magnetron sputtering" International conference on metallurgical coating and thin films, ICMCTF- April 29-May 3, 2013, Town and Country Hotel, San Diego, California, USA.

6. **P. Dubey**, V. Arya, R. Chandra, "Development of Silt Erosion Resistant Nanocomposite Coatings by Physical Vapour Deposition for Hydro Turbine Components" National Workshop on R & D Projects of Hydro Power Sectors, 25th Nov. 2013, New Delhi.

7. **P. Dubey**, S. Chauhan, V. Arya, S. Srivastava, D. Singh, R. Chandra, "Bias Effect on Structure and Mechanical Properties of Magnetron Sputtered Nanocrystalline Zirconium Tungsten Nitride Coatings" 41-International conference on metallurgical coating and thin films, ICMCTF-April 28-May 2, 2014, Town and Country Hotel, San Diego, California, USA.

8. **P. Dubey**, V. Arya, R. Chandra, "Effect of Coating Thickness on the Silt Erosion Properties of Ternary Metal Nitride Thin Films prepared by Magnetron Sputtering," 41-International conference on metallurgical coating and thin films, ICMCTF- April 28-May 2, 2014, Town and Country Hotel, San Diego, California, USA.

CHAPTER 1

INTRODUCTION AND LITERATURE REVIEWS

1.1 Introduction to Nanocrystalline Coatings

Coatings over material surfaces have attracted considerable attention in recent years owing to their promising applications in surface engineering. Surface engineering is a discipline that seeks to control or tailor the properties of a material's surface due to (i) surface has different properties than bulk material (ii) surface can be completely reengineered.

Surface engineering is highly interdisciplinary and needs an integrated approach between designers and surface engineers. The desired properties or characteristics of coatings include:

(a) Improved wear resistance
(b) Improved corrosion/oxidation resistance
(c) Improved mechanical properties, for example; enhanced toughness, hardness etc.
(d) Improved electronic or electrical properties
(e) Improved thermal insulation
(f) Reduced frictional energy losses

A significant advancement in coatings (surface engineering) technology is the development of nanocrystalline (grain size < 100 nm) coatings which show improved performance in aggressive environment as compare to microcrystalline (grain size ~ 0.1 to 0.3 μm) coatings. The unique properties of nanocrystalline coatings/materials are derived from their large number of grain boundaries compared to coarse-grained polycrystalline counterparts. As the grain size reduces to nanoscale (< 100 nm), a large amount of atoms (up to 50%) of solid reside in the grain boundaries. These grain boundary atoms behave in a different way from atoms residing in grains and the properties of material starts to govern by their

behavior. In nanocrystalline region (< 100 nm), ceramics become more ductile (malleable) while metal get stronger and harder (more brittle).

Nanocrystalline coatings generally exhibit considerably higher strength and high hardness relative to their microcrystalline counterparts. The hardness and yield strength tend to increase with decreasing grain size down to a critical value (~ 10 nm). The obstruction in the movement of dislocations by grain boundaries increases the hardness and strength of nano grain size material (Hall–Petch relationship: strength increase is inversely proportion to square root of grain size). When the grain size is reduces to critical value, hardness appears to decrease with further grain refinement. At this stage, grain size is smaller than the length of dislocation and hence the dislocations do not exist in the grains. The dislocation pile-ups cannot form at the grain boundaries and the Hall–Petch relationship is no longer valid. In combination to this, grain boundary sliding also reduces the hardness of material. Among ceramics, coatings in nanocrystalline form (Al_2O_3, ZrO_2, TiO_2 etc.), causes an increase in ductility through grain boundary sliding enhanced the toughness or reduced brittleness and improved ability to bond to a metal component. This increase in toughness increases the wear resistance (2-4 times) of nanocrystalline ceramics coatings than the microcrystalline counterpart. The appearance of ductility in nanocrystalline ceramic coating improves their strength that is most sought after, since ductility is useful not just in manufacturing but also in terms of behavior on impact, an important consideration in automobile, mining and tool industries (Tjong *et al.* 2004, Gao *et al.* 2001, Nayar *et al.* 2014, Singh *et al*. 2006, Dwivedi *et al.* 2001, Gupta *el al.* 2014).

A coating composed of two nanocrystalline phases, or a combination of both a nanocrystalline and an amorphous phase is called nanocomposite coating. Nanocomposite coatings (TiAlN, TiBN, TiSiN, WBN, ZrBN, WSiN, ZrWBN etc.) represent a new generation of materials, exhibiting superior structural and functional properties (high mechanical strength, high thermal stability, high oxidation resistance, high wear and erosion resistance). The properties of nanocomposite coatings can be tune by proper selection of the elements to form various phases of a nanocomposite, and the modification in microstructure of coating, in order to synthesize novel nanocomposite coating systems (Voevodin *et al.* 2004). Nanocomposite

coating is the way to achieve the best blend of the wear resistance, self-lubrication, toughness, and a low friction performance across multiple environments.

Among nanocrystalline coatings, nitride coatings have attracted considerable attention in recent years owing to their remarkable physical and mechanical properties. Nanocrystalline transition metal nitride coatings find wide applications in many industries, such as process, marine, power plant, offshore, aeronautical and mining. In these industries, there is a regular requirement for components such as valves, pumps, pipe work, extrusion dyes, powder mixers, turbine (hydro turbines and gas turbines) and helicopter blades to perform in exotic environments. Depending on the type of application, different nanocrystalline coatings have been developed by various deposition techniques including chemical vapor deposition (CVD), physical vapor deposition (PVD), thermal spray, electro-chemical deposition, sol-gel methods, and electro-spark deposition (Gao *et al.* 2001, Tjong *et al.* 2004, Periasamy *et al.* 2010, Selvakumar *et al.* 2012).

Other properties of nanocrystalline coatings/materials, apart from increased strength and hardness, include higher electrical resistance, increased specific heat, improved thermal expansion properties, lower thermal conductivity and improved magnetic and optical properties. For example, in nanocrystalline silicon electroluminescence, thermal-induced acoustic emission, photoluminescence and refractive index can be tuned easily as compare to microcrystalline silicon (Edelberg *et al.* 1996). Nanoparticles of various oxides like tungsten oxide, titanium oxide, zinc oxide, copper oxides etc have been act as effective catalytic for sulfur reduction, waste water treatment, reduction of toxic metal ions and degradation of hazardous organic as well as waste plastic than traditional micro and macro crystalline oxides. They have also shown greater resistance to poisoning (Gupta *et al.* 2014A, Purwanto *et al.* 2011, Banerjee *et al.* 2000). The nanocrystalline materials behave in a strongly different manner compared to the conventional materials composed of larger ($\geq$ 100 nm) grains and show completely new and enhance properties than bulk. These facts motivate researcher for the synthesis and development of nanocrystalline materials/coatings.

1.2 Background

Hydropower is a highly efficient and competitive electricity generation technology that lies at the heart of the renewable energy family. In India, Himalayan rivers are the main source of hydropower potential and the estimate potential is about 325000 MW. Ganga river in the region itself has a estimated power potential of 10,000 MW up to foot hills. The Himalayas are geologically young and weak sedimentary rocks and the rivers originated from Himalayas bring excessive sediment during monsoon >10,000 ppm **(**Asthana *et al.* 2007**)**. So, the underwater components like guide vanes, bushes, runners etc. of hydro turbine operating in silt laden water suffer from extensive abrasion damage. These parts get eroded so rapidly that it becomes impossible to run the generating units more than one session. There are two main source of erosion on the underwater components as:

(a) Cavitation Erosion: when liquids flow over a surface with high velocity, the momentum difference of the liquid produces a lower pressure down to the vapor pressure of liquid at the solid/liquid interface than in general vicinity of the system. At this stage, bubbles or cavities of vapor will form locally and collapse very quickly near the surface. The collapse of the bubbles may be seen as a flow of liquid with a spherical front toward the solid surface with a very high momentum and produce the high pressure at the centre about 7,000 atm to strain the target material. In most region the strain is much less than the yield strain, but when elastic strain imposed millions of times in small region over surface, local failure of material occur by elastic fatigue. The affected area get spongy and bee hive like pits occur on the surface of material.

(b) Silt Erosion: The silt has, mainly, quartz contain approx 95 weight % which is hard particle have the harness of 7 moh's scale. The hard silt particles impinging on the ductile material surface causes substantial removal of material by forming grooves on the surface. These grooves/lips are formed by ploughing/extrusion of material through silt particles. Continuous impingent of hard silt particles on the lips which is already formed leads to the strain hardening of the lips and their subsequent fracture. On the other hand brittle material shows losses by fragmentation and removal of flakes from surface of material. Wear rate enhanced for ductile material up to low angle ($\leq 30^{o}$ - 40^{o}) and at high angle (80^{o}-90^{o}) for brittle material. Silt erosive wear is depend up on many

factors like particle hardness, angle of impingement, shape and size of particle, density of silt in water, relative velocity of water and wear resistance of base material. Experimentally erosion rate through silt calculated as

$$\text{Erosion rate} = \frac{\text{Total weight loss of material}}{\text{Total weight } of \text{ silt material impacted}} \quad (1.1)$$

Due to the combine effect of both types of erosion damages is accelerate which lead to thinning of blades and then fractures in to two pieces.

1.2.1 Approach to encounter silting problems

A three dimensional approach is desirable to encounter erosion in hydro power plants as stated below

(i) **Effective De-silting Arrangements**: In this type of approach, the modification is done on the design of the dam according to water head and concentration of sediments. Make the hopper type desilting chamber with adequate flushing discharge for excluding heavy particles up to 200 micron size to reduce the erosion damages. Dumping of filtered silt is not a problem now a day. There are arrangement of bypass of heavy silt water and join with main stream far from the dam which is economical and environmental friendly method. Detailed petro-graphic analysis including shape, size and concentration of sediment shall consider along with head and discharge decided the size of the particles to be excluded and size of desilting basin (Asthana *et al.* 2007)**.**

(ii) **Silt resistance equipment design; hydraulic design/Mechanical design:** A few instance have been noticed where under identical condition of silt as shape, size, concentration, the intensity of damages at different power station were not identical while components at a particular station eroded very fast, damages to components at other power station were insignificant. This lead one to believe that equipment design has a role to play in influencing the intensity of erosion. A criterion for selecting most suitable type of machine is easy of replacing or repairing worn out components, speed

of rotation should be selected one or two steps lower than the synchronous speed selected for machine to be used in clean water. The blade curvature is relatively as low as feasible to reduce the resulting centrifugal force on the particles to minimize the intensity of abrasion. It has been found that the peak velocity can be moderated by increasing the blade length and the wearing life can be increasing by increasing the thickness of the blades, especially towards the tip section. It has been was estimated that the cavitation problem can be avoided by setting the reaction turbine deep inside because of clean water operation.

The mechanical design of hydraulic turbine for silty water is different from the design of the same for clear water, so there is a need of modifications and incorporation of special features besides enhanced erosion resistance. From analysis and understand the factors influencing the mechanical erosion of turbine component, following modification have been suggested:

(a) Runner of lower speed should be selected, in order to have lower relative velocity at the runner periphery.

(b) The thickness of the runner blade in areas prone to erosion should be increased e.g. runner of outlet edges in case of Francis turbine and near the peripheral section and outlet edges in case Kaplan turbine.

(c) Whenever generating units in power station are more than one, each unit should have separate inlet valve to facilitate stoppage of the unit for quick maintenance in the unit itself or its cooling water system.

(d) Use rubber ring in place carbon ring in the shaft gland of turbines for handling silt laden flows.

(e) Use a closed circuit cooling system, consisting of a water tank of adequate capacity, heat exchanger and circulating pump to avoid the problem in flowing of silt laden water. This method is more economical as compared to conventional method of cooling (Naidu 1996).

(iii) **Material Technology:** This section deals with materials either used for preparation of different components of hydro turbine or surface protection coatings against wear damages viz. corrosion, erosion, and cavitations processes. Various steels with different

composition have been developed so far for the fabrication of underwater part (Gadhikar *et al.* 2014). The most popular steels are of soft martensitic type, which also termed as 13/4 (Cr/Ni) stainless steel and equivalent martensites with a chromium content of 13–21% and nickel content of 4–6 % have been used for hydro turbine components. Among them, 13/4 steel provide maximum resistance to erosions due to its optimum hardness (300-400 VHN) and fracture toughness (64 $Jm^{1/2}$) combination, but repair welding technology of these steels has not yet been developed. Development of different type of steel like matrensitic steel, duplex steel and nitronic steel with different heat treatment processes and corresponding change in microstructures are still in course of action to get high hardness, high fracture toughness and high percentage elongation of material to fight with erosion problem in a better controlled and advanced ways.

From surface protection point of view different types of wear resistive coatings have been deposited and still wear resistant coatings on different substrates are being deposited with different approach, material and methods (Hedenqvist *et al.* 1990, Gray *et al.* 2008). Many works have been done regarding surface protection through different conventional coating like high velocity oxy fuel (HVOF), detonation gun spray, hard chrome plating and plasma nitriding, but still relation between erosion and coating properties are not define properly, need to more modification. Erosion resistant coatings are frequently used on hydro-electric turbine components, and in particular, the runner and the guide vanes for Francis-type turbine and the runner, needles and seats for Pelton-type turbines as well as various other components that are prone to silt erosion.

1.3 Overview of the Work

In perspective of recent research interest in these coatings, brief overview of the development of these coatings is given below:

Early reports date back to the early eighties, the deposition of coatings has been started with tungsten carbide and chromium carbide-based coatings through conventional way (thermal spray, high velocity oxy fuel and detonation gun spray). These coatings were used for many applications in gas turbine, steam turbine, aero engine as well as hydro turbines to improve the resistance to sliding, abrasive and erosive wear (Sue *et al.* 1987, De *et al.* 1994, Rhys-Jones 1990)**.** As wear (sliding and abrasive) resistant coatings, carbide coatings are considered to be a

viable alternative to hard chrome plating due to the harsh environmental conditions and cost concerns with respect to the electroplating process. These cermets coatings are deposited by plasma spray and high velocity processes namely high velocity oxy-fuel (HVOF) and detonation gun spray processes (Karimi *et al.* 1993, Murthy *et al.* 2006)**.** These types of cermets coating have been reasonably successful against abrasion erosion in components like guide vanes, nozzles etc. at the lower angle but due to their high hardness shows fragment type of failure at high angle of impingement and ineffective for cavitation erosion. Further, these coating are highly porous and have roughness in micron size which intern enhance the wear rate of coating (Tucker *et al.* 1994). Thus, the development of erosive resistance coatings with new and improved materials became vital. Several methods as physical vapor deposition, ion plating, and chemical vapor deposition methods have also been exploited to overcome the drawbacks associated with the conventional coating methods. The enhancement in properties of earlier developed material or development of new materials with specific properties plays a key role with respect to the introduction of new technologies. The surface properties of conventional materials can be improved by applying an appropriate coating. A number of coatings have been deposited using different materials and deposition techniques. Important developments are tabulated in **table 1.1**.

Table 1.1 *A number of overlay and surface modification processes that can be used for deposition of thin films*

Surface coating type	**Coating materials**	**Primary property benefits**	**Limitations**	**Thickness (µm)**	**Ref.**
Organic coatings (paints, polymeric or elastomeric coatings and linings)	Epoxy, Polyurethane, Vinyls	Improved corrosion resistance, wear resistance, and aesthetic appearance	Rapid chalking on exterior exposure, poor resistance to oxidizing acids, low service temperature	800-2000	(Gossner and Tator 1994)

Ceramic coatings and lining (glass linings, cement linings, and porcelain enamels)	porcelain enamels, TiC, SiC, Al_2O_3 TiN, WC, Cr_2O_3, TiCN, $MoSi_2$	Improved corrosion and wear resistance	Low acid-resistance, low resistance to impact		(Carpenter 1994)
Electroplating and Electroless plating (metal or composite coatings)	hard chromium elctroplating, Electroplated nickel + chromium nickel-phosphorus and nickel-boron electroless plating	wear resistance	Non-uniform deposition, Resistance to impact, evolution of hydrogen at the electrodes and metal particle inclusion	12.5- 500	(Browning 1994, Baudrand 1994)
Thermal spraying (metal, plastic, ceramic, or composite coatings)	WC/Ni-Cr-B-Si-C, Ni-Cr-B-SiC-Al-Mo, Ni-Al/Ni-Cr-B-SiC, Co-Mo-Cr-Si, Ni-Cr-B-SiC	Wear, oxidation and corrosion resistance	fragment type of failure at high angle of impingement, ineffective for cavitation erosion , Restoring strength	100-2500	(Tucker 1994)
Chemical vapor deposition (CVD) (metals, graphite, diamond, and ceramics)	TiN, Al_2O_3, TiC, B_4C, diamond like Carbon	Improved wear (e.g., tools and dies), erosion, and corrosion resistance; also used for epitaxial growth of semiconductors	High temperature, complex process, toxics and corrosive gases	1-1300	(Pierson 1994)

Physical vapor deposition (PVD) (metals, ceramics, or solid lubricants)	TiN, TiAlN, TiZrN, WSiN, TiSiN, nc-TiAlN/a-Si_3N_4	Improved wear (e.g., tools and dies) and corrosion resistance, improved optical an electronic properties, and decorative applications	Low deposition rate, line of site coatings, process required high vacuum	0.002-15	(Rhode 1994)

1.4 Metal Nitride Coatings

Metal nitride coatings have been developed as an effective approach to encounter silt erosion problem (material technology). Studies of the metal nitrides coatings have both scientific and technological significance. These compounds exhibit notable physical properties like excellent hardness, good chemical inertness, mechanical strength, high melting point and high electrical conductivity and hence, have wide applications in various fields including engineering, aeronautics and microelectronics. As a result, they are extensively studied in recent years and have become technologically important for applications such as diffusion barriers in microelectronics, wear-resistant coatings in engineering, optical coatings in industry, and electrodes in semiconductor devices (Shen *et al.* 2000A, Khanna . *et al.* 2012). The metal nitrides coatings studied for tribological application are mainly based on transition metal nitrides includes TiN, CrN, TaN, ZrN, W_2N and their alloys like TiAlN, TiCrN, HfON, ZrON, TiAlBN, WSiN, nc-TiN/a-Si_3N_4 and so on (Voevodin *et al.* 2004, Barshilia *et al.* 2004). These are usually referred to as refractory hard metals exhibiting remarkable physical and chemical properties. Therefore, transition metal nitrides coatings are attractive from both fundamental and technological points of view. In transition metal nitrides, nitrogen occupies the octahedral sites in lattice and change the electronic structure. When nitrogen makes bond with transition metal, one additional electron is found inside the non-metal sphere while the charge inside the transition metal sphere remains about constant as expected from simple chemical arguments which increases the p-electron concentration as compare in metal matrix and this lead to filling of non-bonding and anti-bonding electronic states. The high valence electron density enables resistance to elastic and plastic deformation (Le´vy *et al.* 1999). The year vise development of important transition metal nitride coatings is summaries in **table 1.2.**

Table 1.2 *Year wise development of transition metal nitride coatings*

Year	Research works
1980-1990	Titanium Nitride (TiN) deposited by magnetron sputtering has been developed as the most popular hard coating material to prevent tribological breakdown and mechanical failures of interacting mechanical component. The performances of other nitrides like ZrN, W_2N, CrN, AlN, BN and Si_3N_4 has also been studied as wear resistant coatings. Hard metal nitrides belonging to IV group (TiN, ZrN, HfN, Ti-TiN-TiC, Zr-ZrN-ZrC) were also studied as decorative coatings. Colour of the coatings may change by varying the nitrogen concentration in the films (Spalvins 1978, Zega 1989). In respect of material selection for wear resistant coatings, Hollock (1986) stated that the borides and carbides of transition metals are harder and less brittle than their nitrides; they have higher melting points but lower stability. They have a lower thermal expansion coefficient; they show better adherence to metallic substrates but also higher interaction tendency with other materials. This latter point together with favorable fabrication conditions, a splendid color and a relatively high thermal expansion coefficient were the reasons for the commonly used TiN layers.
1991-2000	In this decade the main attention given to development of PVD based ternary nitride coatings for new applications in the field of tool technology. Different industrial case studies demonstrated the effectiveness of PVD coating. Numerous ternary coating systems (Ti-Cr-N, Ti-C-N, Ti-Al-N, Ti-Zr-N, Ti-Hf-N, Zr-Cr-N, Zr-Y-N, Zr-Cu-N, Cr-W-N, Ti-W-N, Al-Si-N, Ti-B-N) were deposited in widely differing compositions with varying properties (Styazhkin *et al.* 2000, Zeman *et al.* 2000, Moser *et al.* 1994, Mollart *et al.* 1995, Grimberg *et al.* 1998, Hones *et al.* 2000, Otani *et al.* 1996, Musil *et al.* 2000). The ternary nitride systems have shown performance advantages over their binary systems. It is soon evident that coatings developed for one application could not be transfer to others. Industrial coating of drills and milling cutters with (Ti,Al)N provided a useful example (Hultman 2000A, Han *et al.* 2005). One representative group is formed by the titanium-based films like TiN, TiAlN on high speed steel (HSS) or cemented carbide tools for drilling, milling and turning. This group was at the most advance stage of the development and has been promoted chiefly for the machining of steel. It can be extended in three directions: firstly, by developing chromium-based, ceramic, diamond or diamond-like coating materials together with other metallic carbide and carbon nitride compounds; secondly, by extending the range of substrate materials, where coatings have been deposited on steel,

1991-2000	glass, silicon wafer, quartz, elastomer plastic etc (Erkens *et al.* 1992). The nitride coatings exhibiting spinodal miscibility gap (a metastable state of two neighbouring phases) have enhanced mechanical properties such as extreme hardness and retaining these properties even at higher operating temperatures (e.g. Zr-Ti-N) (Knotek *et al.* 1989). Four types of titanium based PVD coatings: TiN, Ti(C,N) and (Ti,A1)N and CrN have been frequently used to mitigate wear damages. These coatings exhibit high resistance against adhesive wear, but not for all workpiece materials. For applications where abrasion is predominant or where tough materials have to be machined Ti(C,N) coatings possess better properties. On the other hand, (Ti,Al)N can be used where better oxidation resistance is required. For corrosion protection point of view, a thick CrN coating has been used (Stappen *et al.* 1995).
2001-2010	To meet the challenges of application conditions of future tribo-systems, research in this decade mainly focused on the development of more exotic coatings with various design architectures that can further enhance performance and stability and at the same time self-adapt to the increasingly harsh and rapidly changing application conditions of future tribological systems. Some of the innovative design architectures considered for multifunctional nanostructured coatings were nanograde, self-lubricating nanocomposite and superlattice, or multilayer (Tsotsos *et al.* 2010A, Mitterer *et al.* 2001, Hauert *et al.* 1999, Chung *et al.* 2003, Münz 2000, Khanna et al. 2007, Mayrhofer et al. 2009, Lee *et al.* 2009, Tsotsos *et al.* 2010). In these years, many researchers have concentrated to modify the design of novel nanocomposite coatings in order to achieve hardness near to hardness of diamond (~ 100 GPa) A number of composite coating systems that consist of more than two phases were explored to achieve such level of hardness . It was observed that refractory nitride with little or no miscibility gap between constitute phases could be a potential candidate for such purpose. The use of nanocomposite or nanostructured ceramic coatings has become very popular in this decade for various applications like microelectronics, biomedical field and transportation (Ajayan*et al.* 2003, Verlag *et al.* 2003, Münz 2000). Veprek *et al.* (2000, 2002 and 2005) developed the new architecture (nanograins of metal nitride phase separated to each other by ~ 1 nm thick layer of amorphous hard non-metal nitride phase) of nanocomposite coating and proposed that the coating of such architecture exhibit ultra high hardness. Based on his architecture, synthesis nc-TiN/a-Si_3N_4 nanocomposite coatings in which nanocrystalline TiN phase

2001-2010	imbedded into an amorphous Si_3N_4 phase. The hardness value of this coating was observed more than 100 GPa. Other coating systems like Zr-Si-N, W-Si-N, Ti-Al-N and VN that exhibit super-hardness were synthesis and produced in several PVD systems by similar approach. In these years, several attempts have also been made to incorporate lubricious oxides and oxide-forming elements into hard coating system under the novel design concepts for self-lubricating nanocomposite films for high-temperature applications. Experimental studies have demonstrated that the oxides of Re, Ti, Ni, W, Mo, Zn, V, B, etc. are very lubricious and hence the incorporation of these oxides in to hard coatings systems can provide fairly low friction at elevated temperatures. Potential applications for lubricious oxides include high-temperature seals, bearings, and gears, valves and valve seats, variable stator vanes, and foil bearings (Kanakia *et al.* 1984, Kanakia *et al.* 1987, Lugscheider *et al.* 2001, Gulbinski *et al.* 2003). Some of the most common design strategies for nanostructured coatings include the production of multilayer architectures. In this case; the layer thickness may vary from a few atoms to several angstroms or nanometers. Such coatings may offer superhardness and toughness as well as high thermal stability. Amoung several superhard material systems, only "Ti–Si–N" and "Ti–B–N" systems have been observed to possess high thermal stability (Raveh *et al.* 2007, Zhou *et al.* 2004, Barnett *et al.* 2004, Hultman *et al.* 2000). It has been observed that the high density of interfaces makes nanolaminates susceptible to thermodynamically driven microstructural changes upon annealing, out of which four different types can be distinguished: (i) interdiffusion, (ii) coarsening of the layering, (iii) reactions between the layers to produce a new phase, and (iv) transformation within one or both layer types (Pinheiro *et al.* 2009, Mayrhofer *et al.* 2004, Mitterer *et al.* 2001). Enhanced hardness of up to 300% compared to single-layered (monolithic) material has since been observed for nitrides with a periodicity of 5-10 nm, both for single and polycrystalline nanolaminates of the type TiN/(Ti,Al)N, TiN/Si_3N_4, TiN/TiBN, TiN/Ti, and TiN/NbN (Chen *et al.* 2007, An *et al.* 2009, Chu *et al.* 2008, Cheng *et al.* 2010, Hultman *et al.* 2000). Elastic-moduli differences of the constituting layer materials are considered to be a critical factor for the strengthening by virtue of dislocation hindering across interfaces. The use of nanolaminates or nanolayered thin films as hard protective coatings on cutting tools, however, exposes the structure to elevated temperatures during the cutting process which may subject the tool to temperatures as high as 1000-1200ºC (Martin 2010, Veprek *et al.* 2002).

2011-till date	In these years, main focus of research is the development of new advanced hard nanocomposite coatings with enhanced toughness. It has been observed that the hardness H is not sufficient condition to reach low friction μ and the friction μ decreases with decreasing value of effective Young's modulus E_r. Besides a friction phase which is always the most important part of every tribological coating its mechanical properties (H, E_r, W_e) can also strongly contribute to reduced the friction of coatings. The hard coatings with a high ratio $H/E_r > 0.1$ are highly elastic coatings with the elastic recovery (W_e). $W_e \geq 70\%$ is of a key importance for the development of hard coatings with enhanced toughness. These coatings should exhibit (i) low values of the effective Young's modulus (E_r) satisfying the condition $H/E_r > 0.1$, (ii) high elastic recovery $W_e \geq 60\%$, (iii) strongly improved tribological properties, and (iv) enhanced resistance to cracking (Voevodin *et al.*, Musil 2012A, Kataria *et al.* 2012, Kim *et al.* 2011, Polaki *et al.* 2013, Ramadoss *et al.* 2013). The development of advanced hard nanocomposite coatings with enhanced toughness is a difficult task because the hardness H and the effective Young's modulus E_r are two mutually coupled quantities The coatings fulfilling these requirements can be prepared if the element added into a base material is correctly selected. The magnitudes of H and E_r of the coating depend on the deposition parameters used in its preparation and are controlled not only by the elemental composition of coating but also by its structure, phase composition and microstructure, i.e. by the energy delivered to the growing coating particularly by bombarding ions and condensing atoms. In this regard, many transition metal nitride coatings have been developed so far, however, at present; there are very few information on the formation of metal nitride coatings (CrNiN, ZrNiN) that meet with tribological demands. Musil *et al.* (2001) have investigated that the mechanical properties ($H/E_r > 0.1$, $W_e > 70\%$) of nanocomposites composed of nc-MeN/soft phase (ZrCuN, CrNiN, ZrNiN nanocomposite coatings) and concluded that they are superior in comparision to mechanical properties ($H/E_r < 0.1$, $W_e < 70\%$) of nanocomposite composed of nc-MeN/hard phase (TiSiN, TiZrN, TiAlN). At present, there are no general rules which allow to predict how to prepare the coatings with $H/E_r > 0.1$.

Among the developed coatings, Titanium Nitride (TiN) and its alloy like TiSiN, TiAlN in composite form and nc-TiN/a-Si_3N_4 in multi layer form have been used widely used as wear protective coatings for wide scale applications. Titanium nitride hard coating deposited by PVD has been used on an industrial scale for many years. The (TiN_x) compounds are found to exhibit both covalent (Ti-N) and metallic (Ti-Ti) and bonding features. High melting point, extreme hardness and brittleness are the properties exhibited due to covalent bonding and the properties like electrical conductivity and metallic reflectance show metallic contribution. (111) orientation is the preferred for TiN thin films deposited by PVD. It has been observed that the TiN film which possess the highest hardness are those exhibiting (111) orientation (Ljungerantz *et al.* 1996, Banerjee *et al.* 2002). However, by controlling the ion/metal flux (J_i/J_{Ti}) ratios, the TiN preferred orientation may be changed from (111) to completely (200) (Chun 2010). The hardness of TiN is ~ 2500 kg/mm^2 Knoop or Vicker Hardness (~ 85 Rockwell C Hardness or 24.5 GPa). Due to the formation of a metallurgical bond, the adhesion of TiN is good with the substrate that will not chip, blister, flake, or peel. In fact, the surface layer of the substrate is actually implanted slightly by the coating. It exhibits rocksalt structure (FCC bravais lattice) or NaCl-type crystal structure with a roughly 1:1 stoichiometry; however TiN_x compounds with x ranging from 0.6 to 1.2 are thermodynamically unstable. Due to the steady oxidization of TiN at temperatures ~ 500ºC, poorly adherent TiO_2 rutile phase oxide layer forms on top of the TiN. This leads to the deterioration of the wear protection of TiN coatings (Michalski *et al.* 1995, Wuhrer *et al.* 1996). Due to the limited temperature stability of TiN there is a need for the improvement which leds to the development of TiAlN and further addition of silicon nitride during TiN deposition.

Hirai *et al.* (1982) observed that the partial solution of TiN in Si_3N_4 is obtained by the co-deposition of Si_3N_4 and TiN carried out at high deposition temperatures (1050–1450ºC). It was observed that sharp phase boundaries do not at these temperatures. This is an important requirement for increased hardness. Later Shizhi and coworkers used PACVD to deposit silicon-containing TiN at temperatures around 550ºC which was identified as nanocrystalline TiN in a silicon nitride matrix with hardness values of 6000 Vickers (Shizhi *et al.* 1992). Veprek et al. studied isotropic nanocomposites, especially nc-TiN/a-Si_3N_4 where “a” ans “nc” stand for “amorphous” and “nanocrystalline” respectively (Veprek *et al.* 1995A, Argon *et al.* 2001). It has been observed from Ti-Si-N phase diagram at 700-1000ºC that Ti-Si-N exhibit TiN, Ti_2N, Si_3N_4, Ti_5Si_3, TiSi, and $TiSi_2$ compounds. This was shown by calculations (Barin *et*

al. 1973 and 1977) and confirmed by experiments. (Beyers *et al.* (1984)). This condition makes the Ti-Si-N system very interesting for use as nanocrystalline composite coatings, such as nanocrystalline (nc) TiN embedded in an amorphous (a) matrix of Si_3N_4. Extremely high hardness values of nc-TiN/a-Si_3N_4 exceeding 100 GPa have been reported by Veprek *et al.* (1995A).They could show that in conjunction with a-Si_3N_4, hardness enhancement may also occur for other transition metal nitrides such as W_2N (Argon 2001). But the properties of nc-TiN/a-Si_3N_4 starts to degrade above 500ºC working temperature.

Ti-Al-N ternary system has attracted considerable research and industrial interest. Ti-Al-N is commonly applied in many industrial applications. Normally, the solid solubility of TiN and AlN is extremely limited with less than 2 at.% Al in TiN at 1000ºC (Schuster *et al.* 1984, Oliveira *et al.* 2006). However, Al-content up to x=0.4 was obtained in cubic $Ti_{1-x}Al_xN$ (alloy) films by sputter deposition at 500ºC substrate temperature (WahlstroKm *et al.* 1993). The hardness of Ti-Al-N is higher than TiN and is therefore is an important candidate for machining of abrasive materials, e.g. grey cast iron or cast Al-Si alloys. Moreover, new interesting possibilities have been offered by Ti-Al-N system for the development of coating such as low N contents may be added to Ti-Al films in order to reach a good compromise between a low friction coefficient and high hardness. A higher strength of Ti-Al-N has also been observed at elevated temperatures (over 800ºC), better thermal barrier properties and a higher oxidation resistance compared with TiN and Ti(C, N) and is therefore ideally qualified for abrasive cuts with high cutting temperatures (Löffler 1994, Coil *et al.* 1992, Leyendecker *et al.* 1991) (Ti,Al)N exhibits application in the case of more thermally influenced processes.

As discussed earlier, if a given application is to be affect positively by a tribological coating, several important requirements must be satisfied, including high mechanical hardness and toughness, strong adhesion, uniform and adequate thickness, high thermal/chemical stability, low friction, smooth surface finish etc. Dense morphology must also be exhibited by the coatings (i.e. no open columnar grain boundaries or porosities). During tribological use, the coatings which with wear out rather quickly are those which exhibit porous columnar structures. Due to the repeated bending or tilting of columnar grains exhibiting poor inter-column cohesion, there occurs microfracture-dominated wear during machining or sliding operations. Therefore, it becomes extremely important that a strong cohesive bonding occurs among grains of a coating. For improved performance, another important parameter is

uniformity and adequacy of coating thickness. The tribological coatings in which all of these requirements are fulfilled, can increase performance and durability of those components and parts that are being used in an application.

1.5 Role of Hardness and Toughness in Wear Damages

1.5.1 Role of hardness

The hardness of a material, being defined as the resistance of a material to plastic deformation, is directly linked to its ability to deform under applied pressure by crack initiation, by dislocation movement, or by similar mechanisms. Hindering of dislocation movements can be achieved through: (i) grain boundary hardening, (ii) solid solution hardening. Hard coatings have been successfully used for protection of materials and particularly to enhance the life of cutting tools since the 1970's and it increases with decrease in grain size by Hall-Petch relationship as

$$\sigma_y = \sigma_o + \frac{K}{\sqrt{d}} \tag{1.2}$$

where, σ_y is the yield stress of the material, σ_o is the intrinsic yield stress of the bulk material, *K* is the material constant and *d* is the grain diameter.

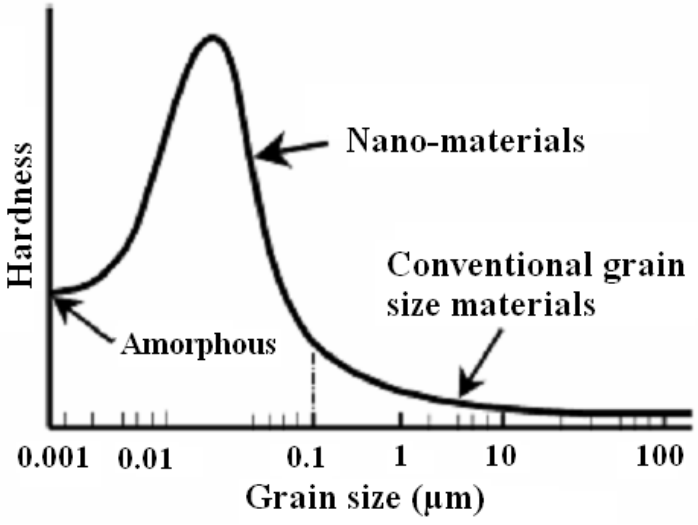

Figure 1.1 *Hardness vs grain size*

It is evident from **figure 1.1** that for conventional materials in which grain size is more than 100 nm, the hardness is very less due to the reason that free movement of dislocation is unaffected by less number of grain boundaries. However, when the grain size decreases and below 100 nm, the grain boundary volume fraction increases which obstruct the movement of the dislocations and therefore hardness increases. Again, when the grain size reduces to less than 10 nm, hardness of the material decreases due to the grain boundary sliding and this is known as inverse Hall- Petch effect. Hard coatings can be divided into three groups according to their hardness (Musil 2000, Shtansky *et al.* 2004).

a) The hard coatings with hardness $H < 40$ GPa
b) The superhard coatings with $40 \leq H \leq 80$ GPa
c) The ultrahard coating with $H > 80$ GPa

The hard coatings are extensively used for tribological applications and their development by various physical and chemical routes are competing with each other to achieve their superior performance in the actual engineering applications such as coatings for cutting tools under dry and high speed machining conditions and protective coatings for turbine blades and engine parts to improve their durability (Chandra *et al.* 2006A). Many binary and ternary metal nitrides coatings belong to hard material but relatively less number of nitrides coatings are superhard such as amorphous diamond-like carbon (DLC), cubic boron nitride (c-BN), polycrystalline diamond coatings and amorphous carbon nitride (a-CN). Moreover, these superhard coatings are thermodynamically unstable, which limits their utilization in some applications (Sankaran *et al.* 2013, Mannling *et al.* 2001). For instance, applicability of diamond coated cutting tools is limited by the high chemical affinity of carbon to iron. Owing to the chemical dissolution of boron in iron, similar issues may be expected when the c-BN coating is used in cutting of steels. Due to these problems, intensive research has been done in this area, and recently nanocomposites based new superhard materials are being developed (Musil 2000).

The ability of the coatings to protect base material from erosive wear is related to their composition and processing; and especially to the structure of the coatings. Hindering of dislocation movements can be achieved by: (i) grain boundary hardening (ii) solid solution hardening (iii) age hardening and (iv) compressive stress hardening. Among the properties of the coating materials responding for wear damages (such are chemical stability, elasticity and

surface roughness, etc.), the hardness and fracture toughness highly influence the impact dynamics of the sand particle-to-coating surface interactions and thus the erosion rate. The hard silt particles, mainly quartz, are transported by the incoming water jet from dam site and cause damage by cutting of the surfaces of underwater parts. Erosion of ductile material by hard silt particles occurs by formation of deep and wide grooves, known as ploughs containing lips on the target surface as shown in **figure 1.2**. As the grooves become deeper, they may appear as through cracks or deep cavities. A coating material exhibiting fine ploughs possesses good erosion resistance. Erosion by silt particles depends on the angle at which the silt particles impinge on the coating surface. At low angles (20°-45°) erosion occurs by formation of surface ploughs and lips. The impinging silt particles provide tangential forces on surface ligaments and extrude the material causing ploughs in the direction of the particle flow. On the edges of the ploughs the extruded target material forms the lips which are in a highly work hardened state. The amount of work hardening continuously increases and causes embrittlement and subsequent removal as debris. Various studies (Hutchings 1981) have shown that hardness is perhaps the most important property as it provides resistance to ploughing and scratching by hard particles. The general trend in the variation of erosion rate with hardness can be divided into two stages. In the first stage the material develops increasing erosion resistance with increasing hardness. After reaching the maximum, however, in the second stage any further increase in hardness leads to the tendency of embrittlement, which results in a decrease in erosion resistance. So the hardness of coatings material in the range of 25-35 GPa may be sufficient to encounter abrasive wear damages (Musil 2012A). On the other hand, for brittle material; the plastic shear is very limited and the sand particle impinging at higher angle (90°) do the removal of chunks of material by a mechanism involving brittle fracture as shown in **figure 1.3**. The eroded surface shows in this case no ploughs. Only surface pits and cavities are formed by hard hitting silt particles. To mitigate fragment type of failure, coatings should have high toughness or ductility, which facilitates plastic flow of the target material by the impact of silt laden water. Poor ductility leads to a tendency for localization of strains and development of cracks.

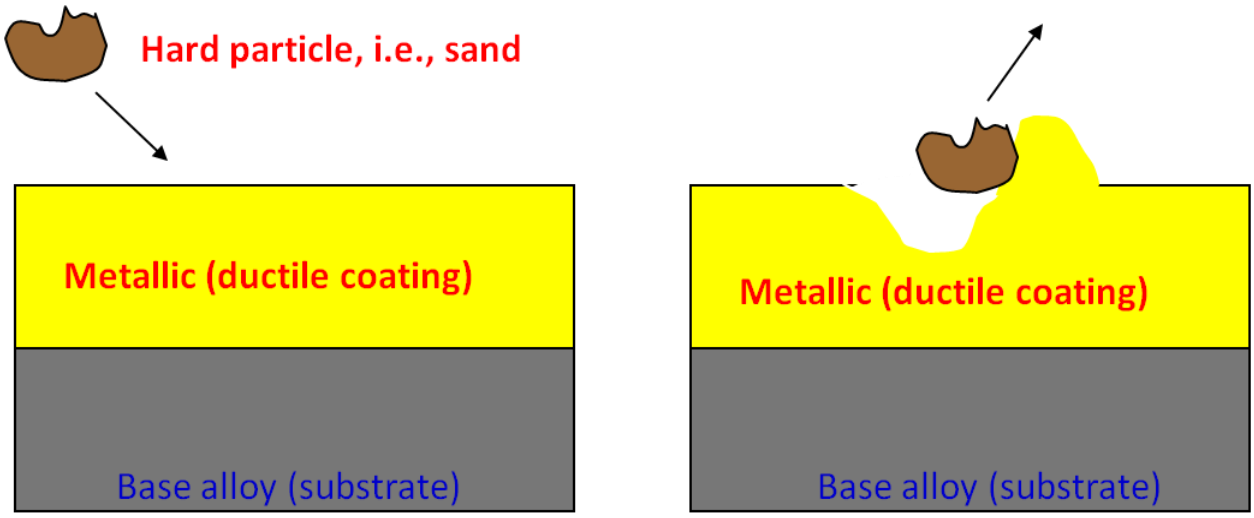

Figure 1.2 *Erosion of ductile material/coating by hard silt particle bombarded at low angle*

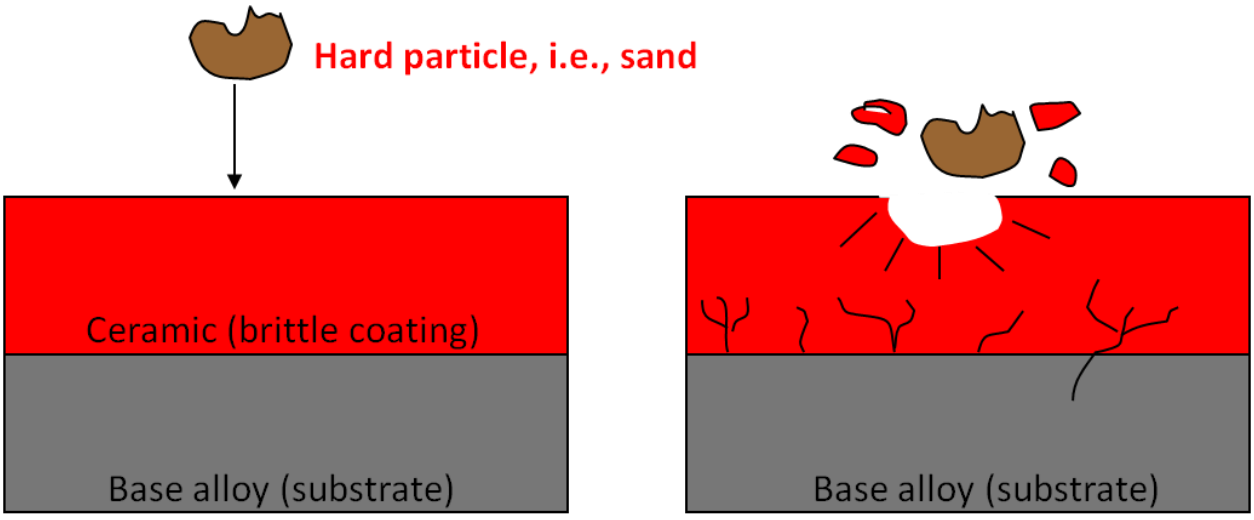

Figure 1.3 *Erosion of brittle material/coating by hard silt particle bombarded at high angle*

1.5.2 Role of toughness

Toughness describes the resistance against the formation of cracks resulting from stress accumulation in the vicinity of structure imperfections. In an energetic context, toughness is the ability of a material to absorb energy during deformation up to fracture. (Zhang *et al.* 2005).

Toughness encompasses the energy required to create a crack and to enable the crack to propagate until fracture. Therefore, a high toughness coating has high resistance to formation of cracks under stress, and in the mean time, high energy absorbance to deter crack propagation, whereby preventing chipping, flaking or catastrophic failure. In general those materials are hard to cut at last has high toughness. In addition to superhardness, high toughness of a coating also has equal importance especially for tribological applications where high shear and normal forces are present. The level of protection needed in a sliding contact or machining application may not be provided by Hardness alone. Sometimes, superhardness may be due to high levels of internal stresses within the films, and such a condition may be detrimental to wear resistance and fatigue and of such coatings. The various methods for toughening the coatings are (i) ductile phase toughening (ii) compressive stress toughening and (iii) phase transformation toughening. In principle, all toughening mechanisms can be applied to the toughening of thin films or coatings, the real challenge lies in the implementation. Recent experimental studies have confirmed that most nanostructured and composite coatings possess relatively high fracture toughness and for industrial applications such as high-speed cutting and forming processes have increasing severe mechanical contact conditions that drive the development of materials with a combination of hardness and toughness. From a practical viewpoint, 'super-tough' can be preferable to 'super-hard' in highly loaded mechanical contact (Zhang *et al.* 2003, Breake *et al.* 2011). It is proposed that their nano-size grain morphology can also provide an ideal condition for resisting crack initiation. Even if a crack has initiated within a grain, strong grain boundaries can arrest or deflect it back to the grain and hence prevent or retard crack growth. Overall, superhardness and toughness are quite achievable in nanostructured or composite coatings by producing high-strength grain boundaries and by controlling the surface and interface energy of nanograins and the extent of texture, residual stress, and strain throughout the films.

Industrial applications such as high-speed cutting and forming processes exhibit severe mechanical contact that drive the development of materials with a combination of hardness and toughness. Coatings which exhibit both hard and tough behavior are the hard nanocomposite coatings with enhanced toughness. Such coatings should exhibit a low plastic deformation, should be very elastic, exhibit resilient properties when the plastic deformation is zero and an enhanced resistance to cracking.

For engineering applications, only super-hardness does not serve the purpose while a combination of hardness and toughness is more favored by academics due to the industrial needs. In this direction, a sensible approach is to toughen superhard coatings so as to achieve what is called as ‘‘hard yet tough’’ coatings.

1.5.3 Hard and tough coatings

Ductility and hardness have a roughly inverse relationship, increasing one invariably reduces the other.

Many research in the field of PVD set as their goal the pursuit of high hardness, apparently believing that this will provide the ultimate level of wear resistance. However, it has been observed that only high hardness can not mitigate the wear damages. Oberle and Hutchings have investigated (Oberle 1951, Hutchings 1981) for a range of material, that the wear resistance actually decrease with increasing hardness, if that increase in hardness was associated with an increase in the elastic modulus. In case of erosion damages, coating material of high hardness with some definite amount of ductility is perhaps the best choice. This has also been theoretically predicted by Hutchings (1981). Naim *et al.* (1986) observed that erosion rate increases with increasing hardness at constant ductility and also noted a decrease in erosion rate as the ductility increases at about constant hardness.

Hooke's law $\sigma = E*\varepsilon$; (ε is the strain and σ is the stress) provides the way to produce tough, hard, and resilient coatings. This shows that for a material to exhibits a higher value of ε or a higher value of elastic deformation at a given value σ, it is required to reduce the Young's modulus E. It means that there is a need to develop those materials which for a given hardness H (σ = const) exhibit lowest value of the Young's modulus E. The solution seems to be very simple but is actually a very difficult task (Musil 2012A).

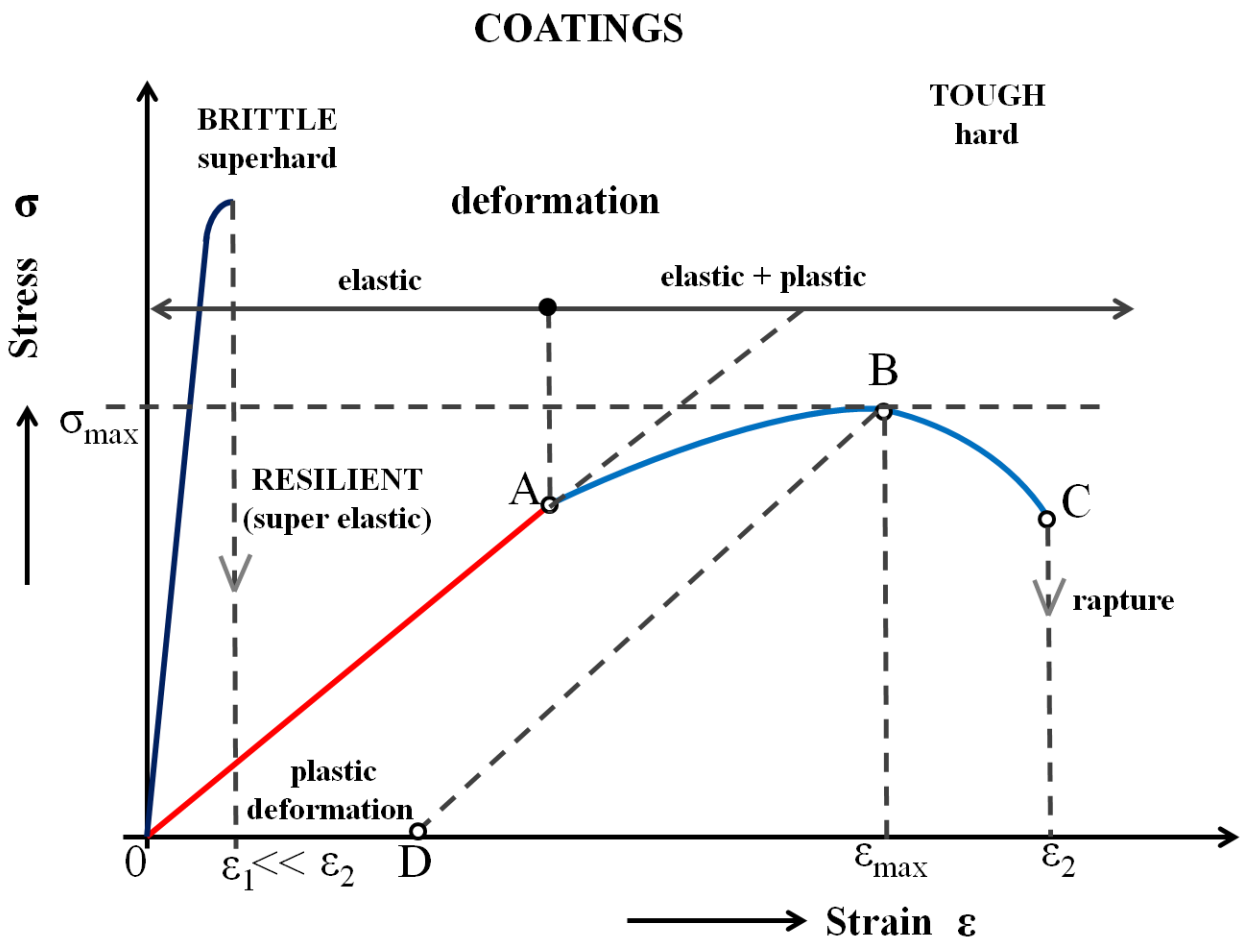

Figure 1.4 *Schematic display of* stress σ vs strain ε dependences for brittle, tough and resilient hard coatings

The stress σ vs strain ε dependences for brittle, tough and resilient hard coatings are schematically displayed in **figure 1.4**. The brittleness of superhard materials is very large, they exhibit very low strain $\varepsilon = \varepsilon_1$ to a rupture and almost no plastic deformation. Both elastic and plastic deformation is exhibited by hard and tough materials exhibit. Higher toughness is exhibited by materials which withstand a higher strain $\varepsilon_1 \ll \varepsilon \leq \varepsilon_{max}$ without cracking. When ε_{max} is achieved at higher values of σ_{max}, the hardness of tough materials is higher. On the contrary, in comparison to hard and tough materials, fully resilient hard coatings exhibit higher elastic recovery W_e, lower hardness H, and no plastic deformation (line 0A). Enhanced resistance to cracking is the main advantage of hard and tough coatings. These are reasons why hard and tough and fully resilient hard coatings should be developed in a very near future. A new generation of advanced hard nanocomposite has been represented by these coatings.

1.6. Overview of ZrWN and ZrWBN

1.6.1 Reason behind combining group IV (Zr-N) and group VI (W-N) transition metal nitride and expected results

The protection of materials by hard coatings is one of the most important and versatile means of improving components performance. Multicomponent refractory material systems can provide opportunities for specific materials for wear resistant coatings. We know of a tremendous number of refractory materials have been used for triboligical applications. A system or a substrate-coatings combination is selected depending upon the application. Because substrate and coating material exhibit vastly differing properties, depending on the required level of system integrity, only a few combinations have been successful. Therefore it is important to have criteria for the selection of most suitable coating material for specific needs. The search for new or alternative materials, whether through experiment or simulation, has been a slow and arduous task.

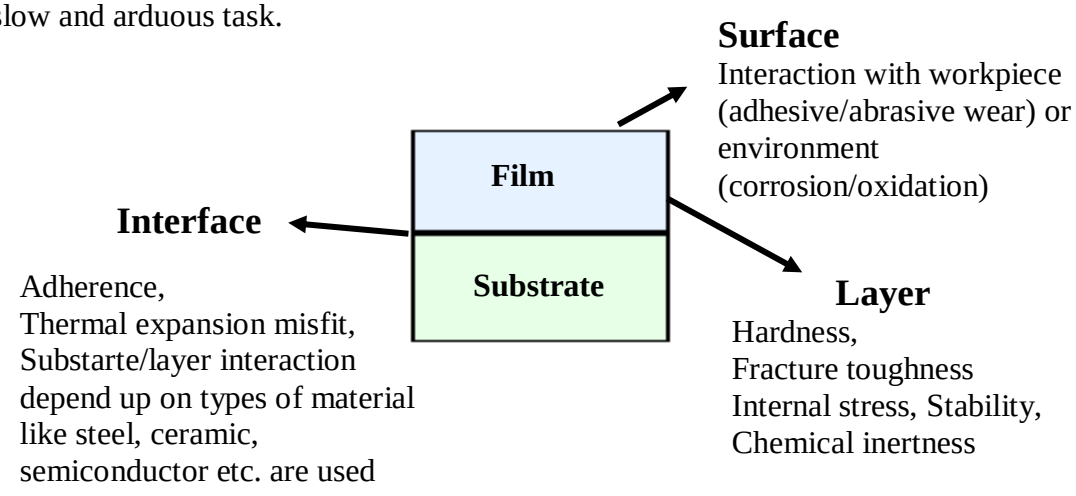

Figure 1.5 *Different zones of a coating*

Figure 1.5 provides some important criteria for the selection of coating system. It can be clearly seen that a coating system has three different zones (layer, surface and interface), having different properties requirements and role for the development of coatings material for specific application.

First, is the layer material where composition and microstructure determine properties such as strength, hardness, fracture toughness, internal stress, thermal conductivity and thermal

stability. Second, is the substrate interface where adherence, strains by thermal expansion misfit and interaction (reaction) of the substrate with the layer are critical points. Finally, the layer surfaces where the interaction tendency of the layer material with a work piece or with the environment has to be considered. Problems with the material selection arise mainly because many desired properties such as good adherence at the substrate-layer interface and no surface interactions, or high hardness and high toughness of the layer cannot be obtained simultaneously. Increasing hardness and strength are concomitant with decreasing toughness and adherence.

The main factors which determine coating material (layer) properties is shown in **figure 1.6**. The relationship between constitutes of coatings and fabrication process/parameters determines the microstructure and finally properties of the coating and consequently pointing out the selection of materials for specific application (Holleck 1986**,** Subramanian and Strafford 1993, Zhao *et al.* 2005)

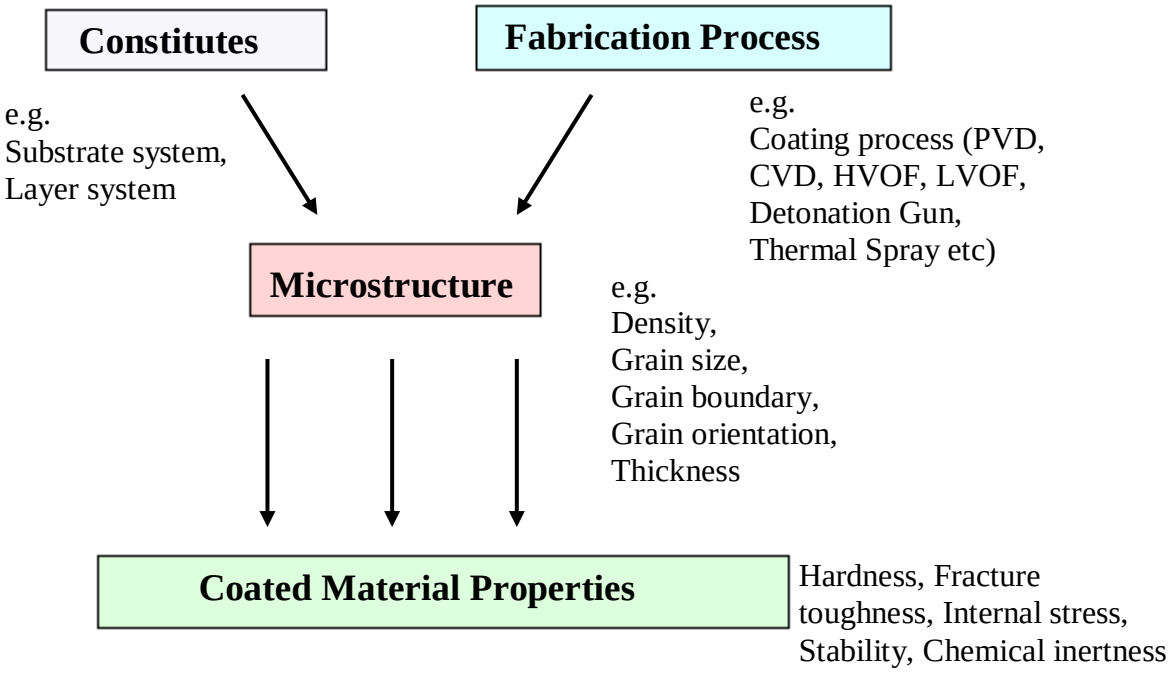

Figure 1.6 *Factors fixing coated materials*

For constitute point of view, many hard materials have been studied so far and they divided in to three groups on the behalf of bonding (metallic, ionic and covalent) between elements as shown in schematic manner in **figure 1.7**. Each of the different group of hard materials shows advantages and disadvantages in respect of an application as hard coating. The

type of bonding between constitutes highly affect the physical and chemical properties of compound. A comparison of coatings relevant properties of the hard material groups is shown in **table 1.3.**

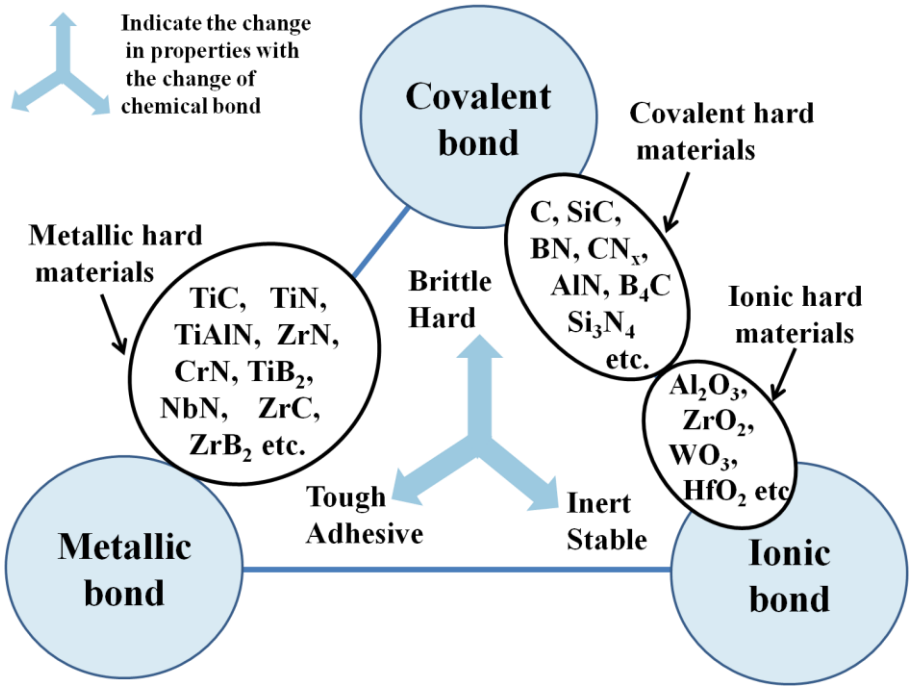

Figure 1.7 *Different group of hard material*

Table 1.3 *Properties and behavior of the different group of hard materials*

Order	Brittleness	Hardness	Elastic modulus	Stability - ΔG	Thermal expansion Coefficient	Melting point	Adherence to metallic substrate
High	I	C	M	I	I	M	M
Medium	C	M	C	M	M	C	I
Low	M	I	I	C	C	I	C

M: metallic, C: covalent, I: ionic

Because of complex requirements for wear resistant coatings such as high hardness, high toughness, good adherence at the substrate-layer boundary and high stability, a alloying of different group hard material seem to be the best negotiation. This alloying can be achieved

either in the form of multicomponent (solid solutions, binary, ternary etc.) or multiphase (solid solution/intermetallic compound) or multilayer coatings. It can also see from **table 1.3** that a blend of metallic hard material and ionic hard material may be the best combination for the development of novel coating material to mitigate erosive damages **(**Chauhan *et al.* 2013, Holleck 1986, Jehn 2000, Zhao *et al.* 2005, Subramanian *et al.* 1993).

In ternary metal nitrides, according to Holleck (1986) blend of ionic bonding and metallic bonding can be obtained if we combine group IV and group VI binary transition metal nitrides. It has been observed in above literature survey, that by proceeding from group IV to group VI transition metal nitrides one gets an increase in amount of metallic bonding, a decrease in room temperature hardness, an increase in hot hardness, an increase in fracture toughness and small interaction tendency with other materials. Moreover, IV group nitride has higher ionic character percentage as compare to VI group nitride.

Group IV binary transition metal nitrides (TiN, HfN, ZrN) are brittle in nature, exhibit high stability and high hardness, while group VI binary transition metal nitrides (CrN, MoN, W_2N) are less reactive in nature, exhibit high toughness and high adhesion. In literature, systems containing the combination of group IV and group VI binary nitrides have been studied. These include Ti-W-N, Zr-Cr-N, Ti-Cr-N, Ti-Mo-N, Zr-Mo-N, Ti-Zr-N and Cr-Mo-N. It has been observed that the mechanical properties of these ternary nitrides is better than their binary nitrides (Song *et al.* 2007, Hsu *et al.* 2013, Moser *et al.* 1994, Yang *et al.* 2005, Regent *et al.* 2001, Kim *et al.* 2009, Purushotham *et al.* 2007, Ryan 1964, Schwarz *et al.* 1985).

In the present research work, zirconium nitride (group IV binary nitride) and tungsten nitride (group VI binary nitride) have been selected for the development of super hard and tough nanostructure Zr-W-N coating material.

1.6.2 Zirconium Nitride Coatings

Since 1960, there has been intense research on ZrN centered around the study of defect properties and diffusion phenomenon. They are sometimes called "refractory hard metals" because of their metallic properties, "interstitial compounds" because the small non-metal nitrogen atom appears to fill the octahedral void between the metal atom and "defect compounds" because both the metal and non-metal lattices can tolerate atom vacancies in rather large concentration. From a chemist's viewpoint zirconium nitride (ZrN) like most of the mononitrides of transition elements, offers a unique collection of properties to be reconciled, namely (Liu *et al.* 2003, Vetter *et al.* 1990).

(i) Metallic bonding indicated by electrical conductivity, Hall effect measurements, magnetic properties, appearance (luster), and presence of homogeneity regions.

(ii) Covalent or ionic bonding suggested by high melting points, hardness and brittleness.

(iii) Ionic bonding inferred from chemical behavior, X-ray emission bands and Mossbauer spectroscopy.

Due to its metallic band structure, the only stable phase is stoichiometric ZrN compound which exhibits a gold-like colour. Other non-stoichiometric metastable phases exist like Zr_2N (Liu *et al.* 2003), Zr_3N_4 (Pichon *et al.* 1999), ZrN_2 (Dauchot *et al.* 1995) and Zr_4N_3 (Ivanovskii *et al.* 2001). Recently, Zr_3N_4 was synthesized using a high temperature (700ºC) and high pressure (~15 GPa) technique. These materials are corrosion resistant and extremely hard (40 GPa) and also exhibit interesting electrical and optical properties. For example, they exhibit semiconducting nature with an energy band gap around 1.4 eV. These properties make them useful in electronic devices such as photovoltaics.

Among group IV and group VI transition metal nitrides, the transition metal nitrides which are based on titanium nitride (TiN) and chromium nitride (CrN) have stimulated commercial interest due to their wear and corrosion resistance, extreme hardness, and thermal and electrical properties. Recently, ZrN coatings attracting much attention over TiN and CrN (Chou *et al.* 2002), due to their characteristics such as high hardness (Brugnoni *et al.* 1998), excellent wear resistance (Vetter *et al.* 1990, Sue *et al.* 1995) and gold like color in the visible

wavelength region (Niyomsoan *et al.* 2002) and have been used for protective coatings in decorative coating and cutting tools (Ramana *et al.* 2000, Sue *et al.* 1989).

In addition, the zirconium nitride film can be used as a diffusion barrier in microelectronic devices (Takeyama *et al.* 2002) and emitter coating for field emission devices (Nagao *et al.* 1998). Since its optical properties are highly dependent on the nitrogen composition, zirconium nitride coating can also be used as optical filters, (Benia *et al.* 2003). The oxidation resistance of ZrN is generally concidered to be poor. It is the main reason why this material received so little application as a refratory compound despite its relatively high thermal stability. Heated in air at atmospheric pressure powdered ZrN begins to oxidize between 400 and 600ºC (Panjan *et al.* 1996).

Larijani *et al.* (2009) have investigated the effects of post annealing treatment (at 700ºC under Ar ambient) on the microstructure and hardness of as deposited ZrN films. They reported that the ZrN films retain their fcc phase but with reduced thickness after annelaing. The formation of zirconium oxides and decrease in residual compressive stress reduces the hardness of ZrN films.

In silicon semiconductor technology, owing to the good diffusion barrier in Cu metallization, ZrN is one of the excellent materials for the use in ultra large-scale integration technology, due to its low electrical resistivity, chemical and metallurgical stability similar to TiN. Takeyama (2002) *et al.* reported ZrN thin film as a good diffusion barrier in Cu/ ZrN/Si contact systems up to 750ºC for 1 h without any Cu penetration through it into the silicon.

ZrN coating also has been attracting interest in biomedical engineering. ZrN has a good compatibility with human tissue and might thus be considered as a biomaterial for use in surgical implants. ZrN coatings have been reported to exhibit better corrosion protection ability compared to TiN and have been used to improve the corrosion resistance of some biomaterials as stainless steels and NiTi alloys (Xin *et al.* 2009, Cheng *et al.* 2006).

However, since zirconium has a higher melting point, a lower vapor pressure, and higher contamination susceptibility by oxygen and carbon, it is more difficult to deposit ZrN film than TiN or CrN films. So far, many techniques such as vacuum arc deposition (Zhitomirsky *et al.* 1997), direct current (dc) reactive magnetron (Wu *et al.* 1997), pulse laser

deposition (Spillmann *et al.* 2001), and ion beam assisted deposition (Ensinger *et al.* 2000) have been used to prepare zirconium nitride films. Although many investigations have revealed that the preferred orientation in other transition metal nitrides is determined by the growth process (Farkas *et al.* 2004, Tung *et al.* 2009A), there are few reports on the mechanism of texture evolution of the texture for zirconium nitride films grown by magnetron sputtering.

1.6.3 Tungsten Nitride Coatings

Tungsten nitride (WN_x) belongs to a class of refractory metal nitrides that have the unique properties of excellent hardness, chemical inertness, high melting point, good chemical stability and high conductivity (Toth 1971). The combination of these properties makes tungsten nitride a suitable material for diffusion barriers in microelectronic devices (Shar 1979, So *et al.* 1988), schottky contacts to GaAs (Lee *et al.* 1995), gate electrodes in metal-oxide-semiconductor field effect transistors (Moriwaki *et al.* 2000, Claflin *et al.* 1998), and hard wear resistant coatings for cutting tools (Yamamoto *et al.* 2005, Polcar *et al.* 2007, Polcar *et al.* 2008) tribological properties of nitrides of transition metal thin films deposited by reactive magnetron sputtering have been thoroughly studied for three decades. Nevertheless, there are still several gaps in knowledge. The majority of studies are focused on a limited number of metals, namely Ti, Al and Cr, while other potentially attractive compounds are aside the main attention. Coatings of transition metals nitrides are known for their high hardness (40 GPa) and excellent wear resistance, being titanium nitride the best known member of this family. However, its tribological properties are significantly diminished when the coating is exposed to elevated temperatures, particularly due to rapid oxidation. In this respect, chromium nitride possesses significant advantages compared to TiN, mainly higher oxidation resistance, thermal stability and, particularly, corrosion resistance. On the other hand, as main drawback CrN exhibits a significantly higher friction coefficient, this is not desired in many applications (Polcar *et al.* 2005). Other nitrides, such as MoN, VN or AlN, could outperform TiN or CrN in many parameters; however, their commercial use is very limited. Tungsten nitride stays still aside of attention despite some significant advantages, such as extremely high hardness and excellent adhesion on typical steel substrates. Yamamoto *et al.* (2005) and Hones *et al.* (2003) have observed a change in the structure for WN_x films in the region of $N/W \leq 1$, from W to tungsten mononitride WN, which exists in two structural modifications (low temperature

hexagonal h-WN and high temperature cubic c-WN) through fcc tungsten subnitride W_2N with increasing N concentration in the films. However it was not clear when stoichiometric hexagonal WN appeared.

Suetin *et al.* (2010) studied the electronic structure, density, cohesion energies, coefficients of low temperature heat capacity (γ) and Pauli paramagnetic susceptibility (χ) of cubic tungsten subnitride W_2N by using a full potential linear augmented plane wave (FLAPW) method with the generalized gradient approximation (GGA) of the exchange correlation potential. They reported that among tungsten nitrides, W_2N subnitride has the maximum density (17.110 g/cm^3), the minimum values of DOS at the Fermi level N^{tot} (E_F) (0.800 state/eV·cell) and γ (1.89 mJ.K^{-2}.mol^{-1}), χ ($0.25*10^{-4}$ em/mol) coefficients, and also the maximum energy (–10.94 eV/atom) of cohesion.

Polcar *et al.* (2007 and 2008) have studied the tribological behavior of tungsten nitride (WN_x, x = 30, 47, 50 at.%) coatings at room temperature up to 600ºC. They reported that all coatings exhibited the cubic β-W_2N phase; however, the hexagonal δ-WN phase also appeared and became dominant when the nitrogen content was 58 at.%. The increasing temperature did not affect significantly the structure up to 400°C. At 500°C, the presence of weak oxide peaks revealed a surface oxidation and a further increase of the temperature led to the entire oxidation of the tungsten nitride coating. At room temperature, $W_{70}N_{30}$ was the hardest coating (~ 41 GPa), while the coatings with higher nitrogen content, $W_{53}N_{47}$ and $W_{42}N_{58}$, exhibited similar hardness values close to 30 GPa. The hardness measured after annealing slightly decreased with temperature and dropped to 6 GPa for 600ºC, a value typical for tungsten trioxide. The tribological performance of the coatings is excellent up to 300ºC with no measurable wear. Further increase in the temperature dramatically changed the wear mechanisms causing a severe coating damage in the centre of the wear track. The entire oxidation of the coating at 600ºC is detrimental for the wear resistance.

Furthermore, many investigations (Jiang *et al.* 2006, Boukhris *et al.* 1997, Yamamoto *et al.* 2005) have revealed that the phase structure and composition in WN_x films have a significant effect on the performance of the layer in certain applications, such as diffusion in microelectronic devices, electrical resistivity, work function, and hardness. However, due to the

complex relationship between processing parameters and physical properties of the layers, an understanding of these relationships is crucial for designing layers with the desired properties and exceptional performances. So far, many techniques have been used to achieve tungsten nitride such as metal organic chemical vapor deposition (Kim *et al.* 1991), DC/RF reactive sputtering (Shen *et al.* 2000, Polcar *et al.* 2007, Migita *et al.* 2001, Hones *et al.* 2003), ion beam sputtering (Abadias *et al.* 2006), reactive laser ablation (Soto *et al.* 2003) and cathodic arc (Yamamoto *et al.* 2005). Among these techniques, reactive sputtering is of special interest because it is an industrial process applicable to large area deposition, and high quality films can be obtained even at a low substrate temperature.

1.6.4 Zirconium Tungsten Nitride (Zr-W-N) Coatings

As the demand for performance exceeds the capabilities of existing materials, new materials with superior properties must be developed. Zr-W-N is a newly developed novel coating material and very few studies have been published on this material.

An another advantage to select zirconium (among group IV transition metals) and tungsten (among group VI transition metals) for making ternary nitride is that Zr-W-N coating has the solid solution of low and high elastic modulus elements which may intern help to retard the growth or generation of cracks inside the grains. Zirconium has the lowest elastic modulus (~ 103 GPa), bulk modulus (~ 128 GPa) and hardness (~ 5.7 GPa) among group IV transition elements. On the other hand tungsten has the highest elastic modulus (~ 280 GPa), bulk modulus (~ 268 GPa) and hardness (~ 16 GPa) among group VI transition elements (Zhou *et al.* 2014, Zhao *et al.* 2005).

Wang *et al.* (2007A) investigate the influence of nanoscale modulation periods (~ 3 to 50 nm at 0.8 Pa sputtering pressure) and working pressures (0.6 to 1.4 Pa at 30 nm modulation period) on structural and mechanical properties of the ZrN/W_2N multilayered coatings deposited by RF magnetron sputtering in an ultra-high vacuum chamber. The results show that the maximum hardness is up to 34 GPa at Λ = 30 nm and at 0.8 Pa sputtering pressure. The sharp ZrN(111) and W_2N(111) preferred orientations are found in all multilayered structures. In higher working pressure, strong W_2N (200) and weak W_2N (311) texture are identified. With

decreasing working pressure, the peak intensity of W_2N (200) decrease and peak intensities of ZrN (111), W_2N (111), and W_2N (311) increase.

Yamamoto *et al.* (2010) have been found that by incorporating appropriate amount of W into Zr containing nitride films, the resulting films can have sufficient lubricity at higher temperature and can exhibit excellent wear resistance even at high temperature. Tungsten forms oxides like WO_2 (melting point ~ 1500ºC) and WO_3 (melting point ~ 1470ºC) when a cutting tool and a workpiece undergo sliding at high speed upon cutting. These oxides formed at sliding faces have melting point near to the "sliding face temperature" upon cutting and they are flexible and exhibit lubricity at these temperatures. To exhibit such lubricity, W should be ≤ 3 atomic percentage in the ZrWN films.

Perevislov *et al.* (Perevislov *et al.* 2005) have studied the optimum process parameters like temperature, composition and environment for the synthesis of $W_{1-x}Zr_xC_{1-y}N_y$ compound by pure grade WC, ZrC, and ZrN powders. The powders were grinded in a titanium mortar with ethanol, and the mixture was dried and pressed. The heat treatment was done within 1300-1900ºC. The samples were kept at constant temperature for different times under a pressure of 1.2 atm in ultrapure argon. The homogeneous $W_{1-x}Zr_xC_{1-y}N_y$ free from the impurities of starting components and W_2C is formed only for two compositions having a low concentration of tungsten and high concentration of nitrogen. They observed that to prepare complex carbonitrides $W_{1-x}Zr_xC_{1-y}N_y$, a temperature of 1700ºC, nitrogen atmosphere, and isothermal annealing for 1 h at the final temperature are the optimal parameters.

1.6.5 Zirconium Tungsten Boron Nitride (Zr-W-B-N) Coatings

Nanocrystalline transition metal nitrides coatings are attractive materials for industrial applications due to their high hardness, high melting point and chemical inertness. However, there are some drawbacks such as poor thermal stability, defects in columnar structure, low oxidation resistance and limited hardness enhancement. Hence such coatings may not mitigate physical and chemical damages of various components used in many industrial sectors, such as material processing, power generation, chemical engineering and aerospace, where need an ability of coating to operate in exotic environment. For these applications, nanocomposite coatings can make a huge positive impact (Zhang *et al.* 2003, Holubar *et al.* 2000, Baker *et al.*

2010). Nanocomposite coatings represent a new generation of materials (Voevod *et al.* 1999, Zhang *et al.* 2003, Holubar *et al.* 2000). They are composed of at least two separated phases with nanocrystalline (nc) and/or amorphous (a) structure or their combination. The nanocomposite materials, due to very small (≤ 10 nm) grains and a significant role of boundary regions surrounding individual grains, exhibit enhanced or even completely new properties and behave in a strongly different manner compared to the conventional materials composed of larger (≥ 100 nm) grains. Nanocomposite coatings exhibiting superior mechanical properties, self-lubricating properties and high thermal stability are extremely well suited for demanding tribological applications. Such coatings can also provide greater resistance to contact deformation and damage during heavily loaded rolling or rotating contacts (Musil 2005, Veprek 2004). Musil (2012A) and Veprek *et al.* (2005) have reported that the nanocomposite coatings composed of nanograins dispersed in amorphous matrix and grain boundaries of nanograins about one-monolayer-thin of nonmetallic, covalent nitride such as Si_3N_4, BN (nc-nitride/a-nitride) are highly elastic and exhibit enhanced resistance to cracking at high applied load. Nanocomposite materials consist of materials formed by light elements (B, C, and N) nitrides and heavy transition metals (Zr, W, Ti, Cr) nitrides that could introduce a high valence electron density into the corresponding compounds. The high valence electron density enables resistance to elastic and plastic deformation. (Tian *et al.* 2012, Gu *et al.* 2008A, Kaner *et al.* 2005, Gonzales *et al.* 2010). Moreover, hard nc-nitride/a-nitride nanocomposite coatings prevent to a direct connection between the external atmosphere and the substrate and thereby they should ensure a good protection of the substrate against oxidation even at temperatures when the amorphous phase start to nanocrystalline. For further increase the thermal stability of nanocomposite coatings, the amorphous phase should have the higher (> 1000ºC) crystallization temperature. Therefore light elements such as boron, and silicon were incorporated for enhancement thermal stability and corrosive resistance of nanocomposite coatings.

Recently role of boron in enhancing mechanical performance and thermal stability of nanocomposite coatings has been also demonstrated. Boron nitride (BN) thin films are of interest because of their excellent physical, chemical and mechanical properties (Shtansky *et al.* 2000, Liu *et al.* 2012, Eichler *et al.* 2008). Due to high crystallization temperature of boron nitride (≥ 800ºC) exhibited high oxidation resistance. Boride-based multicomponent nanocomposite coatings (Mitterer *et al.* 2004) can dramatically increase hardness and thermal

stability and hence reduce wear under harsh sliding or machining conditions. There are many papers reporting on boron based nanocomposite coatings, e.g. W-B-N (Louro *et al.* 2005, Reid *et al.* (1995), Ti–B–N (Mayrhofer *et al.* 2006, Rupa *et al.* 2014, Lee *et al.* 2007), Zr–B–N (Mitterer *et al.* 1991, Urgen *et al.* 1995), Cr-B-N (Mallia *et al.* 2013) and Hf-B-N (Herr a *et al.* 1997) etc. These coatings show high thermal stability, high hardness, and high oxidation resistance. It has been also noticed that by varying the boron concentration in the film, the physical and chemical properties of these nanocomposite can be tuned as per application requirement.

1.7 Objective and scope of the present research work

In many industries, such as offshore, marine, power plant, process, aeronautical and mining, numerous components like pipe work, valves, pumps, extrusion dyes, powder mixers, turbine and helicopter blades are performed in erosive and exotic environments. Such environments cause severe wear damages to these components. The extent of damage and intensity of wear are mainly subjected to surface properties of components, which make surface engineering an effective approach to control wear damages by means of modifying surface properties. Nanocrystalline transition metal nitride coatings over material surfaces have attracted considerable attention in recent years owing to their promising applications in surface engineering. As overlay coatings, transition metal nitrides offer effective way of addressing these issues by taking advantage of the distinctive physical and chemical properties including high hardness, high melting point, chemical inertness, and good thermodynamic stability. Their novel properties originate from the microstructural characteristics in terms of grain size, crystallographic orientation, lattice defects, texture and surface morphology as well as phase composition. Among various PVD techniques, DC/RF magnetron sputtering technique is an effective technique to deposit transition metal nitride coatings because of good control on processing parameters involved. Each parameter has its own role to play and microstructure as well as composition of transition metal nitride thin films can be tuned just by tuning the values of various deposition parameters involved. Moreover magnetron sputtering is of special interest because it is an industrial process applicable to large area deposition, and high quality films can be obtained even at a low substrate temperature. The coatings deposited by this technique are much cheaper to produce than the bulk nanocomposite materials. They can be applied on most ceramic and metallic substrates with strong bonding.

The aim of the present research work is to develop hard and tough advance nanocrystalline transition metal coatings using magnetron sputtering technique to mitigate wear damages like cavitation erosion and silt erosion in hydro turbine components. The transition metal nitride coating exhibiting high hardness (H ~ 20-25 GPa), low effective elastic modulus (E_r < 200 GPa), high wear resistance (H/E_r > 0.1), high elastic recovery (W_e > 60%), compressive macrostress (< 0), high toughness, high thermal stability, dense and voids-free microstructure (non-columnar microstructure) is more demanding for tribological applications. The review of available literature depicts that the transition metal nitrides coatings exhibit above mention properties are rarely reported in literature. Transition metal nitride coating exhibit high hardness with low elastic modulus satisfying H/E_r > 0.2 is not reported in the literature so far. Moreover, there are no general rules which allow to predicting how to prepare the coatings with H/E_r > 0.1. Only the tuning of elemental composition, microstructure and phase composition of coating is the way to develop advance wear resistant transition metal nitride coatings for tribological applications.

In the present work, transition metal nitrides composed of zirconium, tungsten and boron are selected after a thorough literature survey with respect to tribological applications. The main objectives of the present research work are,

- Design a hard and tough advance ternary nitride system.
- Synthesis and development of transition metal nitride coating of zirconium, tungsten and boron on silicon substrate by DC/RF reactive magnetron sputtering technique using N_2 and Ar gases.
- To examine the microstructure, thermal stability and mechanical properties of deposited coatings.
- To investigate the effect of different deposition parameters such as nitrogen flow rate, substrate temperature, post annealing temperature, negative bias voltage and sputtering power on physical and mechanical properties of ZrWN and ZrWBN coatings.
- Identification of different phases, preferred crystallographic orientation, determination of average crystalline size and stress measurement by XRD.
- Identification of crystallographic structure and phase analysis by TEM/SAED.

- To characterize the morphological and cross-sectional features of coatings by FESEM.
- To elucidate the elemental composition by EDS and WDS.
- To characterize the topographic features and surface roughness of coatings by AFM.
- To elucidate mechanical properties (hardness, elastic modulus, elastic recovery, wear resistance, resistance to plastic deformation and adhesion) by Nanoindentation.
- To characterize fracture toughness of coatings by Macroindentation.

The technical objectives of the present work can be enumerated as:

Chapter 3 (*Zirconium Tungsten Nitride coating: Study on Nitrogen Partial Pressure*) discusses the effect of nitrogen partial pressure (pN_2) (0.07 to 0.67 Pa) on structural, composition and mechanical properties of $Zr_xW_{1-x}N_y$ thin films. It has been observed that the structure and elemental composition of the deposited $Zr_xW_{1-x}N_y$ thin films strongly depend on pN_2. XRD analysis shows that for 0.07 Pa $\leq pN_2 \leq$ 0.17 Pa, $Zr_xW_{1-x}N_y$ films exhibit single (fcc) phase, for 0.20 Pa $\leq pN_2 \leq$ 0.27 Pa, an amorphous phase is obtained and for 0.33 Pa $\leq pN_2 \leq$ 0.67 Pa reflections corresponding to fcc phase Zr-W-N and hcp phase ZrN have been observed. The phase formation has been confirmed by TEM diffraction patterns (SAED). The diffuse rings in SAED pattern of film deposited at pN_2 = 0.27 Pa confirm that nanocrystalline grains were not grown during deposition. The film deposited at pN_2 = 0.47 Pa exhibit maximum (6.8 nm) roughness because the XRD peaks of ZrN are relatively prong with the XRD peaks of Zr-W-N phase which indicate that ZrN phase is well established along with Zr-W-N phase and hence roughness increases. Results of nano-indentation analysis confirm moderate hardness, high wear resistance, high resistance to plastic deformation and high adhesiveness of $Zr_xW_{1-x}N_y$ films. Among all the phases, maximum hardness (~ 24 GPa) and maximum reduced elastic modulus (135 GPa) have been obtained for dual phase (fcc+hcp) film while resistance to fatigue fracture (H^3/E_r^2 ~ 0.87 GPa), wear resistance (H/E_r ~ 0.2) and ductility for single phase (fcc) film were found to be maximum. All the films were found to exhibit high adhesion with the substrate surface.

Chapter 4 (*Zirconium Tungsten Nitride coating: Effect of Insitu and Exsitu Annealing Temperatures*) discusses about the structure, thermal stability and mechanical properties of crystalline (fcc) phase and amorphous phase Zr-W-N thin films. This chapter divided into two sections. Section 4.1 describes the effect of substrate temperatures T_s (100º-600ºC) and post annealing temperature T_n (100º-600ºC) on thermal stability and mechanical properties of amorphous phase $Zr_{19}W_{18}N_{63}$ thin films. For 100ºC ≤ T_s ≤ 300ºC, XRD patterns show an amorphous structure of the films and for 400ºC ≤ T_s ≤ 600ºC, a crystalline fcc phase with (111) and (200) orientation has been observed. The XRD findings are further confirmed by TEM and SAED patterns. Maximum wear resistance (H/E_r ~ 0.22) and maximum resistance to fatigue fracture (H^3/E_r^2 ~ 1.1 GPa) have been obtained for the amorphous films deposited at T_s = 200ºC. Post annealing of films deposited at 200ºC have been carried out in air from 100º-600ºC. Oxygen starts to be incorporated in the films at T_n = 300ºC and its content increases with increasing T_n. No crystalline oxide phases are observed up to T_n = 600ºC. The hardness of the annealed films decreases with increasing oxygen incorporation. Indentation and scratch tests for as deposited and annealed films show that no cracks propagate in the films even at a high load of 50mN and all the films exhibit high adhesion with the substrate. Section 4.2 describes the effect of substrate temperatures T_s (100º-600ºC) and post annealing temperature T_n (100º-600ºC) on thermal stability and mechanical properties of crystalline fcc phase $Zr_{22}W_{19}N_{58}$ thin films. For 100ºC ≤ T_s ≤ 600ºC, X-ray diffraction patterns of the deposited films show a crystalline fcc phase with (111) and (200) preferred crystallographic orientations of grains. A close analysis of the diffraction pattern shows that for low T_s (T_s < 400ºC) the coating structure is not simply fcc but probably contains some amorphous parts along with the fcc phase. It can be clearly seen that the contribution of amorphous part is maximum for T_s =100ºC, decreases with increasing T_s and disappears for T_s ≥ 400ºC. The XRD findings are further confirmed by TEM and SAED patterns. Maximum wear resistance (H/E_r ~ 0.22) and maximum resistance to plastic deformation (H^3/E_r^2 ~1.0 GPa) have been obtained for the film deposited at T_s = 400ºC. Post annealing of the films deposited at 400ºC have been carried out in open atmosphere at 100º-600ºC. For the annealed films, no crystalline oxide phase has been detected for 100ºC ≤ T_n ≤ 600ºC, even though oxygen incorporation in the films starts at T_n ≥ 300ºC. The films start peeling off at 500ºC and got completely peeled off at 600ºC. The crystallite size increases with increasing T_n and reaches a maximum value of ~10 nm at T_n = 400ºC. Hardness and elastic modulus of annealed films found to be increasing with increasing strain. For

practical applicability, the film deposited at 400ºC is found to be most suitable for application in the temperature range below 300ºC. But the deposition of wear protective coatings at low substrate temperature (≤ 200ºC) is more feasible for commercial aspects.

In Chapter 5 (*Zirconium Tungsten Nitride Coating: Study on Energetic Ion Bombardment*) discusses the effect of negative substrate bias voltage V_s (-20 V to -120 V) on structure and mechanical properties of fcc phase Zr-W-N coatings deposited at 200ºC substrate temperature has been studied in details. The application of negative bias voltage to the substrate leads to impingement of energetic ions on the coating surface is an effectual way to grow dense and void-free microstructure of coating at low deposition temperatures. The deposition rate and substrate ion current density vary non-monotonically with increasing V_s. XRD patterns of the Zr-W-N coatings revealing one group of peaks of fcc structure, indicating that this coating tends to form a single solid-solution nitride phase rather than the co-existence of separated nitrides. FESEM analysis shows that the morphology evolves from columnar structure to dense and then glassy structure with increasing negative bias voltages. Nanoindentation hardness H and effective elastic modulus E_r of the coating increases as the negative substrate bias goes up. Maximum wear resistance (H/E_r ~0.23) and fracture toughness (K_{IC} ~ 2.25 $MPa.m^{1/2}$) have been obtained for the film deposited at -100 V bias voltage. This indicates that the simultaneous increment of wear resistance and toughness is achievable if the negative bias voltage is properly controlled. Therefore, for the deposition of Zr-W-N system done at low substrate temperature (200ºC) and at -100V bias voltage, pronounced mechanical properties (H~ 34 GPa, $H/E_r > 0.1$, $W_e > 60\%$, $H^3/E_r^2 > 0.1$, K_{IC} ~ 2.25 $MPa.m^{1/2}$) has been achieved.

Chapter 6 (*Zirconium Tungsten Boron Nitride Coatings*) discusses about the effect of microstructure on thermal stability and mechanical properties of Zr-W-B-N nanocomposite coatings. The Zr-W-B-N nanocomposite coatings have been co-sputtered deposited on Si (100) substrates by varying power density (0.1 to 7.5 $watt/cm^2$) to boron target to obtain films of various compositions and microstructure. It has been observed that the Zr-W-B-N films with boron contents ≤ 2.3 at.% exhibited (200) preferred crystallographic orientation of grains and columnar structure. For the boron content ≥ 7.5 at.%, non-columnar films with the crystal phase grain size less than 7 nm and films of crystalline (Zr-W-B-N)-amorphous structure (BN) or high amorphous component are produced. Owing to synergetic contribution of solid solution strengthening and grain boundary hardening, film with boron content ~7.5 at.% exhibits

maximum hardness (~ 37 GPa), wear resistance (H/E_r ~ 0.24) and fracture toughness (2.9 $MPa.m^{1/2}$). Due to the superior mechanical performance of Zr-W-B(7.5 at.%)-N film over other deposited films of varying B content, post annealing of the this films has been carried out at 300º-900ºC in vacuum (T_v) and in air (T_n). Zr-W-B(7.5 at.%)-N film retains the fcc structure after vacuum annealing at T_v = 900ºC. However, film retains the fcc structure during air annealing at $T_n \leq 700$ºC and at T_n = 900ºC, full degradation of the Zr-W-B(7.5 at.%)-N film in crystalline phases of ZrO_2 and WO_3 was observed. The oxygen starts to be incorporated in the film at T_n = 500ºC and its content increases substantially with increasing T_n. The film got completely peeled off at T_n = 900ºC. Hardness H and elastic modulus E_r of the films remains unaffected by vacuum annealing while increased with increasing oxygen concentration in to the films.

CHAPTER 2

Synthesis and Characterization Processes

2.1 Introduction

A synthesis of thin films is a top down approach includes the deposition of individual atoms on a substrate. A thin film is not defined only due to its lower thickness (less than several micrometers), but also due to the process, by which it nucleated i.e. one-by-one condensing of molecules / ions / atoms of matter, coalesces and grows to form low dimension structure on a substrate. That's why, thin films differ from thick films which are created by thinning a three dimensional material or assembling large cluster/aggregates/grain of atomic/molecular/ionic species to form low-dimensional material.

Historically, thin films have been widely used since last four decades in making optical coatings, instrument hard coatings, electronic devices and decorative parts. The thin filmis a traditionally well established material technology. However, thin film technology is still being developed on a daily basis since it is a key in the 21^{st} century development of new materials such as nanometer materials and/or a man made superlattices. Thin film materials and devices are also available for minimization of toxic material since the quantity used is limited only to thesurface. Thin film processing also serves on energy consumption in production and is considered an environmentally being material technology for the next century (Wasa and Hayakawa 1992).

2.2 Thin Film Growth Process

Formation of thin film takes place via nucleation and growth process. The general picture of the step-by-step growth process emerging from the various experimental and theoretical studies can be presented as follows:

(1) The unit species, on impacting the substrate lose their velocity component normal to the substrate (provided the incident energy is not too high) and are physically adsorbed on the substrate surface.

(2) The adsorbed species are not in thermal equilibrium with the substrate initially and move over the substrate surface. In this process they interact among themselves, forming crystals of very small size called nuclei.

(3) The nuclei are thermodynamically unstable and may tend to desorbs in time, depending on the deposition parameters. If the deposition parameters are such that a cluster collides with other adsorbed species before getting desorbed, it starts growing in size. After reaching a certain critical size, the cluster becomes thermodynamically stable and the nucleation barrier is said to have been overcome. This step involving the formation of stable, chemisorbed, critical-sized nuclei is called the nucleation stage.

(4) The critical nuclei grow in number as well as in size until a saturation nucleation density is reached. The nucleation density and the average nucleus size depend on a number of parameters such as the energy of the impinging species, the rate of impingement, the activation energies of adsorption, deposition, thermal diffusion, temperature, topography and chemical nature of the substrate. A nucleus can grow both parallel to the substrate by surface diffusion of the adsorbed species and perpendicular to it by direct impingement of the incident species. In general, however, the rate of lateral growth at this stage is much higher than the perpendicular growth. The grown nuclei are called island.

(5) The next stage in the process of film formation is the coalescence stage, in which the small islands start coalescing with each other in an attempt to reduce substrate surface area. This tendency to form bigger islands is termed agglomeration and is enhanced by increasing the surface mobility (by increasing substrate temperature) of the adsorbed species. In some cases, formation of new nuclei occurs on area freshly exposed as a consequence of coalescence.

(6) Larger islands grow together, leaving channels and holes of uncovered substrate. The structure of the films at this stage changes from discontinuous island type to porous network type. Filling of the channels and holes forms a completely continuous film.

Depending on the thermodynamic parameters of the deposited and the substrate surface the initial nucleation and growth stages may be described as follows:

(a) **Layer by layer mode**:

If the deposition occur layer-by-layer, then it is called Frank Van der Merwe growth. In the layer or Frank-Van der Merwe mode (**figure 2.1**) (Venables *et al.* 1984) the atoms are more strongly bound to the substrate than to each other, the first atoms to condense form a complete monolayer on the surface, which becomes coveredwith a somewhat less tightly bound second layer. This growth mode is observed in the case ofadsorbed gases, such as several rare gases on graphite and on several metals,in some metal-metal systems, and in semiconductor growth on semiconductors (Frank *et al.* 1949). This is also referred as epitaxial growth. The term epitaxy originates from the Greek words, "epi" which means "equal" and "taxis" meaning "in ordered manner". It describes the ordered crystalline growth on a substrate.

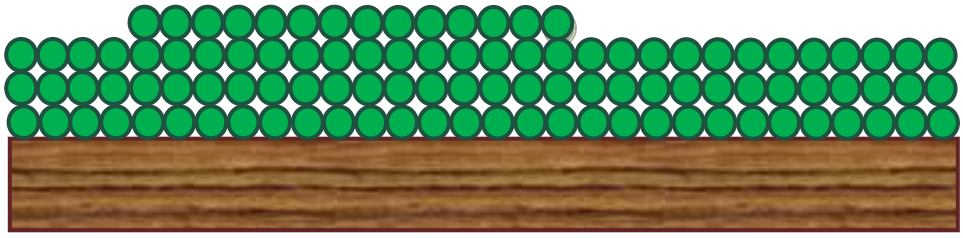

Figure 2.1 *Frank-Vander Merwe: Layer growth (ideal epitaxy)*

(b) **Island growth mode:**

In this mode the depositing material grow initially (first few atomic layers) as islands centered about nucleation sites. These nucleation sites can remain separated during the deposition in a process known as Volmer-Weber growth (**figure 2.2**).This happens when the atoms (or molecules) of the deposit are more strongly bound to each other than to the substrate. This mode is displayed by many systems of metals growing on insulators, including many metals on alkali halides, graphite and other layer compounds such as mica.

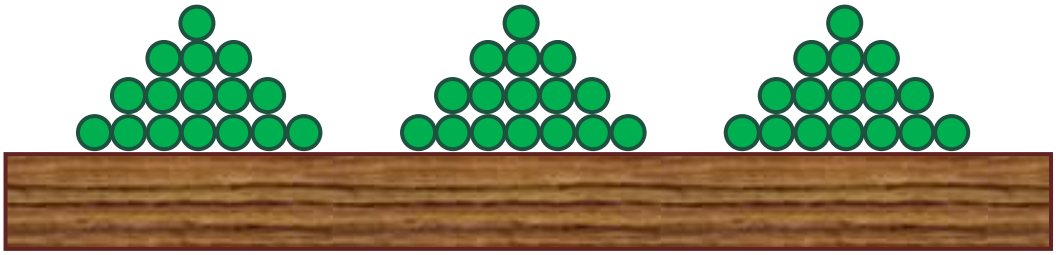

Figure 2.2 *Volmer-Weber: Island growth*

(c) **Layer-plus-island growth mode**:

The mixed layer-island or Stranski-Krastanov growth (**figure 2.3**) (Stranski *et al.* 1938) mode is an interesting intermediate case. After forming the first monolayer (ML), or a few ML, subsequent layer growth is unfavourable and islands are formed on top of this 'intermediate' layer. These islands can grow until they touch each other. This point is known as the percolation threshold. Depending on the material, this percolation threshold can typically be between a few nanometres to submicron ranges (Zadeh and Fry 2008). There are many possible reasons for this mode to occur, and almost any factor which disturbs the monotonic decrease in binding energy, characteristic of layer growth, may be the cause. For example, molecular orientation or symmetry or the lattice parameter in the intermediate layer may not be able to continue into the bulk crystal of the deposit. These results in a high free energy of the deposit intermediate layer interface, which favours subsequent island formation. This growth mode is much more common than was thought just a few years ago. There are now many examples of its occurrence in metal-metal, metal-semiconductor, gas-metal and gas-layer compound systems.

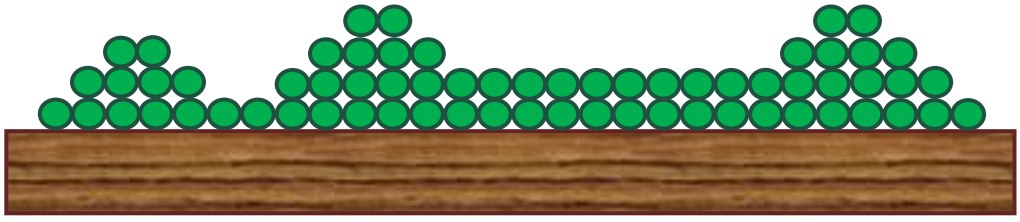

Figure 2.3 *Stranski-Krastanov: Layer + Island growth*

Growth modes can be systematically classified in terms of surface energies **(figure 2.4)** using Young's equation as given below:

$$\gamma_B = \gamma^* + \gamma_A \cos\phi \qquad (2.1)$$

where ϕ is the wetting angle of a liquid nucleus on a substrate, γ_B is the surface energy of substrate, γ_A is the surface energy of thin film material, and γ^* is the interface energy of film-substrate. Layer growth ($\phi = 0$) requires $\gamma_B > \gamma^* + \gamma_A$, whereas island growth ($\phi > 0$) requires that $\gamma_B < \gamma^* + \gamma_A$. Layer-plus-island growth occurs because the interface energy increases with film thickness; typically the layer on top of the substrate is strained to fit the substrate (**Chopra 1969**).

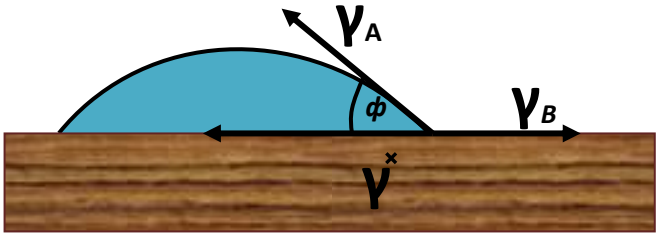

Figure 2.4 *Schematic diagram of surface energy of substrate (γ_B), thin film material (γ_A) and interface energy of film-substrate (γ^*)*

2.3 Thin Film Deposition Process

The basic properties of thin films, such as crystal phase, microstructure, orientation, film composition and film thickness are governed by the deposition method and the deposition parameters. The unique properties of thin films that cannot observe in bulk materials are resulting from the atomic growth process and Size effects, including quantum size effects, characterize by the thickness, crystalline orientation and multilayer aspects

Typically two types of deposition processes, physical process and chemical process are use for the deposition of nanocrystalline thin films and both types of processes involve three main steps:

- Production of appropriate atomic, molecular or ionic species.
- Transport of these species to the substrate through a medium.
- Condensing on the substrate, either directly or via a chemical and/or electrochemical reaction, to form a solid deposit.

The physical process is composed of the physical vapor deposition (PVD) processes like thermal evaporation (Wei 2010), electron beam evaporation (Reinhold and Faber 2011), magnetron sputtering (Som *et al.* 2006, Chandra et al 2006, Chawla *et al.* 2008, Hadian *et al.* 2012), molecular beam epitaxy (MBE) (Wang *et al.* 2007), pulse laser deposition (PLD) (Craciun *et al.* 2014, Chawla *et al.* 2011) and the chemical process is composed of chemical vapor deposition (CVD) processes like metal- organic chemical vapor deposition (MOCVD) (Chioncel *et al.* 2006), Plasma enhanced chemical vapor deposition (PACVD) (Jung *et al.*

2012) and the chemical solvent deposition process like spray pyrolysis (Manivannan *et al.* 2003, Sharma and Rajaram 2010), sol-gel (Pyper *et al.*1998, Mohallem *et al.* 2010).Various CVD and PVD processes used for synthesis nanocrystalline thin films having their own specific advantages and disadvantages. The choice of a particular process usually depends on the specific characteristics of thin films required for a study or application of interest. If the primary requirement is to get highly uniform composite thin films with a moderate size distribution, then physical vapor deposition (PVD) processes such as evaporation, magnetron sputtering and laser ablation are found to be very efficient whereas for large area deposition, PACVD, spin coating and spray pyrolysis processes are found to be more effective.

The selection of a deposition process for thin films usually depends on the specific characteristics of films required for a study or application of interest. The basic requirement of good quality thin films are: i) good uniformity of the films throughout exposed area, ii) the films with good physical and chemical properties such as low stress, good adhesion to the substrates, high density, low films defects (pinhole density), controlled grain size and its distribution, boundary property and orientation and iii) equipment initial cost and running cost. To get highly uniform, nanocrystalline thin films with a moderate size distribution, Physical vapor deposition processes such thermal evaporation, laser ablation, E-beam evaporation and magnetron sputtering are found to be very effective for depositing thin films with the aforementioned microstructural characteristics. In PVD, the deposition of thin films is usually carried out from the same material whose nanoparticles are to be synthesized and its purity is decided by purity of the starting materials, base vacuum and purity of the ambient gas atmosphere. In contrast, in chemical vapor deposition (CVD) technique, some un-reacted chemicals and oxidizing products other than the desired one are often left behind with the nanoparticles and the deposition done at higher substrate temperature.

A comparative study of some most commonly used vapor deposition techniques for thin films is given in **table 2.1**

In the present work, sputtering process has been used to synthesize nanocrystalline transition metal nitride thin films. The detailed description of sputtering technique and process has been given below.

Table 2.1 *Comparative evaluation of thin film deposition processes*

Process	Material	Uniformity	Impurity	Grain Size	Film Density	Deposition Rate	Substrate temperature	Directional	Cost
Thermal Evaporation	Metal or low melting pint material	Poor	High	10-100nm	Poor	1-20 Å/s	50-100°C	Yes	Very low
E-beam Evaporation	Both metals and dielectrics	Poor	Low	10-100nm	Poor	10-100Å/s	50-100°C	Yes	High
Sputtering	Metals, Semiconductors, Insulators and dielectrics	Very Good	Low	1-100nm	Good	Metal: 100Å/s Dielectric: 10Å/s	RT-850°C	Some Degree	High
PECVD	Mainly Dielectric	Good	Very low	10-100nm	Good	10-100Å/s	300-400°C	Some degree	Very high
LPCVD	Mainly Dielectric	Very Good	Very Low	1-10nm	Good	10-100Å/s	600-1200°C	isotropic	Very high

2.4 Sputtering

The deposition process using the irradiation of energetic species is known as sputtering. Sputter deposition is widely used technique for the erosion of surfaces and the deposition of films. Bunsen and groves first observed sputtering in a gas discharge tube over 50 years ago. The sputtering process is a momentum transfer process in which momentum is transfer by bombarding energetic ions/atomic to the target atoms resulting physical vaporization of atoms from the target surface. The bombarding ions are usually neutral gaseous ions (Ar^+, He^+) accelerated by an applied electric field. The removed species or sputtered species from the target surface are compromise of highly energetic atoms and reached at the substrate with energy ranges from 1 to 10 eV which is higher than those of the other deposition processes such as chemical decomposition and thermal evaporation. The disintegration of target or cathode during sputtering is also used for other purposes like cleaning surfaces, depth profiling, for patterning semiconductor wafers, for micromachining and a number of applications which require careful, microscopic erosion of a surface. Sputter deposition is widely used for coating tools and cutting surfaces for wear resistance, for coating the insides of plastic bags and the surfaces of automobile parts, for coating on semiconductor wafers for electronic devices, for reflective coatings on window glass, and a number of other wide ranging applications. The most common approach for growing thin films by sputtering is the use of a unbalanced magnetron source in which positive ions present in the plasma of a magnetically enhanced glow

discharge bombard the target. The target can be powered in different ways, ranging from direct current (DC) for conductive targets to radio frequency (RF) for non-conductive targets, to a variety of different ways of applying current and/or voltage pulses to the target. Among the different physical vapor deposition (PVD) techniques, DC and RF magnetron sputtering is used extensively in the scientific community. The role of magnets in sputtering is discussed in section 2.4.2. The schematic diagram of a simple DC magnetron sputtering system is shown in **figure 2.5** which consists of a vacuum chamber, target, power supply and a substrate holder. Target and substrate face each other and serve as electrodes in this case and target kept at negative potential.

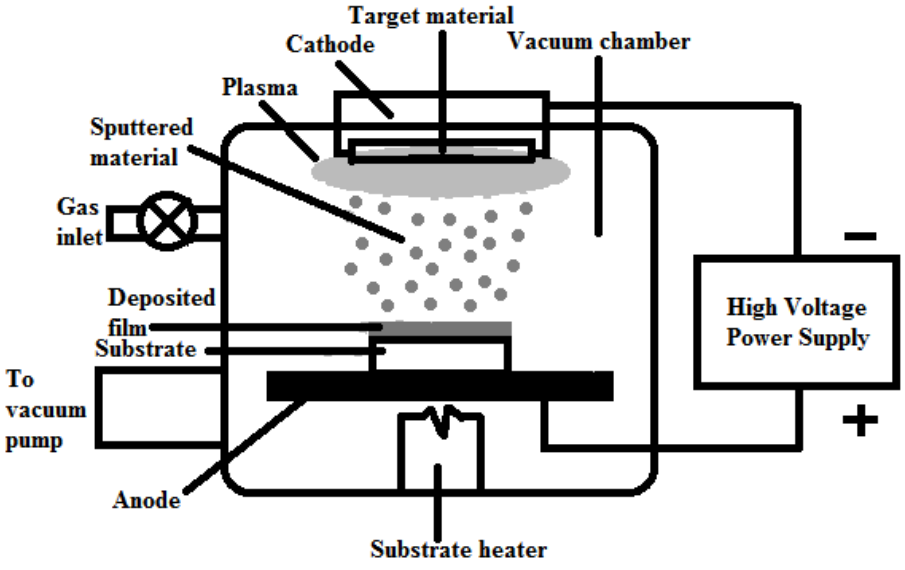

Figure 2.5 *A schematic diagram of a simple DC sputtering system and voltage distribution*

But, the DC magnetron sputtering suffers from arching problem at the target surface during deposition. Arcs often occur during reactive sputter deposition if oxygen/nitrogen as reactive gases is used that may build-up oxide/nitirde on the edges of the erosion groove where the sputter rate is low.Arcs can be characterized as a low voltage and high current discharge. Arcing can seriously damage a target by local melting, but it also degrades quality of the deposited film owing to the presence of particulates and/or pinholes while eventually destroying the power supply.

An effective way to prevent arcing during reactive magnetron sputtering is to use RF at the target end (Sproul *et al.* 2005). When a RF potential is capacitively coupled to an electrode with a large peak to peak voltage, an alternating positive/negative potential appears on the surface. The discharge voltage generally cycles between a high (3/4 of total voltage) negative voltage and a low (1/4 of total voltage) positive voltage. The negative voltage part of the cycle is used to perform the sputtering, as the ions bombard the cathode. The low positive voltage part of the cycle is used to attract electrons to prevent charge build-up. Because of the higher mobility of the electrons, this part of the cycle can be relatively short compared to the total cycle time.At frequencies above 50 kHz, the ions do not have enough mobility to allow establishing a DC diode-like discharge and the applied potential is felt throughout the space between the electrodes. The electrons acquire sufficient energy to cause ionizing collisions in the space between the electrodes and thus the plasma generation takes place throughout the space between the electrodes.Typical RF frequencies employed range from 5 to 30 MHz however; 13.56 MHz has been reserved for plasma processing by the Federal Communications Commission and is widely used (**Cao 2004**).

The self biasing of target to a negative potential and behaves like a DC target are the key points in RF sputtering. This is because of the fact that electrons are considerably more mobile than ions and easily following the periodic change in the applied electric field. It is also important to note that since RF power supplies are designed to look into circuits with a purely resistive 50Ω load, a tunable matching network is required to damp out the complex reactance (both capacitance and inductance) of the discharge. RF sputtering can be performed at low gas pressures (< 1 mtorr) and can be used to sputter electrically insulating and semiconductor materials. The primary disadvantage in the use of RF power supplies for magnetron sputtering in addition of being expensive is the inherently low deposition rate.

Sputtering offers the following advantages over other PVD methods:

(a) The deposited films have high uniformity at large area as well as on complex geometry shape, high flexibility of large-scale production, better reproducibility of deposited films, easy deposition of materials with high melting points and good adhesion of film with substrate.
(b) Large-size targets can easily sputtered by sputtering process which simplifies the deposition of films with uniform thickness over large substrates.

(c) The thickness if deposited film can easily controlled by adjusting the deposition rate.

(d) The step coverage, grain structure and control of alloy composition are more easily accomplished than by deposition through evaporation.

(e) Device damage from X-rays generated by electron beam evaporation is avoided.

(f) Sputter-cleaning of the substrate in vacuum prior to film deposition can be done.

2.4.1 Description of sputtering process

The first step in the sputtering process is the pumping of the vacuum chamber to a typical base pressure of 10^{-6} torr or more by vaccum pumps like rotary and turbo molecular pumps etc. An inert gas, usually argon or helium with a pressure ranging from a few to 100mtorr depending upon the requirement, is introduced into the system as the medium to initiate the discharge and maintain the plasma once initiated. When an electric field of several kilovolts per centimeter is applied between cathode and anode, a glow discharge is initiated and maintained between these two electrodes. A very little current flows at first due to the small number of charge carriers in the system after the initial application of the voltage. Once sufficient number of charge carriers builds up, the free electrons strike the neutral Ar atoms to create Ar^+ ions and more free electrons. The newly created free electrons can now ionize additional Ar neutrals thus multiplying the number of Ar^+ ions. In this visible glow maintained between the electrodes, the Ar^+ ions in the plasma gets accelerated towards direction of the cathode and strike the target. Free electrons are accelerated by the electric field and gain sufficient energy to ionize argon atoms. So, the positive ions (Ar^+) in the discharge strike the cathode (the source target) and this bombardment creates a cascade of collisions in the target material's surface. These multiple collisions results in the ejection of neutral target (or sputter) atoms through momentum transfer from the surface into the gas phase. These atoms are then directed towards the substrate to form a thin film.

Since sputtering is the result of momentum and energy transfer, the incoming argon ions should have high enough energy to break the bonds holding the target atom in place. The typical surface binding energy is ~20-40 eV. With high enough energy of argon ions, the collision cascade can be 5-10 nm below the target's surface. However, the particles ejected are usually within 1nm of the surface. Only a small fraction of collisions produce sputtering. The process of sputtering has been shown schematically in **figure 2.6.** To measure the efficiency of sputtering, the sputter yield (S) is defined as the number of sputtered atoms per incident particle. In a practical sputtering process, the yield is from 0.1 to 10 %. During the collision with the target surface, secondary electrons are emitted. They are accelerated away from the cathode. These electrons then travel back into the argon plasma and collide with the argon atoms, ionizing some of them and sustaining the plasma.

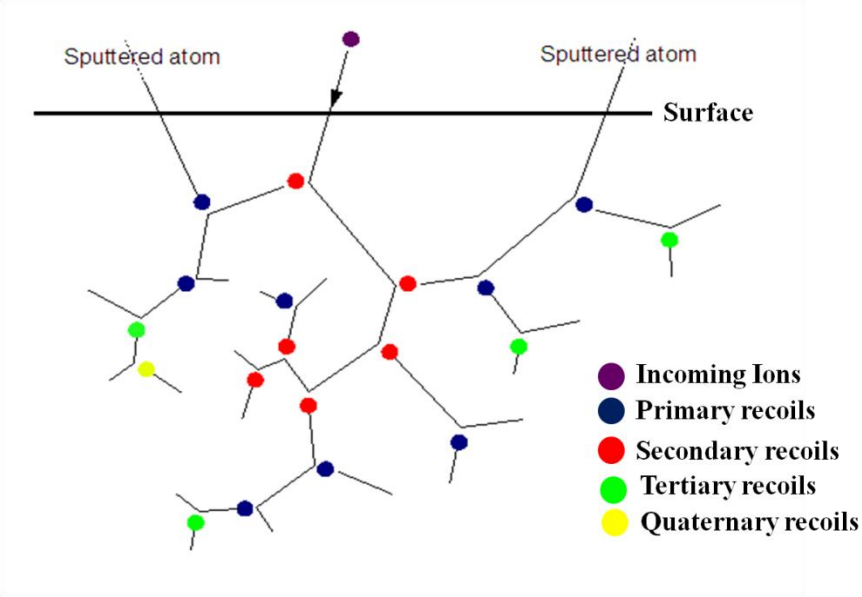

Figure 2.6 *Schematic of physical sputtering process. The thinner lines the ballistic movement paths of the atoms from beginning until they stop in the material*

Sputtering yield depends on the chemical bonding of the target atoms and the energy transferred by collision. Generally, the average energy of sputtered atom is 10-40 eV.

Sputter yield (S) is define as

$$S = \frac{\text{ejected atoms or molecules}}{\text{incident ion}}$$

S values are typically in the range of 0.01 and 4 and increase with the mass of metals and energy of the sputtering gas. The sputter yield depends on: (i) the energy of the incident ions; (ii) the masses of the ions and target atoms; (iii) the binding energy of atoms in the solid and (iv) the incident angle of ions.

Using Sigmund's theory, the sputter yield is given as For E < 1 KeV,

$$S = \frac{3\alpha}{4\pi^2} \frac{4M_1M_2}{(M_1 + M_2)^2} \frac{E}{E_B} \tag{2.2}$$

where, E_B is the surface binding energy of the target atom being sputtered, E is the ion bombardment energy, α is a measure of the efficiency of momentum transfer in collisions, and M_1 and M_2 are the masses of the positive ion of the gas and target material, respectively.

But for E > 1 KeV,

$$S = 3.56\alpha \frac{Z_1Z_2}{Z_1^{2/3} + Z_2^{2/3}} \left(\frac{M_1}{M_1 + M_2}\right) \frac{S_n(E)}{E_B} \tag{2.3}$$

where, Z_1 and Z_2 are the atomic numbers of the incident ion and sputtered target atom respectively and $S_n(E)$ is a measure of the energy loss per unit length due to nuclear collisions, and also it is a function of the energy as well as masses and atomic numbers of the atoms involved (Ohring 1992). The sputtering yields of various materials bombarded by a variety of ion masses and energies have been determined experimentally (Laegried and Wehner 1961, Wehner and Rosenberg 1961, Rosenberg and Wehner 1962) and have been calculated from first principles using Monte Carlo techniques (Yamamura *et al.* 1983). It may be mentioned that the sputtering yields are generally less than one at bombarding energies of several hundred electron volts, indicating the large amount of energy input is necessary to eject one atom.

2.4.2 Magnetron sputtering

In magnetron sputtering, a glow discharge (plasma) is created in the presence of magnetic field (magnetron) in order to improve the sputtering performance. A magnetron uses a

static magnetic field configured at the cathode location. The magnetic field is located parallel to the cathode (target) surface. Secondary electrons which are emitted from the cathode due to ion bombardment are constrained by this magnetic field to move in a direction perpendicular (**E×B** called drift) to both the electric field (normal to the surface) and the magnetic field.This drift causeselectrons to move parallel to the cathode surface in a direction 90 degrees away from the magnetic field. If the magnetic field is set up correctly, this **E×B** drift can be arranged to close on itself, forming a current loop of drifting secondary electrons (**figure 2.7**).

In this arrangement, secondary electrons are essentially trapped in a region close to the cathode. They lose their kinetic energy due to collisions with gas atoms (ionization) or with other electrons (electron heating).This is quite easily visible in a magnetron sputtering system.The location of this ring is also known as the *etch track* because the erosion of the cathode is highest here and deep groves can be eroded onto the cathode (target).Dense plasma near the target increases the deposition rate as it enhances the ionization of sputtering gas.However, this plasma does not affect the ejected atoms, as they have no charge and remain unaffected by the magnetic field.The energetic collisions near the target surface generate ample amount of heat which can damage the magnets and also melt the low melting point target, so to avoid this problem an actively cooling of the magnets and sputtering target is required. Moreover, cold surface minimizes the amount of radiant heat in a sputtering system and is an advantage over thermal evaporation.Cooling also prevents diffusion in the target which could lead to changes in the elemental composition in the surface region when alloy targets are used.

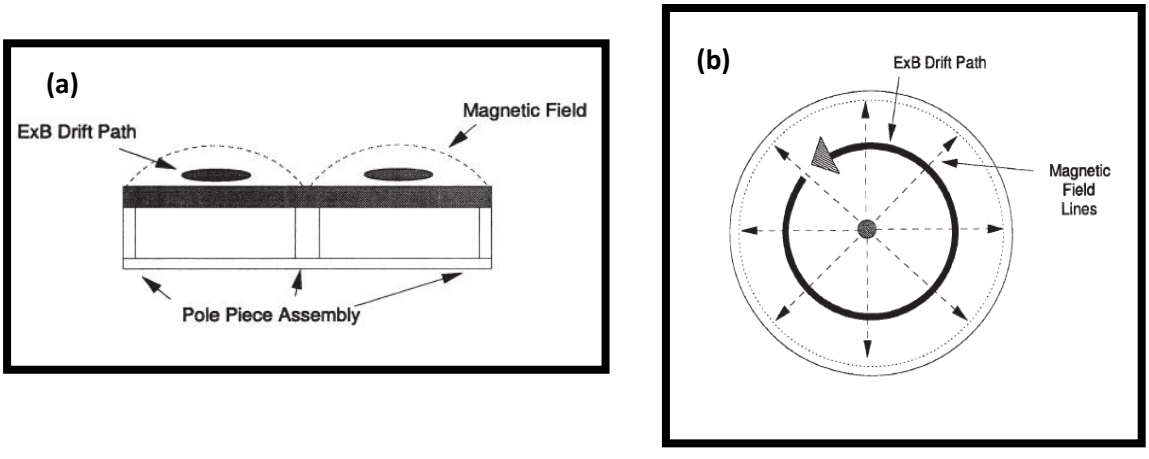

Figure2.7 *(a) Side and (b) top view of magnetic field configuration for a circular planar magnetron cathode*

2.4.3 Reactive magnetron sputtering

Reactive sputtering is the sputtering of an elemental target in the presence of a gas that will react with the target material to form a compound. In one sense, all sputtering is reactive because there are always residual gases in the chamber that will react with the sputtered species. However in reality, reactive sputtering occurs when a gas is purposely added to the sputtering chamber to react with the sputtered material (Rossnagel *et al.* 1990, Sproul *et al.* 2005).Examples are when nitrogen is added with the sputtering of titanium to form titanium nitride or when oxygen is injected into the chamber with the sputtering of aluminum to form aluminum oxide. The reactive gases in magnetron sputtering are in the molecular state (e.g., N_2, O_2). It has been observed that with reactive gases, heavier inert gas such as argon is required in sputtering because reactive gases have a low atomic masses (N=14, O=16) and can not transfer sufficient momentum to the target material for dislodging of atoms. Another advantage of mixing inert gases with the reactive gas is help in activation of reactive gas by the excitation processes. The nature of the sputtering gas influences the rate of sputtering from the target. The use of inert and reactive gas mixtures probably results in a metallic mode of sputtering, while the use of only reactive gas for example (N_2) is likely to result in a nitride mode of sputtering with a significantly lower sputtering rate (Sumi *et al.* 1997, Chandra *et al.* 2005).

The basic issue faced during reactive sputtering is that the reactive gas combines with target material to form a compound. Ideally this reaction takes place on the surface of the substrate, but in reality it occurs not only at the substrate but also on the fixture and chamber walls and on the target. It is the reaction on the target surface that leads to the classic reactive sputtering problem known as “poisoning” of the sputtering target. The sputtering rate for the compound material that forms on the target is usually significantly less than the rate for the elemental target material thus reducing the deposition rate and sputtering efficiency. This problem is controlled by having a high sputtering rate (magnetron sputtering) and controlling the availability of the reactive gas by mass flow controller such that there will be enough reactive species to react with the film surface to deposit the desired compound but not so much that it will unduly poison the target surface.

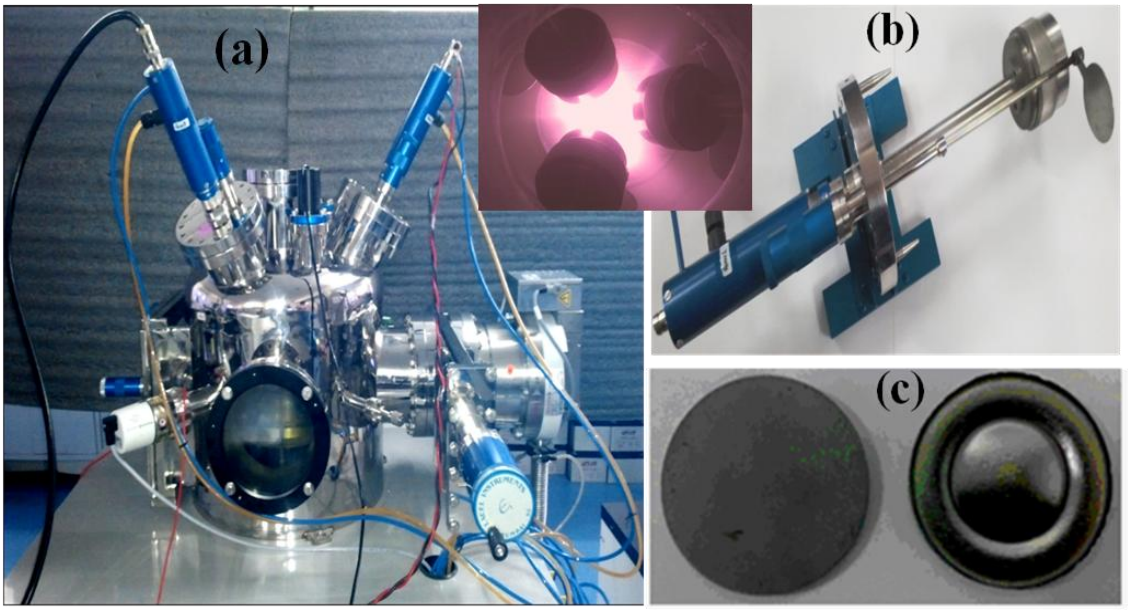

Figure 2.8 *(a) Custom designed DC/RF magnetron sputtering unit set-up in Nano Science Lab (b) sputtering gun (c) new & used sputtering target and inset shows the co-sputtering view with tree targets*

In our lab, we use DC/RF magnetron sputtering system. **Figure 2.8(a)** shows the turbo based magnetron sputtering system assembled in our laboratory (Nanoscience Laboratory, Institute Instrumentation Centre, IIT Roorkee). The pumps and gauges fitted in to the chamber are from Pfeiffer Vacuum. For DC sputtering, 'Aplab' high voltage DC power supply (50-1000 V, 0-1 A) was used. The RF power supply from ΔE advance energy (Cesar 136) has been used for the deposition. In the chamber shown in **figure 2.8a**, co-deposition with three different targets can be done at the same time by mounting the targets in the sputtering guns and using them in oblique angle (45° to substrate normal) ports given in the chamber. The substrate is put on the heater cum substrate holder which can be rotated by a DC motor during deposition to insure the uniformity in the deposited films. The sputtering pressure measurement inside the chamber was done by compact full range gauge (pirani and cold cathode in single case) (Pfeiffer PKR 251). Flow of gases is carefully monitored by mass flow controllers (MKS

Instruments USA).The sputtering gun used for mounting the target is shown in **figure 2.8b.** The unused and eroded targets are shown in **figure 2.8c.**

2.5 Characterization Techniques

After deposition of nanocrystalline transition metal nitride thin films using DC/RF magnetron sputtering technique with different process conditions, the structural and mechanical properties were investigated by XRD, FESEM, EDS, EPMA (WDS), TEM, AFM and Nano & micro indentation techniques. The brief descriptions of all these techniques used for characterization of zirconium tungsten nitride and zirconium tungsten boron nitride are discussed in the following sections.

2.5.1 X-ray diffraction (XRD)

X-ray diffraction (XRD) is most widely used technique for phase identification of a crystalline material and can provide information on unit cell dimensions. It is most widely used for the identification of unknown crystalline materials and also information related to the crystal structure of the films, including lattice constants, crystallite size, phase analysis, crystal defects, stress, etc. The XRD methods are generally applied to films thicker than several angstroms on account of the strong penetrating power of the X-rays.

2.5.1.1 Fundamental principles of X-ray diffraction (XRD)

X-ray diffraction is based on constructive interference of monochromatic X-rays from a crystalline sample. These X-rays are generated by a cathode ray tube, filtered to produce monochromatic radiation, collimated to concentrate, and directed toward the sample. **Figure 2.9** shows the basic principles of X-ray diffraction. In this figure, a parallel beam of X-rays strikes the crystal where the atoms are placed on two parallel planes, which are separated by a distance of *d* (inter atomic space). The parallel X-ray beams on the left impinge onto the planes at an angle of θ and the atoms scatter the X-ray beams in all directions. If the detector is placed at an angle of θ on the right, then only the path difference between the two reflected beams is an integral number of wavelengths. The interaction of the incident rays with the sample

produces constructive interference (and a diffracted ray) and mathematically this is expressed by Bragg's Law

$$2d\sin\theta = n\lambda \tag{2.4}$$

Where d, is the spacing between two adjacent atomic planes, θ, is the angle between the atomic plane and the incident X-rays, n, is the order of diffraction maximum, and λ is the wavelength of the X-rays (Cullity and Stock 2001).

The resulting diffraction pattern comprising both the positions and intensities of the diffraction effects is a fundamental physical property of the substance. Analysis of the positions of the diffraction effect leads immediately to a knowledge of the size, shape and orientation of the unit cell.

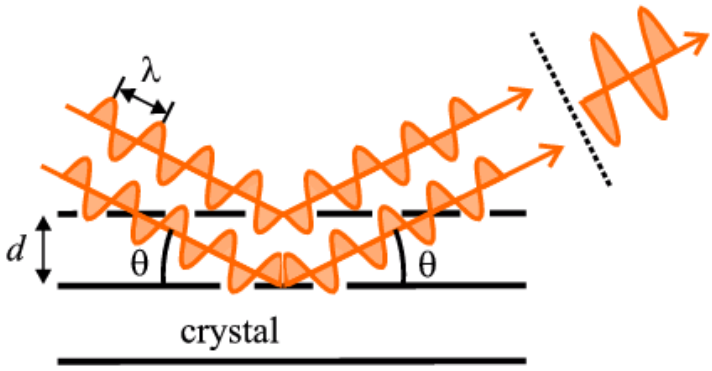

Figure 2.9 *Diffraction of X-ray by a single crystal material*

2.5.1.2 X-ray diffraction (XRD) instrumentation

X-ray diffractometer consist of three basic elements: an X-ray tube, a sample holder, and an X-ray detector as shown in **figure 2.10**. X-rays are generated in a cathode ray tube by heating a filament to produce electrons, accelerating the electrons toward a target by applying a voltage, and bombarding the target material with electrons. When electrons have sufficient energy to dislodge inner shell electrons of the target material, characteristic X-ray spectra are produced. Filtering, by foils or crystal monochromators, is required to produce monochromatic X-rays needed for diffraction. $K_{\alpha 1}$and $K_{\alpha 2}$ is sufficiently close in wavelength such that a weighted average of the two is used. Copper is the most common target material for single-crystal diffraction, with CuK_{α} radiation 1.5418Å. These X-rays are collimated and directed onto the sample. As detector is rotated, the intensity of the reflected X-rays is recorded. When

the geometry of the incident X-rays impinging the sample satisfies the Bragg's Equation, constructive interference occurs with a peak in intensity. A detector records and processes this X-ray signal and converts it into a count rate. A graph between 2θ versus counts per second is plotted and the output data is monitored in a device such as a printer or computer.

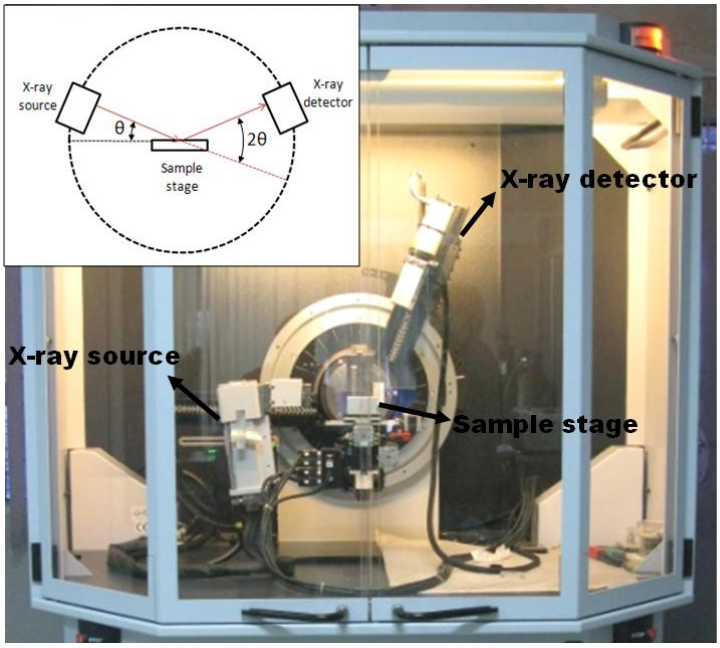

Figure 2.10 Schematic *diagram of X-ray Diffractometer (Bruker AXS, D8 Advance, Gremany) in IIT roorkee*

2.5.1.3 Applications

X-ray diffraction is most widely used for the identification of unknown crystalline materials (e.g. minerals, inorganic compounds). Determination of unknown solids is critical to studies in geology, environmental science, material science, engineering and biology. Other applications include:

- characterization of crystalline materials:
  - identification of fine-grained minerals such as clays and mixed layer clays that are difficult to determine optically
  - determination of unit cell dimensions
  - measurement of sample purity
- With specialized techniques, XRD can be used to:
  - determine crystal structures using Rietveld refinement

- determine modal amounts of minerals (quantitative analysis)

- characterize thin films samples by:
  - determining lattice mismatch between film and substrate and inferring strain
  - determining dislocation density and quality of the film by rocking curve measurements
  - measuring superlattices in multilayered epitaxial structures
  - determining the roughness, density and thickness of the film using glancing incidence X- ray reflectivity measurements

2.5.1.4 Micro strain measurement by XRD

Stresses and strains are always present in thin films deposited on substrates. In the majority of cases, these stresses are residual stresses, introduced into the system during deposition or subsequent processing (Segrnuller *et al.*1989). The residual stress consist of an intrinsic component resulted from the growth process and an extrinsic component (thermal stress) due to the presence of different thermal expansion coefficients between the coating and the substrate (Chang *et al.* 2005). These stresses are induce in the film either by energetic ion bombardment or the thermal expansion coefficients of each phase present or phase composition (Polychronopoulou *et al.* 2008). It has been observed that the films deposited by PVD processes typically exhibit compressive stress resulting high hardness of the material (Mayrhofer *et al.* 2006). However, that stress is not measured directly, it is always strain that is measured; the stress is determined indirectly, by calculation or calibration.

There are two types of strain accumulate in the thin films namely uniform strain and non-uniform strain. The effect of both type of strain on the XRD peak is illustrates in **figure 2.11a-c**. A portion of an unstrained grain appears with equilibrium interplaner spacing d_0 is shown on the left of **figure 2.11a** and XRD peak corresponding to these planes is appears on the right. If the grain is subjected to an uniform tensile strain at right angles to the reflecting planes, their spacing becomes larger than d_0 and the corresponding

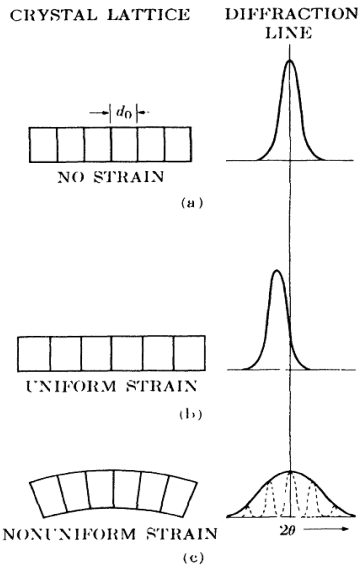

Figure 2.11a-c S*train affected XRD pattern (Cullity 2001)*

diffraction line shifts to lower angles but does not otherwise change, as shown in **figure 2.11b**. This line shift is the basis of the x-ray method for the measurement of macro stress. In **figure 2.11c** the grain is bent and the strain is non-uniform; on the top (tension) side the plane spacing exceeds d_0, on the bottom (compression) side it is less than d_0, and somewhere in between it equals d_0.

2.5.1.4.1 Uniform strain

When a polycrystalline thin film are deformed elastically in such a manner that the strain is uniform over relatively large distances, the lattice plane spacing in the constituent grains change from their stress-free value to some new value corresponding to the magnitude of the accumulated stress in the film, this new spacing being essentially constant from one grain to another for any particular set of planes. This uniform macro-strain as shown in **figure 2.11b,** causes a shift of the diffraction peaks to new 2θ positions. The shift in X-rd peaks of deformed sample depend upon the nature of residual stress. Compressive residual stress shifts the X-rd peaks toward higher angle and tensile residual stress toward lower angle. From this shift the strain may be calculated and, knowing the strain, we can determine the stress present, either by a calculation involving the mechanically measured elastic constants of the material, or by a calibration procedure involving measurement of the strains produced by known stresses. However, that stress is not measured directly, it is always strain that is measured; the stress is determined indirectly, by calculation or calibration.

On should note that, residual stresses are not only the cause of shifting, change in chemical composition and growth of phases may shift the X-rd peaks.

The accumulate macro strain in the thin films can be calculated as follows:

$$micro\ strain\ (\alpha) = \frac{a - a_0}{a_0} * 100 \qquad (2.5)$$

where, a (a or c) is the lattice parameter of the strained film calculated from XRD data and a_0 (a_0 or c_0) is the unstrained lattice parameter of film (Cullity and Stock 2001).

2.5.1.4.2 Non-uniform strain

If the thin film is deformed plastically, the lattice planes usually become distorted in such a way that the spacing of any particular (hkl) set varies from one grain to another or from one part of a grain to another. This non-uniform microstrain as shown in **figure 2.11(c)**, causes a broadening of the corresponding diffraction peaks.

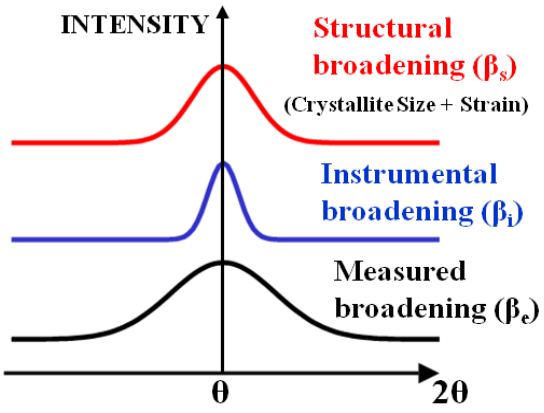

Figure 2.12 *XRD peak broadening*

The microstrain not solely does the broadening of the peaks but the crystallite size and instrument also lead the broadening of the X-rd peaks as shown in **figure 2.12**. In order to calculate microstrain through peak broadening by eliminating the effect of instrumental and crystallize size broadening, Williamson-Hall method is used (**equation 2.6**).

$$\beta_s \cos\theta = \frac{k\lambda}{D} + 2\varepsilon \sin\theta \qquad (2.6)$$

where D is the coherent scattering length (crystalline size); k is a constant whose value is approximately 0.9 for spherical shape particle, **λ** is Cu-Kα radiation (1.54 Å), **ε** is the inhomogeneous internal strain (in %), θ is the Bragg reflection angle and β_s is the measured full width at half maximum (FWHM) of the peak.

The analysis includes two steps:

First step: the width (**β_s**) of every peak was measured as the integral breadth. The instrumental broadening (**β_i**) was determined from polycrystalline silicon standard and found to be 0.01 in our case. The peak breadth due to sample (strain + size), **β_e** was calculated according to Gaussian profile:

$$\beta_s^2 = \beta_e^2 - \beta_i^2 \qquad (2.7)$$

Second case: the crystalline size and internal strain were obtained by fitting the Williamson-Hall equation (equ. 2xxx) in a straight line equation:

$$Y = mX + C \qquad (2.8)$$

Where $\beta_s \cos\theta$ and $\sin\theta$ values of different peaks of same phase are treat as Y and X coordinates of the line. Hence the slope (m) and intercept of straight line give the value of crystallite size and microstrain.

2.5.2 Field emission scanning electron microscopy (FESEM)

The scanning electron microscope (SEM) is a rapid analytical technique primarily used in materials research laboratories and is common in various forms in fabrication plants. The SEM provides information relating to phase distribution, morphology, topographical features, crystal structure, crystal orientation, and compositional differences. The strength of the SEM lies in its inherent versatility due to the multiple signals generated, simple image formation process, wide magnification range and excellent depth of field. To understand the working principle of field emission scanning electron microscopy (FESEM), first we need to know the kind of interaction of an energetic electron beam has with samples and the phenomena which take place after this interaction.

The electron beam is a focused probe of electrons of similar energy and trajectory, accelerated toward the sample by electromagnetic fields. When an incident electron beam strikes the specimen, it undergoes a series of complex interactions with the nuclei and electrons of the atoms of the sample. These interactions can be divided into two major categories: elastic interactions and inelastic interactions.

(a) Elastic interactions: Elastic scattering results from the deflection of the incident electron by the specimen of similar energy. This kind of interaction is characterized by negligible energy loss during the collision. Incident electrons that are elastically scattered through an angle of more than 90° are called backscattered electrons (BSE) and yield a useful signal for imaging the sample.

(b) Inelastic interactions: Inelastic scattering occurs through a variety of interactions between the incident electrons and the electrons and atoms of the sample, and results in the primary

beam electron transferring substantial energy to that atom. As a result, the excitation of the specimen electrons during the ionization of specimen atoms leads to the generation of secondary electrons (SE), which are conventionally defined as possessing energies of less than 50 eV and can be used to image or analyze the sample. In addition SE and BSE signals, a number of other signals are produced like emission of characteristic X-rays, auger electrons and cathodoluminescence.

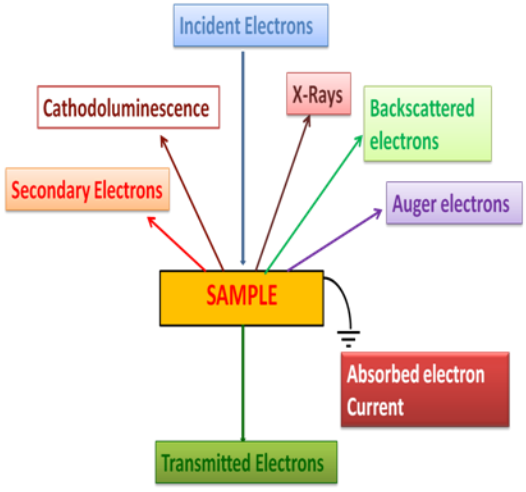

Figure 2.13 *Schematic view of electron beam interaction with specimen*

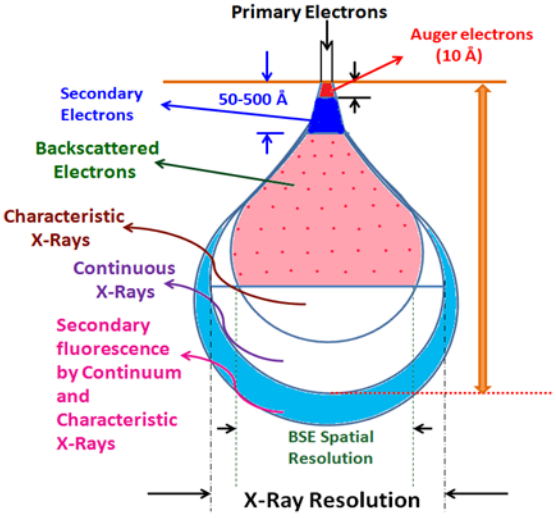

Figure 2.14 *Tear drop model for electron beam interaction with solids*

Figure 2.13 schematically shows the interaction of electron beam with the specimen. **Figure 2.14** shows the tear drop model for electron beam interaction with solids and explains the interaction volume in the specimen and shows different kind of signals coming from the sample from various depths.

(1) **Auger Electrons:** Auger electrons are produced following the ionization of an atom by the incident electron beam and the falling back of an outer shell electron to fill an inner shell vacancy. The excess energy released by this process may be carried away by an Auger electron. This electron has a characteristic energy and can therefore be used to provide chemical information. Because of their low energies, Auger electrons are emitted only from near the surface. They have escape depths of only a few nanometers and are principally used in surface analysis.

(2) **Secondary electrons:** When the primary beam strikes the sample surface causing the ionization of specimen atoms, loosely bound electrons may be emitted and these are referred to as secondary electrons (SE). Secondary are influenced more by surface properties than by atomic number. The depth from which SE escapes the specimen is generally between 5 and 50 nm due to their low energy. So, secondary electrons accurately mark the position of the beam and give topographic information with good resolution.

(3) **Backscattered electrons:** A backscattered electron (BSE) is defined as one which undergoes a single or multiple scattering events and which escapes from the surface with energy greater than 50 eV. The elastic collision between an electron and the atomic nucleus of specimen causes the electron to bounce back with wide-angle directional change. Approximately 10–50% of the beam electrons are backscattered toward their source with on an average 60–80% of their initial energy retained. The depth from which BSE escape the specimen is dependent upon the beam energy and the specimen composition, but > 90% generally escape from less than one-fifth the beam penetration depth. Elements with higher atomic numbers have more positive charges on the nucleus, and as a result, more electrons are backscattered, causing the resulting backscattered signal to be higher. Thus, the backscattered yield, defined as the percentage of incident electrons that are reemitted by the sample, is dependent upon the atomic number of the sample; higher Z phases appear brighter than lower Z phases in compositional images. Since BSEs have a large energy (that prevents them from being absorbed by the sample) the region of the specimen from which BSEs are produced is considerably larger than it is for secondary electrons.

(4) **Characteristic X-rays:** When an inner shell electron is displaced by collision with a primary electron, an outer shell electron may fall into the inner shell to reestablish the proper charge balance in its orbital following an ionization event. Thus, by the emission of an X-ray photon, the ionized atom returns to ground state. The X-ray obtained is known as characteristic X-ray. The analysis of these characteristic X-rays is very helpful in providing chemical composition of the specimen.

(5) **Cathodoluminescence:** Cathodoluminescence is the emission of light from a material under the electron beam. By the energy obtained from the incident electron, an electron in the valence band can be promoted to the conduction band. The result is a so-called electron-hole pair. This excited state of the semiconductor is energetically instable, and the material can relax by filling this electron hole by an electron dropping down from the conduction band. This process, designated as recombination, leads to the emission of a photon carrying the difference energy E = hν. This energy corresponds to that of the band gap. Cathodoluminescence is therefore useful in the characterization of semiconductors, especially in cases where a contactless, high-spatial-resolution method is needed (Yacobi and Holt 1986).

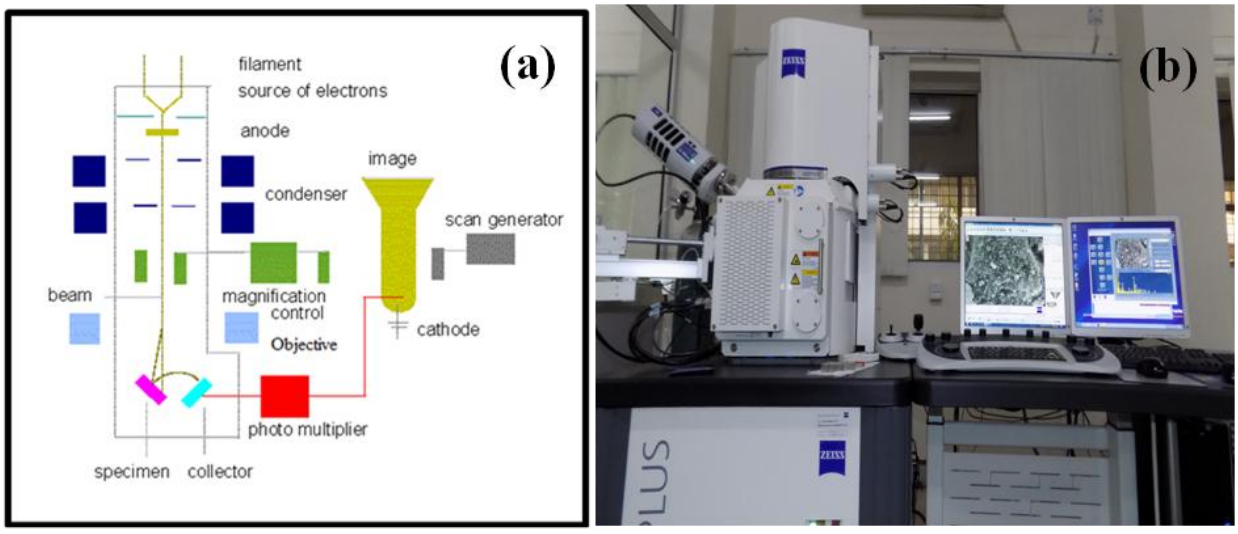

Figure 2.15 *(a) A Schematic diagram of the Scanning electron microscope, (b) photograph of FESEM available in IIT Roorkee*

Modern SEM systems require that the electron gun produces a stable electron beam with high current, small spot size, adjustable energy, and small energy dispersion. Several types of electron guns are used in SEM system and the qualities of electrons beam they produced vary considerably. The first SEM systems generally used tungsten "hairpin" or lanthanum hexaboride (LaB_6) cathodes, but for the modern SEMs, the trend is to use field emission sources in place of thermionic sources, which provide enhanced current and lower energy

dispersion. Thermionic sources depend on a high temperature to overcome the work function of the metal so that the electrons can escape from the cathode. Though they are inexpensive and the requirement of vacuum is relatively low, the disadvantages, such as short lifetime, low brightness, and large energy spread, restrict their applications. For modern electron microscopes, field emission electron guns (FEG) are a good alternative for thermionic electron guns. FESEM uses field emission electron gun which provides improved spatial resolution down to 1.5 nm that is 3 to 6 times better than conventional SEM and minimized sample charging and damage. The basic mechanism of field emission is that a high voltage applied between a pointed cathode and a plate anode caused a current to flow. The field emission process itself depends on the work function of the metal, which can be affected by adsorbed gases. This is the reason a very high vacuum is required. A schematic diagram of the optical column of the FESEM is shown in **figure 2.15 a**

The electron beam is energized by the accelerating potential of few hundred eV to 50 keV and the divergent beam is focused by two condenser lenses into a beam with a very fine focal spot size. The first condenser lens that works in conjunction with the condenser aperture helps to narrow the beam and also limit its current. The second condenser lens then makes the electron beam more thin and coherent. The objective lens does the final focusing of the beam onto the sample. During scanning, electron beam is thus made to deflect over the specimen in the raster form. At each point the secondary and back-scattered electrons reaching the detector are counted to be used for determining the relative intensity of the pixel representing that point in the final image. Limitation associated with the SEM is that the specimen that has to be analyzed should be conducting. In case of non-metals, it is required to make them conducting by covering the sample with a thin layer of conductive material like gold or platinum in order to enhance the imaging.

In the present study, field emission scanning electron microscope (Carl Zeiss, Germany, ULTRA *plus* model) with resolution of 0.8 nm and upto 100000X magnification were used to study the surface morphology of the deposited nanocomposite thin films (**figure 2.16b**). Elemental composition analysis can also be performed by using the energy dispersive X-ray spectrometry (EDS) attached with the FE-SEM system. An EDS spectrum normally displays peaks corresponding to the energy levels for which the most X-rays had been received. Each of these peaks is unique to an atom, and therefore corresponds to a single element. The higher a

peak in a spectrum, the more concentrated the element is in the specimen. The working principle of EDS is explained below.

2.5.3 Energy dispersive X-ray spectrometry (EDS)

EDS makes use of the X-ray spectrum emitted by a solid sample bombarded with a focused beam of electrons to obtain a localized chemical analysis. All elements from atomic number 4 (Be) to 92 (U) can be detected in principle, though not all instruments are equipped for 'light' elements (Z < 10). An EDS system comprises three basic components that must be designed to work together to achieve optimum results: the X-ray detector or spectrometer, the pulse processor, and the analyzer. The ED spectrometer converts the energy of each individual X-ray into a voltage signal of proportional size. This is achieved through a three stage process. Firstly the X-ray is converted into a charge by the ionization of atoms in a semiconductor crystal. Secondly this charge is converted into the voltage signal by the FET (Field Effect Transistor) preamplifier. Finally the voltage signal is input into the pulse processor for measurement. The output from the preamplifier is a voltage 'ramp' where each X-ray appears as a voltage step on the ramp. EDS detectors are designed to convert the X-ray energy into the voltage signal as accurately as possible. At the same time electronic noise must be minimized to allow detection of the lowest X-ray energies. An ED detector has several components like Collimator assembly, 'Be' window, a semiconductor crystal, Field-effect transistor, Cryostat etc. The functioning of each component is described below.

(a) Collimator assembly: The collimator provides a limiting aperture through which X-rays must pass to reach the detector. This ensures that only X-rays from the area being excited by the electron beam are detected and stray X-rays from other parts of the microscope chamber are not included in the analysis.

(b) 'Be' window: The window provides a barrier to maintain vacuum within the detector whilst being as transparent as possible to low energy X-rays. Beryllium (Be) is highly robust, but strongly absorbs low energy X-rays meaning that only elements from sodium (Na) can be detected accurately. Light element atoms (below carbon) return to fundamental

state mainly by Auger emission. For that reason, their K-lines are weak. In addition their low energy makes them easily absorbed.

(c) Semiconductor crystal: The crystal is a semiconductor device that, through the process of ionization converts an X-ray of particular energy into electric charge of proportional size. To achieve this, a charge-free region within the device is created. When an incident X-ray strikes the detector crystal, its energy (~3.8 eV/ electron-hole pair) is absorbed by a series of ionizations within the semiconductor to create a number of electron-hole pairs (**figure 2.16a).** A high bias voltage, applied between electrical contacts on the front face and back of the crystal, then sweeps the electrons and holes to these opposite electrodes, producing a charge signal, the size of which is directly proportional to the energy of the incident X-ray. EDS detectors are available with different sizes of crystals. The crystal size is often measured in area: 5 mm^2, 10 mm^2, 30 mm^2, 50 mm^2 etc. Normally the larger the crystal, the worse will be its resolution, particularly at low energy.

(d) Field-effect transistor: The field-effect transistor (FET) **(figure 2.16b)** is positioned just behind the detecting crystal. It is the first stage of the amplification process that measures the charge liberated in the crystal by an incident X-ray and converts it to a voltage output.

(e) Cryostat: The charge signals generated by the detector are small and can only be separated from the electronic noise of the detector and cooling the crystal and FET reduce the noise. Most EDS detectors work at close to liquid nitrogen temperatures. The vacuum is maintained at a low enough level to prevent the condensation of molecules on the crystal.

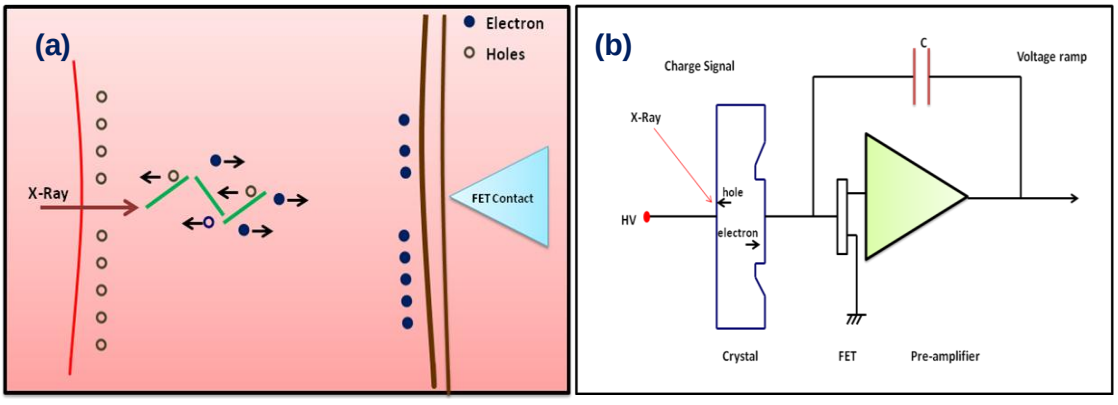

Figure 2.16 *Conversion of X-ray signals into a voltage 'ramp' by the EDS detector (a) generation and measurement of electron-hole pairs in the crystal, (b) circuit diagram of the EDS detector*

In the present study, EDS (Model: OXFORD, X-Max, United Kingdom) attached to FE-SEM with variation of ± 0.3 atomic% for heavy elements (Zr, W) and ± 2 atomic% for light elements (N, O) have been used for elemental composition analysis of Zr-W-N thin films.

2.5.4 Electron probe micro analyzer (EPMA)

An electron probe micro-analyzer (EPMA) is a microbeam instrument used primarily for the *in-situ* non-destructive chemical analysis of minute solid samples. EPMA is also informally called an electron microprobe, or just probe. It is fundamentally the same as an SEM, with the added capability of chemical analysis by wavelength-dispersive spectroscopy (WDS). The electron optics of an EPMA is similar to SEM (**section 2.5.2**). Our most common interest of using EPMA is the elemental compositional analysis of thin film materials through wavelength dispersive spectroscopy.

2.5.4.1 Wavelength-dispersive spectroscopy (WDS)

In principle we can determine two things from the X-ray spectrum emitted by any specimen. Measurement of the wavelength or energy of each characteristic X-ray that is emitted per second should tell us how much of the element is present in the specimen, i.e. to carry out quantitative analysis. The three areas in which the EDS system performs badly i) light element detection ii) peak separation and iii) peak to background ratio. These are the strong points of the other major X-ray detection system for electron microscopes, the wavelength dispersive spectroscopy (WDS).

The principle of the WDS is that the X-radiation coming from the specimen is filtered so that only X-rays of a chosen wavelength (usually the characteristics wavelength of the elements of interest) are allowed to fall on a detector. The filtering is achieved by a crystal spectrometer which employs diffraction to separate the X-rays according to their wave length. A common arrangement for WDS is shown in **figure 2.17a**. The X-ray leaving the specimen at certain angle, the *take-off angle* (ϕ), is allowed to fall onto a crystal of lattice spacing 'd'. If the angle between the incident X-ray and the crystal lattice plane θ, then the only X-ray which will diffract by the crystal and thus reach the detector will be those obeying Bragg's Law at angle 'θ'. The wavelength of the transmitted X-rays is therefore given by

$$\lambda = \frac{2d \sin\theta}{n} \quad (\mathbf{2.9})$$

If the spectrometer is to be used to detect, say ZrK_{α}, then the characteristic wavelength (0.08 nm) is substituted into above equation and the appropriate value of θ can be calculated for the particular crystal in use. If the spectrometer is set to this angle them only the ZrK_{α} characteristic X-ray will reach the detector and be counted. The detector no longer has to discriminate between X-rays of different energies. A much simpler detector than is found for EDS is used. This is the gas proportional counter, in which much faster count rate can be tolerated. One of the disadvantages is that because the X-rays must be reasonably well collimated before reaching the crystal, two sets of slits (S_1 and S_2) are generally used. In order that as many as possible of the X-rays leaving the crystal arrive at the detector the geometry of the spectrometer is chosen so that, as shown in **figure 2.17a**, all possible X-ray paths are focused onto detector. In order to achieve this focusing effect the specimen, crystal and detector must lie on a circle of radius R known as the Rowland circle. Also, the crystal must be bent to a radius 2R. These requirements place several restrictions on the analysis system: the spectrometer is necessarily quite large; its mechanism is complicated, since, in order to discriminate between very close lines, the angle θ be set to an accuracy of better than one minute of arc; finally the position of the specimen is absolutely critical, since if it lies off the Rowland circle by as little as a few micrometers the number of X-rays reaching the spectrometer will be severely reduced. These restrictions make the design of a crystal spectrometer difficult and expensive. Despite the difficulties and expenses of a crystal spectrometer, it remains an essential tool for analysis in the electron microscopy because of:

(a) The peak to background ratio of each line is much higher (often by a factor of ten).
(b) X-ray detector used in crystal spectrometer is capable of high counting (~ 500,000 cps) that make the instrument to collect data from a single element in a very short counting time.
(c) Its ability to detect X-ray from light elements. With suitable crystal of large lattice spacing it is possible to detect and count X-rays as soft as boron Kα or even beryllium Kα.

In the present study, electron probe micro analyzer (Cameca, SX-100 model, france) with beam diameter from 0.6 μm to 100 nA and upto 300000X magnification were used to

study the surface morphology of the deposited nanocomposite thin films (**figure 2.17b**). EPMA consists of five major components:

(1) An electron source, commonly a W-filament cathode referred to as a "gun" with 10^{-5} to 10^{-12} A beam current.

(2) A series of electromagnetic lenses located in the column of the instrument, used to condense and focus the electron beam emanating from the source; this comprises the electron optics and operates in an analogous way to light optics.

(3) A sample chamber, with movable sample stage (X-Y-Z) having X axis = 50mm, Y axis = 80mm and Z axis=1.5mm with a resolution of 0.1µm. A light microscope allows for direct optical observation of the sample.

(4) A variety of detectors arranged around the sample chamber that are used to collect x-rays and electrons emitted from the sample.

(5) Wave length dispersive spectroscopy (WDS) for elemental composition analysis.

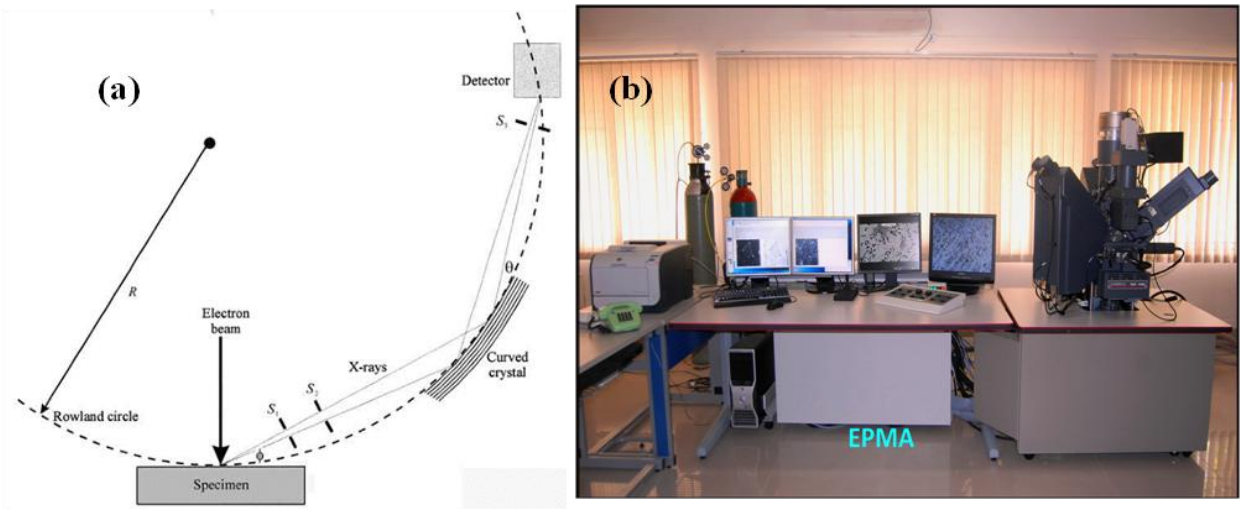

Figure 2.17 *(a) A crystal spectrometer. X-rays emitted from the specimen are collimated by two silts S_1 and S_2, diffracted by curved crystal and then focused on to the detector, (b) photograph of EPMA (Cameca, SX-100 model, France) available in IIT Roorkee*

2.5.5 Transmission electron microscopy (TEM)

Transmission electron microscopy (TEM) is the premier tool for understanding the internal microstructure of materials at the nanometer level. TEM is a high magnification measurement technique that images the transmission of a beam of electrons through a sample. Amplitude and phase variations in the transmitted beam provide imaging contrast that is a function of the sample thickness (the amount of material that the electron beam must pass through) and the sample material (heavier atoms scatter more electrons and therefore have a smaller electron mean free path than lighter atoms). Although X-ray diffraction techniques generally provide better quantitative information than electron diffraction techniques, electrons have an important advantage over X-rays in that they can be focused using electromagnetic lenses. This allows one to obtain real-space images of materials with resolutions on the order of a few tenths to a few nanometers, depending on the imaging conditions, and simultaneously obtain diffraction information from specific regions in the images (e.g., small precipitates) as small as 1 nm. Transmission electron microscope (TEM) operates on the same basic principle as the optical (light) microscope but uses electrons instead of visible light (Reimer 1993, Fultz and Howe 2002). The shorter wavelength of electrons (200 keV electrons have a wavelength of 0.025 Å) makes it possible to get a high-resolution (0.2 nm) and high-magnification thousand times better than the light microscope. The electromagnetic lenses are constructed with ferromagnets and copper coils. The focal length of electromagnetic lenses could be changed by varying the current through the coil. TEM is used to characterize the microstructure of materials such as grain size, morphology, crystal structure and defects, crystal phases and composition, and in biological sciences, especially in the study of cells at the molecular level. The microstructure is studied by use of the image mode, while the crystalline structure is studied by the diffraction mode. In addition, the chemical composition of small volumes, for example grain boundaries, can be obtained by detection of X-rays emitted from the films.

Figure 2.18a-b show **t**he ray-diagram and photograph of TEM (200kV, FEI, TECNAI G^2, USA) at Institute Instrumentation Centre, Indian Institute of Technology Roorkee, respectively. The system consists of an electron source made of a LaB_6 (Lanthanum hexaboride), focusing column and fluorescent screen. The accelerating voltage is variable between 20-200 kV. The objective lens forms the so-called first intermediate image of the object, which will be enlarged by a lens lower in the column. Because defects of the objective

lens are magnified by the total magnification factor, this lens is the most critical lens in the microscope.

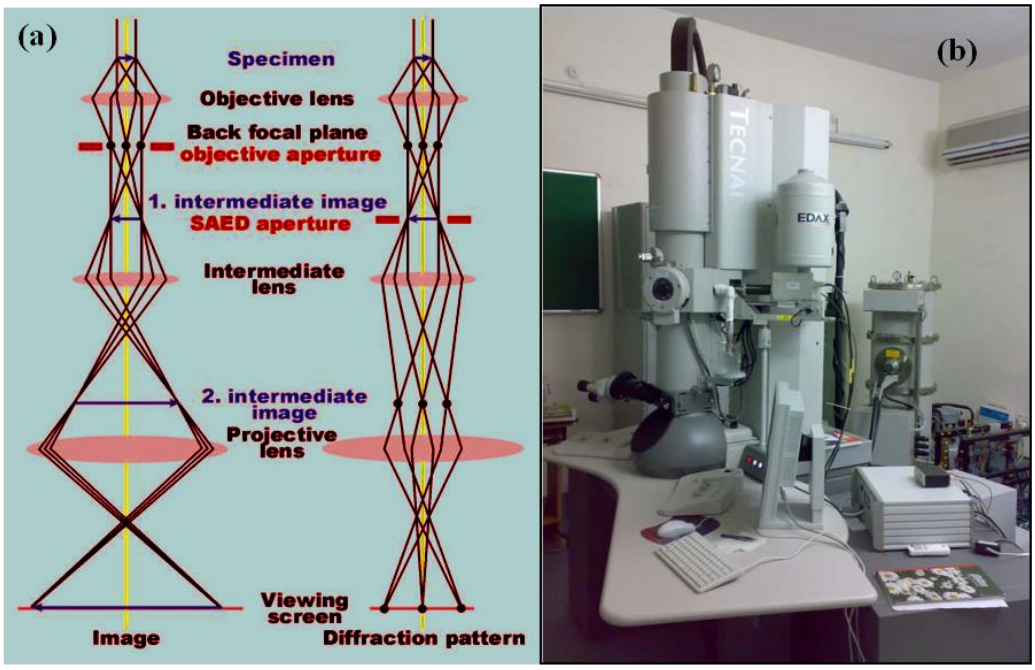

Figure 2.18 *(a) Ray diagram for the production of specimen image and diffraction pattern, (b) photograph of FEI Tecnai-20 TEM at IIT Roorkee*

In general, smaller the focal length (1 to 5 mm) and the lens aberration constants better will be the resolving power of the microscope. The objective aperture is positioned in the back focal plane of the objective lens for two main reasons:

(a) Limiting the angular aperture to reduce spherical and chromatic errors, which otherwise would blur the image and reduce the resolving power.

(b) Intercepting unwanted strongly scattered electrons from the specimen to prevent them from contributing to the image which would otherwise reduce the contrast of the final image.

Final image magnification in TEM is the result of the magnification of each magnifying lens: the objective lens, the diffraction lens, the intermediate lens and the projector lens. The

objective lens, the first magnifying lens in the TEM, is a high power lens. The diffraction lens, below the objective lens, is a very low power lens. The intermediate lens is a weak lens but with variable power. The current of this lens is adjusted to control the final magnification of the image. The last lens is the projector lens, which is a high power lens that projects the final magnified image on to the viewing screen.

TEM has following modes of operation:

(1) **Image Mode:** Imaging mode allows the imaging of the crystallographic structure of a specimen at an atomic scale. In image mode, image contrast comes from the scattering of the incident electron beam by the specimen. By using electrons accelerated to high voltages, atomic planes of the crystal can be resolved. In this mode, intermediate aperture is removed and only objective aperture is used. Intermediate lens is used to focus on the image plane of the objective lens. In image mode, two imaging systems are used:

(a) Bright field image: When an incident electron beam strikes a sample, some of the electrons pass directly through, while others may undergo slight inelastic scattering from the transmitted beam. Contrast in an image appears by differences in scattering. By inserting an aperture in the back focal plane, an image can be produced with these transmitted electrons. The resulting image is known as a bright field image. Bright field images are commonly used to examine micro-structural related features.

(b) Dark field image: If a sample is crystalline, many of the electrons will undergo elastic scattering from the various planes. This scattering produces many diffracted beams. If any one of these diffracted beams is allowed to pass through the objective aperture, an image can be obtained. This image is known as a dark field image. Dark field images are particularly useful in examining microstructural detail in a single crystalline phase.

(2) **Diffraction mode:** The diffraction pattern that is always present in the back focal plane of the objective is brought into focus by the objective lens. In diffraction mode, objective aperture is removed and only intermediate aperture is used which passes the diffraction pattern of a selected region. Individual spots are seen when the specimen is a single crystal, while for polycrystalline material concentric rings are observed. For a single crystal, the

diffraction spots from planes which are equivalent by symmetry are placed symmetrically around the central spot. Interplanar distance, *d* can be calculated from the expression:

$$R.d = L.\lambda \tag{2.10}$$

where, λ is the wavelength of the electron beam (0.025 Å for 200 kV), *R* is the distance of a particular spot form the central bright spot and *L* is the distance between the specimen and the diffraction plane, known as the lens constant or camera length.

TEM also has various drawbacks. Many materials require extensive sample preparation to produce a sample thin enough to be electron transparent, which makes TEM analysis a relatively time consuming process. The structure of the sample may also be changed during the preparation process. The sample may also be damaged by the electron beam in some cases. In TEM, a high-energy electron beam (≥ 200 keV) interacts with an electron transparent (~ 50-100 nm thick) specimen in order to study the microstructure and composition of the material. Preparation of a sample with such a thickness is not an easy job. It is both an art and a science. It needs utmost care in preparing and skills as the specimens are extremely thin and hence prone to bending.

There exist several TEM sample preparation techniques but which technique to be used it depends on various parameters e.g. the material of the specimen and what has to be observed in the sample. The adopted method should not create too much artifacts in the sample which could alter the result of the observation. There are currently three major methods, jet electro-polishing, ion milling technique, and focused ion beam (FIB) technique **(Williams and Carter 2009)** are using for sample preparation. Jet electro-polishing is used for the preparation of most metallic materials and superconductors. Ion milling technique consists of the ultrasonic cutting, initial grinding, dimpling and ion milling. This technology is usually applicable for cross-sectional and plan-view TEM sample for most of the electronic materials and composites coatings. FIB technology uses for semiconductor integrated circuits (ICs) to prepare the specific site cross-sectional sample etc. In the present study Ion milling technique was used to prepare plan view TEM samples for Zr-W-N and Zr-W-B-N nanocomposite thin films.

2.5.6 Atomic force microscopy (AFM)

Table 2.2 *Comparison of various microscopes (Kaufmann 2003)*

Technique	Probe/ Principle	Environment	Sample Requirements	Resolution (nm) XY	Z
Scanning Tunneling Microscopy (STM)	Electron tunneling	Air, vacuum, liquid	Flat, conductor	0.1-0.2	10^{-3}
Atomic Force Microscopy (AFM)	Forces: attractive, Repulsive, contact, noncontact	Air, vacuum, liquid	Flat, insulator, conductor	0.1-1.0	0.01
Transmission Electron Microscopy (TEM)	Electron transmission	High vacuum	Solid, 10nm thin	0.2	-
Scanning Electron Microscopy (SEM)	Secondary electrons	High vacuum	Solid, conductive	2	-
Scanning Auger Microscopy (SAM)	Auger emission	Ultrahigh vacuum	Conductive	10	-
Scanning Secondary Ion Mass Spectroscopy (SIMS)	Ion sputtering	Ultrahigh vacuum	Most samples	100	-

Atomic force Microscopy (AFM) provides a number of advantages over different microscopy techniques as observed from the comparisons of various microscopes given in **table 2.2** (Kaufmann 2003). With these advantages, AFM has significantly impacted the fields of materials science, chemistry, biology, physics, and the specialized field of semiconductors. AFM monitors the force between a sharp tip and the sample and utilizes this force to produce images. There is a piezoelectric actuator to precisely control the sensor above the surface and to raster the tip across the sample, there is a control system to provide feedback to the piezoelectric actuators and display the images, and there is an isolation system to dampen ambient vibrations. A schematic diagram of an atomic force microscope is shown in **figure 2.19a** and the laboratory set up of the AFM system used in the present studies is shown in **figure 2.19b** which is the NTEGRA model from NT-MDT, Russia.

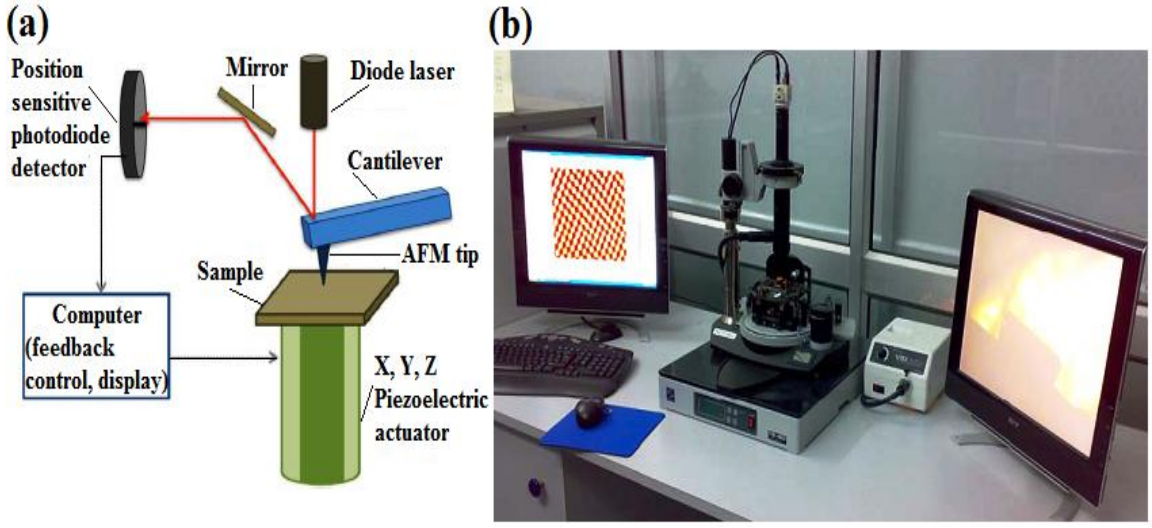

Figure 2.19 *(a) A schematic diagram of an atomic force microscope (AFM), (b) the laboratory set up of AFM (NT-MDT: NTEGRA)*

The probe is a microfabricated, force sensitive and attached with a cantilevered that deflects as a result of the sample-induced forces placed on the sharp tip that is positioned on or above the sample surface. Cantilevers typically range from 100 to 200 µm in length (l), 10 to 40 µm in width (w), and 0.3 to 2µm in thickness (t).The cantilever deflects upward in the case of a net repulsive force or downward in the case of a net attractive force. In the case of an AFM, this deflection, usually associated with topography, is utilized to generate an image of the sample surface. The deflection can be measured using an optical lever, in which a laser diode is focused on the end of the cantilever, which is typically angled downward from horizontal at around 10°. A laser is focused onto the end of the cantilever, the reflective coating on the back side of the cantilever permits reflection of the laser light to a position-sensitive photodiode detector located some distance away from the cantilever. Any forces acting on the tip result in a bending (vertical forces) or twisting (lateral forces) of the cantilever and therefore result in a different reflection angle. The difference of the output of the photodiodes is used as output signal, which is proportional to the deflection of the cantilever. Depending on the mode of operation, the photodiode signal is used directly or as a feedback signal. A feedback loop continuously checks the feedback signal, compares it to some user defined set point value and

adjusts the height of the tip over the sample such that the difference is minimized. Stable operation is possible if the feedback signal is monotonous in the tip-surface distance. The AFM can be operated under a wide array of controlled operating environments such as ambient, condensed phase (aqueous) and vacuum conditions, at elevated temperatures and pressures, and at cryogenic temperatures. This permits AFM to be utilized in a large number of scientific disciplines, including biology, materials synthesis and characterization, geochemistry, and nanomechanics.

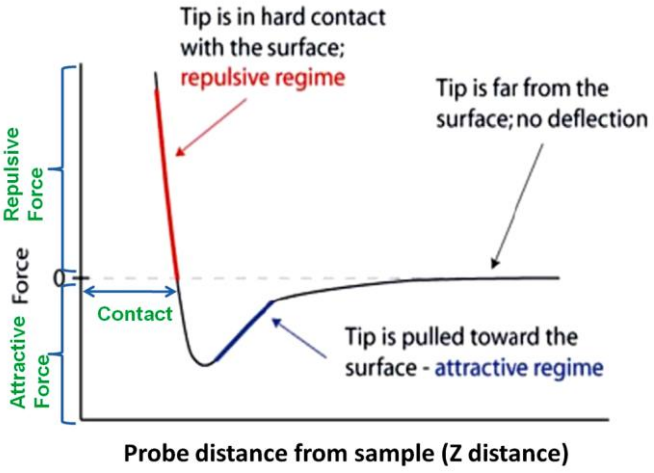

Figure 2.20 *Interaction force between tip and the sample surface as function of distance*

The interaction force between the scanning tip and sample surface is the essential parameter to determine the AFM scanning mode. These interactions are often described by using the Lennard-Jones Potential, which gives the potential energy of two atoms separated by a distance ‘r’. In the force-distance diagram illustrated in **figure 2.20**, the contact and non-contact regime are clearly indicated as the function of the distance between tip and sample surface. By decreasing the gap between the scanning tip and sample surface, the interaction forces can change from attractive to repulsive (electrostatic repulsion). As the atoms are gradually coming closer to each other, they first attract each other by van der Waal forces (1-50 nN, 1 N is little less than 1/4 pound) and cantilever deflections of less than 0.1 nm can be detected.

This attraction increases until the atoms are so close together that they begin to repel each other. With further reducing the gap, the repulsive force can dramatically increase due to the Pauli Exclusion principle and become the dominant interaction with progressive weakening

of the attractive force. Further reduction in distance than this distance (zero force), the total Van der Waals force becomes positive (repulsive). This distance will not change, therefore any more attempt to force the sample and tip closer will result in deformation or damage to the sample or the tip. With varying interaction force, the cantilever deflects in different ways. It can be bent upward, downward or twisted. There are two other forces that arise during the scan:

(i) A capillary force that is caused by a build-up of water. In real conditions (in ambient air), practically always some humidity is present in air and a water layer is adsorbed on the sample and tip surfaces.

(ii) On the tip; the force is caused by the cantilever itself, which is like a force caused by a compressed spring.

The AFM can operate in a number of imaging modes including contact mode, non-contact mode and tapping mode (also called semi-contact or intermittent mode).

(1) **Contact mode** is the most common method of operation of the AFM and is useful for obtaining 3D topographical information on nanostructures and surfaces. As the name suggests, the tip and sample remain in close contact as the scanning proceeds. In contact mode the tip either scans at a constant small height above the surface or under the conditions of a constant force. In the constant height mode the height of the tip is fixed, whereas in the constant force mode the deflection of the cantilever is fixed and the motion of the scanner in z direction is recorded. In contact mode, a relatively soft silicon nitride cantilever is typically used to probe the surface. Most cantilevers have spring constants < 1 N/m, which is less than effective spring constant holding atoms together. The force on the tip is repulsive with a mean value of 10^{-9} N and around 0.5nm probe-surface separation distance. This force is set by pushing the cantilever against the sample surface with a piezoelectric positioning element. In contact mode AFM, the deflection of the cantilever is sensed and compared in a DC feedback amplifier to some desired value of deflection. If the measured deflection is different from the desired value the feedback amplifier applies a voltage to the piezo to raise or lower the sample relative to the cantilever to restore the desired value of deflection. The voltage that the feedback amplifier applies to the piezo is a measure of the height of features on the sample surface.

Advantages: (i) High scan speeds, (ii) Atomic resolution is possible, (iii) Easier scanning of rough samples and (iv) Lateral forces, can be used to provide information on the friction (drag resistance)

Disadvantages: (i) Lateral forces can distort the image, (ii) Capillary forces from a fluid layer can cause large forces normal to the tip-sample interaction, (iii) Combination of these forces reduces spatial resolution and (iv) Tip may scratch the surface, change its intrinsic features and can cause damage to soft samples (however imaging in liquids often resolves this issue)

(2) **Non-contact** mode is a method where the cantilever is oscillated above the surface of the sample at distance such that it is no longer in the repulsive regime but in the attractive regime of the inter-molecular force curve. In non-contact imaging, the tip is oscillated at its resonant frequency at around 0.1-10nm probe-surface separation distance above the surface. Changes in the long-range attractive Van der Waals forces exerted on the tip due to topography cause the resonant frequency of the cantilever to shift. The signal applied to the piezoelectric actuators needed to keep the resonant frequency constant is then used to generate a topographic image. So attractive Van der Waals forces acting between the tip and the sample are detected, and topographic images are constructed by scanning the tip above the surface. Since the attractive forces from the sample are substantially weaker than the forces used by contact mode, therefore the tip is given a small oscillation so that AC detection methods can be used to detect the small forces between the tip and the sample by measuring the change in amplitude, phase, or frequency of the oscillating cantilever in response to force gradients from the sample. Non-contact imaging is mostly used in vacuum systems, where instabilities due to surface adsorbents (i.e. water, contamination) are minimal.

Advantages: (i) Very low force is exerted on the sample (10^{-12}N) surface, (ii) No damage is caused to soft samples and (iii) Extended probe lifetime

Disadvantages: (i) Lower lateral resolution limited by tip-sample separation, (ii) Contaminant layer on surface can interfere with oscillation, (iii) Slower scan speed, (iv) Usually only applicable in extremely hydrophobic samples with a minimal fluid layer (v) Need ultra high vacuum to have best imaging

(3) **Tapping mode** is another mode of operation for AFM. Unlike the operation of contact mode, where the tip is in constant contact with the surface, in tapping mode, the tip makes intermittent contact having around 0.5-2nm probe-surface separation distance. In this mode, the cantilever is made to oscillate at its natural frequency by using a piezo-electric crystal. The oscillating tip is moved close to the sample surface till it begins to just tap it and is then immediately lifted off again, while the sample is continuously scanned below the tip. Because the contact time is a small fraction of its oscillation period, the lateral forces are reduced dramatically. The change in oscillation amplitude during the tapping period is used as a feedback to maintain constant height or force between the tip and the sample. In constant height mode, the tip is kept at a fixed height at or above the surface and the cantilever deflection, is used to generate an image. The feedback voltage serves as a measure of the surface features. As the tip is not dragged over the sample, there is no damage caused to the sample and also the tip is prevented from sticking to the sample surface due to adhesion. This method usually gives higher resolution than the previous two methods. Tapping mode is usually preferred to image samples with structures that are weakly bound to the surface or samples that are soft (polymers, thin films). There are two other types of image contrast mechanisms in tapping mode:

(a) Amplitude imaging The feedback loop adjusts the *z*- axis movement so that the amplitude of the cantilever oscillation remains (nearly) constant. The voltages needed to keep the amplitude constant can be compiled into an (error signal) image and this imaging can often provide high contrast between features on the surface.

(b) Phase imaging The phase difference between the driven oscillations of the cantilever and the measured oscillations can be attributed to different material properties. For example, the relative amount of phase lag between the freely oscillating cantilever and the detected signal can provide qualitative information about the differences in chemical composition, adhesion, and friction properties.

Advantages: (i) Higher lateral resolution (1nm to 5nm), (ii) Lower forces and less damage to soft samples in air, (iii) Almost no lateral forces and (iv) Also good for biological samples

Disadvantages: (i) Slower scan speed than in contact mode and (ii) More challenging to image in liquids

2.5.7 Nanoindentation

Indentation testing is a simple method that consists essentially of touching the material of interest whose mechnical proprties such as elastic modulus and hardness are unknown with another material whose properties are known. Nanoindentation is simply an indentation test in which the length scale of the penetration is measured in nanometeres rather than in microns or millimeters. The present field of nanoindentaion grew from a desire to measure the mechanical properties of hard thin films and other near surface treatments in the early 1980's. Microhardness testing instruments available at the time could not apply low enough forces to give penetration depth less than the required 10 % or so of the film thickness so as to avoid the influence of the substrate. Even if they could, the resulting size of the residual impression cannot be determined with sufficient accuracy to be useful (Pollock 1992). Its attractiveness stems largely from the fact that mechanical properties can be determined directly from indentation load and displacement measurements without the need to image the hardness impression.

Nanoindentation is a technique used to investigate hardness, elastic modulus and other mechanical properties of materials in which an indenter tip of known geometry is driven into a specific site of the sample by applying an increased normal load (Hay *et al.* 2000, Fischer-Cripps 2001, Han *et al.* 2005) and then the load is decreased linearly; while it continuously measures the force-displacement response. The materials with features less than 100 nm across and thin films less than 5 nm thick can be tested to understand its mechanical behavior. It is used to study the relationship between microstructure and strength and toughness of materials. In film-substrate system, a "rule of thumb" for hardness measurements is 1/10-rule that the indentation depth is smaller than 10-15% of the film thickness, so that there will be no substrate effect on the measured mechanical properties of the film and this statement is a first approximation. However, in cases like soft films on hard substrates or hard films on soft substrates, it tends to be either too strict or too lax. The applications of nanoindentation technique include: to study the mechanical behavior of thin films (such as hardness, elastic modulus, adhesion evaluations and wear durability), bone, and biomaterials. Hardness measurements for submicron-size features, elastic behavior of metals, ceramics, polymers, etc.

The photograph of nanoindenter (NT-MDT prima Nanosclerometry, Russia) used for measuring mechanical properties of Zr-W-N and Zr-W-B-N films is shown in **figure 2.21**. In

this nanoindenter Atomic Force Microscope (AFM) attached with measuring head (performing indentation with varying loads) for selecting a specific location prior to the indentation and to image the residual imprint after indentation. The precise positioning (0.5 µm) capability of the X-Y motorized table combine with the large X-Y ranges (140 × 140 µm) of the objective ensures that the indent will always be in the centre of the field of view in AFM mode.

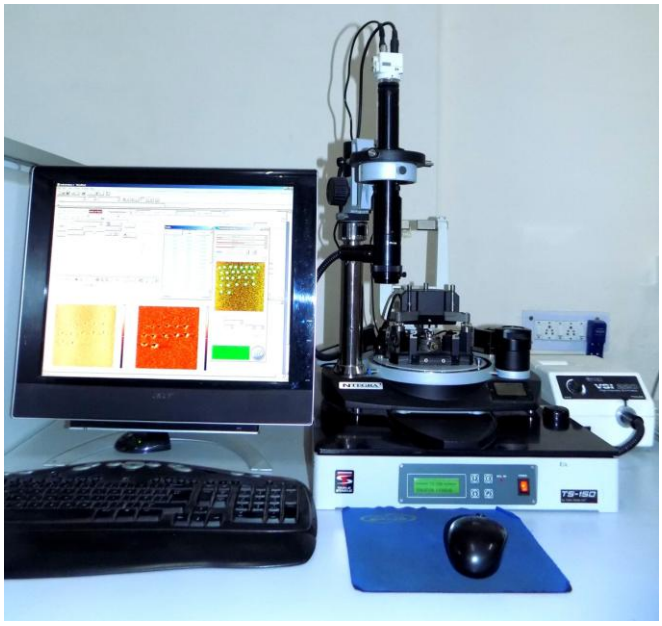

Figure 2.21 *Nanoindenter (NT-MDT prima Nanosclerometry)*

Indentations were made on the desired area of the sample whose properties are unknown by using a three-sided, pyramid-shaped Berkovich diamond indenter with nominal angle of 65.3º between the tip axis and the faces of the pyramid.

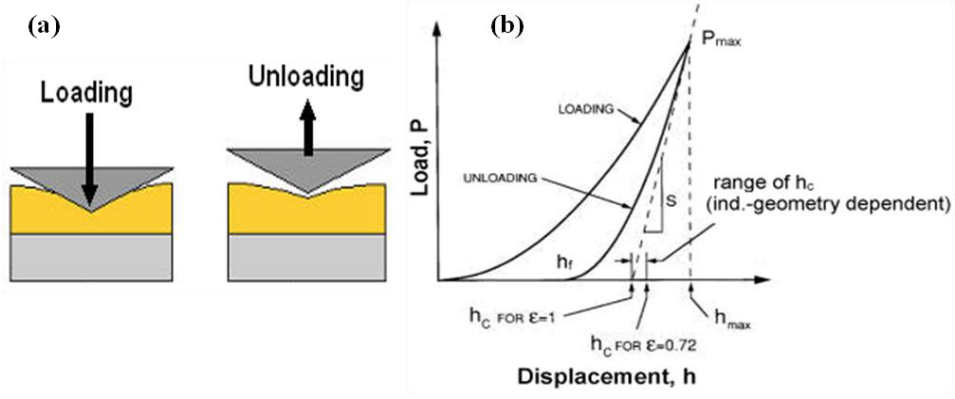

Figure 2.22: *(a) Loading and unloading of the indenter on the sample, (b) load is plotted against the displacement*

The Nanoindenter works on load control. In load control, the load placed on the indenter tip is increased gradually as the tip penetrates into the specimen at a selected rate and soon reaches to a selected maximum load. At this point, the load may be held constant for a period of time and then unloaded. During loading and unloading cycle, the load is increased and decreased in a linear fashion, the area of indentation is continually measured and this area is used to obtain the load-penetration depth characteristics from which the hardness and elastic modulus values are calculated. **Figure 2.22a** shows the loading and unloading of the indenter on the sample. For each loading and unloading cycle, the load is plotted against the displacement of the indenter as shown in **figure 2.22b**. The maximum load for thin film is selected as there is no influence of the substrate material on the mechanical properties of the film.

The analysis of elastic modulus is based on the Oliver and Pharr Method (Oliver *et al.* 1992). The modulus of a material was calculated from the load-displacement curves by modeling the unloading curve with a power law relationship instead of assuming linear unloading. At any time during loading, the total displacement h is written as

$$h = h_c + h_s \tag{2.11}$$

where, h_c is the vertical distance through which contact is made (contact depth) or the contact depth of the indenter with the sample under load and h_s is the displacement of the surface at the perimeter of the contact or sample deformation when the load is applied.

From Sneddon's solution for a conical indenter, h_s becomes

$$h_s = \frac{(\pi - 2)}{\pi}(h - h_f) \tag{2.12}$$

where, h_f is the final depth upon unloading the indenter. The quantity $(h - h_f)$ appears rather than h by itself.

Sneddon's contact solution (Sneddon 1965) predicts that the unloading data for an elastic contact for many simple indenter geometries (sphere, cone, flat punch and paraboloids of revolution) follows a power law that can be written as follows:

$$P = \alpha h^m \tag{2.13}$$

where, P is the indenter load, h is the displacement and α and m are constants.

Oliver and Pharr apply this formulation (**equation 2.13**) to determine the contact area at maximum load as it is valid even if the contact area changes during unloading. To do this, they derived the following relationship for the contact depth from Sneddon's solutions. The contact depth h_c is expressed as

$$h_c = h_{\max} - \varepsilon \frac{P_{\max}}{S} \tag{2.14}$$

where, *S* is stiffness constant and equal to *dP/dh*, i.e derivative of a power law fit to the unloading curve and evaluated at the maximum load, $P_{\max}$, $h_{\max}$ is the maximum depth, and ε refers to tip shape constant and is equal to 0.72 for a conical indenter, 0.75 for parabolic indenter and 1 for a flat indenter. The procedure for Oliver and Pharr analysis includes a fitting of power law function to the unloading segment. This yields the contact stiffness as slope of this function at maximum load. This slope in addition to the appropriate value of ε is used in order to determine the actual contact depth so that it is finally possible to derive the elastic modulus and the hardness. To find the hardness, a measure of the indentation area is needed. A convenient way to do this is to use the projected contact area at maximum load. The area function for a perfect Berkovich tip is given as

$$Af(h_c) = 24.56h_c^2 \tag{2.15}$$

In the nanoindentation analysis, the hardness is calculated by utilizing the contact area at maximum load and the equation is given as

$$H = \frac{P_{\max}}{Af(h_c)} \tag{2.16}$$

Both values, elastic modulus as well as hardness, depend strongly on the area function $Af(h_c)$ and the accuracy with which it is determined.

The reduced elastic modulus (E_r) is calculated from

$$E_r = \frac{1}{\beta}\frac{\sqrt{\pi}}{2}\frac{S}{\sqrt{Af(h_c)}} \tag{2.17}$$

where β is a constant or correction factor related to the tip geometry and equals to 1, 1.034 and 1.012 for spherical tip, Berkovich tip and Vickers tip, respectively (Oliver *et al.* 2004).

The elastic modulus of the sample can be derived from the following equation.

$$\frac{1}{E_r} = \frac{(1-\nu^2)}{E} + \frac{(1-\nu_i^2)}{E_i} \qquad (2.18)$$

where, E & ν are the elastic modulus and Poisson's ratio, respectively, for sample and E_i & ν_i are the elastic modulus and Poisson's ratio, respectively, for the indenter. For a diamond indenter tip, E_i is 1140 GPa and ν_i is 0.07 (Oliver *et al.* 2004).

2.5.8 Microindentation

The microindentation was used to calculate the fracture toughness of the deposited coatings. The microindentation with a Vickers micro hardness tester (UHL VMHT, Germany) as shown in **figure 2.23** was used for this purpose in the present study. The micro indentations were done at varying loads (100 mN to 5000 mN) for a dwell time of 15 sec. For each load, at least three readings were taken. The toughness K_{IC} is calculate by equation (2.18) (Lawn 1980).

$$K_{IC} = \delta\left(\frac{Er}{H}\right)^{1/2}\left(\frac{P}{C}\right)^{3/2} \qquad (2.19)$$

Where P is the applied indentation load; E_r and H are the effective elastic modulus and hardness of the coating, respectively. δ is an empirical constant which depends on the geometry of the indenter, for Vickers indenter δ= 0.016. C is the crack length which was measured from optical microscopy (Olympus DME3) images. In order to reduce the substrate effect on film toughness, K_{IC} calculated from equation (2.19) was plotted versus indentation depth and then the curve was extrapolated to one-tenth of the film thickness to obtain the film toughness.

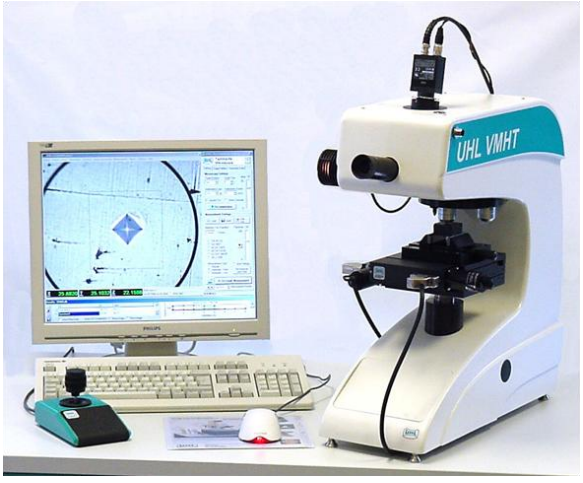

Figure 2.23 *Photograph of Microindenter (UHL VMHT)*

CHAPTER 3

Zirconium Tungsten Nitride coating: Study on Nitrogen Partial Pressure

The effect of nitrogen partial pressure (pN_2) on structural, composition, deposition rate and mechanical properties of Zirconium Tungsten Nitride ($Zr_xW_{1-x}N_y$) coatings have been studied in detail.

3.1 Introduction

In recent years, research in the area of wear protection of materials using mechanically hard, tough and thermally stable coatings has been very fascinating. Ternary nitride coatings promise manifold applications by improving the life and performance of machining components. Many ternary nitrides, e.g., Ti-Al-N, Ta-Zr-N, Cr-W-N, Zr-Al-N (Hasegawa *et al.* 2000, Tang *et al.* 2012, Gu *et al.* 2008, Yang *et al.* 2012, Klostermann *et al.* 2007) belonging to metal-metal nitride group and Zr-Si-N, Ti-Si-N, W–Si–N, Ti-B-N (Sun *et al.* 1997, Soderberg *et al.* 2005, Kim *et al.* 2002A, Chawla *et al.* 2010, Musil *et al.* 2005, Marques *et al.* 2003, Wiedemann *et al.* 1999) belonging to metal-metalloids nitride group have been studied to achieve the best blend of toughness, wear resistance and low friction performance across multiple environments. Among metal-metal ternary nitrides, it has been observed that those ternary nitrides which exhibit blend of metallic bonding and ionic bonding exhibit the best mechanical properties against wear damage (Holleck *et al.* 1986, Zhao *et al.* 2005, Yamamoto *et al.* 2010). According to Holleck *et al.* (1986), blend of metallic bonding and ionic bonding in ternary metal nitrides can be achieved by a combination of group IV and group VI binary transition metal nitrides. Because of complex requirements for wear resistant coatings such as high hardness, high toughness, good adherence at the substrate-layer boundary and high stability, a alloying of different group hard material seem to be the best negotiation. Group IV binary transition metal nitrides (TiN, HfN, ZrN) exhibit high hardness, high stability and are brittle in nature while group VI binary transition metal nitrides (CrN, MoN, W_2N) exhibit high toughness, high adhesion and are less reactive in nature. In literature, the studied ternary metal nitrides exhibiting the combination of group IV and group VI binary nitrides are Ti-Cr-N, Ti-

W-N, Ti-Mo-N, Zr-Cr-N, Ti-Zr-N, Zr-Mo-N and Cr-Mo-N. The mechanical properties of these ternary nitrides have been found better than their binary nitrides (Song *et al.* 2007, Hsu *et al.* 2013, Moser *et al.* 1994, Yang *et al.* 2005, Regent *et al.* 2001, Kim *et al.* 2009A, Purushotham *et al.* 2007, Ryan *et al.* 1964, Schwarz *et al.* 1985).

Kim *et al.* (2009A) have studied the tribological and corrosion properties of Cr-Zr-N coatings deposited on silicon and tool steel by magnetron sputtering. The average friction coefficient of Cr-Zr-N coating against a steel ball was reported ~ 0.17 which is lower than those for CrN (0.49). The corrosion resistance of the Cr-Zr-N coating was significantly improved in comparison with that of CrN and the coroosion current density and corrosion rate decreased with increasing Zr content.

Lamni *et al.* (2005) have studied the effect of Al and Cr concentrations on microstructure and mechanical properties of zirconium based ternary transition metal nitrides $Zr_{1-x}M_xN$ with M = Al ($0 \leq x \leq 0.43$), Cr ($0 \leq x \leq 0.48$) deposited on silicon and WC–Co substrates by reactive magnetron sputtering. All the deposited Zr-M-N coatings exhibited single-phase fcc NaCl type of structures (B1) and columnar morphology. The increasing aluminum and chromium content in the Zr-M-N films did not change the structure and morphology of the films. The hardness and Young's modulus values of $Zr_{1-x}Al_xN$ coatings, gradually increase from H = 21 GPa up to H = 28 GPa and from E = 250 GPa up to E = 300 GPa as the Al content increase from x = 0 to x = 0.43. In contrast, the hardness and Young's modulus in $Zr_{1-x}Cr_xN$ remains unchanged for selected Cr content in the films.

Gu *et al.* (2008) have compared the mechanical and tribological properties of Cr–W–N and Cr–Mo–N multilayer thin films by using a nanoindentor and a ball-on-disk tribometer, respectively. These films were deposited on high speed steel substrate by unbalanced DC reactive magnetron sputtering technique. The Cr–W–N multilayer films had much better mechanical properties (H ~ 29 GPa, E_r ~ 375 GPa, H^3/E_r^2 ~ 0.167 GPa) than the Cr–Mo–N (H ~ 24 GPa, E_r ~ 325 GPa, H^3/E_r^2 ~ 0.118 GPa) films. The wear resistance of both the Cr–W–N and Cr–Mo–N multilayer films increased with decreasing the bilayer period. The Cr–W–N multilayer film with a bilayer period of 12 nm exhibited excellent wear resistance and mechanical properties.

Earlier research represents a lot of work being done on single systems of zirconium nitride (ZrN) (group IV) and tungsten nitride (W_2N) (group VI). Individually (ZrN) is very promising material in various applications because of its attractive properties like high hardness, good wear resistance, good electrical conductivity, high melting point and stability as diffusion barriers in microelectronic devices and decorative coatings (Pilloud *et al.* 2003, Rizzo *et al.* 2006, Pelleg *et al.* 2007, Sue *et al.* 1995). On the other hand W_2N belongs to a class of refractory metal nitrides that have unique properties like excellent hardness, chemical inertness, good chemical stability and high conductivity (Toth *et al.* 1971, Yamamoto *et al.* 2005, Wen *et al.* 2010, Suetin *et al.* 2010). A blend of ZrN (group IV) and W_2N (group VI) is thus expected to show excellent hardness, high toughness, high adhesion, high wear resistance and good thermal and chemical stability. Zr-W-N thin films can be very interesting with regard of a combination of ZrN and W_2N.

In the present work, tungsten nitride (W_2N) and zirconium nitride (ZrN) have been selected for the development of super hard and tough nanostructure Zr-W-N coating material. The films have been deposited by DC/RF reactive magnetron sputtering on Si (100) substrates. The effect of nitrogen partial pressure (pN_2) on structural, composition, deposition rate and mechanical properties of these coatings has been investigated in detail.

3.2 Experimental Details

3.2.1 Deposition of $Zr_xW_{1-x}N_y$ thin films

Ternary nitride $Zr_xW_{1-x}N_y$ films have been deposited on 'p' type Si (100) substrates using DC/RF reactive magnetron co-sputtering. Si substrates were cleaned by first rinsing in hydrofluoric acid to remove the native SiO_2 layer followed by ultrasonic bath treatment in acetone and finally drying under nitrogen gas. Sputtering targets (5 cm diameter and 0.5 cm thick) of Zr and W with purity 99.98% and 99.95% respectively have been used for deposition. Targets were fixed at an angle of 45° to the substrate normal. Si substrates were mounted on the grounded substrate holder with the help of silver paste. The substrate holder was rotated at 5 rpm by using a DC motor to ensure uniformity in the deposited thin films. The residual gas

pressure was < 0.4×10^{-3} Pascal (Pa) and sputtering was carried out in N_2 and Ar atmosphere with varying partial pressure of N_2 gas. Prior to deposition, the targets were pre-sputtered for 15 min to remove the impurities present on the surface. All depositions were performed at a fixed substrate to target distance of 6 cm. The details of sputtering parameters for $Zr_xW_{1-x}N_y$ films are given in **table 3.1**.

Table 3.1 *Sputtering parameters for Zr-W-N films*

Target	Tungsten (W) and Zirconium (Zr)
Gas used	Ar and N_2
N_2 Partial Pressure	0.07 Pa to 0.67 Pa
Sputtering pressure	0.67 Pa
Deposition time	1.5 h
Power density for W target	~ 4 Watt/cm^2
Power density for Zr target	~ 6 Watt/cm^2
Substrate	Si (100)
Substrate temperature	350ºC

3.2.2 Characterization

The $Zr_xW_{1-x}N_y$ thin films deposited using different parameters have been characterized by grazing angle X-ray diffraction (GAXRD) (Bruker, D8 advance, Cu-K_α radiation, λ = 1.54Å), field emission scanning electron microscopy (FE-SEM) (FEI, QUANTA 200F), atomic force microscopy (AFM) (NT-MDT, NTEGRA) and transmission electron microscopy (TEM) (FEI, TECNAI G^2) for their structural, cross-sectional, and morphological studies. The elemental composition analysis of these films carried out using an energy dispersive X-ray analysis (OXFORD, X-Max) with variation of ± 0.3 at.% for heavy elements (Zr, W) and ± 2 at.% for light elements (N_2). Mechanical properties have been studied by nano-indentation (NT-MDT, Nanoslerometry). Nanoindentation uses a triangular pyramid Berkovich diamond indenter with

normal angle of 65.3° between the tip axis and the faces of triangular pyramid and the effective size of apex is about 70 nm. It is a very powerful tool to study the mechanical properties of coatings such as hardness (H), reduced elastic modulus (E_r) and percentage elastic recovery (W_e) with the help of loading and unloading curves. The results obtained have been reported in detail in the following section.

3.3 Results and Discussion

3.3.1 Structural analysis

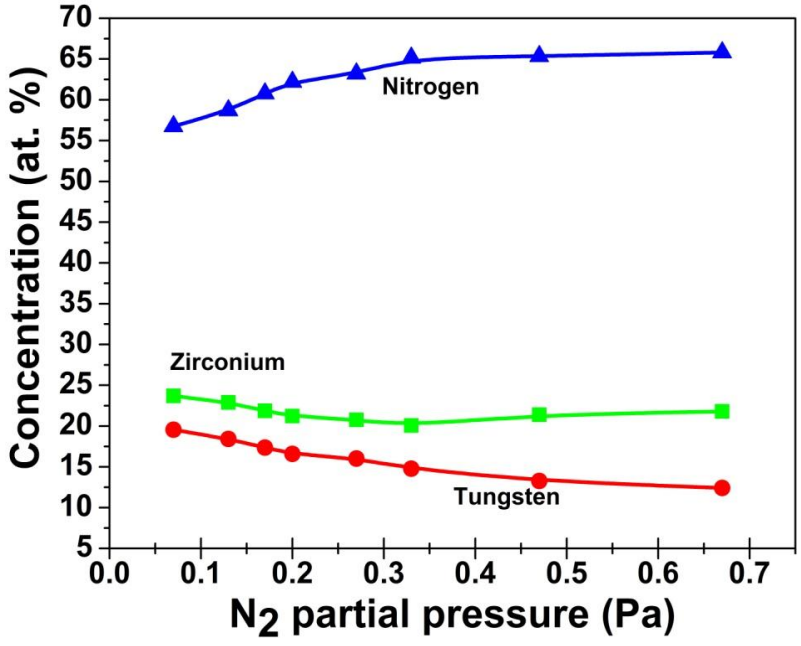

Figure 3.1 *The elemental composition of the films deposited at different nitrogen partial pressure (pN_2)*

It can be clearly seen that with increasing pN_2, the at.% of Zr and W elements decrease while the at.% of nitrogen increases. This is because, as the pN_2 increases, the assimilation of N_2 molecules (Φ = 3.14 Å)/N_2^+ ions in gaseous phase in the sputtering chamber increases over heavier Ar atoms (Φ = 1.76 Å)/Ar^+ (Φ = 1.54 Å) which results in an increase in the collision frequency in the plasma and hence the sputtering yield of W and Zr decrease (Moser *et al.* 1994) as depicted in **figure 3.1**. However, Zr/W ratio was found to increase with increasing

pN_2 due to lower sputtering threshold energy of Zr (22 eV) in comparison to W (33 eV) (Wasa *et al.* 2004).

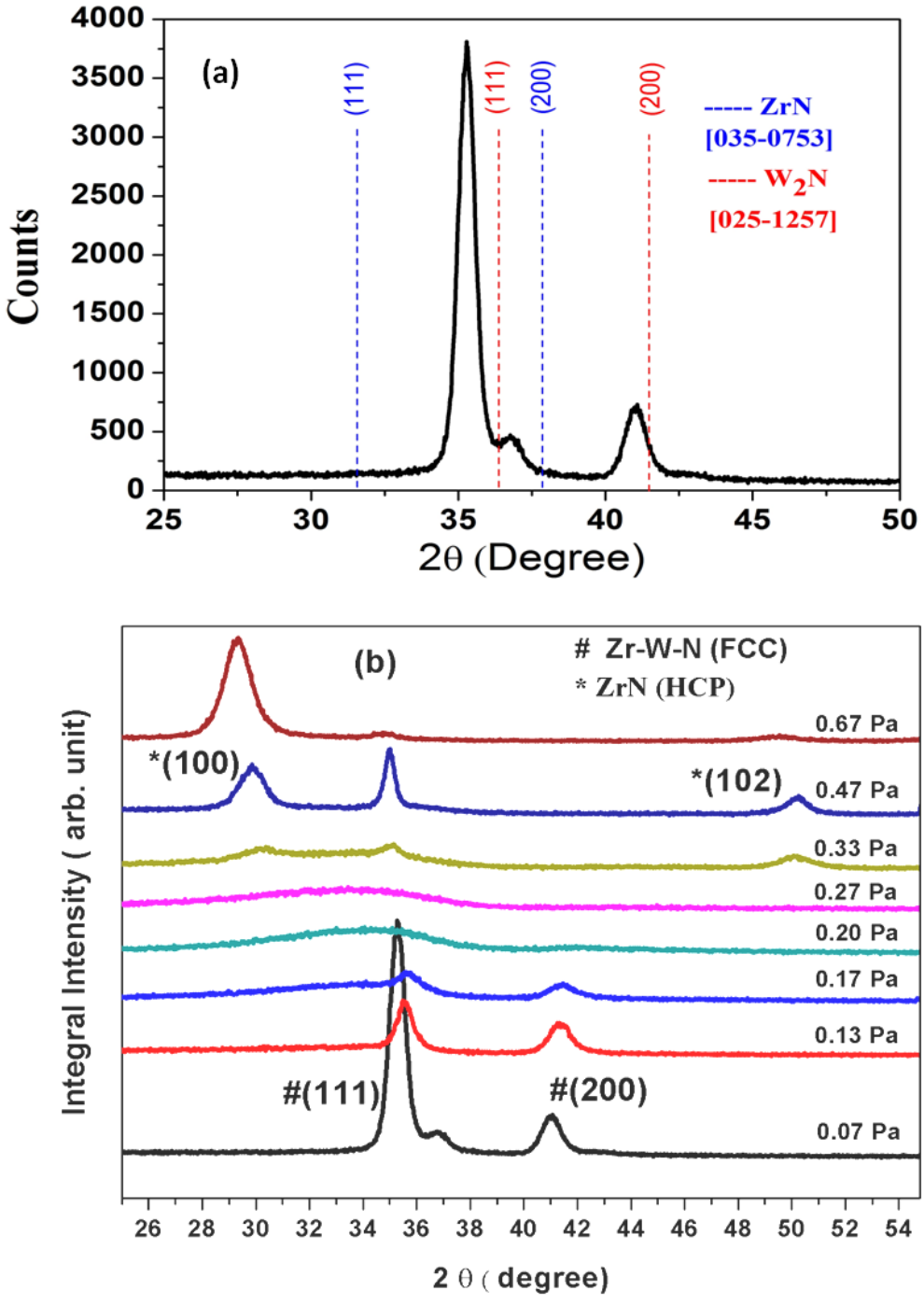

Figure 3.2 *(a) Confirmation of Zr-W-N compound formation at 0.07 pN_2 by standard XRD pattern and (b) XRD patterns of Zr-W-N coatings at varying pN_2*

All the deposited $Zr_xW_{1-x}N_y$ films have dark gray colour in visible light. XRD pattern of Zr-W-N film deposited at pN_2 = 0.07 Pa as shown in **figure 3.2a** indicates the formation of single phase (fcc) Zr-W-N compound. **Figure 3.2b** shows the XRD patterns of all the films deposited at different pN_2.

For 0.07 Pa ≤ pN_2 ≤ 0.17 Pa, a shift in fcc phase peaks towards higher angles have been observed. This shift may be associated with increasing Zr/W ratio with increase in pN_2. However, since the atomic radius of Zr (2.16 Å) is larger than W (2.02 Å), the XRD peaks are expected to shift towards lower angles with increasing Zr/W ratio, on the contrary, in the present case, shifting of peaks towards higher angles with increasing Zr/W ratio may be explained on the basis of bond character of Zr and W with nitrogen. Zr has a tendency for ionic character with nitrogen (Pauling 1939), while W rich films exhibit covalence level with nitrogen (Hones *et al.* 2000). A comparison of ionic radius (1.09 Å) of Zr in Zr-N bond and covalent radius (1.30 Å) of W in W-N bond shows that although Zr has larger atomic radius than W, the ionic radius of Zr is smaller than the covalent radius of W, thus an increase in Zr/W ratio reduces the lattice parameter of the fcc unit cell and consequently a shifting of peaks towards higher angles have been observed in the XRD patterns. For 0.20 Pa ≤ pN_2 ≤ 0.27 Pa, Zr/W ratio increases further, this in turn increases the mixture of elements with different radii leading to reduced diffusion rates in the films and an amorphous phase (Johnson 2002, Inoue *et al.* 1993) is observed in the XRD patterns. For pN_2 > 0.27 Pa, XRD patterns show some additional reflections along with the reflections of fcc Zr-W-N phase. These additional reflections may be indexed with hcp structure associated with the ZrN phase which starts nucleating along with the pre existing Zr-W-N (fcc) phase with increasing pN_2. The formation of hcp ZrN phase may be associated with lower free energy (-347 kJ/ mol) of this phase in comparison to fcc W_2N (-72 kJ/mol) and hcp WN (-68 kJ/mol) crystallographic phases. Although, the free energy of fcc ZrN (-357 kJ/mol) is comparable to the free energy of hcp ZrN phase, the reflections corresponding to fcc ZrN have not been observed in the XRD pattern of the sample (Suetin *et al.* 2010, Ogawa 1994). At very high pN_2 (~ 0.67 Pa), the XRD pattern shows dominant growth of ZrN (hcp) phase over Zr-W-N (fcc) phase.

To further confirm the evolution of phases with increasing pN_2, TEM analysis of the films has been carried out. **Figure 3.3a-c** shows the bright field TEM images and selected area

electron diffraction (SAED) patterns of the films deposited at 0.13 Pa, 0.27 Pa and 0.47 Pa pN_2 respectively. For pN_2 = 0.13 Pa (**figure 3.3a**), the SAED patterns confirm the formation of fcc phase, for pN_2 = 0.27 Pa (**figure 3.3b**), SAED pattern shows an amorphous phase formation and the diffuse rings in SAED pattern confirm that nanocrystalline grains were not grown during deposition. For pN_2 = 0.47 Pa (**figure 3.3c**), reflections corresponding to dual phase of fcc and hcp can be seen in the SAED pattern. The TEM analysis is in agreement with the XRD results.

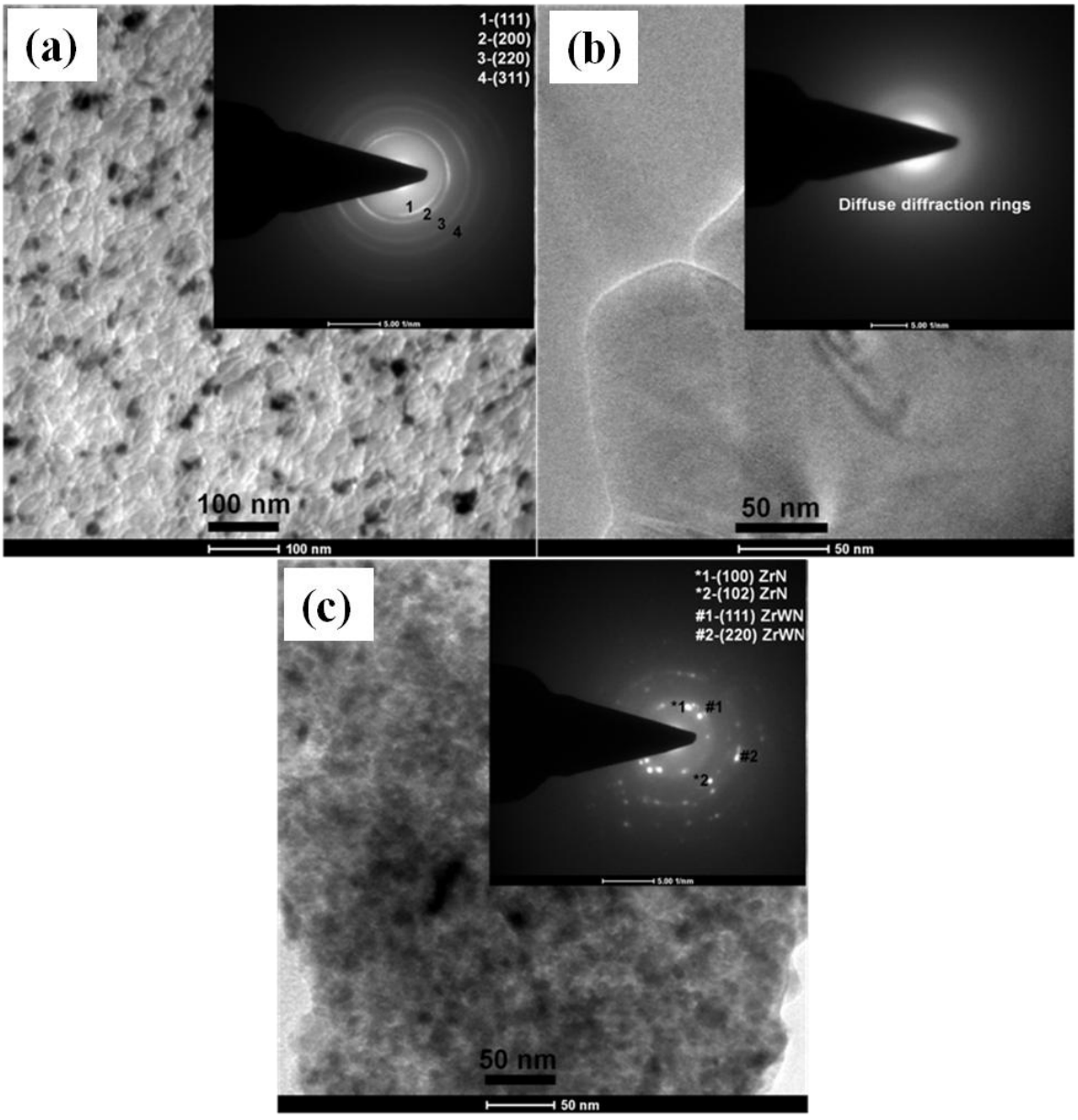

Figure 3.3 *Topological bright field images and SAED patterns of different phases; (a) single fcc phase (0.13 Pa), (b) amorphous phase (0.27 Pa) and (c) dual (fcc+hcp) phase (0.47 Pa)*

The variation of crystallite size and lattice parameter of Zr-W-N films as a function of pN_2 is shown in **figure 3.4a** and **3.4b**, respectively. The crystallite size has been calculated for all the films by using Debye-Scherrer's formula for most intense peak having orientation (111) in the fcc structure. For 0.07 Pa $\leq pN_2 \leq$ 0.17 Pa, the crystallite size of the film decreases as shown in the Bar graph. This may be attributed to the increase in Zr/W ratio (with increasing pN_2) that reduces the mobility of adatoms in deposited Zr-W-N films resulting in decreased crystallite size (Inoue *et al.* 1993). For $pN_2 \leq$ 0.17 Pa, Zr/W ratio increases further, crystallite size decreases below 9 nm resulting in amorphization of the deposited film.

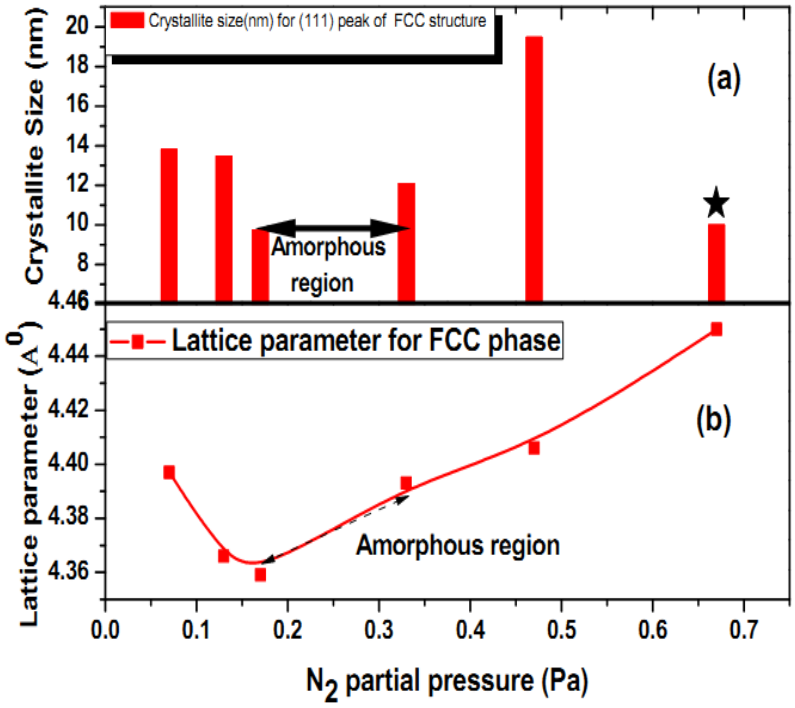

Figure 3.4 *Effect of pN_2 on (a) crystallite size of fcc phase (* intensity is very low) and (b) lattice parameter of fcc phase*

The lattice parameters have been calculated from XRD patterns by Nelson Riley function (Cullity 1978). It is clear that as pN_2 increases from 0.07 Pa to 0.17 Pa, the lattice parameter of single phase (fcc) Zr-W-N film also decreases. The probable reason may be the increase in the occupancy of zirconium and nitrogen atoms at the substitutional and interstitial sites in comparison to W atoms in single (fcc) phase film with increasing pN_2 (Wen *et al.* 2010, Baker and Shah 2002). As Zr/W ratio increases further ($pN_2 \geq$ 0.27), a new phase (ZrN) starts

appearing along with the fcc Zr-W-N phase (as shown in **figure 3.2b** and **figure 3.3c**).Due to the incorporation of Zr in this new phase, although, overall Zr/W ratio increases (with increasing pN_2), the Zr/W ratio within the fcc Zr-W-N phase decreases which results in bigger crystallite size and higher lattice parameter for $pN_2 \geq 0.27$.

3.3.2 Morphological Studies

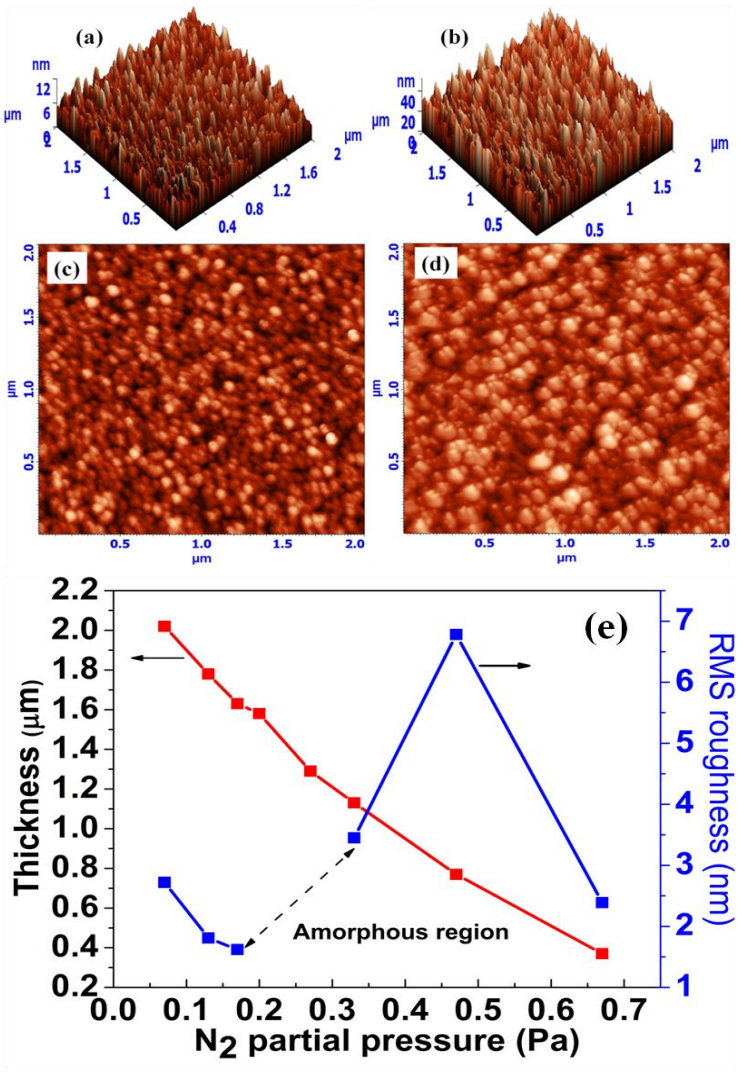

Figure 3.5 *(a)-(d) 3D & 2D topographical AFM images: (a) &(c) single phase fcc structure at low (0.13 Pa) pN_2, (b) & (d) dual phase fcc+hcp structure at high (0.47 Pa) pN_2. (e) RMS roughness and thickness of deposited films at varying pN_2*

3D and 2D views of the surface of films at low (0.13 Pa) and high (0.47 Pa) pN_2 are shown in **figure 3.5a-d**. The RMS roughness (δ_{rms}) and thickness of the deposited films are shown in **figure 3.5e**. For 0.07 Pa ≤ pN_2 ≤ 0.17 Pa, surface roughness decreases and for 0.27 Pa ≤ pN_2 ≤ 0.47 Pa, roughness increases substantially due to the competitive growth between hcp ZrN phase and fcc Zr-W-N phase. At pN_2 = 0.47 Pa, the δ_{rms} is maximum (6.8 nm) because the XRD peaks of ZrN are relatively prong with the XRD peaks of Zr-W-N phase which indicate that ZrN phase is well established along with Zr-W-N phase and hence roughness increases. The change in shape and size of the particles, as shown in **figure 3.5c-d** further support the observed trend in roughness. For pN_2 > 0.47 Pa, surface roughness again decreases due to the stabilization of ZrN phase. The thickness of the films was found to decrease with increasing pN_2 due to the combined effect of increased collision frequency (between ions, N_2 molecules and target atoms) and increased flux of N_2^+ ions (lower momentum transfer as compare to Ar^+) which reduces the deposition rate (Moser *et al.* 1994, Shi *et al.* 2013). AFM analysis shows that all the films have smooth surface.

3.3.3 Mechanical Properties

Table 3.2 *Nanoindentation parameters and mechanical properties of coatings deposited at different pN_2*

S. No.	*pN_2 (Pa)*	*Phase present*	*Load L(mN)*	*Hardness H(GPa)*	*Elastic modulus E_r(GPa)*	*% Elastic recovery W_e*	*Plastic deformation energy U_p(x10^{-10} joule)*	*Plasticity Index parameter H/E_r*	*Resistance to fatigue fracture H^3/E_r^2(Gpa)*
1	0.13	Single (S)	10	21	103	66	9.4	0.20	0.87
2	0.27	Amorphous (A)	10	16	98	60	10	0.16	0.42
3	0.47	Dual (D)	10	24	135	74	8.6	0.18	0.75

Mechanical properties of all the films have been studied by triangular pyramid Berkovich diamond nanoindenter. The fracture toughness of coatings is calculated by measuring the length of crack which is generating during indention on the films under constant load (Zhang *et al.* 2005). While for adhesion testing, a diamond indenter is drawn across the coating surface under an increasing load, until the film is removed in a regular fashion; the load corresponding to adhesive failure gives a guide to the adhesion strength and is referred to as the 'critical load' (Ashrafizadeh 2000). It has been observed that Zr-W-N films exhibit high hardness with high toughness. The supporting data for toughness and hardness for all the samples are given in **table 3.2**.

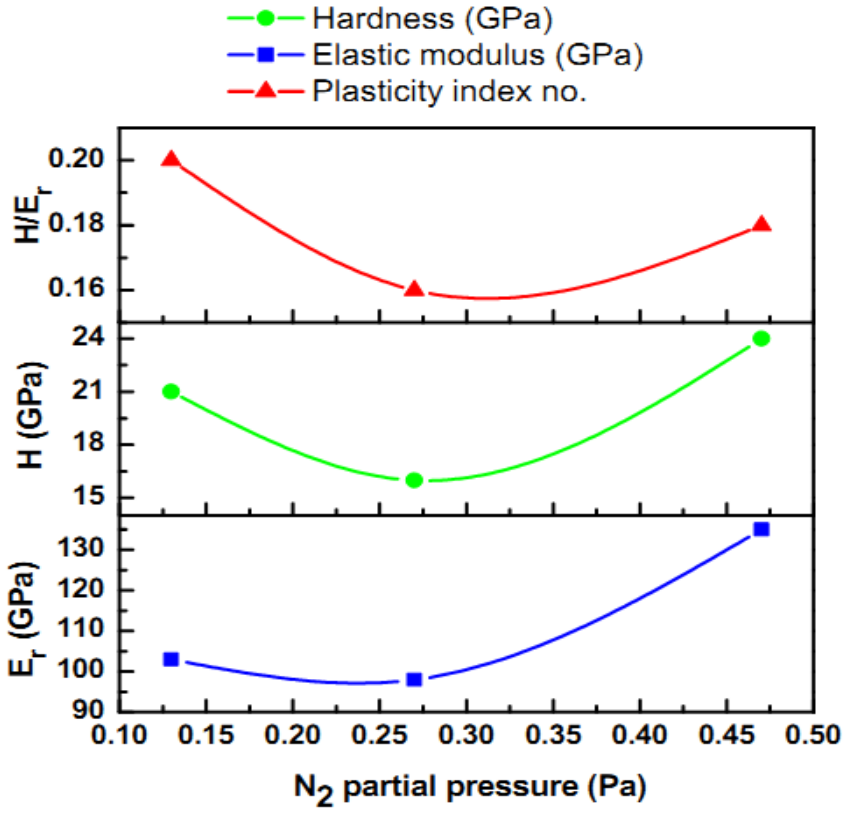

Figure 3.6 *H, E_r and H/E_r values of coatings exhibit fcc, amorphous and fcc+hcp crystallographic phases at different deposition pN_2*

Considering the nano-indentation criterion that penetration depth should not exceed 10 to 15 % of total thickness of the coating (to minimize the substrate effect), 10 mN load has been used for indentation. The variation of hardness (H), reduced elastic modulus (E_r) and plastic index parameters (H/E_r) with pN_2 is shown in **figure 3.6**. Among all the deposited films, maximum values of H (~ 24 GPa) and E_r (~ 135 GPa) are obtained for the dual phase (fcc+hcp) film. An additional hindrance to dislocation movements by multi oriented grains of both the phases in the dual phase structure was found to be the reason for increased hardness. The minimum values of H (~ 16 GPa) and E_r (~ 98 GPa) obtained for the amorphous phase film are associated with the decrease in crystallite size, which is in agreement to the inverse Hall-Petch effect.

The effect of pN_2 on H/E_r is shown in **figure 3.6**, differentiating between elastic (> 0.1) and elastic-plastic (< 0.1) behavior of the films (Charitidis 2010). It has been reported that the films having higher value of H/E_r (> 0.11) show more wear resistance in sliding/abrasive wear contacts (Leyland and Matthews 2000). Although, the single phase (fcc) film has lower (103 GPa) value of E_r in comparison to dual phase (fcc+hcp) film (135 GPa) but the H/E_r value of single phase (~ 0.20) film is higher than dual phase (~ 0.18) film which confirms that the single phase (fcc) film is more ductile and wears protective in comparison to dual phase (fcc+hcp) film. The effect of pN_2 on the percentage elastic recovery (W_e) and plastic deformation energy (U_p) has been shown in **table 3.2**. The single phase (fcc) film shows lower value (66 %) of W_e in comparison to dual phase (74 %) film. This is because single phase film has fcc nanocrystalline structure and hence the twinning mechanism in the slip systems along with nanocrystalline grain size effect may result in the deformation of fcc film at lower applied stress resulting in lower W_e. This is in contrary to coarse-grained fcc metals (Zhu *et al.* 2009).

Fracture toughness plays a very important role for wear protective coatings, especially erosion at higher impact angle. The fracture toughness and adhesion for all three phases of the films deposited at 0.17 Pa, 0.27 Pa and 0.47 Pa pN_2 have been evaluated with the help of Berkovich diamond tip. All the films have been indented with high (50 mN) load for fracture toughness test, while adhesion test has been done by making a scratch on the films with varying 2 to 50 mN loads. **Figure 3.7** shows the AFM topographical view of scratch scars and

indentation marks at 50 mN load for all the phases. It has been observed that no crack propagates on the surface of the films and consequently, toughness cannot be calculated quantitatively; however, it can be concluded that the toughness of the deposited films is appreciable to the extent so as to bear a high load of 50 mN without crack. To estimate the film resistance to cracking, H^3/E_r^2 has been calculated as shown in **table 3.2**. A high value (> 0.1 Gpa) of H^3/E_r^2 confirms a high resistance to cracking and hence high fracture toughness (Beaks *et al.* 2011). A comparison of H^3/E_r^2 ratio for the deposited films shows that the single phase fcc films deposited at $0.07<pN_2<0.17$ exhibit the highest value (~ 0.87 GPa) of H^3/E_r^2 ratio. From **figure 3.7a**, **c**, **e**, reveals that the films neither peeled off nor developed any crack during the scratch test at 50 mN load. This indicates that all the films have high adhesion with the substrate surface.

Sakai (1993) suggests that plastic deformation energy (U_p) is also an important parameter of the mechanical properties of wear protective coatings. Plastic deformation energy (U_p) of the film is calculated by the area surrounded by the loading- unloading curve in the load displacement profile. U_p can be calculated by the equation (3.1)

$$U_p = P^{3/2} / [3\, H^{1/2} (w_0 \tan^2\theta)^{1/2}] \qquad (3.1)$$

Where 'P' is applied load, 'w_0' is the geometry constant and can be taken as 1.3 for pyramid indenter, H is hardness and θ is the angle (65.3º) between the tip axis and the faces of triangular pyramid. The single phase (fcc) film has higher value of U_p over dual phase (fcc+hcp) films. Thus, more energy consumption during deformation without making any crack shows more ductile behavior of film.

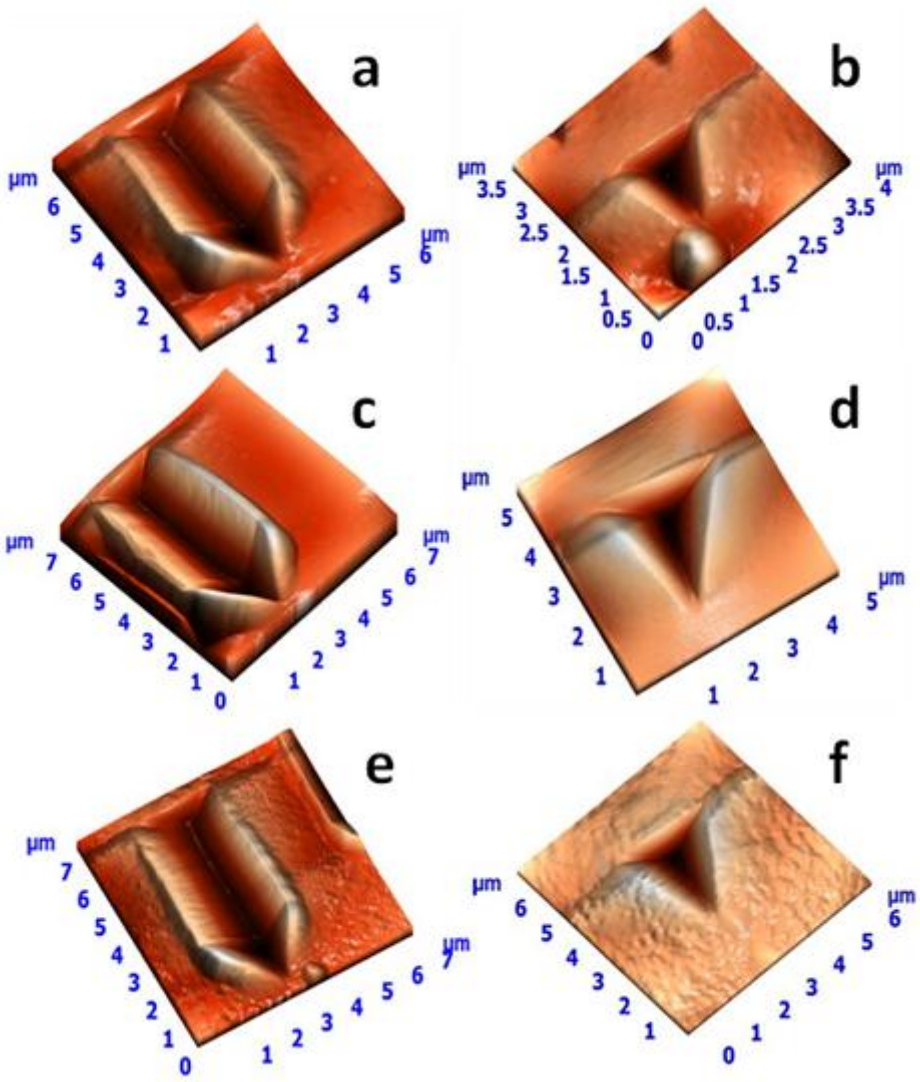

Figure 3.7 *Scratch at 50 mN load (for adhesion test) and indentation at 50 mN load (for fracture toughness test) on all three phase films deposited at different pN_2. (a), (b): Single (fcc) phase film deposited at 0.13 Pa pN_2. (c), (d): Amorphous phase film deposited at 0.27 Pa pN_2. (e), (f): Dual (fcc+hcp) phase film deposited at 0.47 Pa pN_2*

3.4 Conclusions

Thin films of Zirconium Tungsten Nitride ($Zr_xW_{1-x}N_y$) have been deposited by DC/RF reactive magnetron sputtering on p-type Silicon (100) substrate. The films have been characterized by different techniques such as XRD, FE-SEM, AFM, TEM and Nanoindentation. The results discussed previously are summarized in the following:

(1) With increase in pN_2, $Zr_xW_{1-x}N_y$ films exhibit single (fcc) phase, amorphous phase and dual (fcc+hcp) phase.

(2) A strong correlation has been found between structure of the films and their chemical compositions.

(3) The crystallite size and lattice parameter of single (fcc) phase films vary non-monotonically with increase in pN_2. The roughness (δ_{rms}) also follows the same trend according to phases present in films.

(4) The thickness of the films decreases continuously with increasing pN_2.

(5) Maximum hardness (~ 24 GPa) has been obtained for dual phase (fcc+hcp) film while resistance to fatigue fracture (H^3/E_r^2 ~ 0.87 GPa) and wear resistance (H/E_r ~ 0.2) of the single phase (fcc) film was found to be highest among all the phases.

(6) Scratch tests confirm high adhesion of the deposited films with the substrate surface.

CHAPTER 4

Zirconium Tungsten Nitride coating: Effect of Insitu and Exsitu Annealing Temperatures

The thermal stability and mechanical properties of amorphous and crystalline (fcc) phase Zr-W-N coatings have been discussed in detail. This chapter divided into two sections. First section namely, ***section 4.1*** *describes the effect of substrate temperatures T_s (100º-600ºC) (Insitu) and post annealing temperature T_n (100º-600ºC) (Exsitu) on thermal stability and mechanical properties of amorphous Zirconium Tungsten Nitride ($Zr_{19}W_{18}N_{63}$) coatings. Second section namely,* ***section 4.2*** *describes the effect of substrate temperatures T_s (100º-600ºC) (Insit) and post annealing temperature T_n (100º-600ºC) (Exsitu) on thermal stability and mechanical properties of crystalline fcc phase Zirconium Tungsten Nitride ($Zr_{22}W_{19}N_{58}$) coatings.*

4.1 Study of thermal stability and mechanical properties of amorphous $Zr_{19}W_{18}N_{63}$ coatings deposited by DC/RF reactive magnetron sputtering

4.1.1 Introduction

In recent years research in the area of wear protection of materials using hard, tough and thermally stable coatings has been very fascinating. Most studied ternary nitride coatings promise manifold applications by improving the life and performance of machine components and machining tools. Many ternary nitrides, e.g., Ti-Si-N, TiN/Si_3N_4, Zr-Si-N, W-Si-N and Ti-B-N (Sun *et al.* 1997, Soderberg *et al.* 2005, Kim *et al.* 2002, Chawla 2010 *et al.*, Musil *et al.*

2005, Marques *et al.* 2003, Wiedemann *et al.* 1999) belonging to metal-metalloids nitride group and Ti-Cr-N, Ti-Zr-N, Ta-Zr-N, Cr-W-N (Hasegawa *et al.* 2000, Tang *et al.* 2012, Gu *et al.* 2008, Grimberg *et al.* 1998) belonging to metal-metal nitride group have been studied to achieve the best blend of toughness, wear resistance and low friction performance across multiple environments.

Kim *et al.* (2002) have reported the effect of silicon content on the mechanical properties of Ti-Si-N hard coatings deposited on steel substrates. The two deposition techniques namely; (i) arc ion plating (AIP) for the deposition of TiN coatings and (ii) magnetron sputtering for the encapsulation of Si in the matrix of TiN coatings, have been used for the synthesis of Ti-Si-N coatings. The Ti-Si-N film exhibit crystalline (TiN) phase and amorphous (Si_3N_4) phase microstructure in which TiN grain of multiple orientations were distributed in the amorphous Si_3N_4 phase. The crystallites size and surface roughness of Ti-Si-N coatings were decreases with increasing silicon concentration in the films. Ti-Si-N coating with Si content ~ 7.7 at.% exhibit maximum hardness value of 45 GPa. Mei *et al.* (2005) and Chawla *et al.* (2010) have studied the effect of Si concentration on microstructure and mechanical properties of Ti-Si-N nanocomposite films sputtered by reactive magnetron sputtering. It has been noticed that silicon formed the amorphous silicon nitride phase at the grain boundaries of TiN grains and volume fraction of amorphous Si_3N_4 phase was increasing with increasing Si content. This indicating that crystallizes size of TiN phase decreases with increasing Si content. The TiN phase with grain size of about 20 nm was grown in the Ti-Si-N films with Si content ~ 13.6 at.%. A strong correlation in microstructure and mechanical properties has been observed. The mechanical properties (hardness (H) and elastic modulus (E_r)) of films varied non-monotonically with increasing Si contents and the maximum H and E_r values were obtained ~ 34.2 GPa and 398 GPa, respectively at 10.6 at.% Si content.

Musil *et al.* (2006) have studied the physical and mechanical properties of magnetron sputtered W-Si-N thin films with a high (≥ 20 at.%) content of Si. The elemental compositions of the films have been controlled by a variation (0 to 0.5 Pa) in nitrogen partial pressure (pN_2). The W–Si–N film with a low (< 1.33) ratio N/Si exhibits a crystalline structure and those with a high (≥ 1.33) ratio N/Si are amorphous. All the amorphous films contain a high (≥ 50 vol.%) amount of the Si_3N_4 phase. The hardness continuously increases with increasing pN_2 and the

maximum hardness (~ 35 GPa) is achieved at $pN_2 > 0.4$ Pa. The W-Si-N film composed of two co-existing Si_3N_4 and overstoichiometric $WN_{x>1}$ phases at higher pN_2 exhibits the highest oxidation resistance achieving 800°C.

Musil *et al.* (2005) have reported structure, oxidation resistance and mechanical properties of Zr–Si–N films deposited at varying (0 to 0.5 Pa) nitrogen partial pressure (pN_2). Zr–Si–N films deposited at very low nitrogen partial pressure (≤ 0.03 Pa) are crystalline, electrically conductive, optically opaque and exhibit microhardness values of H ~ 17–20 GPa and Zr–Si–N films deposited at very low nitrogen partial pressure (≥ 0.1 Pa) are X-ray amorphous, electrically insulating, optically transparent and exhibit high microhardness H ~ 30 GPa. H is almost two times greater than that of the Si_3N_4 (17.2 GPa) and ZrN (16 GPa). The Zr–Si–N films with high (≥ 25 at.%) Si content composed of a mixture of a-Si_3N_4 and $ZrN_{x>1}$ phase with ≥ 55 vol.% of the a-Si_3N_4 phase, exhibit a high oxidation resistance (> 1300ºC) in flowing air.

It has been observed in literature survey that the metal + metalloids nitride group have an amorphous structure over a wide range of composition. These compounds usually contain about 15-30 at.% metalloids and show excellent hardness (~ 40 GPa), high resistance against oxidation and crystallization upon thermal annealing. A selection of Si, B and C etc. as metalloids in the ternary nitride system is based on the fact that these metalloids forms hard amorphous structure like Si_3N_4, BN and CN and remain amorphous to higher temperatures due to its high crystallization temperature considerably exceeding 1000ºC. The amorphous structure is an excellent barrier for a penetration of oxygen to the substrate surface through the coating and thus an improved oxidation resistance is expected to be achieved in metal + metalloids nitride thin films. However, they exhibit limited macroscopic plastic deformability especially at higher load (Sun *et al.* 1997, Soderberg *et al.* 2005, Kim *et al.* 2002, Chawla 2010 *et al.*, Musil *et al.* 2005, Marques *et al.* 2003, Wiedemann *et al.* 1999). High metastability and superior strength of the amorphous like structure in comparison to crystalline structure is the most striking aspect of ternary nitride alloys in wear protective coatings (Nicolet *et al.* 2001, Musil *et al.* 2012). The metal + metal nitride group has moderate hardness and higher adhesion with metal substrates. The thermal stability and mechanical properties of crystalline materials of the metal + metal nitride group has been studied in detail in literature (Hasegawa *et al.* 2000, Tang *et al.* 2012, Gu *et al.* 2008, Grimberg *et al.* 1998). However, detailed studies on amorphous

materials of the metal + metal group are lacking in literature. In the present work, thermal stability and mechanical properties of amorphous and crystalline Zr-W-N thin films has been studied in detail.

New Zr-W-N thin films can be very interesting with regard of a combination of ZrN and W_2N. Individually ZrN is a very promising material in various domains because of its attractive properties like high hardness, excellent wear resistance, high melting point, good electrical conductivity, and suitability as diffusion barriers in microelectronic devices and decorative coatings etc (Brugnoni *et al.* 1998, Pilloud *et al.* 2003, Chhowalla *et al.* 2005, Ruan *et al.* 2005). On the other hand W_2N belongs to a class of refractory metal nitrides that has unique properties like excellent hardness (~40 GPa), low melting point (< 800ºC), high conductivity and good chemical stability (Polcar *et al.* 2008, Baker *et al.* 2002, Yamamoto *et al.* 2005, Wen *et al.* 2010). To the best of our knowledge, this is one of the first reports on novel Zr-W-N thin films, which could be interesting candidates for wear protection.

4.1.2 Experimental Details

4.1.2.1 Deposition of Zr-W-N thin films

Ternary nitride Zr-W-N films have been deposited on Si (100) substrates using DC/RF reactive magnetron co-sputtering in a cylindrical chamber (30 h x 40 φ cm^2) designed by Excel Instruments, India. Sputtering targets (5 cm diameter and 0.5 cm thick) of Zr and W with purity 99.98% and 99.95% respectively have been used for deposition. The Si substrates were cleaned by first rinsing in hydrofluoric acid to remove the native SiO_2 layer followed by ultrasonic bath treatment in acetone. Targets were fixed at an angle of 45° to the substrate normal. Si substrates were mounted on the grounded substrate holder with the help of silver paste. The substrate holder was rotated at 5 rpm by using a DC motor to ensure uniformity in the deposited thin films. Prior to deposition, the targets were pre-sputtered for 15 min to remove the impurities present on the surface. The residual gas pressure was < 0.5×10^{-3} Pa, N_2 partial pressure and working pressure were 0.27 Pa and 0.67 Pa respectively. Sputtering was carried out at constant N_2 (16 sccm) and Ar (24 sccm) flow with varying substrate temperature T_s (100º-600ºC) for 1.5 h. The power densities for W and Zr targets were 4 watt/cm^2 and 6 watt/cm^2 respectively. All

depositions were carried out at a fixed substrate to target distance of 6 cm. The post annealing (100º-600ºC) of the films deposited at T_s = 200ºC have been carried out in air for 1 h.

4.1.2.2 Characterization

The elemental composition analysis of Zr-W-N thin films was carried out using an energy dispersive X-ray analysis. The structural, morphological and cross-sectional studies of Zr-W-N thin films have been carried out using grazing angle X-ray diffraction, atomic force microscope, field emission scanning electron microscope and high resolution transmission electron microscope (HRTEM). Mechanical properties of as deposited and post annealed samples have been studied by nano-indentation. Nano-indentation uses a triangular pyramid Berkovich diamond indenter with normal angle of 65.3° between the tip axis and the faces of triangular pyramid. All the indentation measurements have been carried out at 10 mN to minimize the substrate effect. The loading velocity (100 nm/s) was kept constant during indentation. A higher load of 50 mN has been chosen for fracture toughness measurement through indentation. The films were scratched with 2 to 10 mN loads at constant loading velocity (20 nm/s) and scratch velocity (500 nm/s) for adhesion test purpose. The hardness (H), reduced elastic modulus (E_r) and percentage elastic recovery (W_e) were calculated by loading and unloading curves generated during nanoindentation. Plastic deformation energy (U_p) (Sakai 1993) of the films is calculated by the area of the loading-unloading curve in the load-displacement profile.

4.1.3 Results and Discussion

4.1.3.1 Effect of substrate temperatures on film structure and mechanical properties

4.1.3.1.1 Structural and morphological analysis

Figure 4.1 shows the stoichiometry (Y=N/(Zr+W)) of ternary nitride ($Zr_{19}W_{18}N_{63}$) films at different substrate temperature T_s. It can be clearly seen that the nitrogen concentration decreases with increasing T_s.

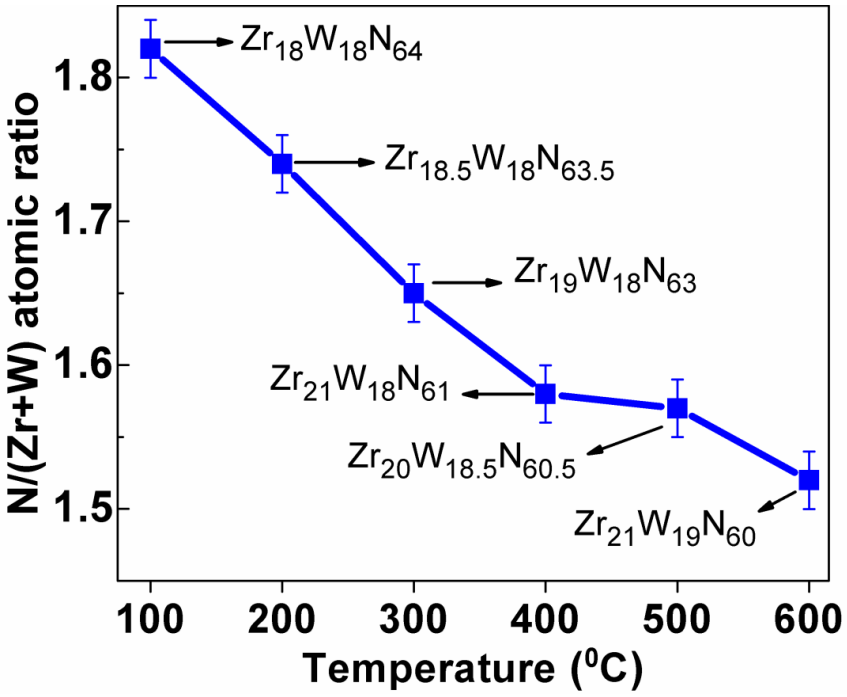

Figure 4.1 *Stoichiometry of Zr-W-N films deposited at varying substrate temperature*

Figure 4.2a shows the XRD patterns of as deposited films at different substrate temperature T_s. For $T_s \leq 300^oC$ and $Y \geq 1.65$, amorphous Zr-W-N thin films were obtained. The glass forming ability of Zr-W-N thin films is similar to the behavior observed in other ternary nitride systems around eutectic point (Park *et al.* 2009). For $400^oC \leq T_s \leq 600^oC$ and $1.52 \leq Y \leq 1.58$, polycrystalline Zr-W-N films were obtained. For $400^oC \leq T_s \leq 600^oC$ Zr-W-N films exhibit single fcc phase with (111) and (200) crystallographic orientations of grains. Adatoms mobility and surface diffusion increases with increasing T_s, thereby enhancing grain growth which contributes to the crystalline phase evolution above $T_s=300^oC$ (Abadias *et al.* 2006). With increasing T_s, loss of nitrogen is accompanied with the crystallization of Zr-W-N phase, this is similar to the results reported on (Mo, Ta, W)-Si-N nitride system (Reid *et al.* 1993), wherein with increasing annealing temperature, loss of nitrogen is accompanied by crystallization of phase.

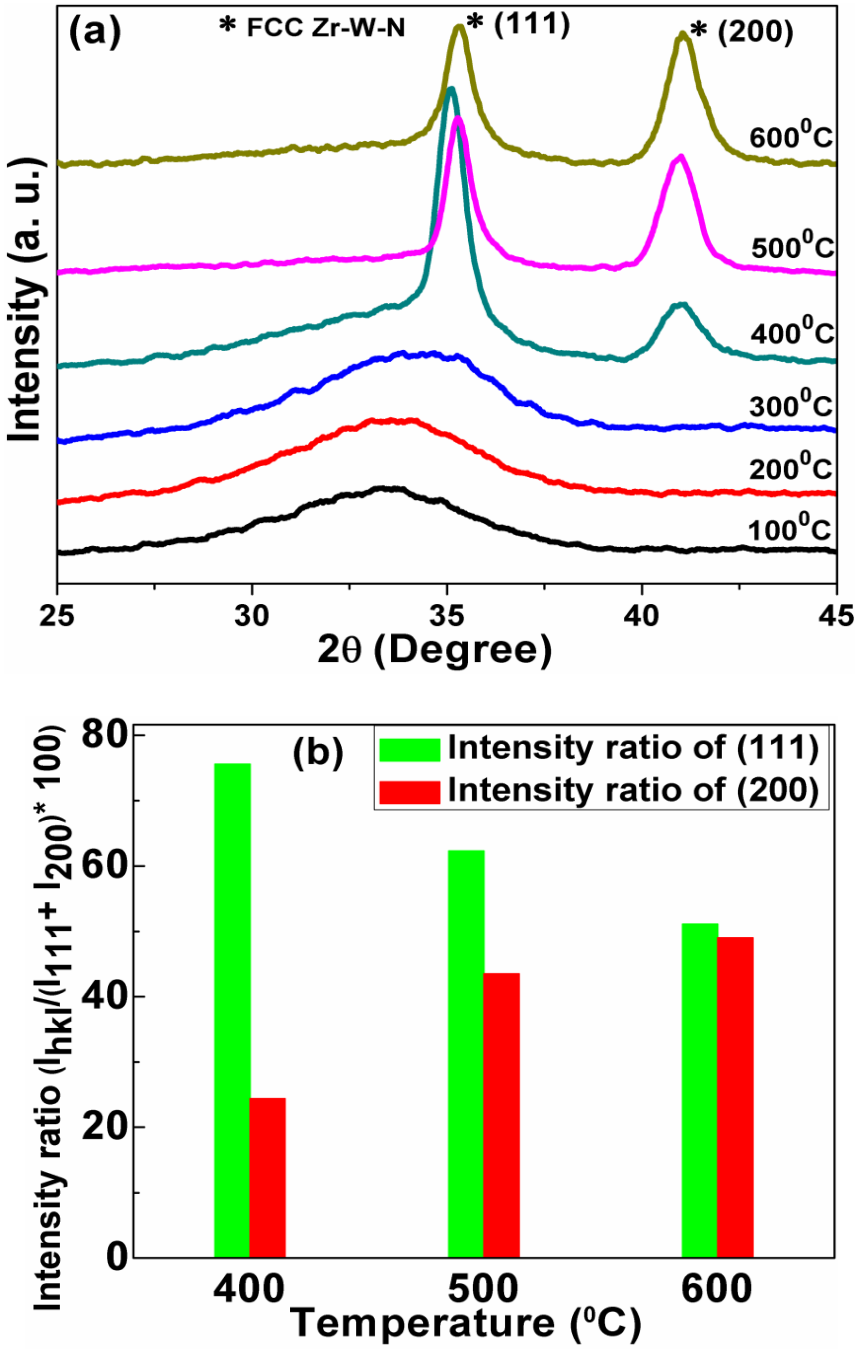

Figure 4.2 *(a) XRD patterns of Zr-W-N coatings at varying substrate temperatures and (b) peak intensity ratio of (111) and (200) lattice planes for 400ºC ≤ T_s≤ 600ºC*

Figure 4.2b shows an evolution of preferred grain orientation as a function of T_s in the form of peak intensity ratio as the Bragg intensity is proportional to the volume of grains

having corresponding orientations (Zhang and Kuznetsov 2011). The intensity of the (200) reflex, exactly $I_{(200)}/(I_{(111)}+I_{(200)})$, gradually increases in comparison to intensity ratio of (111) with increasing T_s (400º–600ºC). Once the films acquire crystalline nature, competitive growth of (111) and (200) oriented grains is observed It is well known that in the fcc crystal, (111) lattice planes are found to be least diffusive and highly dense while (200) lattice planes correspond to high diffusivity and least defect dense orientation (Abadias *et al.* 2008). Thereby with increasing T_s, the growth is kinetically enhanced and mobility of adatoms is sufficient to form the low density (200) structure. To further explain the evolution of microstructure and the effect of increasing T_s on occupancy of nitrogen atoms, detailed TEM studies are required.

Thickness of the films varies monotonically with increasing T_s as shown in **figure 4.3**. For 100ºC ≤ T_s ≤ 300ºC, the amorphous films show a continuous decrease in thickness with increase in T_s. For 400ºC ≤ T_s ≤ 600ºC, the crystalline fcc films show a continuous increase in thickness with increasing T_s.

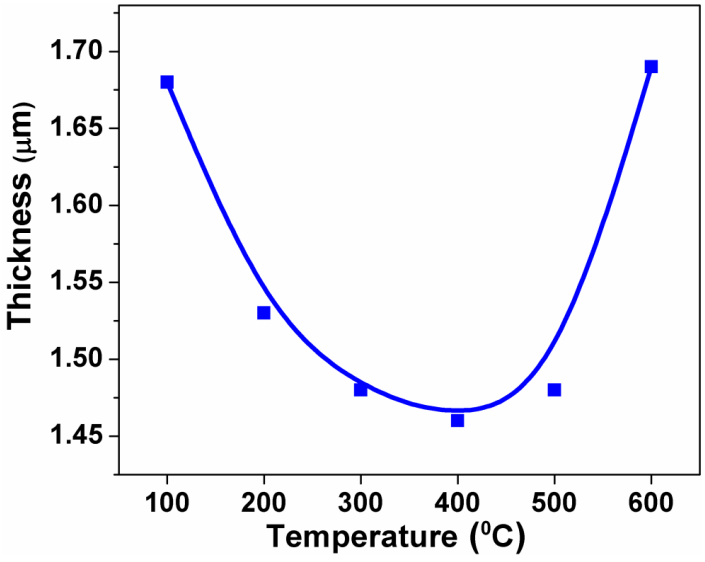

Figure 4.3 *Variation of thickness (± 10 nm) with substrate temperature*

To further confirm the presence of an amorphous phase at T_s = 300ºC and crystalline phase at T_s = 400ºC, TEM bright field images and the corresponding selected area electron diffraction (SAED) patterns are shown in **figure 4.4a-b**, respectively. The observation of

diffuse diffraction rings in SAED pattern clearly shows the absence of any nanocrystalline phase in these films. The indexed SAED patterns of Zr-W-N film deposited at T_s = 400ºC confirms the formation of polycrystalline fcc phase. This is in accordance with the XRD data.

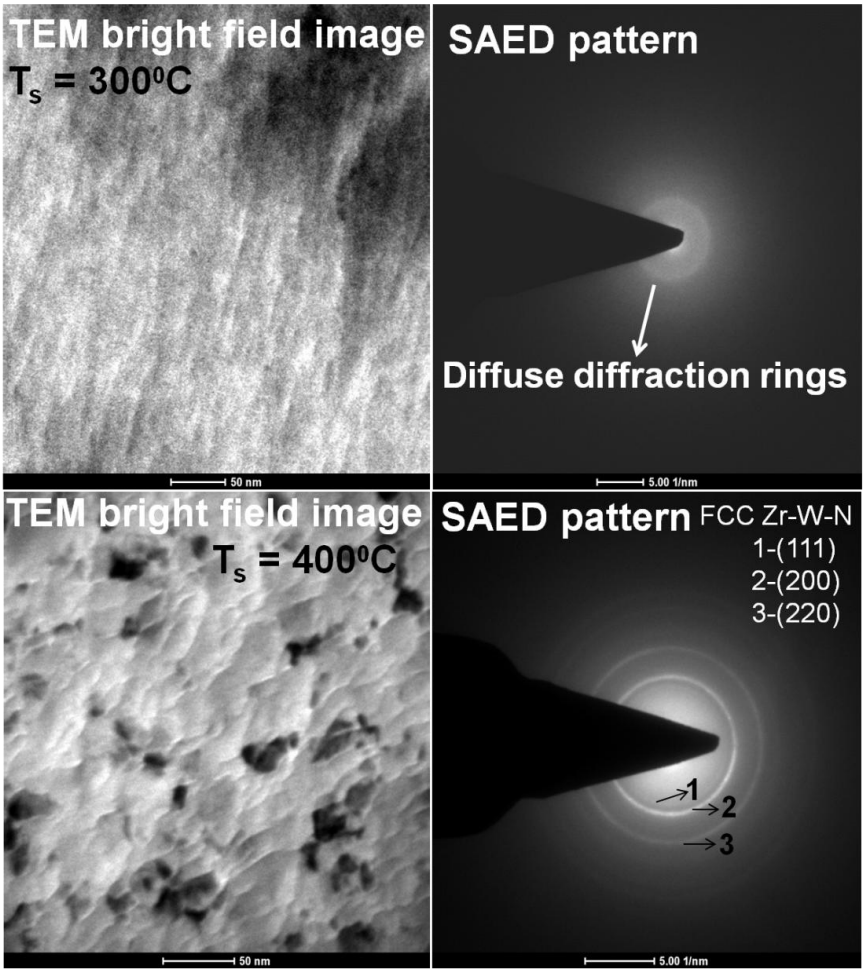

Figure 4.4 *TEM bright field images and corresponding SAED patterns for (a) amorphous Zr-W-N film deposited at T_s = 300ºC and (b) polycrystalline Zr-W-N film deposited at T_s = 400ºC*

4.1.3.1.2 Mechanical properties

For ensuring the practical applicability of the developed coatings in wear protection, it is necessary to study the influence of thermal treatments on their mechanical properties like hardness, reduced elastic modulus, and fracture toughness etc. Zhang *et al.* (2005) have suggested a method to calculate the fracture toughness of a coating by measuring the crack length which is generated during indentation on the films under constant load. While for

adhesion testing, a diamond indenter is drawn across the coating surface under a increasing load, until the film is removed in a regular fashion; the load corresponding to adhesive failure gives a guide to the adhesion strength and is referred to as the 'critical load' (Ashrafizadeh 2000). Mechanical properties like H, E_r, U_p, W_e and H^3/E_r^2 of Zr-W-N films deposited at varying T_s are shown in **table 4.1**.

Table 4.1 *Mechanical properties of Zr-W-N thin films deposited at different substrate temperatures*

Substrate temperature	*Load*	*Hardness*	*Elastic modulus*	*% Elastic Recovery*	*Plastic deformation energy*	*Plasticity Index parameter*	*Resistance to fatigue fractue*
(°C)	*L(mN)*	*H(GPa)*	*E(GPa)*	W_e	*Up ($x10^{-10}$ joule)*	*H/E*	H^3/E^2
100	**10**	**15**	**93**	**68.3**	**10.8**	**0.16**	**0.4**
200	**10**	**22**	**96**	**71.3**	**9.40**	**0.22**	**1.1**
300	**10**	**25**	**176**	**74.7**	**8.54**	**0.14**	**0.5**
400	**10**	**21**	**99**	**73.0**	**9.33**	**0.21**	**0.9**
500	**10**	**20**	**96**	**71.6**	**9.92**	**0.20**	**0.8**
600	**10**	**18**	**92**	**70.3**	**9.62**	**0.19**	**0.7**

The W_e gives information about the elastic and elastic-plastic behavior of the films. Wear resistive coatings having W_e in the range of 90 to 100% in indentation, show elastic behavior, while the films having W_e in the range of 68 to 80% show elastic-plastic behavior (Musil 2012, Lejeune *et al.* 2005). For 100ºC ≤ T_s ≤ 300ºC, H, E_r, W_e increase and U_p decreases with increasing T_s. The increase in the hardness of the films up to T_s = 300ºC was due to growing microstructure of the films at the corresponding T_s. For 400ºC ≤ T_s ≤ 600ºC, H, E_r, W_e decrease and U_p increases with increasing T_s. Among all the deposited films, maximum values of H (~25 GPa), E_r (~176 GPa) and W_e (75%) are observed for the film deposited at T_s = 300ºC. A Minimum value ($8.5x10^{-10}$ joule) of U_p has also been obtained for films deposited at T_s = 300ºC. This shows that the film deposited at T_s = 300ºC has lower ductility in comparison to other deposited films. Musil (2012) and Charitidis (2010) have explained the way to measure the wear resistance of coatings qualitatively by calculation of the H/E_r ratio (hardness to reduced elastic modulus), called plasticity index parameter. For wear protective coatings for practical purposes, the value of H/E_r should be high (> 0.1), which means films should show

more resistance to plastic deformation or have high abrasive resistance. The highest value (0.22) of H/E_r was recorded for amorphous films deposited at T_s = 200ºC.

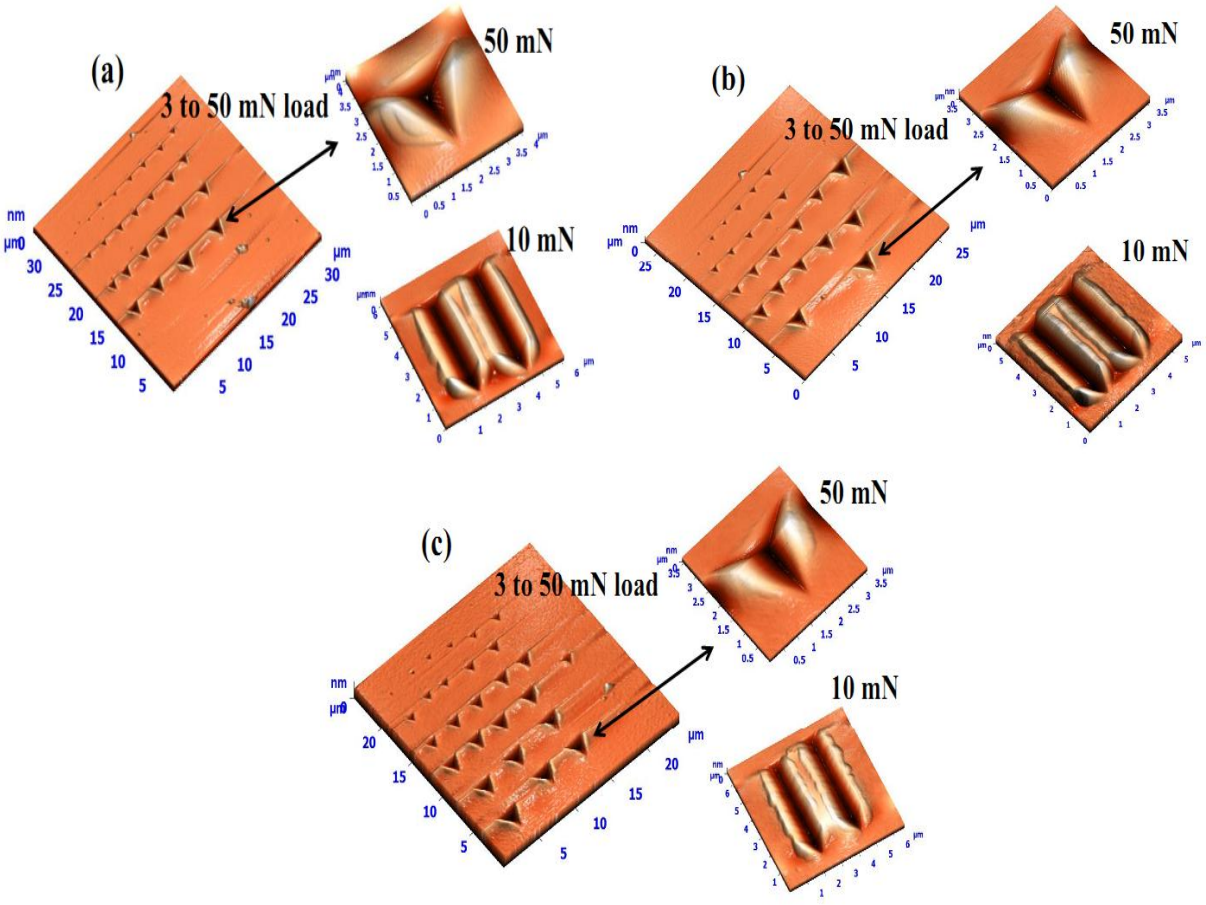

Figure 4.5 *(a)-(c) AFM topographical views for indentation at 3 to 50 mN load and for scratch scars at 10 mN load on Zr-W-N films deposited at 200ºC, 300ºC and 400ºC, respectively*

Figure 4.5a-c show the AFM topographical view of scratch scars and indentation marks on the films deposited at T_s = 200ºC, 300ºC and 400ºC. The scratch scars at 10 mN load and indents at 3-50 mN loads have been made on the films for adhesion and fracture toughness measurements, respectively. Enlarged views of indents at 50 mN loads reveal that no crack propagates on the surface of the films and consequently, toughness cannot be calculated quantitatively; however, it can be concluded that the toughness of the deposited films is

appreciable to the extent so as to bear a high load of 50 mN without crack. To estimate the film resistance to cracking, H^3/E_r^2 has been calculated as shown in **table 4.1**.

A High value of H^3/E_r^2 (> 0.1 GPa) confirms a high resistance to cracking and hence high fracture toughness (Koutsokeras *et al.* 2011). A comparison of H^3/E_r^2 ratio for as deposited films shows that films deposited at 200ºC exhibit the highest values (1.1 GPa) of H^3/E_r^2 ratio. **Figure 4.5a-c** also reveal that the films neither peeled off nor developed any crack during the scratch test at 10 mN load. This indicates that all the films have high adhesion with the substrate.

4.1.3.2 Effect of post annealing temperatures on film structure and mechanical properties

4.1.3.2.1 Structural and morphological analysis

Due to the superior mechanical properties of Zr-W-N film deposited at T_s = 200ºC over other films, post deposition thermal annealing of the films deposited at 200ºC have been carried out at different annealing temperature T_n (100º-600ºC). **Figure 4.6** shows the EDS analysis (N, O atomic fraction) of the Zr-W-N films annealed in air at different T_n.

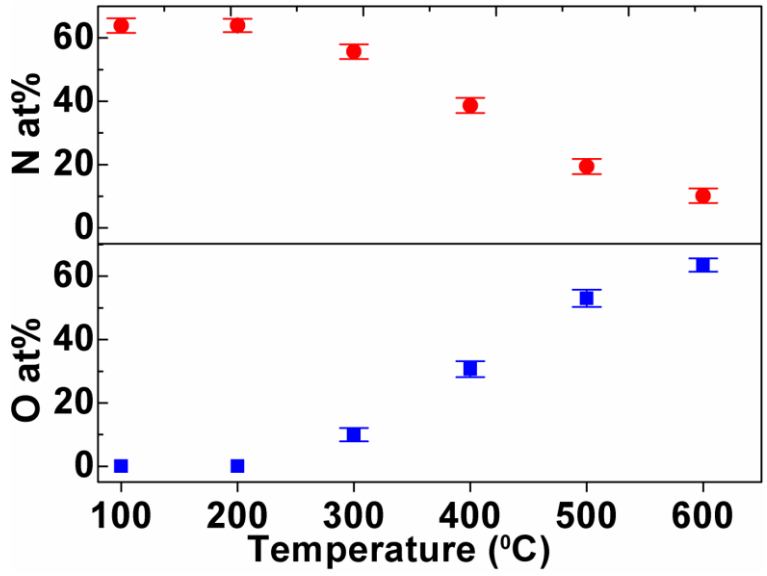

Figure 4.6 *EDS analysis (atomic fraction of O and N gases) of Zr-W-N films annealed at different temperatures*

It has been observed by elemental analysis that the oxygen starts to be incorporated in the films at T_n = 300ºC and its content increases with increasing T_n. The maximum O content (~ 63 at.%) is found for the films annealed at T_n = 600ºC. On the other hand, the N concentration starts to decrease continuously above T_n = 200°C and reaches ~ 10 % in the film at T_n = 600ºC. The films begin to peel off at 500ºC and got completely peeled off at T_n = 60ºC. This may be associated with diffusion of some of the O atoms toward interface through grain boundaries with increasing T_n (Abadias *et al.* 2013). The oxide formations at the interface deteriorate the adhesion of the films with the substrate resulting in peeling off.

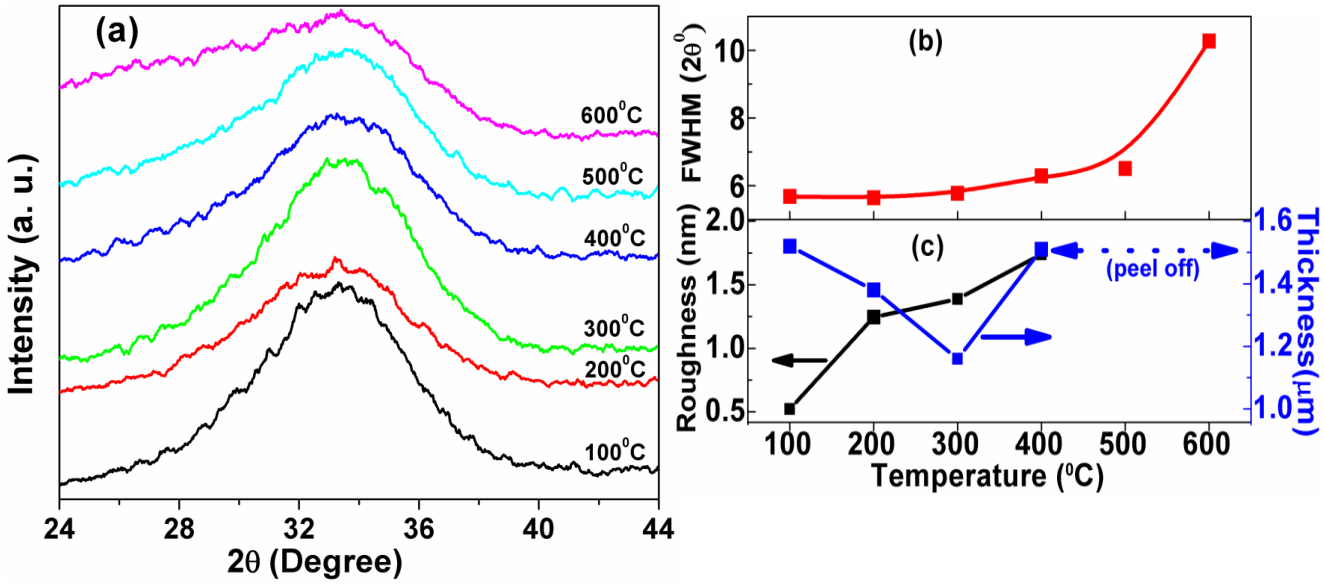

Figure 4.7 *(a) XRD patterns of Zr-W-N films annealed at different temperatures (100º-600ºC), (b) broadening of hump measured by FWHM and (c) change in thickness and RMS roughness of the annealed films with increasing T_n*

XRD patterns (**figure 4.7a**) of post annealed films show that the films retain amorphous structure up to T_n = 600ºC without forming any crystalline oxide phase. The broadening of the hump is the only noticeable change in the XRD patterns with increasing T_n. The effect of incorporated O atoms is pronounced at $T_n \geq$ 300ºC in the form of a higher value of FWHM as shown in **figure 4.7b**. Presumably, the incorporated O atoms indulged in atomic diffusion,

structure conversion and inducing stresses in the films which promote the broadening of the hump during air annealing (Mohamed 2008). **Figure 4.7c** shows the thickness and RMS roughness of annealed films as function of T_n with ± 10 nm and ± 0.03 nm errors in measurements, respectively. The thickness of post annealed films varied monotonically with T_n. For $T_n \leq 300^oC$, thickness decreases and then starts to increase. The trend observed in thickness during air annealing shows resemblance with the trend observed for Ti-Ta-N and Ti-Zr-N coatings during air annealing (Koutsokeras *et al.* 2011, Abadias *et al.* 2013,Thornton 1986).The RMS roughness increases with increasing T_n. This may be attributed to enhancement of adatoms mobility and surface diffusion, which in turn contributes to increase in surface roughness

4.1.3.2.2 Mechanical properties

Table 4.2 shows the variation of H, E_r, H/E_r and H^3/E_r^2 of Zr-W-N coatings with increasing T_n. The delaminating of the films above 400ºC restricted the indentation study of Zr-W-N films for T_n = 500ºC and 600ºC. H was found to increase up to 18 GPa at T_n = 200ºC and then start to decrease up to 11 GPa at T_n = 400ºC as long as the incorporation of O atoms increases in the films with T_n. This may be attributed to an increasing number of defects in the films with increasing atomic fraction of O in annealed films (Charitidis 2010). E_r was found to increase continuously with increasing T_n and attains a maximum value (94 GPa) for films annealed at T_n = 400ºC. The increase of E_r indicates that films become more brittle relatively with increasing T_n. The maximum value (0.20) of H/E_r was achieved at T_n = 200ºC. The other mechanical properties like U_p and W_e of annealed Zr-W-N films are also shown in **table 4.2**.

Table 4.2 *Mechanical properties of Zr-W-N thin films annealed in air at different temperatures*

Annealing temperature	*Load*	*Hardness*	*Elastic modulus*	*% Elastic Recovery*	*Plastic deformation energy*	*Plasticity Index parameter*	*Resistance to fatigue fractue*
(ºC)	*L(mN)*	*H(GPa)*	*E(GPa)*	*W_e*	*U_p(x10^{-10} joule)*	*H/E*	*H^3/E^2*
100	**10**	**15**	**83**	**70**	**10.91**	**0.18**	**0.5**
200	**10**	**18**	**87**	**72**	**10.05**	**0.20**	**0.8**
300	**10**	**14**	**90**	**70**	**11.32**	**0.15**	**0.3**
400	**10**	**11**	**94**	**67**	**12.31**	**0.13**	**0.2**

W_e was found to decrease with increasing O atomic fraction in the annealed films. A Minimum value (67%) of W_e was obtained for annealed film with 30 at.% O at T_n = 400ºC revealing the higher ductile behavior among other films annealed at different T_n. A minimum value (10 x 10^{-10} joule) of U_p was found for Zr-W-N film annealed at 200ºC, indicating lower ductility of the films annealed at varying (100º-400ºC) temperatures. The topographical view of scratch scars (at 10 mN) and indent (at 50 mN) marks have been analyzed by AFM. Similar to the as deposited films, the annealed films exhibit no crack formation even after indentation at 50 mN. A comparison of H^3/E_r^2 ratio for annealed films shows that the film annealed at 200ºC exhibit the highest value (0.8 GPa) of H^3/E_r^2 ratio. **Figure 4.8a-d** also reveal that the films neither peeled off nor developed any crack during the scratch test at 10 mN load. Again, this indicates that all the films have high adhesion with the substrate.

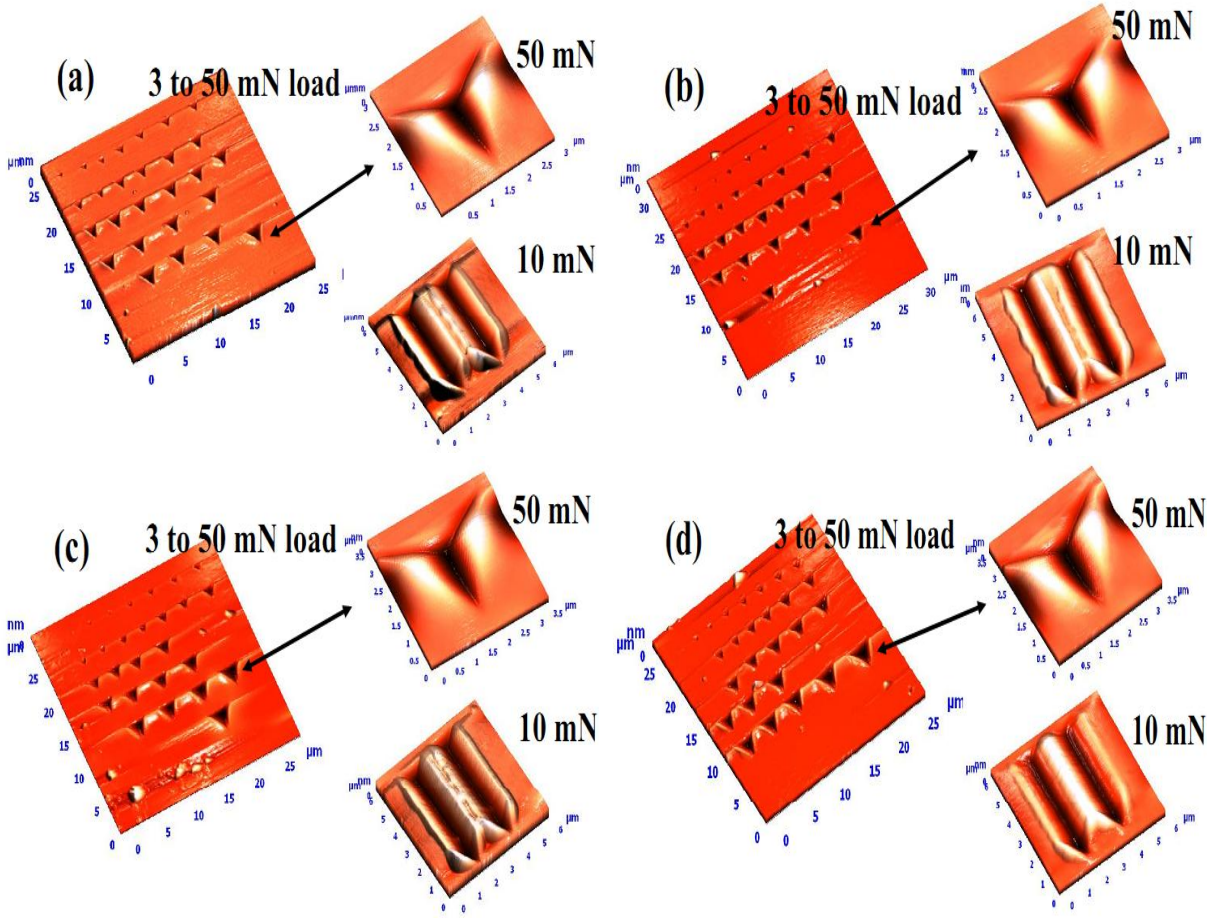

Figure 4.8 *(a)-(d) AFM topographical views for indentation at 3 to 50mN load and for scratch scars at 10 mN load on Zr-W-N films annealed at 100ºC, 200ºC, 300ºC and 400ºC, respectively*

4.1.4 Conclusions

In conclusion thermal stability and mechanical properties of novel Zr-W-N thin films have been studied. With increase in T_s, the structure of the deposited films changes from amorphous (100ºC $\leq T_s \leq$ 300ºC) to crystalline (400ºC $\leq T_s \leq$ 600ºC). A comparison of mechanical properties shows that the amorphous films deposited at T_s = 200ºC exhibit maximum wear resistance (H/E_r~0.22) and maximum resistance to fatigue fracture (H^3/E_r^2~1.1 GPa). Annealing of the films deposited at T_s = 200ºC at different T_n (100ºC $\leq T_n \leq$ 600ºC) results in no change of its amorphous structure to crystalline up to T_n = 600ºC. Oxygen starts to be incorporated in the films at T_n = 300ºC and its content increases with increasing T_n. The hardness of the annealed films decreases with increasing oxygen incorporation. Indentation and scratch tests for as deposited and annealed films show that no cracks propagate in the films even at a high load of 50 mN and all the films exhibit high adhesion with the substrate. For practical applicability, the amorphous film deposited at T_s = 200ºC is found to be most suitable in the temperature range below 300ºC. The present study opens the scope of Zr-W-N nitrides as a potential coating material. Detailed studies like TEM on the films are required to further understand the evolution of microstructure. Other compositions of Zr-W-N system may be more promising as coating material.

4.2 Study of thermal stability and mechanical properties of fcc phase $Zr_{22}W_{19}N_{58}$ thin films deposited by reactive magnetron sputtering

4.2.1 Introduction

A surface coating is an effective overlay process to enhance the properties and stability of base materials used in exotic environments. The transition metal nitrides coatings deposited using PVD method particularly by magnetron sputtering on various industrial components have prolonged the service life of a component significantly and also increase their commercial value. Owing to their favorable mechanical and thermal properties, transition metal nitrides have been adopted as protective thin films since last decade (Sproul 1996, Dey and Deevi 2003, Hultman 2000, Daniel *et al.* 2006). Hultman (2000) explained in his review article that the structural metastability is the main factor for high thermal stability and those transition metal nitrides in which metastability comes from compositional modulation (nanostuctured) rather

than induced stresses (high compressive stress induced in the coatings by energetic ion bombardment) in the films show high thermal stability. It has been also observed (Dey and Deevi 2003, Hultman 2000, Daniel *et al.* 2006, Otani and Hofmann 1996, Uglov *et al.* 2008, Kim *et al.* 2009, Oliveira *et al.* 2006, Abadias *et al.* 2013) that the thermal stability and mechanical properties of ternary nitride films are highly affected by the oxide layer formation on the surface of the films. During operation in aggressive environments or open air, some chemical changes are expected to occur in nitride coatings (especially at or near their sliding surfaces). Despite being some-what inert or chemically stable, these coatings may oxidize. Other factors affecting thermal stability and performance of nitride films are phase separation, recrystallization, metal, nitrogen and impurity diffusion along with interfacial reactions. It has been observed that the preferred orientation, phase stability, oxidation and mechanical properties of polycrystalline thin films depend on the deposition temperature (T_s) and post annealing temperature (T_n) (Hultman 2000, Daniel *et al.* 2006, Otani and Hofmann 1996, Uglov *et al.* 2008, Kim *et al.* 2009, Oliveira *et al.* 2006, Abadias *et al.* 2013). Thermal stability of many polycrystalline ternary metal nitride films belonging to metal-metal nitride group such as Ti-Al-N (Hultman 2000), Ti-Cr-N (Otani and Hofmann 1996), Ti-Zr-N (Uglov *et al.* 2008), Cr-Zr-Si-N (Kim *et al.* 2009), Ti-Ta-N (Abadias *et al.* 2013) etc. have been studied by different authors.

Chen *et al.* (2012) have reported that thermal stability and oxidation resistance including mechanical properties of $Ti_{1-x}Al_xN$ coatings depend to a great extent on the Al content. The structural investigations indicate that $Ti_{1-x}Al_xN$ is single phase cubic for $x \leq 0.62$, mixed cubic and wurtzite for $x = 0.67$, and single phase wurtzite for $x \geq 0.75$. The hardness was decreased with increasing Al content. Thermal annealing of metastable $Ti_{1-x}Al_xN$ coatings causes a structural transformation toward their stable constituents of c-TiN and w-AlN. During exposure of the $Ti_{1-x}Al_xN$ coatings to ambient air at elevated temperatures Al_2O_3, TiO_2 and Al_2TiO_5 oxides are formed. The oxidation resistance of as-deposited single-phase $Ti_{1-x}Al_xN$ coatings, cubic or wurtzite structured, increases with increasing Al content. Only the single phase wurtzite structure coating w-$Ti_{0.25}Al_{0.75}N$ shows a better oxidation resistance with ~ 0.7μm oxide scale thickness, which only slightly increases to 1.1μm by increasing the oxidation time at 850ºC to 40 h, where all other coatings tested here are completely oxidized.

Yang *et al.* (2012) have reported that cubic $Cr_{0.32}Al_{0.68}N$ coating exhibits better oxidation resistance than Ti-Al-N coatings show at elevated temperatures. The Cr-Al-N coatings exhibits a dense oxide layer of ~ 1.4μm with the uniform distribution of dense protective α-Al_2O_3 and Cr_2O_3 after oxidation at 1050ºC for 10 h, whereas Ti–Al–N coatings are already completely oxidized at 950ºC.

Uglov *et al.* (2008) have studied the structural and mechanical stability of Ti–Zr–N coatings after vacuum annealing at 850ºC for 3.5 h. The $Ti_{1-x}Zr_xN$ coatings with higher Zr (x = 0.58) content shows higher hardness (~ 35 GPa) but lower harness stability during thermal annealing in comparison to harness value obtained for lower Zr (x = 0.49) content Ti-Zr-N coatings.

Kim *et al.* (2009) have studied the thermal stability of CrZr–Si–N thin films as a function of the Si content (0 to 23.5 at. %) by annealing of the films at 300 and 800ºC temperatures for 30 min in air. It was found that the addition of the Si into the CrZrN film improved its thermal stability. While the $Cr_{37.7}Zr_{12.0}N_{50.3}$ film without any Si content oxidized completely at 600ºC and its hardness decreased significantly from ~ 32 to 6 GPa after annealing. The $Cr_{19.7}Z_{7.5}Si_{23.5}N_{49.2}$ film maintained its hardness of ~ 25 GPa even after annealing at up to 800ºC.

Novel metal-metal Zr-W-N amorphous films have been studied by our group (Dubey *et al.* 2013A, Dubey *et al.* 2013B. It has been shown that the amorphous films exhibit interesting mechanical properties.

In the present work, effect of deposition temperatures and post annealing temperatures on structural, morphological and mechanical properties of crystalline (fcc) Zr-W-N ternary nitride composed of group IV (ZrN) and group VI (W_2N) nitride films have been studied in detail. In literature, ZrN and W_2N nitrides systems have been studied separately in detail, however, to the best of our knowledge there is no report on Zr-W-N nitride thin films. Individually ZrN shows three stable structures with the increase in nitrogen percentage in the films. For lower N atomic percentage (< 10%) ZrN film acquires the bcc structure and then fcc for higher N atomic percentage (> 45%) with hcp as transition structure between them (Zhou *et al.* 2013). However, the WN_x films show the hexagonal (α-W) structure for lower value of $N_2/Ar+N_2$ ratio. Furthermore, the crystal structure changes to cubic W_2N with the ratios

between 0.1 and 0.35. When the ratios exceed 0.35, the films show hexagonal WN structure (Yamamoto *et al.* 2005). The W_2N phase starts to decompose into two oxide phases (WO_3 and $WO_{2.92}$) at 500ºC in the process of air annealing (Vemuri *et al.* 2010 Mohamed 2008, Ramana *et al.* 2006).

4.2.2 Experimental Details

4.2.2.1 Deposition of Zr-W-N thin films

Zr-W-N films have been deposited on Si (100) substrates using reactive magnetron co-sputtering. Sputtering targets (5 cm diameter and 0.5 cm thick) of Zr and W with purity 99.98% and 99.95% respectively have been used for deposition. Sputtering was carried out at constant N_2 (8 sccm) and Ar (32 sccm) flow at different T_s (100º-600ºC) for 1.5 h. The residual pressure was < 0.5×10^{-3} Pa, N_2 partial pressure and working pressure were 0.13 Pa and 0.67 Pa respectively. The power densities for W and Zr targets were 4 watt/cm^2 and 6 watt/cm^2 respectively. All depositions were carried out at ground potential and at a fixed substrate to target distance of 6 cm. The post annealing (100º-600ºC) of the films deposited at T_s = 400ºC have been carried out in air for 1 h.

4.2.2.2 Characterization

The characterization of as deposited and post annealed films have been carried out using X-ray diffraction (XRD), transmission electron microscopy (TEM) and field emission scanning electron microscopy (FE-SEM) for their structural, morphological and cross-sectional studies. The elemental composition analysis of Zr-W-N thin films was carried out using an energy dispersive X-ray analysis. Mechanical properties of as deposited and post annealed films have been studied by Nano-indentation. All the indentation measurements have been carried out at 10 mN to minimize the substrate effect. A higher load of 50 mN has been chosen for fracture toughness measurement through indentation. The films were scratched with 2 to 10 mN load at constant loading velocity (20 nm/s) and scratch velocity (500 nm/s) for adhesion test purpose. The hardness (H), effective elastic modulus (E_r) and percentage elastic recovery (W_e) were calculated by loading and unloading curves generated during nanoindentation.

4.2.3 Results and Discussion

4.2.3.1 Effect of substrate temperatures on film structure and mechanical properties

4.2.3.1.1 Structural and morphological analysis

The concentration of various elements in the Zr-W-N films as a function T_s is shown in **figure 4.9**. It can be clearly seen that the at.% of Zr, W and N elements are almost independent of T_s. The average elemental composition of the films is found to be $Zr_{22}W_{19}N_{58}$.

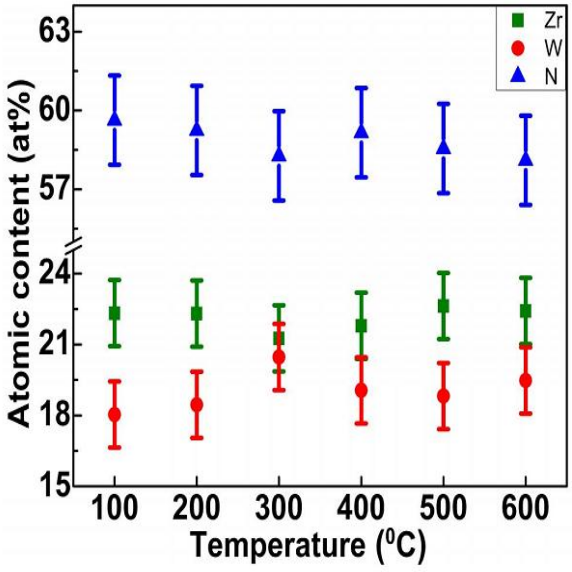

Figure 4.9 *EDS analysis of Zr–W–N films deposited at different substrate temperature T_s*

The XRD patterns of films show single fcc phase for all the films deposited at different substrate temperatures (T_s) as shown in **figure 4.10**. A close analysis of the diffraction pattern shows that for low T_s (T_s < 400ºC) the coating structure is not simply fcc but probably contains some amorphous parts along with the fcc phase. It can be clearly seen that the contribution of amorphous part is maximum for T_s = 100ºC, decreases with increasing T_s and disappears for T_s ≥ 400ºC.

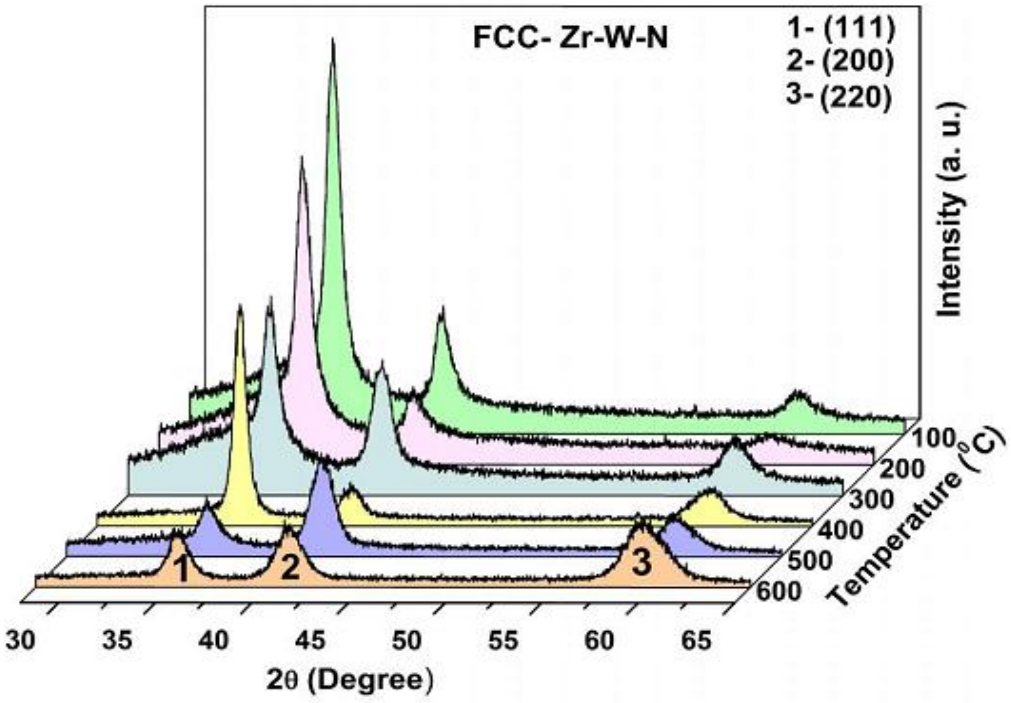

Figure 4.10 *XRD patterns of Zr-W-N thin films deposited at varying T_s*

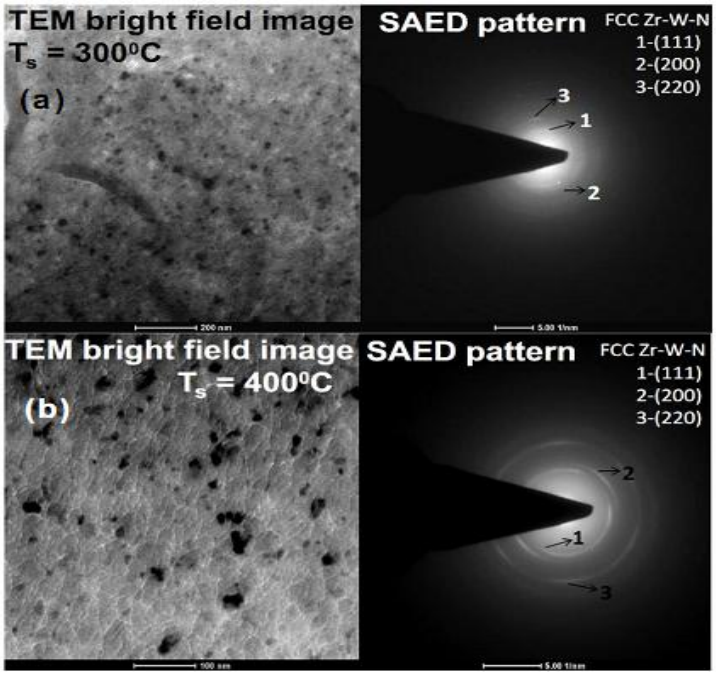

Figure 4.11 *TEM images and SAED patterns (a) amorphous and nanocrystalline Zr-W-N film deposited at T_s = 300ºC, (b) pure nanocrystalline Zr-W-N film deposited at T_s = 400ºC*

To further confirm the evolution of microstructure, TEM analysis of the films has been carried out. The TEM bright field images and the corresponding selected area electron diffraction (SAED) patterns of the films deposited at T_s = 300ºC and 400ºC are shown in **figure 4.11a** and **4.11b**, respectively. The SAED patterns are indexed by proper calculations. For T_s = 300ºC (**figure 4.11a**), along with the ring pattern for the nanocrystalline phase, diffuse rings from the amorphous phase can also be observed. For T_s = 400ºC (**figure 4.11b**), clear ring pattern can be seen which corresponds to nanocrystalline phase.

The micro-strain and crystallite size 'd' have been calculated using Williamson-Hall method (Lemine 2009). Due to the presence of some amorphous parts, the micro-strain and crystallite size for the films deposited at 100ºC ≤ T_s ≤ 300ºC can not be calculated correctly. The micro-strain and crystallite size for the films deposited at 400ºC ≤ T_s ≤ 600ºC has been calculated as shown in **figure 4.12a** and **4.12b**, respectively.

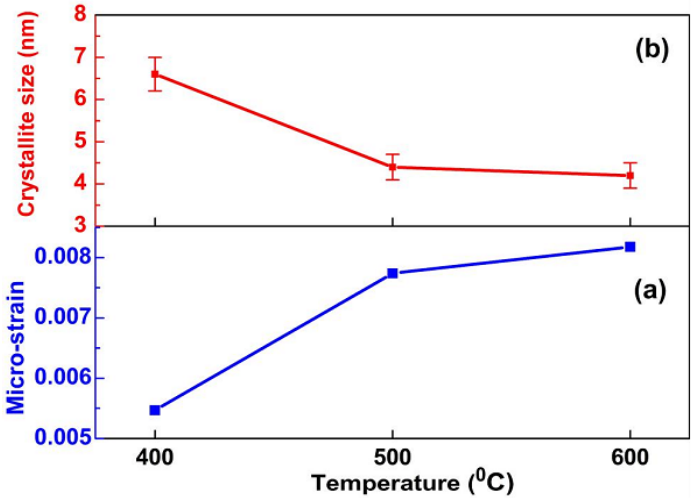

Figure 4.12 *(a) Micro-strain and (b) Crystallite size of the films deposited at different T_s*

With increasing T_s, the micro-strain was found to increase. This may be due to thermal strain associated with the difference in thermal expansion coefficient (α) of substrate (α_{Si} = 2.33 × 10^{-6} C^{-1}) and the film (α_{ZrN} = 7.24 × 10^{-6} C^{-1}, α_{W2N} = 5.66 × 10^{-6} C^{-1}) (Meng *et al.* 2011, Lahav and Grim 1990). With increasing T_s, crystallite size decreases from ~ 7 nm at T_s = 400ºC to ~ 4 nm at T_s = 500ºC, with further increase in T_s, crystallite size decreases marginally (**figure 4.12b**). In general, crystallite size increases with increasing T_s (Abadias *et al.* 2006, Ni *et al.* 2008, Meng *et al.* 1993), however, in the present case, crystallite size decreases with increasing

T_s. It is well known that the increase of deposition temperature leads to the enhancement of adatom mobility and surface diffusion. It has been observed that the lowest surface energy plane was (200), while the lowest strain energy plane was (111). Accordingly, the (200) orientation was preferred in the deposition conditions where the strain energy was small and the surface energy was dominant. On the other hand, the (111) preferred orientation was predicted in the deposition conditions in which the strain energy was large and dominant (Abadias *et al.* 2006, Oh and Je 1993). In the present case, from the change in peak profile for $T_s > 400^oC$, it can be clearly seen that none of the orientation is clearly favored. This may be due to a competition between strain energy and surface energy which further results in a competitive grain growth (evolutionary selection rule) and a decrease in grain size with increasing substrate temperature (Abadias *et al.* 2006).

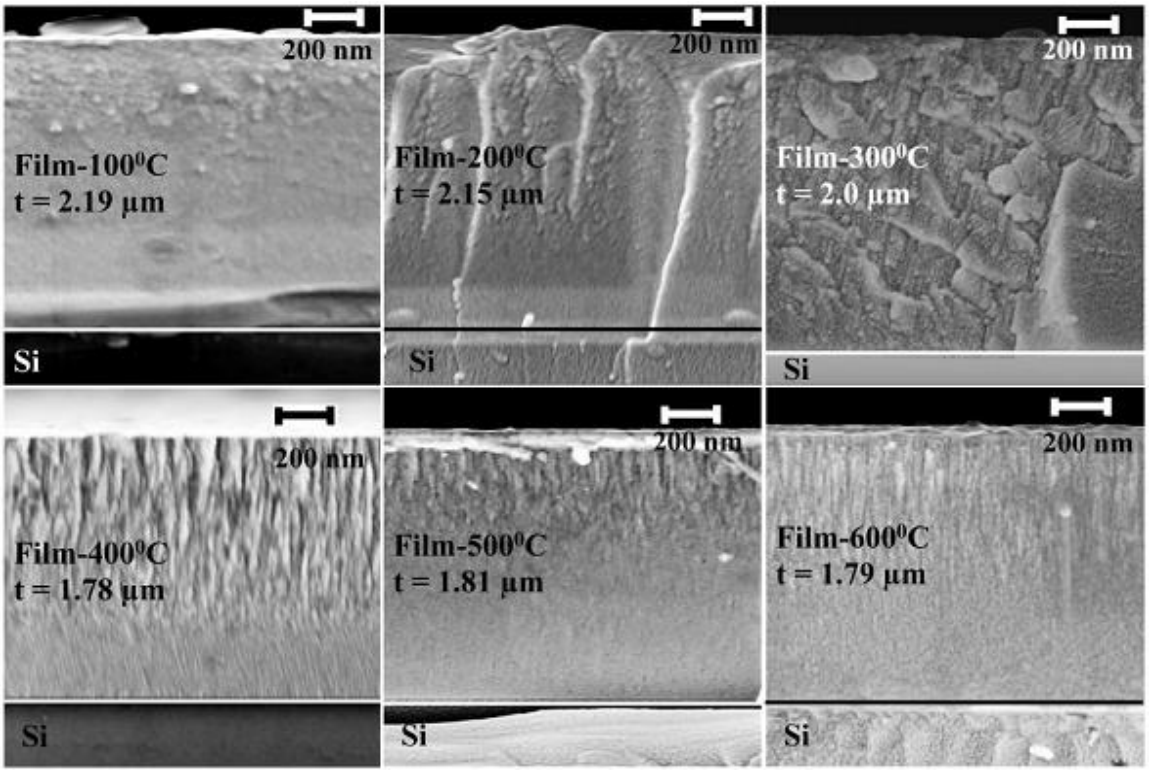

Figure 4.13 *FESEM cross-sectional images of the films deposited at varying T_s*

Figure 4.13 shows the cross-sectional FE-SEM images for all the deposited films. For $T_s \geq 400^oC$, the FE-SEM images show a columnar structure which becomes denser with increasing T_s (the columns are only distinguished in the upper part of the film due to thermal

drift near the silicon substrate). The thickness of the films varies non-monotonically with increasing T_s. For T_s < 400ºC, thickness decreases with increasing T_s and for $T_s \geq$ 400ºC, thickness remain almost constant (~ 1.8 µm). This may be associated to increased mobility, diffusion of the adatoms and strain with increasing T_s (Meng *et al.* 2011, Jimenez *et al.* 2006). Thus for $T_s \geq$ 400ºC, the morphology of the films changes from under dense to dense growth (Abadias 2008).

4.2.3.1.2 Mechanical properties

The results of nanoindentation test for as deposited films have been shown in **table 4.3**. With increasing T_s, hardness (H) and effective elastic modulus (E_r) were found to increase. This may be associated with lowering of the crystallite size with increasing T_s (Patsalas 2010). The maximum values of H (~23 GPa) and E_r (~118 GPa) are obtained for the films deposited at T_s = 600ºC. The observed value of E_r is lower than the E_r values reported in literature (Oh and Je 1993, Koutso keras *et al.* 2011, Jimenez *et al.* 2006, Abadias 2008, Patsalas *et al.* 2000, Musil 2012). In general, elastic modulus (elastic stiffness) has been observed to be related to atomic bonding/bond strength. When microstructure reduces in nanocrystalline range (grain size < 100 nm), most of the atoms reside on grain boundaries and hence grain boundaries play an important role in deformation of nanocrystalline material. It has been found that the elastic moduli of the metallic nanocrystalline materials (Pd, Mg) reduce by 30% or less whereas ionic crystal (CaF_2) showed a reduction of more than 50% from their bulk values. Further, the magnitude of H and E_r of the Me1-Me2-N type of coatings depend on the deposition parameters used in its preparation and are controlled by the selection of Me1 and Me2 elements (Musil 2012). Thus, for the novel Zr-W-N coatings, the nanocrystalline grain size and combination of IV (ZrN) and VI (W_2N) transition metal nitrides (exhibiting the blend of metallic and ionic bonding) may result in low elastic modulus.

Plasticity index parameter (H/E_r) is another important parameter for wear protective coatings. For practical purposes the value of H/E_r should be high (> 0.1), this means films should show more resistance to plastic deformation or have high abrasive resistance (Charitidis 2010). The highest value of H/E_r (0.22) was recorded for the films deposited at T_s = 400ºC. Presumably, the ratio of I_{111}/I_{200} (5.146) at 400ºC gives the higher value of H/E_r (Logothetidis 2007). The W_e gives information about the elastic and elastic-plastic behavior of the films. The upper limit corresponds to the fully elastic and lower limit corresponds to the elastic-plastic

behavior (Lejeune *et al.* 2005). The higher value of W_e (≥ 75%) at higher T_s (≥ 400ºC) reveals the highly elastic behavior of the films deposited at higher T_s.

Table 4.3 *Mechanical properties of the films deposited at different T_s and post annealed in air at different T_n*

Substrate temperature (T_s)	***Load***	***Hardness***	***Elastic modulus***	***% Elastic recovery***	***Plastic deformation energy***	***Plasticity index parameter***	***Resisitance to fatigue fracture***
(^{0}C)	***L(mN)***	***H(GPa)***	***E_r(GPa)***	***W_e***	***U_p ($*10^{-10}$ joule)***	***H/E_r***	***H^3/E_r^2(GPa)***
100	10	14	88	69.2	11.3	0.16	0.35
200	10	16	91	72.4	10.6	0.18	0.49
300	10	18	94	73.5	9.81	0.19	0.66
400	10	21	96	74.0	9.22	0.22	1.00
500	10	22	109	77.2	9.19	0.20	0.89
600	10	23	118	80.1	8.92	0.19	0.87
Annealing temperature (T_n)							
100	10	21	98	74.4	9.10	0.214	0.96
200	10	21.8	96	75.8	9.13	0.226	1.12
300	10	22.6	99	76.3	8.94	0.228	1.18
400	10	25	110	81.2	8.56	0.227	1.29

The higher value of U_p substantiate the higher ductility of the films deposited at lower T_s as compared to the films deposited at higher T_s. This may be attributed to the lower crystallite size (< 10 nm) of the films deposited at higher T_s (Musil 2012). Indentations at 50 mN load for all the films deposited at different T_s reveal that no crack propagates on the surface of the films and consequently, the toughness of the films cannot be calculated quantitatively; however, it can be concluded that the toughness of the deposited films is appreciable to the extent so as to bear a high load of 50 mN without crack. To estimate the film resistance to cracking, H^3/E_r^2 has been calculated as shown in **table 4.3**. High value of H^3/E_r^2 (> 0.1GPa) confirms a high resistance to cracking and hence high fracture toughness (Besks *et al.* 2011). No delamination of the films is observed during scratch test at 10 mN load revealing that all the

films have high adhesion with the substrate. A comparison of H^3/E_r^2 ratio for the deposited films show that the film deposited at 400ºC exhibits highest value (1.0 GPa) of H^3/E_r^2 ratio.

4.2.3.2 Effect of post annealing temperatures on film structure and mechanical properties

4.2.3.2.1 Structural and morphological analysis

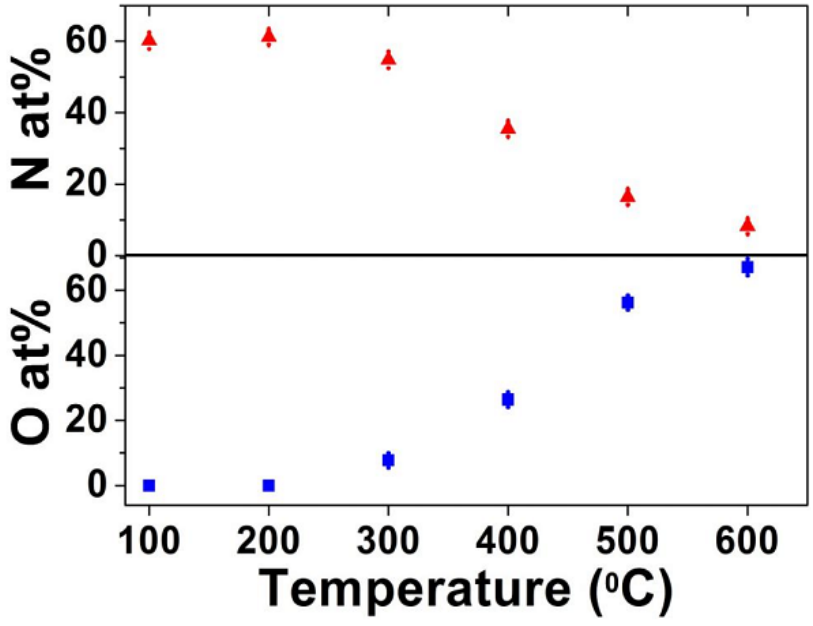

Figure 4.14 *EDS analysis (atomic fraction of O and N gases) of Zr–W–N films annealed at different T_n*

Due to the superior mechanical properties of the film deposited at T_s = 400ºC over other films, post annealing of the films deposited at 400ºC have been carried out at different annealing temperatures T_n (100º-600ºC). The EDS analysis (N, O atomic fraction) of the films annealed in air at different T_n is shown in **figure 4.14**. It has been observed that the oxygen starts to be incorporated in the films at T_n = 300ºC and its content increases substantially with increasing T_n. The maximum O content (~ 67 %) is found for the film annealed at T_n = 600ºC. On the other hand, the N atomic concentration starts to decrease continuously above T_n = 200ºC and reaches ~ 8 % in the film annealed at T_n = 600ºC.

XRD patterns (**figure 4.15**) of the post annealed films show that the films retain the fcc structure up to T_n = 600ºC without forming any crystalline oxide phase. For $T_n \geq$ 400ºC, along with the peaks corresponding to crystalline zirconium tungsten nitride, an amorphous contribution can be clearly seen. This amorphous contribution increases with increase in T_n and accounts for the large O% observed in the films annealed at $T_n \geq 400^{\circ}$C. This amorphous part may be attributed to the formation of oxides of zirconium, tungsten, zirconium tungsten and zirconium tungsten oxynitride (Reddy *et al.* 2007, Khamseh 2014, Xiao *et al.* 2007), further, oxygen can be incorporated in the lattice interstitials also. Shifting (in $2\theta^{o}$) in peaks is the only noticeable change in the XRD patterns with increasing T_n.

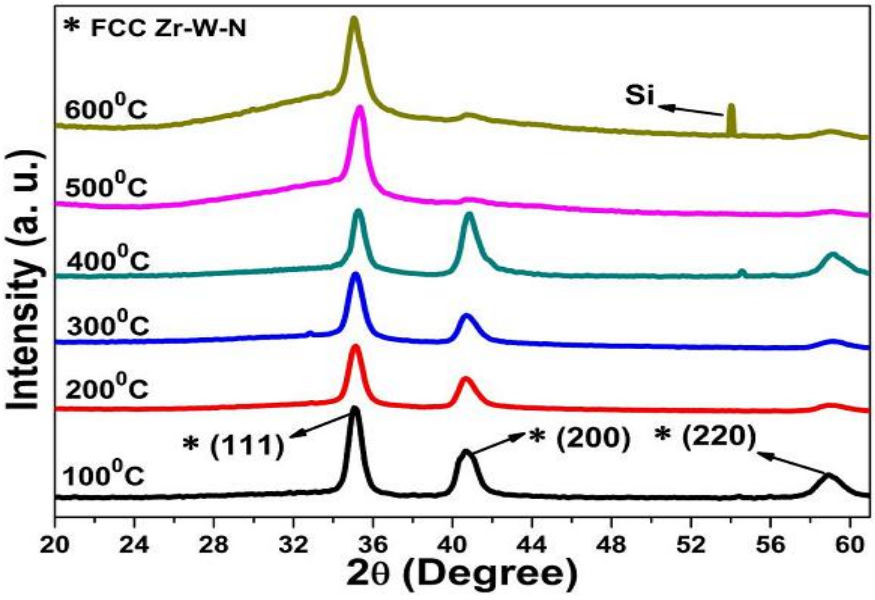

Figure 4.15 *XRD patterns of Zr-W-N thin films annealed at different T_n*

It has been observed that with increasing O at.% in the films, internal stress increases resulting in shifting of the peaks as observed in **figure 4.15**. The effect of internal stresses is tangible at $T_n \geq$ 300ºC, when the O atomic fraction is higher than 8% in the annealed films. The films begin to peel off at 500ºC and got completely peeled off at T_n = 600ºC. This may be associated with diffusion of some of the O atoms toward interface through grain boundaries with increasing T_n (Abadias *et al.* 2013).

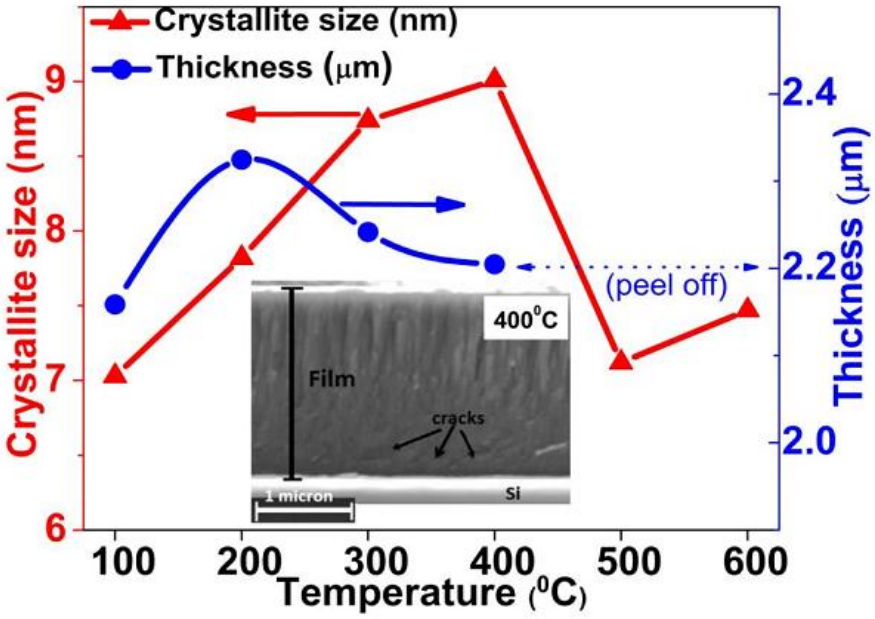

Figure 4.16 *Variation of crystallite size and thickness of films with increasing T_n. The inset shows cross-section FESEM image of film annealed in air at 400ºC. The cracks were formed at the interface during annealing process*

Figure 4.16 also shows that the thickness of the Zr-W-N films first increases (up to T_n = 200ºC) and then starts to decease continuously before the films got peel off from the substrate. Inset of **figure 4.16** shows the cracks formation near the interface during annealing at 400ºC. It may be the case that at this temperature the induced strain due to incorporation of O atoms was sufficient to develop cracks in the films and further annealing at higher temperature leads to delaminating of Zr-W-N films (Abadias *et al.* 2013).

Crystallite size for each T_n has been calculated using Williamson-Hall method (Lemine 2009). The crystallite size increases with increasing T_n and reaches a maximum value of ~ 9 nm at T_n = 400ºC and for T_n > 400ºC, the crystallite size decreases as shown in **figure 4.16**. This may be due to competition between mobility of adatoms and the induced stress (due to O atoms incorporation) in the films during annealing which controls the crystallite size in the films as the T_n increases (Daniel *et al.* 2006, Jimenez *et al.* 2006).

4.2.3.2.2 Mechanical properties

The delaminating of the films above T_n = 400ºC restricted the indentation studies of all post annealed Zr-W-N films. **Table 4.3** shows the result of nanoindentation for all the films annealed at different T_n. H and E_r were found to increase with increasing T_n. This may be associated with the combined effect of covalent bonding and induced stress with increasing T_n (Patsalas *et al.* 2000). Maximum value of H (25 GPa) and E_r (110 GPa) were found for the films annealed at 400ºC. The maximum value of H/E_r (0.228) is obtained for the film annealed at 300ºC. Other mechanical properties like U_p, W_e and H^3/E_r^2 for all annealed films have been given in **table 4.3**. The Films annealed at higher T_n showed higher value of W_e and lower value of U_p as compare to films annealed at lower T_n indicating the highly elastic behavior of the films annealed at higher T_n. The maximum value of W_e (78%) was achieved at T_n = 400ºC because dense materials with strong covalent bonds show more resistance to plastic deformation resulting in higher elastic recovery of the films (Patsalas *et al.* 2000). To estimate the resistance of annealed films to cracking, H^3/E_r^2 has been calculated as shown in **table 4.3**. High value of H^3/E_r^2 confirms a high resistance to cracking and hence high fracture toughness. Scratch test at 10 mN load reveals that all studied films have high adhesion with the substrate.

4.2.4 Conclusions

In conclusion, thermal stability and mechanical properties of as deposited and post annealed Zr-W-N thin films have been studied in detail. For the as deposited films, a single fcc phase has been observed for 100ºC ≤ T_s ≤ 600ºC. The crystallite size of Zr-W-N films was found to decrease with increasing T_s. H and E_r were found to increase with increasing T_s. Absence of adhesive kind of failure during scratch tests confirms the high adhesion of all the deposited films with the substrate. Highest values of H/E_r (~ 0.22) and H^3/E_r^2 (~ 1.0 GPa) has been obtained for T_s = 400ºC.

For the annealed films, no crystalline oxide phase has been detected for 100ºC ≤ T_n ≤ 600ºC, even though oxygen incorporation in the films starts at T_n ≥ 300ºC. The films start peeling off at 500ºC and got completely peeled off at 600ºC. The crystallite size increases with increasing T_n and reaches a maximum value of ~10 nm at T_n = 400ºC. For practical

applicability, the film deposited at 400ºC is found to be most suitable for application in the temperature range below 300ºC.

Mechanical response of amorphous phase Zr-W-N is found superior to crystalline fcc phase Zr-W-N coatings. But Zr-W-N coatings exhibit amorphous phase at low $T_s \leq 300$ºC which restricts the further enhancement of mechanical properties and thermal stability of Zr-W-N coatings either by varying other sputtering parameter likes negative biasing (**chapter 5**) or by changing the architecture of coatings through substitution of amorphous non-metal nitride phases like boron nitride, silicon nitride into the film (**chapter 6**). Hence, crystalline (fcc) phase Zr-W-N has been selected for further study in the present research work.

CHAPTER 5

Zirconium Tungsten Nitride Coating: Study on Energetic Ion Bombardment

Effect of microstructure features, altered by ions bombardment, on mechanical properties of magnetron sputtered nanocrystalline fcc phase Zr-W-N Coatings have been discussed in detail.

5.1 Introduction

A surface coating is an effective overlay process to enhance the properties and stability of base materials used in exotic environments. The transition metal nitrides coatings deposited using PVD method particularly by magnetron sputtering on various industrial components have prolonged the service life of a component significantly and also increase their commercial value (Sproul 1996). The magnetron sputtered transition metal nitride coatings like TiN, ZrSiN, TiAlN, TiSiN, TiAlVN, CrTiAlN, CrAlN (Bhaduri *et al.* 2010, Tillmann *et al.* 2013, Wang *et al.* 2012, Shi *et al.* 2010, Sandu *et al.* 2009, Dey and Deevi 2003, Chawla *et al.* 2010) etc. have been successfully explored in the last decades as wear protective coatings due to their good mechanical and thermal properties. Many transition metal nitride coatings have been developed so far (Voevodin *et al.* 2004, Mawella and Sheward 1990, Musil 2012, Leyland and Matthews 2000); however, at present, there is very few information on the formation of metal nitride coatings (CrNiN, ZrNiN, ZrWN) that meet with tribological demands (Musil and Vlcek 2001, Dubey *et al.* 2013A). Musil *et al.* (2001) have reported that the optimal performance (physical and mechanical properties) of any nanocomposite coatings composed either from two hard phases (TiSiN, TiZrN, TiAlN) or one hard and one soft phase (ZrCuN, CrNiN, ZrNiN) are strongly depend on their structure, relative content of individual phases, chemical composition and on conditions of their preparation. The development of metal nitride coating exhibiting

high hardness (H), low effective elastic modulus (E_r), satisfying the high value (> 0.1) of H/E_r ratio, high elastic recovery (W_e > 60%), compressive macrostress (< 0), dense and voids-free microstructure (non-columnar microstructure) is more demanding for tribological applications. Such micro-structural growth is sensitive to two main factors which include deposition temperature and negative bias applied (Bull 1992). For some metallic nitrides such micro-structures has been observed at high temperature since the low temperature deposition leads to kinetically limited growth in combination with self shadowing that grow the non-homogeneous, porous and low dense columnar microstructure (Voevodin *et al.* 2004 and references therein).

The bombardment of the films with ions of sufficient energy acts as an alternative to increasing the deposition temperature. Energetic ions bombardment causes the filling of the voided boundaries by coating atoms (adatoms) leading to a denser microstructure of the film. This filling can take place mainly due to bombardment-induced mobility of coating atoms (Mawella and Sheward 1990). In PVD processes, such bombardment of the coating during growth can be provided by the application of a suitable negative bias to the substrate, providing that the coating flux is sufficiently ionized. Though the energy of the bombarding ions is controlled by the substrate bias, the flux which the substrate receives depends on the ion current which is a function of the pressure in the system as well as the plasma intensity at the substrate. Adatom mobility and hence microstructure is a function of the momentum transfer from the ions which depends on both energy and flux. It is often necessary to increase the degree of ionization of the flux, e.g. by the use of a plasma, as in plasma assisted PVD. A direct consequence of the denser microstructures formed at higher bias voltages is that substantial stresses can be generated within the coating. Micro-structures can also be correlated with the levels of residual stress present in the coatings. But the high level of stress or elastic strain energy leads to peel off the coatings. This is because, increase in the levels of elastic strain energy stored within the coating accompany these micro-structural changes and with increasing coating thickness it eventually becomes favorable for the system to minimize its stored elastic energy by coating spallation. Thus, the presence of internal stresses limits the maximum thickness to which a coating may be deposited. The general term for all those processes where a substrate bias is used to promote the formation of dense coatings is ion plating. For few other metallic nitrides, negative bias voltage applied at low temperature has also been observed to

affect the evolution of such micro-structure (Sandu *et al.* 2009, Bull 1992, Lai *et al.* 2006 and Tung *et al.* 2009).

It has been also reported that the use of negative bias voltage suppress the effect of oxygen contamination in magnetron sputtered thin films (Rizzo *et al.* 2012). This contamination comes from the surfaces of deposition chamber exposed to air during the loading/unloading process steps. The plasma discharge during the growth process stimulates the oxide decomposition, causing the entry of oxygen in the residual atmosphere. The mechanism of interaction between adatoms and the residual atmosphere is dominated by adsorption of gas molecules on the freshly deposited film surface. However, high temperature baking of vacuum chamber has been done for removing gas molecules (thermal desorption) from the surface of chamber. Thermo-desorption removes from the surface only physically and chemically adsorbed molecules or metal hydrides with low binding energy ($E_b < 1$ eV), hence only nitrogen, hydrogen and inert gasses removed from the chamber walls. On the contrary, oxygen cannot be removed by baking because the binding energy of surface oxides exceeds 6–10 eV. Their decomposition requires more than heating in a reducing atmosphere such as energetic particle bombardment.

Petrov *et al.* (2003) have reported that only a high flux of mid-energy ions (~ 20 eV) benefits thin film structure modification, including increased density and reduced surface roughness and refining of the grain size, while excessive ion energy may roughen the surface and reduce the tribological properties of nano-scaled multilayer coatings.

Sandu *et al.* (2009) have reported that the increased negative bias voltage have the opposite effect on the microstructure and hence mechanical properties of Zr-Si-N to that of increasing substrate temperature. These studies indicate that by increasing the bombarding ions energy, the solubility limit of Si atoms in the lattice of ZrN nanocrystallites increase whereas the thickness of SiN layer covering ZrN nanocrystallites remains unaffected. The increase in hardness was attributed to a combined effect of film densification and crystallite size reduction.

Wang *et al.* (2012) have studied the influence of negative bias voltage on mechanical performance (hardness and toughness) of CrAlN coatings. It has been observed that due to combine effect of refined structure with increased compressive stress, hardness increases from 10 to 26 GPa and toughness improves from 1.67 to 2.02 MPa.$m^{1/2}$. The lowering grain size with increasing bias voltage creates more complicated grain boundaries. This gives rise to crack branching or bending, resulting in more energy being consumed to allow cracks to propagate. Wang *et al.* (2008) have noticed that the hardness (14 to 29 GPa), elastic modulus (208 to 302 GPa) and toughness (1.2 to 1.9 MPa.$m^{1/2}$) of TiC coatings increased with increasing negative bias voltage from -20 V to -200 V. However, adhesion strength varied non-monotonically with negative bias voltage, high substrate bias (> -100 V) lead to the deterioration of adhesion strength.

It has been noticed that the deposition of wear protective coatings at low temperature (≤ 200ºC) is more feasible for commercial aspects. Recently in our group, novel Zr-W-N coatings have been developed. It has been observed that Zr-W-N coatings show sub-optimal mechanical properties at low substrate temperature (≤ 200ºC) in comparison to mechanical properties (H ~23 GPa, E_r ~ 118 GPa, W_e ~ 80%, H/E_r ~ 0.22, H^3/E_r^2 ~ 1.0) obtained at high substrate temperatures (≥ 400ºC) (Dubey *et al.* 2014). In the present work Zr-W-N coatings have been further explored to study the effect of bias voltage (at low substrate temperature) on these coatings. The coatings have been deposited at 200ºC substrate temperature on Si (100) substrates by DC/RF reactive magnetron sputtering. The effect of negative bias voltages (V_s) on microstructure, composition, deposition rate and mechanical properties of these coatings has been investigated in detail. The application of negative bias voltage to the substrate leads to impingement of energetic ions on the coating surface which is an effectual way to grow dense and void-free microstructure coatings at low deposition temperature (Mawella and Sheward 1990).

5.2 Experimental Details

5.2.1 Deposition of Zr-W-N thin films

Zr-W-N coatings have been deposited on mirror polished Si (100) (~ 0.067 cm thick) substrates at 200°C substrate temperature by DC/RF unbalanced magnetron co-sputtering from Zr target (5 cm in diameter, 0.5 cm thick, 99. 98% purity) and W target (5 cm in diameter, 0.5 cm thick, 99. 95% purity) in Ar (8 sccm) and N_2 (32 sccm) discharge. Prior to deposition all substrates were ultrasonically cleaned in acetone. Targets were fixed at an angle of 45º to the substrate normal. Si substrates were mounted on the substrate holder held at negative potential with the help of silver paste. The substrate holder was rotated at 5 rpm by using a DC motor to ensure uniformity in the deposited thin films. The residual pressure was $< 0.5\times10^{-3}$ Pa. The N_2 partial pressure and working pressure were 0.13 Pa and 0.67 Pa respectively. The sputtering power density of the Zr target and W target was kept at 6 watt/cm^2 and 4 watt/cm^2, respectively. All the depositions were carried out at fixed target to substrate distance of 6 cm for 1.5 h. The bias voltage (V_s) applied on the substrate was -20,-40,-60, -80, -100 and -120 V, respectively. The curvature of uncoated and coated substrate was determined by using Stylus profilometer (XP-2).The typical thickness (h) of films was varied from 1.6 to 2 µm with increasing negative bias voltage.

5.2.2 Characterization

The crystallographic structure of the films were characterized using x-ray diffraction (XRD) (Bruker, D8 advance, Cu-K_α radiation, λ =1.54 Å, step=0.02º, scan speed=2 sec/step) and transmission electron microscopy (TEM) (200 kV, FEI, TECNAI G^2). The surface and cross-section of the coatings were observed by field emission scanning electron microscopy (FE-SEM) (FEI, QUANTA 200F). Atomic force microscopy (AFM) (NT-MDT, NTEGRA) was used in semi-contact mode to evaluate the coating topography and root-mean-square (RMS) roughness. The elemental composition analysis of Zr-W-N films carried out using energy dispersive x-ray analysis (OXFORD, X-Max) with variation of ± 0.3 at.% for heavy

elements (Zr, W) and ±2 at.% for light elements (N_2). The hardness (H), effective elastic modulus (E_r) and elastic recovery (W_e) of these coatings were measured by a nano-indentation (NT-MDT, Nanoslerometry) using a Berkovich diamond indenter with normal angle of 65.3º between tip axis and faces of triangular pyramid. The effective size of apex is about 70 nm. The H, E_r and W_e of coatings have been measured at 10 mN load to assure the penetration depth should not more than the 10% of total thickness of coatings to minimize the substrate effect. The films were scratched with 2 to 10mN loads at constant loading velocity (20 nm/s) and scratch velocity (500 nm/s) for adhesion test purpose. Plastic deformation energy (U_p) (Sakai 1993) of the films is calculated by the area of loading-unloading curve in the load-displacement profile. The toughness was evaluated using micro indentation with a Vickers micro hardness tester (UHL VMHT). The micro indentations were done at varying loads (100 mN to 2000 mN). For each load, at least three readings were taken. The toughness K_{IC} is calculate by equation (5.1) (Lawn *et al.* 1980).

$$K_{IC} = \delta (E_r/H)^{1/2} (P/C^{3/2}) \quad (5.1)$$

Where P is the applied indentation load; E_r and H are the effective elastic modulus and hardness of the coating, respectively. δ is an empirical constant which depends on the geometry of the indenter, for Vickers indenter δ= 0.016. C is the crack length which was measured from optical microscopy (Olympus DME3) images. In order to reduce the substrate effect on film toughness, K_{IC} calculated from Eq. (5.1) was plotted versus indentation depth and then the curve was extrapolated to one-tenth of the film thickness to obtain the film toughness.

5.3 Result and Discussion

The effect of increasing energy (bias controlled) of the ions impinging onto the growing coatings to form a denser and more perfect structure has been explored.

5.3.1 Deposition rate and elemental composition

Table 5.1 *Summary of experimental results of* Zr-W-N *coatings deposited at varying* V_s

Negative Bias (V_s)	*Thickness*	*Deposition rate (a_D)*	*Substrate ion current density (i_s)*	*Kinetic energy (U_k)*	*crystallite size*	*Micro strain*	*Macro strain*	*Compressive stress*
(Volt)	*(µm)*	*(nm/min)*	*(A/cm^2)*	*(J/cm^3)*	*(nm)*			*(GPa)*
20	1.70	18.8	5.1E-5	9.04	10.6	0.0077	0.010	1.7± 0.3
40	1.85	20.5	6.8E-5	22.11	8.4	0.0121	0.015	2.9± 0.4
60	2.02	22.4	8.5E-5	37.94	6.3	0.0132	0.021	4.2± 0.3
80	1.83	20.3	8.5E-5	55.82	4.6	0.0152	0.028	5.8± 0.2
100	1.70	19.5	8.5E-5	72.64	3.8	0.0173	0.033	8.0± 0.3
120	1.55	17.2	8.5E-5	98.80	3.3	0.0122	0.019	3.7± 0.3

The variation in thickness and deposition rate (a_D) of Zr-W-N coatings, substrate ion current density (i_s) and kinetic energy (U_k) of ions bombarding on the films as a function of substrate bias (V_s) voltages are shown in **table 5.1**. The kinetic energy (U_k) of bombarding ions is calculate by the following equation 5.2 (Musil 2007).

$$U_k\,(J/cm^3) \approx (i_s\, V_s)/a_D \qquad (5.2)$$

This shows that the energy of bombarding ions strongly depends not only on V_s and i_s but also on a_D.

The deposition rate and substrate ion current density vary non-monotonically with increasing V_s from -20 V to -120 V. For -20 V $\leq V_s \leq$ -60 V, the a_D and i_s increased from ~19 nm/min to ~22 nm/min and 5.1E-5 A/cm^2 to 8.5E-5 A/cm^2 respectively. With further increase in V_s, a_D decreased up to ~ 17 nm/min and i_s became constant at 8.5E-5 A/cm^2 for V_s > -60 V. The increase in i_s at $V_s \leq$ -60 V indicate that the ionization of the coating flux was increased at

selected deposition parameters (sputtering pressure ~ 0.67 Pa and target substrate distance ~ 6 cm) which results in an increase in a_D (Bull 1992). The drop of deposition rate is caused by resputtering of the coating, i.e., kicking off the adatoms or growing surface by the incoming ions (Tillmann *et al.* 2013). The increase in resputtering of the coating at V_s > -60V is expected to result from an increase in the kinetic energy of the ions (U_k) bombarding the growing films as shown in **table 5.1**.

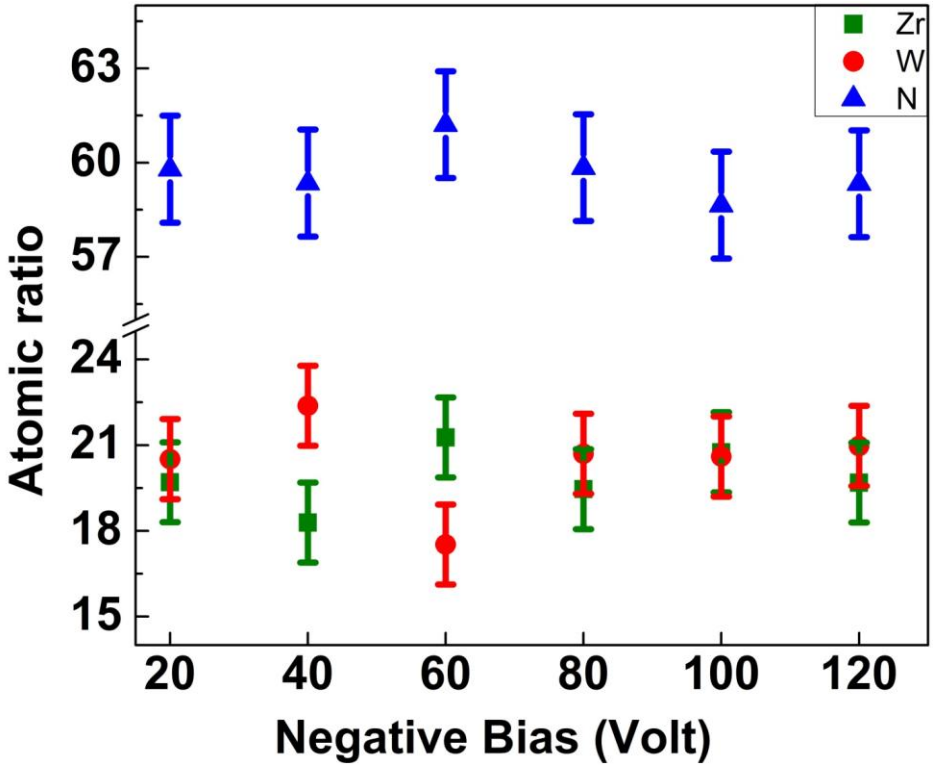

Figure 5.1 *EDS analysis (atomic fraction of O and N gases) of* Zr-W-N *coatings deposited at different* V_s

The atomic concentration of the various elements in Zr-W-N coatings as a function of substrate bias is shown in **figure 5.1**. The atomic percentages of Zr, W and N in the films varies from 22.3–19.6%, 21.2–17.8% and 60.8–58.9%, respectively indicating that V_s poses no

significant effect on the elemental composition of Zr-W-N coatings. The average elemental composition of the films is found to be $Zr_{21}W_{19}N_{60}$.

5.3.2 Microstructure analysis

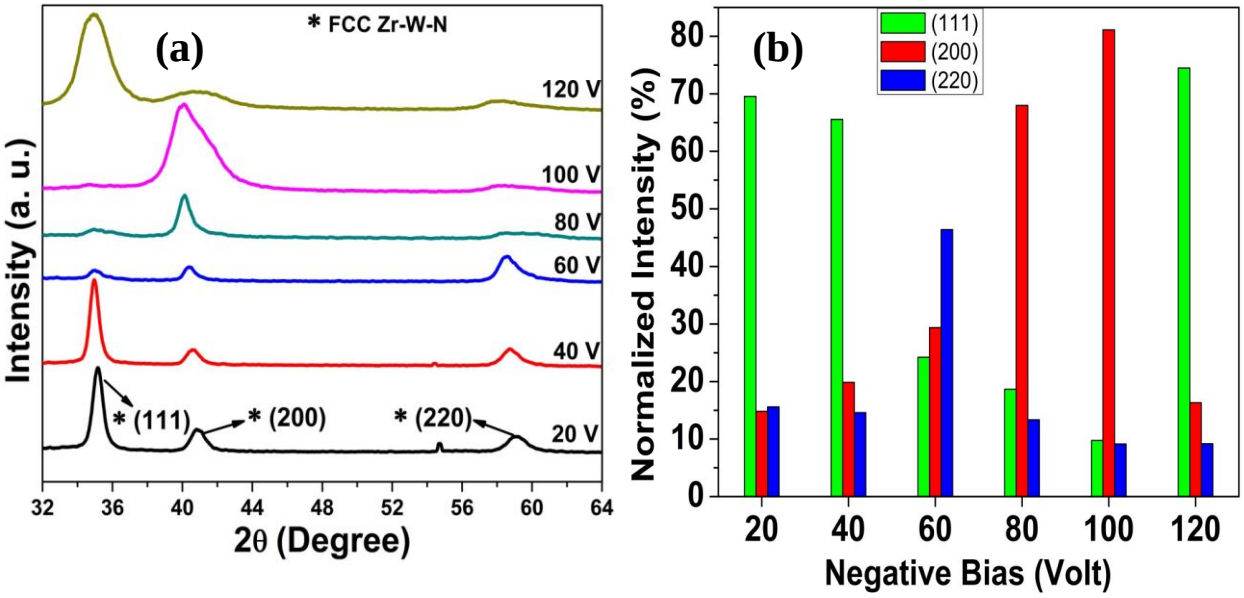

Figure 5.2 *(a) XRD patterns of Zr-W-N coatings deposited at different V_s and (b) The dependence of the normalized hkl XRD peak intensities, N_{hkl} (I_{hkl} /[I_{111} +I_{200} +I_{220}], of the Zr-W-N coatings as a function of substrate bias*

The effects of negative substrate bias on the microstructure of Zr-W-N films are characterized by X-ray diffraction. **Figure 5.2a** shows the diffraction peaks of crystalline Zr-W-N, demonstrating a strong dependence of film texture on the negative bias voltage applied to the substrate. **Figure 5.2b** shows the normalize peak intensities N_{hkl} (I_{hkl} /[I_{111} +I_{200} +I_{220}]) of (111), (200) and (220) peaks. XRD patterns of the Zr-W-N coatings revealing one group of peaks of fcc structure indicating that this coating tends to form a single solid-solution nitride phase rather than the co-existence of separated nitrides (Dubey *et al.* 2013A). For $V_s \geq$ -60 V, the preferred crystallographic orientation (**figure 5.2b**) of grains is changed from (111) to (200).

In general, kinetically limited growth processes are linked to adatom mobility, anisotropy in surface diffusivity and collisional cascades effects which are likely to control the texture development under energetic ionic bombardment (Abadias 2008, Abadias *et al*. 2006A). In the normal condition, the vertical build of grains is on low energy surfaces. With increasing negative bias voltage the atomic peening and adatoms kinetic energy (mobility) increases due to increase in energy of bombarding ions (Patsalas *et al.* 2000). The atomic peening leads to re-arrangement of the lattice atoms thus render considerable stress into the coating and lower adatoms mobility.

To minimize the accumulated stress, adatoms will arrange along a less stressed plane i.e. (111) orientation in fcc structure (Bhaduri *et al.* 2010). Simultaneously, intensive ion bombardment increases the localize substrate temperature which leads to a higher mobility of adatoms. By minimization of surface free energy due to increased surface mobility of adatoms, the microstructure evolved with (200) preferred crystallographic orientation of grains. Thus the mobility of adatoms and induced stress control the microstructure of coatings with increase in negative bias voltage (Abadias 2008, Abadias and Tse 2006). It has been observed that the intensity of (111) XRD peak decreases with increasing negative bias voltage, except at V_s = -120 V. The kinetic energy of most of the impinging ions ≤ -100 V was transferred to adatoms inplace to penetrate into the atomic layers, thereby increasing the surface mobility and decreasing the intensity of (111) XRD peak. The change of preferred growth orientation from (002) to (111) at high negative bias voltage (-120 V) was attributed to point defect growth (Abadias and Tse 2006). At V_s= -120 V, the higher kinetic energy (~ 100 J/cm^3) and momentum of the bombarding ions lead to the displacement of atoms through a series of primary and recoiling collisions, and thus creating point defects. The fcc structure of Zr-W-N films has been identified by XRD peaks for the studied range of negative bias voltage.

Figure 5.2a also shows the broadening and shifting of diffraction peaks. The shifting of XRD peaks toward lower angle is a result of energized ion bombardment and atomic peening effect that may expand the interplaner spacing. The broad diffraction peaks of Zr-W-N coatings indicate the formation of small crystallites and the occurrence of micro-strain in the coatings (Tillmann *et al.* 2013, Wang *et al.* 2012). The effect of broadening and peak shifting on properties is given in *section 5.3.3*.

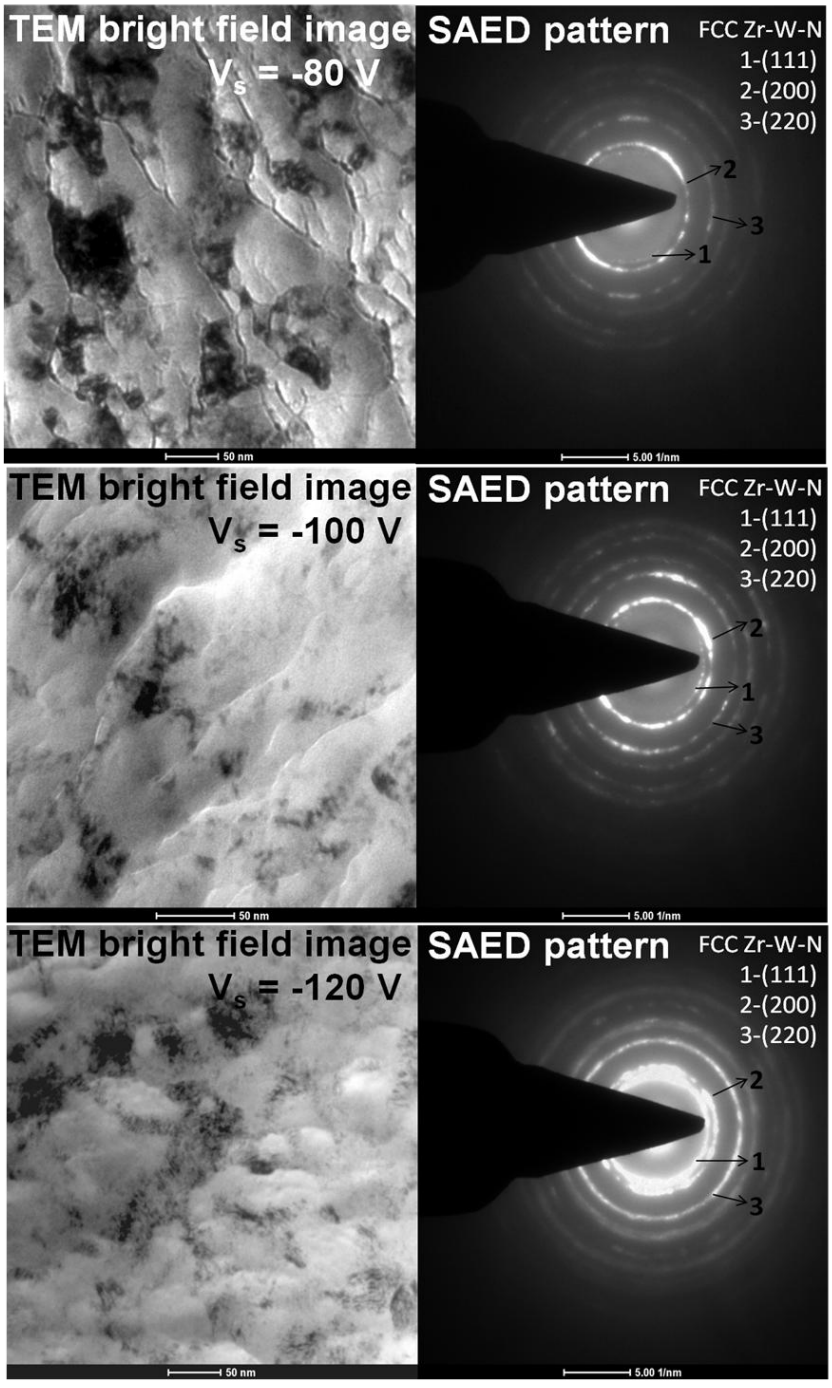

Figure 5.3 TEM bright field images and corresponding SAED patterns of Zr-W-N coatings deposited at Vs = -80 V, -100 V and -120 V

To further confirm the XRD finding and the presence of any secondary (nanocrystalline) phases at higher negative bias voltages, TEM analysis has been carried out. **Figure 5.3** shows the TEM bright field images and corresponding selected area electron diffraction patterns (SAED) of Zr-W-N coatings deposited at -80 V, -100 V and -120 V. It can be seen clearly from the SAED patterns that any secondary phases have not grown except fcc Zr-W-N phase during deposition at higher negative bias voltage. Moreover the higher intensity of (111) ring at V_s = -120 V in comparison to V_s = -80 V and -100 V confirms the higher grain growth in (111) orientation.

5.3.3 Morphological analysis

5.3.3.1 Crystallite size and microstrain

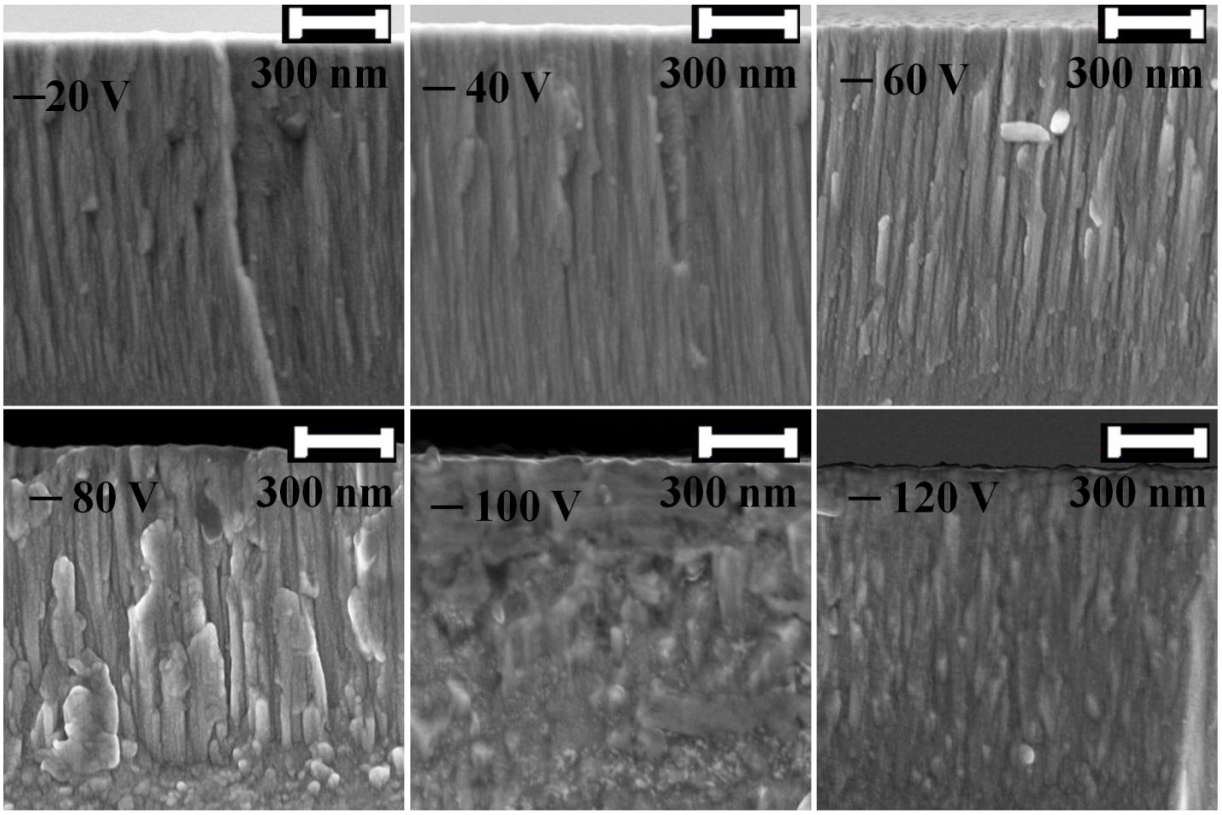

Figure 5.4 *Cross-sectional FESEM images of Zr-W-N coatings deposited at varying V_s*

FESEM micrographs of the cross-sections of the films deposited at different substrate bias voltages are shown in **figure 5.4**. For V_s> -80 V, morphology evolves from columnar structure to dense glassy structure. This is attributed to higher momentum transfer by the impinging ions to the growing surface with increasing negative substrate bias V_s which creates more chance of crystal re-nucleation. As such, the grain boundary migration and restructuration become prevalent and lead to a dense structure (Wang *et al.* 2008). The morphology became finer with increasing V_s agrees with the decreasing crystallite size with increasing V_s.

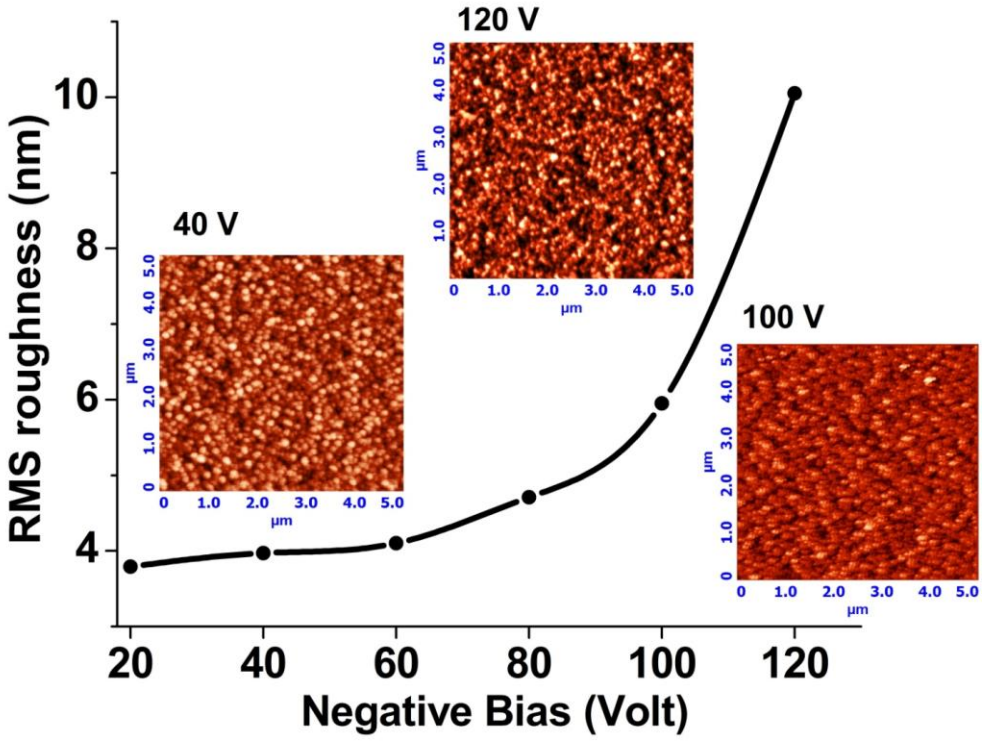

Figure 5.5 *The AFM topographical view of scratch scars and indentation marks on Zr-W-N coatings deposited at varying V_s*

Figure 5.5 shows the surface roughness and topological view of Zr-W-N coatings as a function of bias voltage. For -20 V $\leq V_s \leq$ -40 V, RMS roughness increases gradually form ~ 4 nm to 6 nm and then became two fold (10 nm) at V_s= -120 V. The bombardment of the growing film surfaces with ions having kinetic energy $\leq$ 70 J/cm^3 result in non-penetration of ions beyond the first atomic layer, and thus their energy is essentially transferred to adatoms

which results in smooth surface with rms roughness remains nearly constant during growth. Maximum kinetic energy (U_k ~ 100 J/cm^3) at -120 V induced bulk displacements of adatoms and resputtering of the near-surface atoms. Consequently, films grown at V_s = -120 V have a rough surface whose rms roughness increases substantially due to the contribution of a shadowing effect (Abadias and Tse 2006). This effect can see from the insets of **figure 5.5**.

The crystallite size and microstrain of Zr-W-N coatings were calculated by Williamson-Hall method (Lemine 2009). The variation of crystallite size and microstrain with negative bias voltages is given in **table 5.1**. The (111), (200) and (220) reflection peaks of the coatings were used in the peak broadening analysis. The crystallite size drops from ~11 to 3 nm as the substrate bias increases. This is attributed to intensive bombardment of ions to the growing surface of the film and the increased generation of defects with increasing V_s which may lead to an increased number of preferential nucleation sites, resulting in smaller crystallite (Wang *et al.* 2012). The microstrain increases with increasing negative substrate bias V_s. Maximum microstrain (0.017) has been obtained at V_s = -100 V. The energy delivered by the impinging ions to the growing surface is not only related to bias voltage but also depends upon ion flux. Hence, all the bombarding ions were not of equal energy at constant V_s (Musil *et al.* 2007). The momentum transfer by the impinging ions of different energy during deposition leads to different rearrangement of lattice atoms in the lattice planes resulting in microstrain in the films.

5.4 Mechanical Properties

There are numerous factors that may affect the mechanical properties of Zr-W-N coatings which include preferred orientation, crystallite size, densification and residual stress of coatings.

Table 5.2 *Mechanical response of the* Zr-W-N *coatings deposited at varying* V_s

Negative Bias (V_s)	*Hardness*	*Elastic modulus*	*% Elastic recovery*	*Plastic deformation energy*	*Plasticity index parameter*	*Resisitance to Plastic deformation*	*Toughness*
(Volt)	*H(GPa)*	*E_r(GPa)*	*W_e*	*U_p ($*10^{-10}$ joule)*	*H/E_r*	*H^3/E_r^2(GPa)*	*K_{IC} ($MPa.m^{1/2}$)*
20	22.3	104	75.2	9.0	0.21	1.0	1.4
40	24.2	112	76.3	8.6	0.21	1.1	1.65
60	26.5	120	78.5	8.2	0.22	1.3	1.77
80	28.3	122	79.7	7.7	0.23	1.5	2.06
100	33.6	145	84.3	7.3	0.23	1.8	2.25
120	27.8	136	81.6	8.0	0.20	1.2	1.93

The residual stress as a function of bias voltages is demonstrated in **table 5.1**. The residual stress calculated by Stoney's equation (Lai *et al.* 2006) using the substrate curvature determined by a surface profiler was found to be compressive in nature and increases from -1.7 GPa to -8 GPa with increasing V_s from -20 to -100 V (Chhowalla and Unalan 2005). The lattice parameter of these coatings is evaluated from the Nelson relay function (Cullity 1978). The increase in lattice parameter from 4.367 to 4.511nm with an increase (-20 V to -100 V) in substrate bias is likely to result somewhat from increase in compressive stress. This is because the bombarding ions with sufficient kinetic energy knock out the loosely bond atoms from their lattice position and bring about atom collision cascade. As such, rearrangement of lattice atoms takes place and leads to the resultant internal stress in the coatings. However, compressive stress decreases at V_s> -100 V. This may be due to the energy of impinging ions was sufficient to make resputtering prominent than atoms rearrangement.

The mechanical response of Zr-W-N coatings deposited at different substrate bias voltages is shown in **table 5.2**. Hardness (H) and effective elastic modulus (E_r) of coatings increase as V_s increases. Maximum hardness of ~33 GPa as well as effective elastic modulus of ~ 145 GPa are obtained at V_s= -100 V. The increase in H and E_r values is attributed to combine effect of decreased grain size, densification and increased compressive stress with increasing V_s. The obtained hardness (22 to 33 GPa) of Zr-W-N coatings deposited at various V_s belongs

to the range of high hardness for tribological coatings but the obtained elastic modulus (104 to 145 GPa) is substantially lower than as quoted elastic modulus (250 to 400 GPa) for tribological coatings (Musil 2012, Musil *et al.* 2002). Musil *et al.* (2012) have demonstrated that a high hardness is not necessarily prime requirement of tribological coatings indeed high elastic recovery, low elastic modulus with high hardness play an important role for tailoring the mechanical properties of coatings for a given application. The elastic recovery (W_e) gives information about the elastic and elastic-plastic behavior of the films. Wear resistive coatings having high (> 60 %) value of W_e exhibit a higher elasticity. A continuous increase in W_e has been observed for Zr-W-N coatings with increasing V_s. Maximum (84%) value of W_e obtained for coating deposited at V_s = -100 V shows that this film exhibit high elasticity in comparison to other deposited films. Oberle (Oberle 1951) has introduced a parameter called plasticity index (H/E_r) which is quoted as a valuable measure of determining the elastic strain to failure in a surface contact. The higher value (> 0.1) of H/E_r ratio is a strong indication of the coating resistance to wear damages (Oberle 1951). All the studied Zr-W-N coatings exhibit H/E_r ~2.0 and maximum value (0.23) of H/E_r is obtained for Zr-W-N coating deposited at V_s= -80 V, -100 V. It has been observed that combined effect of induced stress and growing microstructure (normalized intensity ratio, grain size, point defects, dense columnar) played important role to keep the H/E_r value ~ 0.2.

Figure 5.6a-c show the AFM topographical view of scratch scars and indentation marks on the films deposited at V_s= -20 V, -80 V and -120 V. The scratch scars at 10 mN load and indents at 3-50mN loads have been made on the films for adhesion and fracture toughness measurements, respectively. The higher value of H/E_r index is a strong indication of the coating resistance to wear, but such coatings do not always show improvement of elastic deformation and fracture toughness. Enlarged views of indents at 50mN loads reveal that no crack propagates on the surface of the films and consequently, toughness cannot be calculated quantitatively by nano indentations; however, micro indentations by vicker hardness tester have been done at varying loads (200 mN to 2000 mN) to calculate the fracture toughness of coatings.

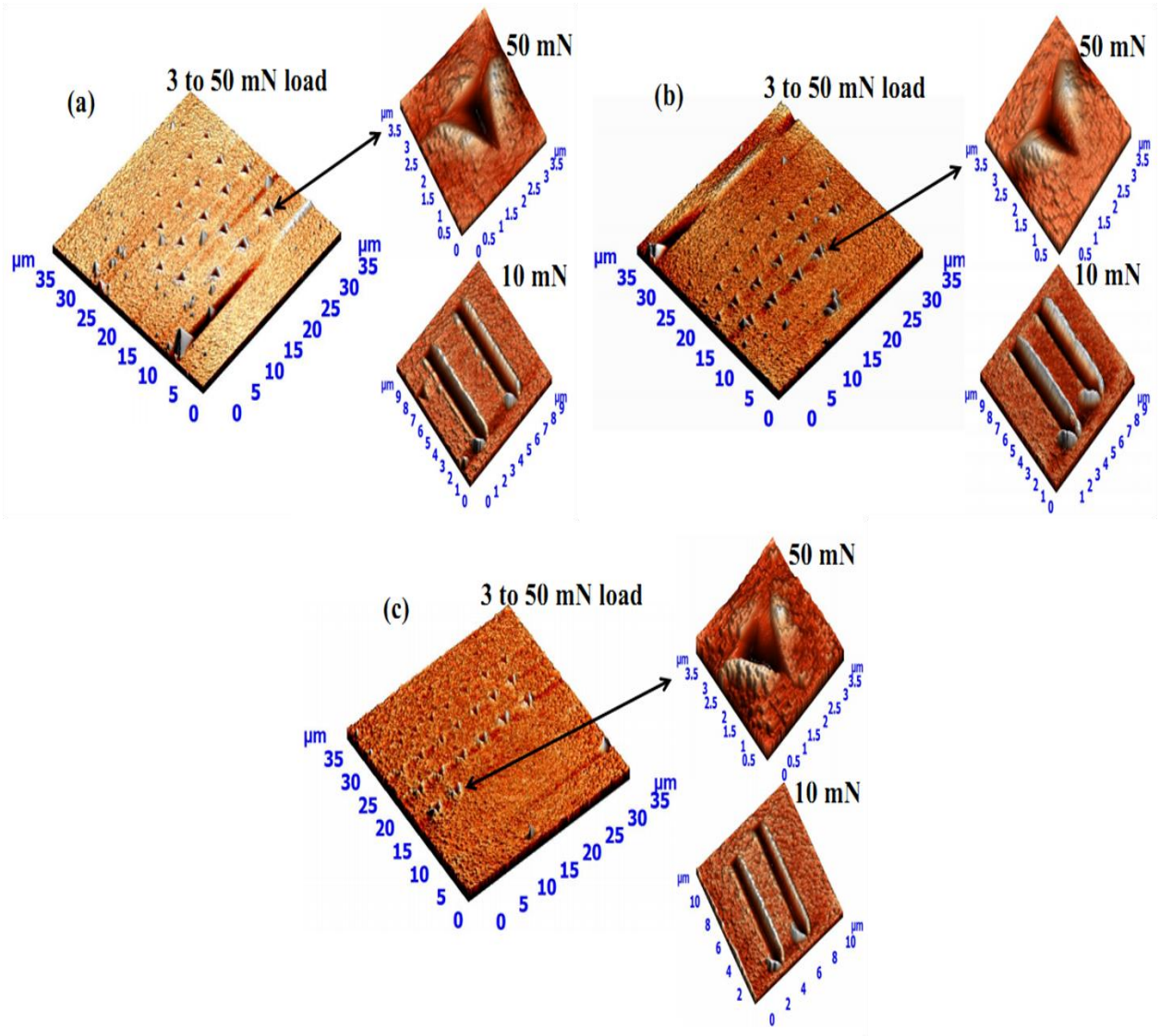

Figure 5.6 *The AFM topographical view of scratch scars and indentation marks on Zr-W-N coatings deposited at varying* V_s

Musil *et al.* (2002) introduced another important parameter H^3/E_r^2 which is not given the direct assessment of toughness but gives an assessment of film resistance to plastic deformation. To estimate the film resistance to plastic deformation, H^3/E_r^2 has been calculated as shown in **table 5.2**. A comparison of H^3/E_r^2 ratio for deposited films shows that films deposited at V_s= -100 V exhibit the highest values (1.8 GPa) of H^3/E_r^2 ratio. In general, those materials that are hard to cut till last have high toughness, further, H^3/E_r^2 of such materials simulates the same assessment as confirms from **table 5.2** (Musil *et al.* 2002). **Figure 5.6a-c**

also reveal that the films neither peeled off nor developed any crack during the scratch test at 10 mN load. This indicates that all the films have high adhesion with the substrate.

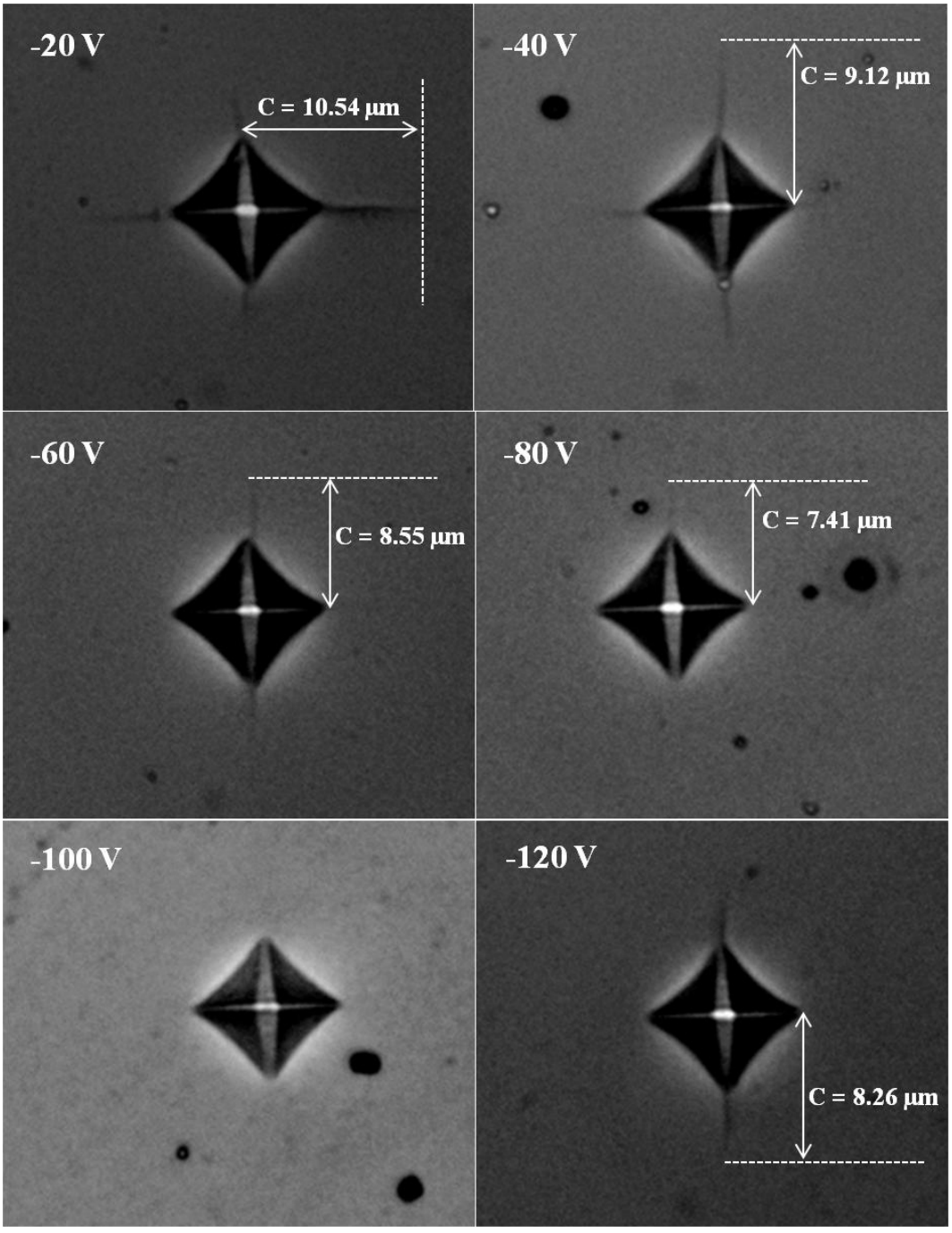

Figure 5.7 *The optical micrographs of diamond indenter impressions created at 1000 mN load into the Zr-W-N films deposited at varying* V_s

Figure 5.7 displays diamond indenter impressions created at 1000 mN load into the Zr-W-N films deposited at -20 V ≤ V_s ≤ -120 V. From **figure 5.7**, it is evident that no radial cracks have been generated into Zr-W-N film deposited at V_s = -100 V under the load of 1000mN, however, radial cracks were generated at 2000mN load. It has been also observed that the value of crack threshold load (L_t) has been increased for -20 V ≤ V_s ≤ -100 V. For example, Zr-W-N films deposited at -40V ≤ V_s were easily fractured at 200mN ≤ L_t ≤ 500mN and the films deposited at V_s = -60 V, -80 V, -120 V were fractured at 500 mN ≤ L_t ≤ 1000 mN. Only the film deposited at V_s = -100 V was fractured at L_t ~ 2000 mN. The higher values of L_t at higher negative bias voltage are attributed to induced compressive stress into the films. The toughness trend as shown in **table 5.2**, indicates that the coating with glassy microstructure (deposited at V_s = -100 V) exhibit maximum toughness (2.25 MPa.$m^{1/2}$). Ion bombardment can densify the microstructure and prevent the formation of voids and large columnar boundaries which are detrimental in terms of microcrack initiation and propagation under load. Another possible contributions to the highest toughness are highest compressive stress (-8 GPa), maximum value of H^3/E_r^2 (1.8 GPa) and highest elastic recovery W_e ~ 84% at V_s = -100 V (Musil 2012, Musil *et al.* 2002). Since cracking is generally initiated by tensile stress, compressive residue stress has to be overcome first.

M. Sakai (1993) suggests that plastic deformation energy (U_p) is also an important parameter of the mechanical properties of wear protective coatings. Plastic deformation energy (U_p) of the film is calculated by the area surrounded by the loading-unloading curve in the load displacement profile. U_p can be calculated by the equation (5.3)

$$U_p = P^{3/2} / [3\, H^{1/2} (w_0 \tan^2\theta)^{1/2}] \quad (5.3)$$

Where 'P' is applied load, 'w_0' is the geometry constant and can be taken as 1.3 for pyramid indenter, H is hardness and θ is the angle (65.3º) between the tip axis and the faces of triangular pyramid. A higher value ($9 * 10^{-10}$ joule) of U_p of film deposited at V_s=20 V over value ($7.4 * 10^{-10}$ joule) of U_p of film deposited at V_s= -100 V reveal that with increasing V_s, Zr-W-N films consume less energy during deformation and show less ductile behavior.

5.5 Conclusions

In conclusion, effect of negative bias voltage on the structural and mechanical properties of nanocrystalline fcc phase Zr-W-N coatings, deposited by reactive DC/RF magnetron sputtering has been reported. The studied films exhibit (i) high wear resistance $H/E_r > 0.1$ (ii) high elastic recovery $W_e > 60\%$ (iii) compressive macrostress ($\sigma < 0$) and (iv) dense, voids-free microstructure. With increasing V_s from -20 to -120 V, coatings morphology evolves from columnar structure to dense glassy structure with decreasing crystallite size. In parallel, the compressive stress increases from -1.7 to -8 GPa. Owing to synergetic contributions of dense structure, preferred orientation, crystallite size and compressive stress, wear resistance increased from 0.21 to 0.23 and fracture toughness improved from 1.4 to 2.25 MPa.$m^{1/2}$. This indicates that the simultaneous increment of wear resistance and toughness is achievable if the negative bias voltage is properly controlled. Therefore, for the deposition of Zr-W-N system done at low substrate temperature (200ºC) and at -100 V bias voltage, pronounced mechanical properties (H ~ 34 GPa, $H/E_r > 0.1$, $W_e > 60\%$, $H^3/E_r^2 > 0.1$, K_{IC} ~ 2.25 MPa.$m^{1/2}$) has been achieved.

CHAPTER 6

Zirconium Tungsten Boron Nitride Coatings

The effect of microstructure on thermal stability and mechanical properties of co-sputtered deposited Zr-W-B-N coatings with varying boron concentration have been studied in detail

6.1 Introduction

A crucial factor of many major industrial sectors, such as material processing, power generation, chemical engineering and aerospace, is an ability to operate in exotic environment. For these applications, nanocomposite coatings can make a huge positive impact. Nanocomposite coatings represent a new generation of materials (Voevodin *et al.* 1999, Zhang *et al.* 2003, Holubar *et al.* 2000). They are composed of at least two separated phases with nanocrystalline (nc) and/or amorphous (a) structure or their combination. The nanocomposite materials, due to very small (≤ 10 nm) grains and a significant role of boundary regions surrounding individual grains, exhibit enhanced or even completely new properties and behave in a strongly different manner compared to the conventional materials composed of larger (≥ 100 nm) grains. Because of their superior mechanical properties (in particular, superhardness and supertoughness) and high chemical inertness, these coatings can significantly lower friction, wear losses and at the same time increase resistance to fatigue and corrosion, which have increasingly become the life-limiting factors for mechanical components in many industrial applications. Such coatings can also provide greater resistance to contact deformation and damage during heavily loaded rolling or rotating contacts (Musil 2005, Veprek 2004) Moreover, the protection of a base material, operated at elevated temperature, from the reaction with ambient oxygen is usually ensured by deposition of a high oxidation resistance nanocomposite coating on the substrate. But, the major challenge in the field of nanocomposite hard metal nitride coating is to obtain their better combination of high thermal stability, wear resistance and fracture toughness. The nanocomposite coating exhibiting mentioned properties can be most suitable surface protection candidate for tribological applications (Veprek and Reiprich 1995, Korotaev *et al.* 2007, Singh *et al.* 2012, Musil 2012, Veprek *et al.* 2005, Musil

et al. 2012) have reported that the nanocomposite coatings (nc-nitride/a-nitride) composed of nanograins dispersed in amorphous matrix and grain boundaries of nanograins about one-monolayer-thin of nonmetallic, covalent nitride such as Si_3N_4 and BN are highly elastic and exhibit enhanced resistance to cracking at high applied load. Moreover, hard nc-nitride/a-nitride nanocomposite coatings prevent to a direct connection between the external atmosphere and the substrate and thereby they should ensure a good protection of the substrate against oxidation even at temperatures when the amorphous phase starts to nanocrystalline. For further increase the thermal stability of nanocomposite coatings the amorphous phase should have the higher (> 1000ºC) crystallization temperature. Experimental studies indicate that the selection of elements and the control of the amount of individual phases are very efficient ways to optimize the physical and functional properties of the nc-nitride/a-nitride nanocomposite coatings.

Recently role of boron in enhancing mechanical performance and thermal stability of nanocomposite coatings has been also demonstrated. Boron nitride (BN) thin films are of interest because of their excellent physical, chemical and mechanical properties (Shtansky *et al.* 2000, Liu *et al.* 2012, Eichler and Lesniak 2008). Due to high crystallization temperature of boron nitride (≥ 800ºC) exhibited high oxidation resistance. Boride-based multicomponent nanocomposite coatings (Mitterer and Mayrhofer 2004) can dramatically increase hardness and thermal stability and hence reduce wear under harsh sliding or machining conditions. There are many papers reporting on boron based nanocomposite coatings, e.g. W-B-N (Louro *et al.* 2005, Reid *et al.* 1995, Mayrhofer *et al.* 2006, Karuna *et al.* 2014, Mitterer *et al.* 1991, Urgen *et al.* 1995, Mallia *et al.* 2013, Herra and Broszeit 1997) etc. These coatings show high thermal stability, high hardness, and high oxidation resistance. It has been also noticed that by varying the boron concentration in the film, the physical and chemical properties of these nanocomposite can be tuned as per application requirement.

Mayrhofer and Stoiber (2007) have reported that Ti–B–N coatings with B contents < 18 at.% exhbit a crystalline NaCl structure phase with a strong dependence of their lattice parameter on the B content. As a result of annealing (up to 900°C), the metastable cubic phase decomposes to precipitate TiB_2, which influence dislocation mobility and hence the hardness increases to ∼43 GPa. The Ti-B-N coatings with B contents above∼18 at.% results in the

formation of nm sized TiN and TiB_2 crystallites embedded in a high volume fraction of disordered boundary layer.

Lin *et al.* (2010) studied the mechanical and tribological properties of TiBCN nanocomposite coatings, deposited using TiBC compound target with various Ar/N_2 mixtures in a closed field unbalanced pulsed magnetron sputtering system. It has been observed that the coatings with a nitrogen content of less than 8% exhibit superhardness values in the range of 44–49 GPa but show poor adhesion and low wear resistance. However, improvements in these properties together with reduced coating hardness to 35–45 GPa have been achieved when the 'N' content in the coatings was increased.

Louro *et al.* (2005) have reported that boron concentration in to the W-B-N films highly affect the phase composition, grain size and lattice parameter of the deposited films. The amorphous structure of as deposited W-B-N films becomes crystalline with the formation of the bcc W and/or the fcc-W_2N phases during annealing at 850º and 950ºC. The maximum hardness (~ 36 GPa) has been obtained for the film having B concentration ~ 17 at.%.

Mitterer *et al.* (1991) have studies the mechanical properties of Zr-B-N system. It has been observed that the increase nitrogen concentration in the film causes grain refinement and subsequently in amorphous coatings. The harness of Zr-B-N coatings increases with increasing substrate temperature and negative bias voltage to the substrate.

Nanocomposite Zr-W-B-N thin films deposited on Si (100) substrate require a detailed investigation as a function of varying deposition parameters to substantiate the influence of microstructures on its mechanical properties. In order to ensure compatibility and stability of the sputter deposited Zr-W-B-N thin films in tribological applications, the present work has been focused to investigate the DC/RF magnetron sputtered nanocomposite Zr-W-B-N thin films with varying B content. The films were characterized by XRD, FE-SEM, AFM and TEM to reveal the influence of processing parameters on microstructural characteristics. The atomic percentages of B, N, Zr, W and O in the Zr-W-B-N thin films were measured using Wavelength Dispersive Spectroscopy (WDS) attached with EPMA. The mechanical response of Zr-W-B-N films was measured by nano and micro indentation techniques.

6.2 Experimental Details

6.2.1. Deposition of Zr-W-B-N thin films

Zr-W-B-N coatings have been deposited on mirror polished Si (100) (~0.067 cm thick) (**figure 6.1 a**) substrates at 200°C substrate temperature and -100 V negative bias voltage by DC/RF unbalanced magnetron co-sputtering from Zr target (5 cm in diameter, 0.5 cm thick, 99. 98% purity), W target (5 cm in diameter, 0.5 cm thick, 99. 95% purity) and B target (5 cm in diameter, 0.5 cm thick, 99. 9% purity) in Ar (8 sccm) and N_2 (32 sccm) discharge. An arrangement of magnetic guns for the deposition of Zr-W-B-N films is shown in **figure 6.1b**.

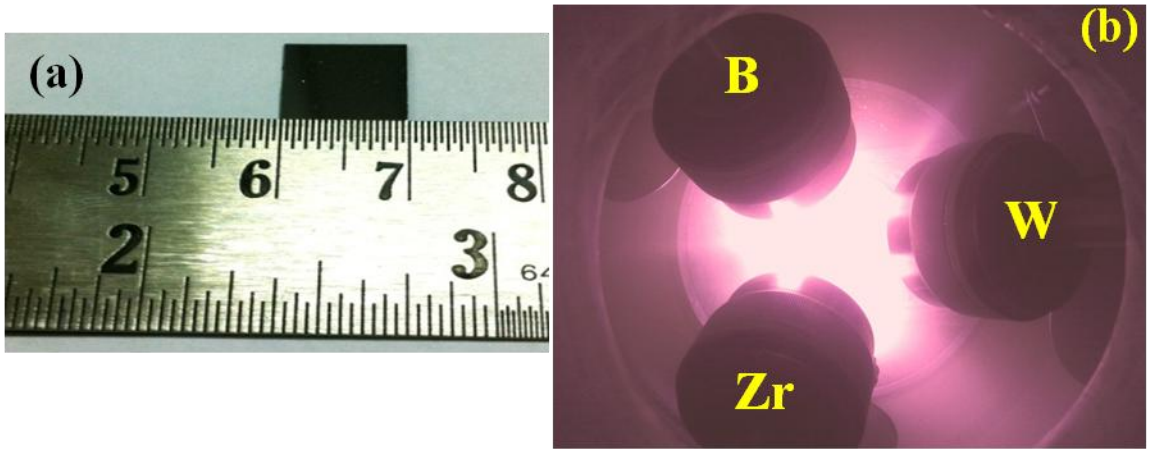

Figure 6.1*(a) Image of Si (1 × 1 cm^2) substrate and (b) an arrangement of magnetic guns for the deposition of Zr-W-B-N films*

Prior to deposition all substrates were ultrasonically cleaned in acetone. Targets were fixed at an angle of 45º to the substrate normal. Si substrates were mounted on the substrate holder held at negative potential with the help of silver paste. The substrate holder was rotated at 5 rpm by using a DC motor to ensure uniformity in the deposited thin films. The residual pressure was < 0.5×10^{-3} Pa. The N_2 partial pressure and working pressure were 0.13 Pa and 0.67 Pa respectively. The sputtering power density of the Zr target and W target was kept at 6 watt/cm^2 and 4 watt/cm^2, respectively. The power density of the B target was varied from 0.1 to 7.5 watt/cm^2 to vary the boron concentration (1.4 to 21.6 at %) in Zr-W-B-N films. All the depositions were carried out at fixed target to substrate distance of 6 cm for 2 h. The post annealing of the film with ~7.5 at.% boron content has been carried out in vacuum and air up to 900ºC (T_v) and 900ºC (T_a) respectively for 1 h.

6.2.2 Characterization

The crystallographic structure of the films were characterized using x-ray diffraction (XRD) (Bruker, D8 advance, Cu-K_α radiation, λ =1.54 Å, step=0.02º, scan speed=2 sec/step) and transmission electron microscopy (TEM) (200 kV, FEI, TECNAI G^2). The surface and cross-section of the coatings were observed by field emission scanning electron microscopy (FE-SEM) (FEI, QUANTA 200F). Atomic force microscopy (AFM) (NT-MDT, NTEGRA) was used in semi-contact mode to evaluate the coating topography and root-mean-square (RMS) roughness. The elemental composition analysis of Zr-W-B-N films was carried out using wavelength dispersive x-ray analysis attached with electron probe micro analyzer (EPMA) (Cameca, SX-100 model). The hardness (H), effective elastic modulus (E_r) and elastic recovery (W_e) of these coatings were measured by a nano-indentation (NT-MDT, Nanoslerometry) using a Berkovich diamond indenter with normal angle of 65.3º between tip axis and faces of triangular pyramid. The effective size of apex is about 70 nm. The H, E_r and W_e of coatings, calculated by the loading-unloading curve in the load-displacement profile, have been measured at 10 mN load to assure the penetration depth should not more than the 10% of total thickness of coatings to minimize the substrate effect. The films were scratched with 2 to 35 mN loads at constant loading velocity (20 nm/s) and scratch velocity (500 nm/s) for adhesion test purpose. The toughness was evaluated using micro indentation with a Vickers micro hardness tester (UHL VMHT). The micro indentations were done at varying loads (100 mN to 5000 mN). For each load, at least three readings were taken. The toughness K_{IC} was calculated by **equation (6.1)** (Lawn *et al.* 1980).

$$K_{IC} = \delta (E_r/H)^{1/2} (P/C^{3/2}) \qquad (6.1)$$

Where P is the applied indentation load; E_r and H are the effective elastic modulus and hardness of the coating, respectively. δ is an empirical constant which depends on the geometry of the indenter, for Vickers indenter δ= 0.016. C is the crack length which was measured from optical microscopy (Olympus DME3) images. In order to reduce the substrate effect on film toughness, K_{IC} calculated from **equation (6.1)** was plotted versus indentation depth and then the curve was extrapolated to one-tenth of the film thickness to obtain the film toughness.

6.3 Results and Discussion

6.3.1. Effect of boron contents on film microstructure and mechanical properties

6.3.1.1 Structural and morphological analysis

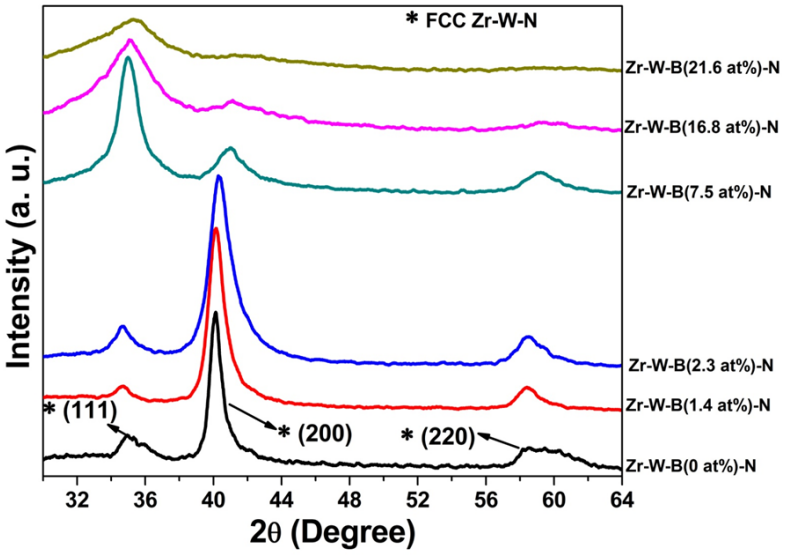

Figure 6.2 *XRD patterns of Zr-W-B-N nanocomposite films with different B contents*

The XRD patterns of Zr-W-B-N nanocomposite films deposited at varying B contents on Si substrates are shown in **figure 6.2**. The X-rd patterns revel that Zr-W-B-N contains a single nanocrystalline phase (NaCl structure) except the change in preferred crystallographic orientations with increasing B content (≤ 16.8 at.%) in the films. For B = 21.6 at.%, film exhibited XRD amorphous structure. Zr-W-B-N films with B content ≤ 2.3 at.%, exhibited (200) preferred crystallographic orientation of grains and for B content above 2.3 at.%, the intensity of (111) peak grows up. However, no signals corresponding to crystalline BN and various phases of zirconium boride, tungsten boride could be observed. It shows that B might be present either in solid solution form in the films or in an amorphous phase of BN, which are in agreement with previous reports on Zr-B-N and W-B-N nanocomposite films prepared by magnetron sputtering (Mitterer *et al.* 1991, Louro *et al.* 2005). With increase in B content in Zr-W-B-N films, the broadening of XRD peaks increases and was significant at B ≥ 7.5 at.%. The increase in broadening indicates that the Zr-W-B-N crystals size decreased with increasing B

content and coatings becomes XRD amorphous at B = 21.6 at.%. The average crystallite size of Zr-W-B-N film as a function of B concentration is shown in **figure 6.3a.** The crystallite size calculated from the XRD peak broadening, decreases with increasing B content. The crystallite size of the films reduced from ~ 9 nm for 0 at.% B to ~ 2 nm for 16.8 at.% B content. This indicates that Zr-W-B-N crystals become finer with the incorporation of the amorphous BN phase. The grain growth of Zr-W-B-N crystals is inhibited due to the presence of second phase particles causing Zener drag effect, which result in reduction of size of Zr-W-B-N crystals (Nes *et al.* 1985).

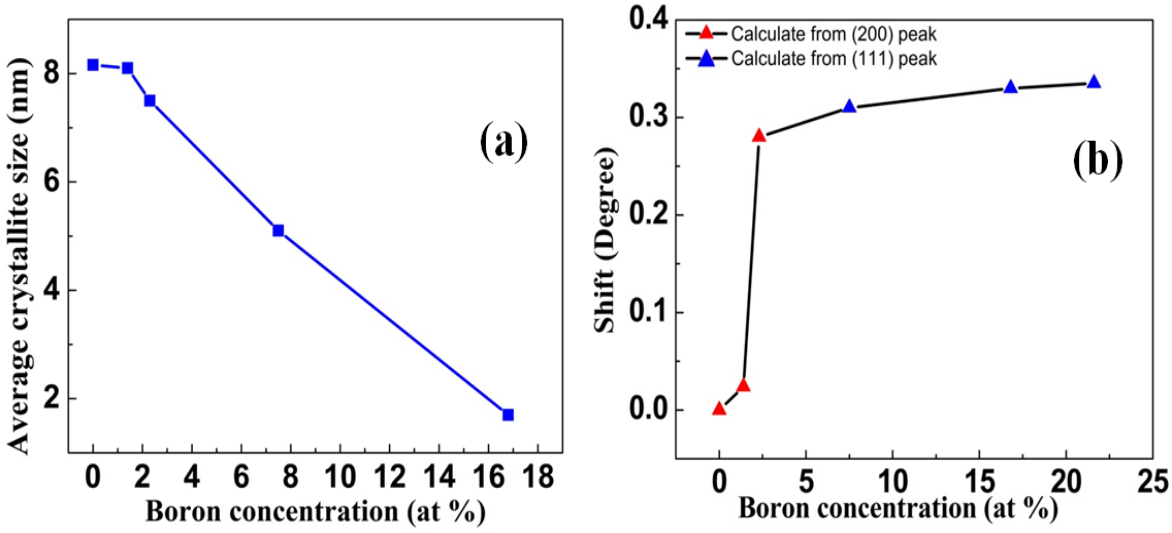

Figure 6.3 *(a) The average crystallite size of Zr-W-B-N film as a function of B concentration and (b) a shift in XRD peaks positions with increasing B concentration*

Figure 6.3b shows a shift in XRD peaks positions with increasing B concentration in the films. A significant shift of diffraction peak (200, preferred orientation) of the Zr-W-B-N coatings toward higher diffraction angles was observed as the B at.% was increased upto 2.3 at %, indicating a decrease in the coating lattice parameter. There are two effects could be considered in this case: (i) lattice contraction due to the formation of a substitution solid solution by replacing Zr or W atoms with smaller sized B atoms in the Zr-W-N lattice; (ii) lattice expansion due to the formation of an interstitial solid solution by incorporating B atoms

into the lattice interstitial sites (Mayrhofer and Stoiber 2007). It is evident that more B atoms go to the lattice sites than to the interstitial ones, which leads to an overall lattice contraction in the Zr-W-B-N coating with B content of 2.3 at.%. The lattice parameter a_0 decreases from 4.50110 Å for 0 at.% B to 4.46952 Å for 2.3 at % B. However, the shift (100, preferred orientation) is not significant above 2.3 at.% B content, which indicates that B starts to segregate in grain boundaries during deposition and form the amorphous phase BN in boundaries.

To further confirm the XRD findings and the presence of any secondary (nanocrystalline) phases at higher (16.8 at.%) B concentration, TEM analysis has been carried out. **Figure 6.4** shows the TEM bright field images and corresponding selected area electron diffraction patterns (SAED) of Zr-W-B-N coatings with 0 at.%, 2.3 at.%, 7.5 at.% and 16.8 at.% boron content. It can be seen clearly from the SAED patterns that any secondary phases of zirconium boride and tungsten borides compounds have not grown in Zr-W-B(2.3 to 16.8 at.%)-N films during deposition. Only fcc phase of Zr-W-B-N with (111), (200) and (220) reflections has been identified. Moreover the higher intensity of (111) diffraction ring for B = 7.5 at.% in comparison to B = 2.3 at.% content film confirms the higher grain growth in (111) orientation in respect of (200) as observed for films with B ≤ 2.3 at.% content (**figure 6.2**). The intensity of individual diffraction rings correspond to (111), (200) and (220) which is gradually non-uniform (non continuous rings) for B = 2.3 at %, uniform for B = 7.5 at.% and diffuse for B = 16.8 at.%, indicating reduction in grain size of Zr-W-B-N with increasing B content. The diffused ring pattern, bright field image and inset image of the film with B content ~ 16.8 at.% reveal that the microstructure of the coatings was changed due to the increased fraction of the amorphous BN phase. The inset of **figure 6.4** is indicate that the amorphous phase formed individual grains of size > 1nm, rather than as a thin intergranular amorphous layer of uniform thickness.

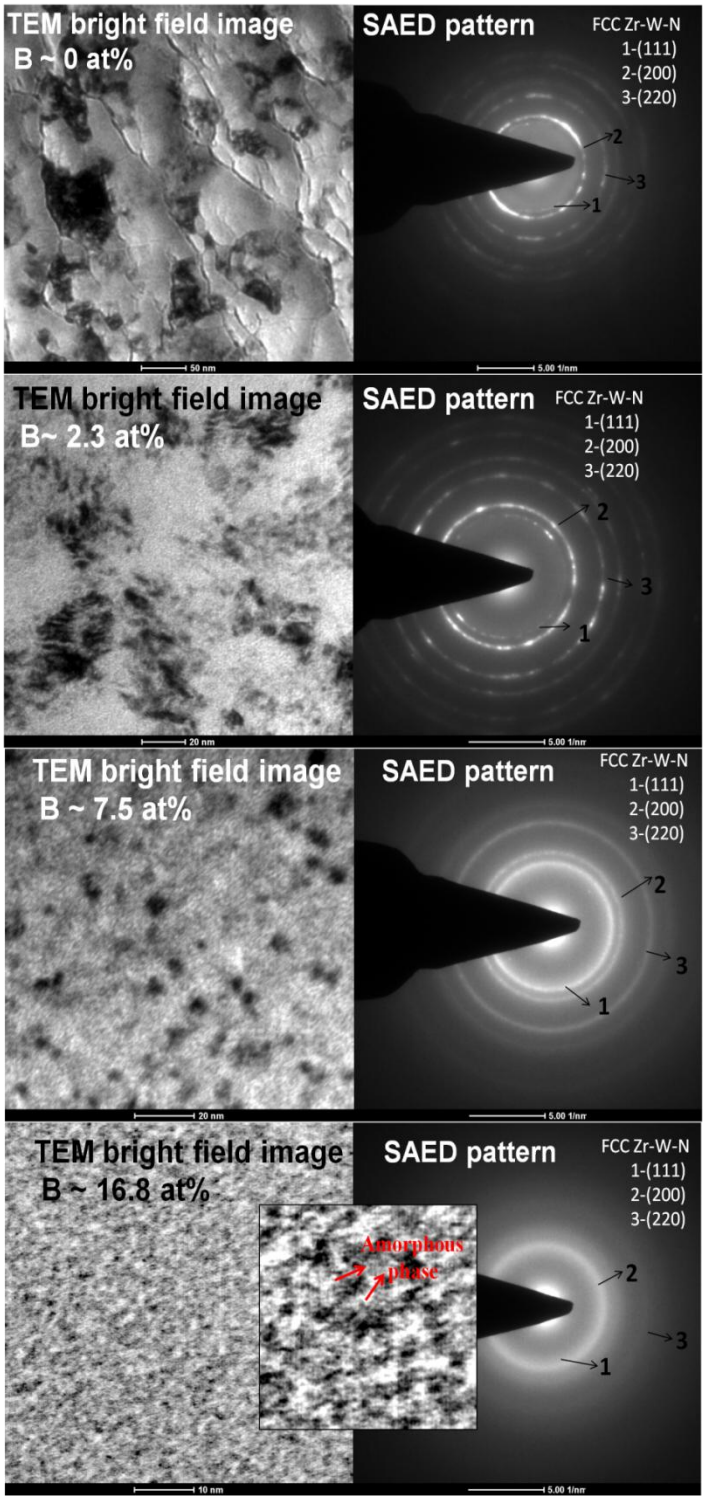

Figure 6.4 *TEM bright field images and corresponding selected area electron diffraction patterns (SAED) of Zr-W-B-N coatings with 0 at.%, 2.3 at.%, 7.5 at.% and 16.8 at.% boron contents*

Based on the results from XRD and TEM analyses, it is clear that the B addition into Zr-W-B-N films resulted in crystal size refinement and the Zr-W-B-N films had a fine composite microstructure consisting of nano-sized Zr-W-B-N crystallites surrounded by amorphous phase of BN. The formation of the nanocomposite in the Zr-W-B-N films might be related to the spinodal phase segregation due to immiscibility between crystal Zr-W-B-N and amorphous phase (BN).

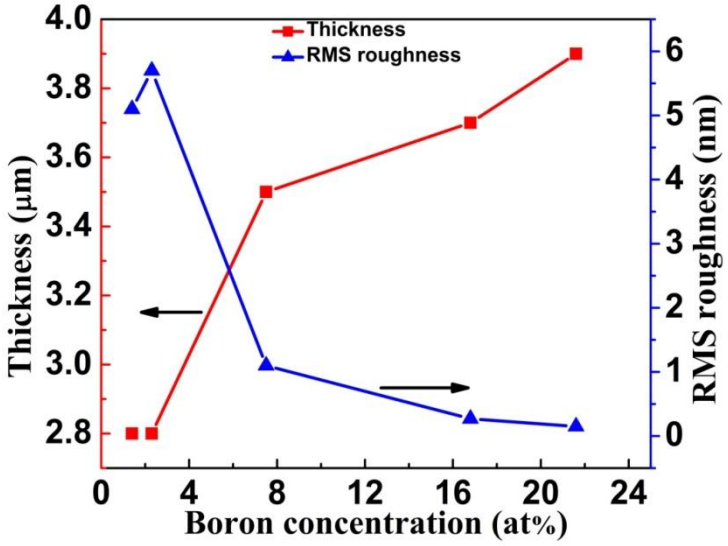

Figure 6.5 *The variation of thickness and route mean square (RMS) roughness of Zr-W-B-N coatings as a function of boron concentration*

Figure 6.5 shows the variation of thickness and route mean square (RMS) roughness of Zr-W-B-N coatings with increasing boron concentration in the films. The thickness was unaffected (~ 2.8 μm) up to B ≤ 2.3 at.% and increase for B ≥ 7.5 at.% (the horizontal lines distinguished in the films due to thermal drift effect). The maximum thickness (~ 4 μm) was obtained for Zr-W-B (21.6 at.%)-N film. **Figure 6.6a-c** show the FESEM micrographs of the cross-sections of the Zr-W-B-N films with 2.3 at.%, 7.5 at.% and 16.8 at % B contents, respectively. It is seen clearly that the morphology evolves from fine columnar structure (B = 2.3 at.%) to dense glassy structure (B = 16.8 at.%) with increasing B concentration in the films. The RMS roughness decreases with increasing B content in the films and lowest roughness (0.3 nm) was obtained for Zr-W-B(21.6 at.%)-N film. **Figure 6.6d-f** shows the 3D AFM images of the Zr-W-B-N films with increasing (2.3, 7.5 and 16.8 at.%) B contents, respectively. It is

evident from these images that with increasing B contents, grain size and surface roughness decreases, which could be explained from the XRD results.

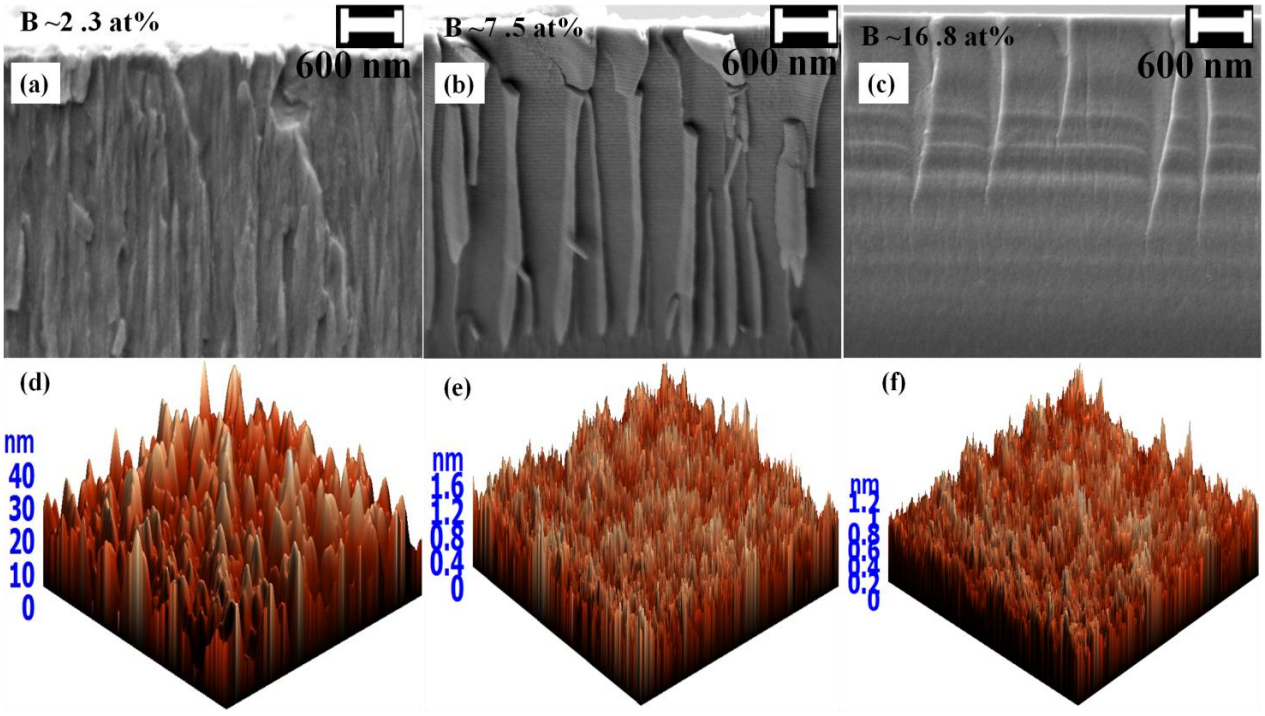

Figure 6.6 *(a)-(c) FESEM micrographs of the cross-sections of the Zr-W-B-N films with 2.3 at.%, 7.5 at.% and 16.8 at % B contents respectively and (d)-(f) 3D AFM images of the Zr-W-B-N films with increasing (2.3, 7.5 and16.8 at.%) B contents, respectively*

6.3.1.2 Mechanical response

Table 6.1 represents the mechanical response of Zr-W-B-N coatings as a function of B concentration. It has been observed that mechanical properties of deposited coatings are highly correlated to their microstructure. Hardness (H) and effective elastic modulus (E_r) of Zr-W-B-N coatings varied non-monotonically with increasing B content in the films. It is observed that the H and E_r values increases with increasing B content and the film with 7.5 at.% B content shows a maximum H and E_r values of 37.4 GPa and 153 GPa, respectively. However, these values drop when the B content was increased beyond 7.5 at.%. Initially, the solid solution hardening effect, as summarized in the results of XRD and TEM, contributed to the increase in the hardness of the Zr-W-B($\leq$ 2.3 at.%)-N coatings. A possible phenomenological explanation to

the observed maximum hardness at 7.5 at.% B content can be deduced from results of structural analyses and their comparison with existing concepts on nanocomposite mechanisms (Veprek and Reiprich 1995). The formation of superhard nanocomposites requires 3-10 nm crystallite sizes with less than 1 nm thick separation in an amorphous matrix (Karvankova *et al.* 2003, Voevodin *et al.* 2004). At these conditions, both dislocation formation and in coherence stress relaxation is suppressed, providing hardness > 40 GPa. However in Zr-W-B(7.5 at.%)-N coating, the separation (> 1nm) between crystallites limit the hardness < 40 GPa. Nevertheless, with further increase of the B contents, H and E_r of Zr-W-B-N films are decreased even though the crystallite size was further decreased. The decrease in the hardness of the coatings appears to be affected by the increased volume fraction of amorphous BN phase in the coatings. The coatings gradually lost the interface strengthening effects as the distance between the nanocrystallites increased. Thus the observed trend in the hardness is governed by a two-phase structure consisting of nanocrystalline Zr-W-B-N and amorphous BN coexists and by a Hall-Petch relation derived from crystal size refinement (Hertzberg 1989, Hall 1951).

Table 6.1 *Represents the mechanical response of Zr-W-B-N coatings as a function of B concentration*

B concentration	*Hardness*	*Elastic modulus*	*% Elastic recovery*	*Plasticity index parameter*	*Resisitance to plastic deformation*	*Fracture toughness*
(at%)	*H(GPa)*	*E_r(GPa)*	*W_e*	*H/E_r*	*H^3/E_r^2(GPa)*	*(K_{IC}) (MPa.$m^{1/2}$)*
1.4	29.3	129	73	0.22	1.5	2.17
2.3	31.6	135	76	0.23	1.7	2.32
7.5	37.4	153	81	0.24	2.2	2.90
16.8	26.7	141	78	0.19	0.95	2.07
21.6	19.8	131	74	0.15	0.42	1.87

The elastic recovery (W_e) gives information about the elastic and elastic-plastic behavior of the films. Wear resistive coatings having high (> 60 %) value of W_e exhibit a higher elasticity. Maximum (81%) value of W_e obtained for Zr-W-B(7.5 at.%)-N coating shows that this film exhibit high elasticity in comparison to other deposited films. Recently, the ratio

of hardness (H) to effective elastic modulus (E_r), H/E_r (plasticity index parameter) has been proposed as a key parameter to indirectly estimate the wear resistance of the hard and tribological coatings (Leyland and Matthews 2000). Musil (2012) reported that the Al–Cu–O nanocomposite films with $H/E_r > 0.1$, which is a critical value to show an enhanced resistance of coating to cracking, had highly elastic recovery without any cracks after diamond indenter load test. However, the films with $H/E_r \leq 0.1$ exhibited relatively low elastic recovery with many cracks on the corner of the indenters. Hence, the plasticity index (H/E_r) parameter is a valuable measure of determining the elastic strain to failure in a surface contact. The wear resistance of Zr-W-B-N coatings increases with increasing B content up to 7.5 at.% and then decrease for B > 7.5 at.%. A maximum value (0.24) of H/E_r is obtained for Zr-W-B(7.5 at.%)-N film.

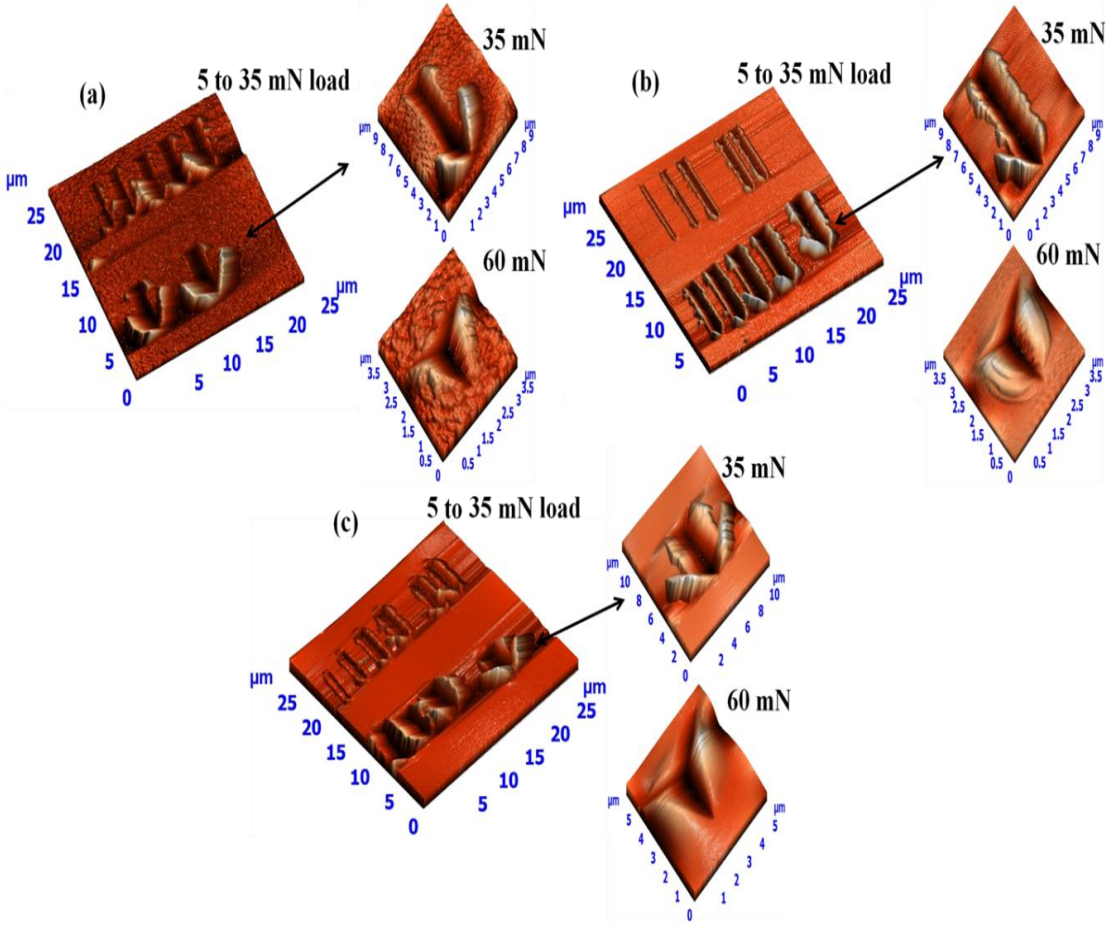

Figure 6.7 *(a-c) The AFM topographical view of scratch scars and indentation marks on the films of B = 2.3 at.%, 7.5 at.% and 16.8 at.% contents, respectively*

Figure 6.7a-c show the AFM topographical view of scratch scars and indentation marks on the films of B = 2.3 at.%, 7.5 at.% and 16.8 at.% contents, respectively. The scratch scars at 5 to 35 mN loads and indent at 60 mN load have been made on the films for adhesion and fracture toughness measurements, respectively. The higher value of H/E_r index is a strong indication of the coating resistance to wear, but such coatings do not always show improvement of elastic deformation and fracture toughness. Enlarged views of indents at 60mN loads reveal that no crack propagates on the surface of the films and consequently, toughness cannot be calculated quantitatively by nano indentations; however, micro indentations by vicker hardness tester have been done at varying loads (200 mN to 5000 mN) to calculate the fracture toughness of coatings.

Another important parameter H^3/E_r^2 which is not given the direct assessment of toughness but gives an assessment of film resistance to plastic deformation has been calculated for deposited films. To estimate the film, H^3/E_r^2 has been calculated as shown in **table 6.1**. A comparison of H^3/E_r^2 ratio for deposited films shows that the Zr-W-B(7.5 at.%)-N film exhibit the highest values (2.2 GPa) of H^3/E_r^2 ratio. **Figure 6.7a-c** also reveal that the films neither peeled off nor developed any crack during the scratch test upto 35mN load. This indicates that all the films have high adhesion with the substrate. **Figure 6.8a-d** displays diamond indenter impressions created at 5000 mN load into the Zr-W-B-N films with B = 2.3 at.%, 7.5 at.%, 16.8 at.% and 21.6 at.% contents, respectively. From **figure 6.8**, it is evident that radial crack length increases with increasing B content in the films. Moreover, Zr-W-B(21.6 at.%)-N shows the adhesive failure at 5000 mn load. No radial cracks have been generated into Zr-W-B-N films under the load of 1000 mN; however, radial cracks were generated at 2000 mN load.

The toughness trend as shown in **table 6.1**, indicates that the coating with 7.5 at.% B content exhibit maximum toughness (2.9 $MPa.m^{1/2}$) and the toughness was decreases with increasing B content above 7.5 at.% in the films. The increase in toughness ($\leq$ 7.5 at.%) is attributed to changed microstructure of coating at B = 7.5 at.%; segregation of boron in the grain boundaries and the formed amorphous BN phase, which has high resistance to formation of cracks under stress, and in the mean time, high energy absorbance to deter crack propagation, whereby preventing chipping, flaking or catastrophic failure as observed for Zr-W-B(21.6 at.%)-N film at 5000 mN load (**figure 6.8d**). The formation of amorphous phase of individual grains of size > 1nm, rather than as a thin intergranular amorphous layer of uniform

thickness lower the fracture toughness of Zr-W-B-N coatings with increasing B content > 7.5 at.%.

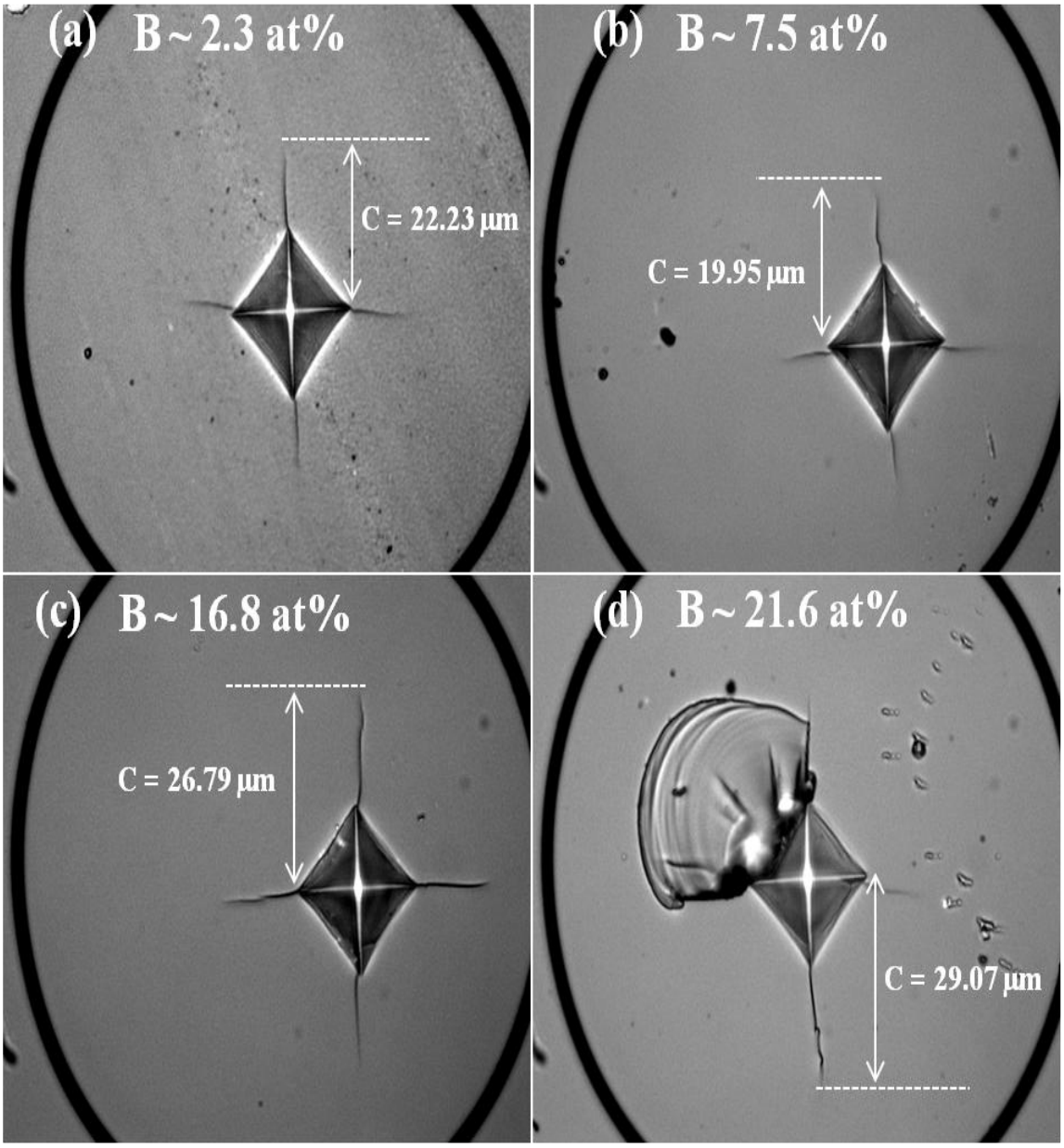

Figure 6.8 *(a-d) Optical micrograph of diamond indenter impressions created at 5000 mN load into the Zr-W-B-N films with B = 2.3 at.%, 7.5 at.%, 16.8 at.% and 21.6 at.% contents, respectively*

6.3.2 Effect of post annealing temperatures on film structure and mechanical properties

6.3.2.1 Structural and morphological analysis

Due to the superior mechanical performance of Zr-W-B(7.5 at.%)-N film over other deposited films of varying B content, post annealing of the films with 7.5 at.% B content has been carried out at different annealing temperatures (300º-900ºC) in vacuum (T_v) and in air (T_n).

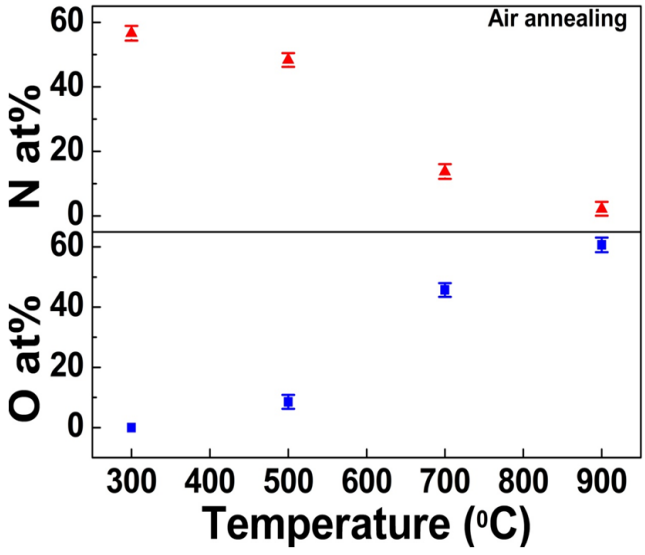

Figure 6.9 *The WDS analysis (N, O atomic fraction) of the Zr-W-B(7.5 at.%)-N films annealed in air at different T_n*

The WDS analysis (N, O atomic fraction) of the Zr-W-B(7.5 at.%)-N films annealed in air at 300ºC ≤ T_n ≤ 900ºC is shown in **figure 6.9**. It has been observed that the oxygen starts to be incorporated in the films at T_n = 500ºC and its content increases substantially with increasing T_n. The maximum O content (~ 61 at.%) is found for the film annealed at T_n = 900ºC. On the other hand, the N atomic concentration starts to decrease continuously above T_n = 300ºC and reaches ~ 2 at.% in the film annealed at T_n = 900ºC. The film got completely peeled off at T_n =

900ºC. This may be associated with diffusion of some of the O atoms toward interface through grain boundaries with increasing T_n (Abadias *et al.* 2013).

Figure 6.10 shows the FESEM topographical images of as deposited and air annealed (700ºC and 900ºC) Zr-W-B(7.5 at.%)-N films. It is clearly seen that the morphology of Zr-W-B(7.5 at.%)-N has changed substantially during annealing. The surface morphology was changed from smooth to quailflower at T_n = 700ºC and then porous at T_n = 900ºC. Moreover, the visibility of film have changed from metallic (as deposited) to yellowish at T_n = 900ºC.

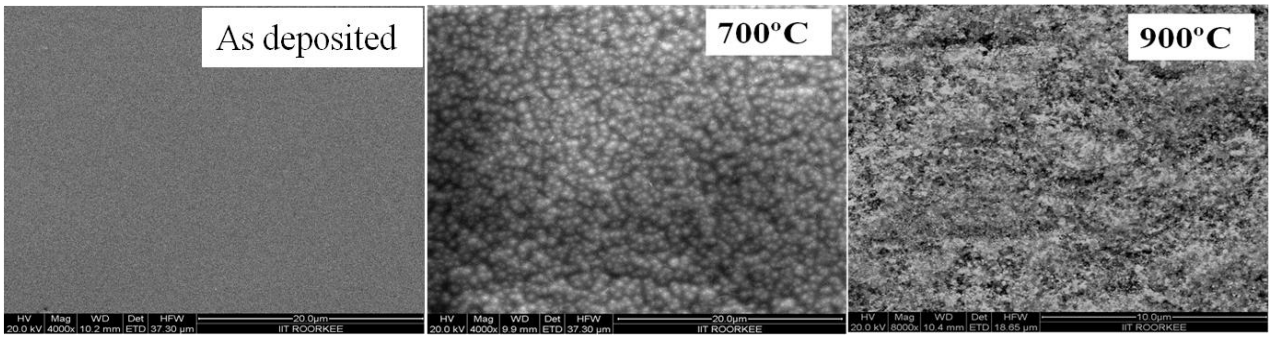

Figure 6.10 *The FESEM topographical images of as deposited and air annealed (700ºC and 900ºC) Zr-W-B(7.5 at.%)-N films*

Figure 6.11a-b show the XRD patterns of Zr-W-B(7.5 at.%)-N films annealed at 300º, 500º, 700º and 900ºC for 1 h in vacuum and in air, respectively. **Figure 6.11a** shows that the film retains the fcc structure up to 900ºC without forming any other boron-based crystalline phase like ZrB_2, and W_2B etc. The peak broadening and peak intensity lowering are the detectable changes in the XRD peaks of Zr-W-B(7.5 at.%)-N film with the increases in T_v. Maximum peak broadening observed at T_v = 900ºC. The broadening of peaks might be due to decomposition induced effects occurred in the film during annealing and further annealing above may decompose the single fcc phase Zr-W-B-N film in its stable phases (Mayrhofer *et al.* 2003).

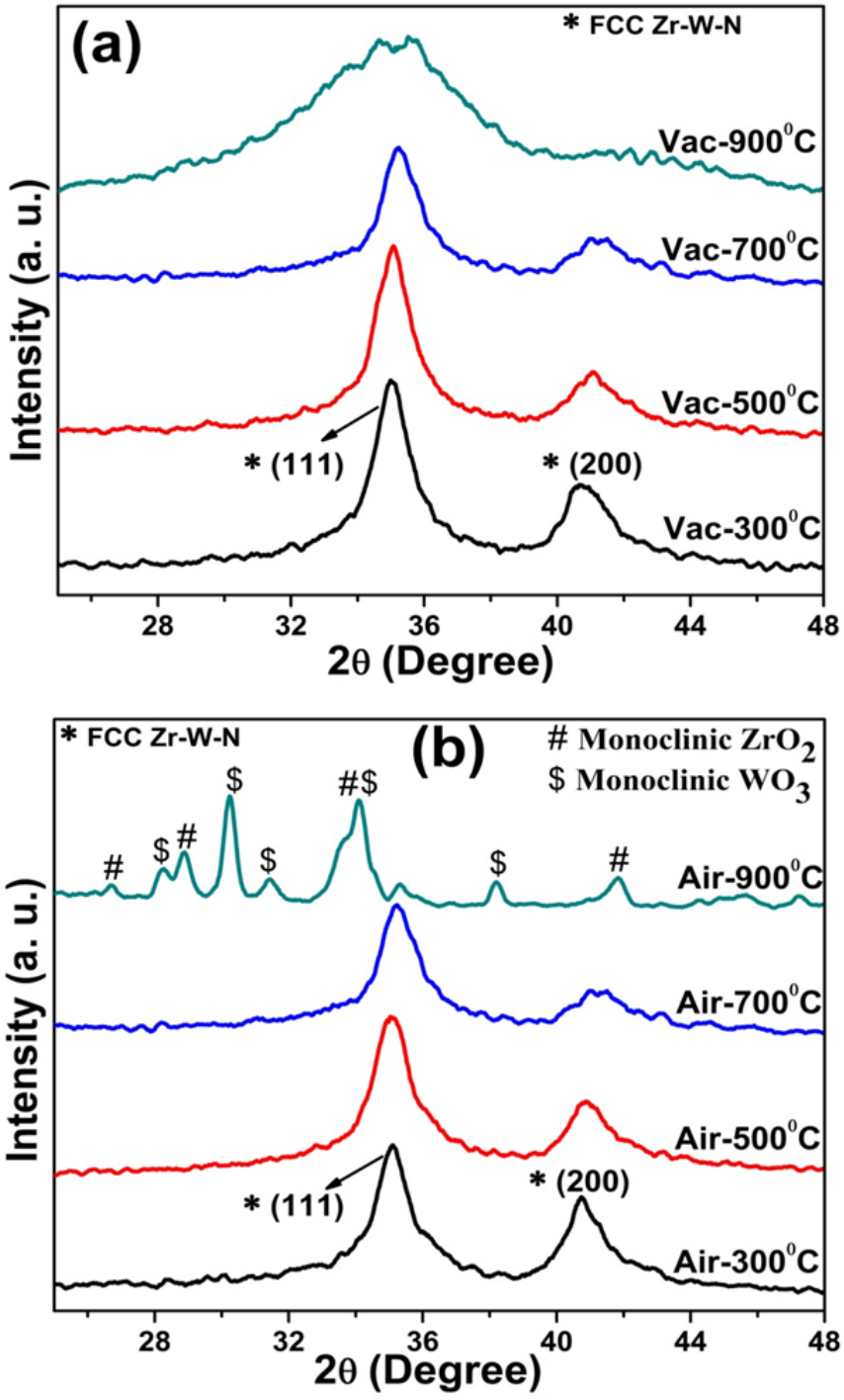

Figure 6.11 *(a-b) XRD patterns of Zr-W-B(7.5 at.%)-N films annealed at 300ºC, 500ºC, 700ºC and 900ºC for 1 h in vacuum and in air, respectively*

Figure 6.11b reveals that the film retains the fcc structure during air annealing at $T_n \leq$ 700ºC and no traces of crystalline oxides of zirconium, tungsten and boron were detected. However, at T_n = 900ºC, full degradation of the Zr-W-B(7.5 at.%)-N film was observed and film was degraded in crystalline monoclinic ZrO_2 and WO_3 phases during annealing. Moreover Zr-W-B(7.5 at.%)-N film was peel off at 900ºC air annealing temperature.

6.3.2.2 Mechanical properties

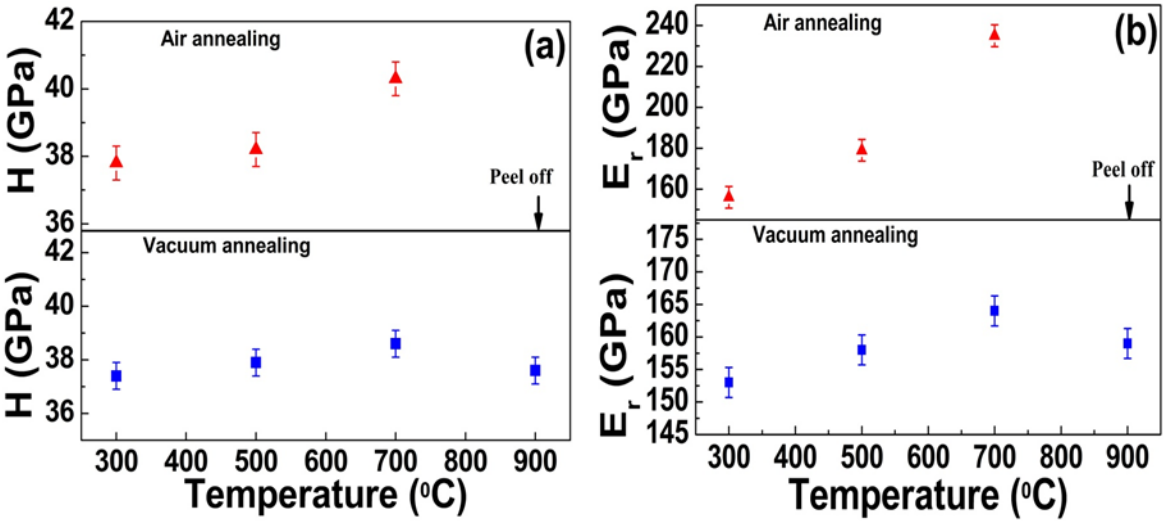

Figure 6.12*(a) The change in hardness and (b) elastic modulus values of Zr-W-B(7.5 at.%)-N films annealed in air and vacuum up to 900ºC, respectively*

Figure 6.12a and **6.12b** show the change in hardness and elastic modulus values of air and vacuum annealed Zr-W-B(7.5 at.%)-N films as a function of annealing temperatures. Both the hardness (H) and elastic modulus (E_r) of Zr-W-B(7.5 at.%)-N film were gradually affected in vacuum annealing. This is because of microstructure was not significantly changed during vacuum annealing. On the other hand, a continuous increase in H and E_r values was observed in air annealing upto 700ºC. The delaminating of the films at T_n = 900ºC restricted the nanoindentation studies at this temperature. As the air annealing temperature was raised, the hardness increased from ~ 37 GPa to 40 GPa reaching maximum values at 700ºC. Annealing

above the 300ºC initiated the nucleation of oxides phases (ZrO_2 and WO_3) and their volume fraction increased as the oxygen concentration increases (**figure 6.9**), which influence dislocation mobility and hence the hardness increased to high level of ~ 43 GPa at T_n = 900ºC.

6.4 Conclusions

Zr-W-B-N coatings were deposited on Si substrates by DC/RF reactive magnetron sputtering technique. The B content in the coatings was varied by varying the power density (0.1 to 7.5 watt/cm^2) to the B target. The influence of the B content on the microstructure and hence on mechanical properties of the Zr-W-B-N coatings was investigated. Post annealing of the Zr-W-B(7.5 at.%)-N film has been carried out in vacuum and air up to 900ºC to comment on its thermal stability. The main results were summarized as follow:

(1) The XRD, FESEM and TEM results indicated that as the B content increased from 0 to 7.5 at.%, the coatings transformed from a columnar structure to nanocomposite structure with a nano-sized (2-5 nm) Zr-W-B-N crystallites embedded in amorphous BN matrix. With further increase of B content, the crystalline Zr-W-B-N films gradually transformed into amorphous-like structure. The Zr-W-B-N films with B contents ≤ 2.3 at.%, show a strong dependence of their lattice parameter on the B content.

(2) The coatings with a B content of 7.5 at.% exhibited the maximum hardness (H ~ 37 GPa), effective elastic modulus (E_r ~ 153 GPa), wear resistance (H/E_r ~ 0.24) and fracture toughness (K_{IC} ~ 2.9 MPa.m$^{1/2}$). The microstructure, solid solution strengthening and grain boundary hardening were considered to be responsible for the enhanced mechanical properties of the Zr-W-B-N coatings.

(3) Zr-W-B(7.5 at.%)-N film retains the fcc (NaCl-B1type) structure after vacuum annealing at T_v = 900ºC. However, film retains the fcc structure during air annealing at $T_n \leq$ 700ºC and at T_n = 900ºC, full degradation of the Zr-W-B(7.5 at.%)-N film in crystalline monoclinic ZrO_2 and WO_3 phases was observed. The oxygen starts to be incorporated in the film at T_n = 500ºC and its content increases substantially with increasing T_n. The film got peeled off at T_n = 900ºC.

(4) The hardness (H) and elastic modulus (E_r) of Zr-W-B(7.5 at.%)-N film were gradually affected in vacuum annealing, while a continuous increase in H and E_r values was observed in air annealing.

CHAPTER 7

Conclusions and Future Scope

The main objectives of the present research work was to synthesize and develop hard and tough nanocrystalline Zirconium Tungsten Nitride (Zr-W-N) and Zirconium Tungsten Boron Nitride (Zr-W-B-N) coatings by DC/RF magnetron sputtering technique and investigate the effect of sputtering parameters on microstructure, thermal stability and mechanical properties of these coatings for obtaining high quality films. The motivation for the development of hard and tough nanocrystalline metal nitride coatings is centered on prevention of wear damages like cavitation and silt erosion in hydro turbine components. The following is a brief summary and conclusions made based on the results obtained on the aforementioned coatings. The suggestions for the future work are proposed at the end.

7.1 The effect of nitrogen partial pressure (pN_2) on structural, composition, deposition rate and mechanical properties of Zirconium Tungsten Nitride ($Zr_xW_{1-x}N_y$) coatings

Tungsten nitride (W_2N) and zirconium nitride (ZrN) have been selected for the development of high hard and tough nanostructure Zirconium Tungsten Nitride ($Zr_xW_{1-x}N_y$) coating material. The films of $Zr_xW_{1-x}N_y$ have been deposited by DC/RF reactive magnetron sputtering on Si (100) substrates. The effect of nitrogen partial pressure (pN_2) on structural, composition, deposition rate and mechanical properties of these coatings has been investigated in detail. Structure and elemental composition of the deposited $Zr_xW_{1-x}N_y$ thin films strongly depend on pN_2. XRD analysis shows that for 0.07 Pa $\leq pN_2 \leq$ 0.17 Pa, $Zr_xW_{1-x}N_y$ films exhibit single (fcc) phase, for 0.20 Pa $\leq pN_2 \leq$ 0.27 Pa, an amorphous phase is obtained and for 0.33 Pa $\leq pN_2 \leq$ 0.67 Pa reflections corresponding to dual (fcc + hcp) phase have been observed. The

phase formation has been confirmed by TEM diffraction patterns. The crystallite size and lattice parameter of single (fcc) phase films vary non-monotonically with increase in pN_2. The roughness (δ_{rms}) also follows the same trend according to phases present in films. The thickness of the films decreases continuously with increasing pN_2. Results of nano-indentation analysis confirm moderate hardness, high wear resistance, high resistance to fatigue fracture and high adhesiveness of $Zr_xW_{1-x}N_y$ films. Among all the phases, maximum hardness (~ 24 GPa) and maximum reduced elastic modulus (135 GPa) have been obtained for dual phase (fcc + hcp) film while resistance to fatigue fracture (H^3/E_r^2 ~ 0.87 GPa), wear resistance (H/E_r ~ 0.2) and ductility for single phase (fcc) film were found to be maximum. No crack was observed to propagate in the films at a high load of 50 mN. All the films were found to exhibit high adhesion with the substrate surface.

Among various phase films, FCC phase Zr-W-N coatings deposited at **pN_2 = 0.13** Pa shows the best mechanical performance.

7.2 The effect of substrate temperatures (Insitu) and post annealing temperatures (Exsitu) on thermal stability and mechanical properties of amorphous phase and crystalline (fcc) phase Zirconium Tungsten Nitride coatings

The thermal stability and mechanical properties of amorphous phase $Zr_{19}W_{18}N_{63}$ thin films have been studied in detailed. Zr-W-N films of various structure have been deposited on Si substrates by DC/RF reactive magnetron sputtering at various substrate temperatures T_s (100º-600ºC) and at constant N_2 partial pressure (0.27 Pa). The decrease in nitrogen concentration with increasing T_s change the stoichiometry (Y=N/(Zr+W)) of the films. For 100ºC ≤ T_s ≤ 300ºC , Y ≥ 1.65, amorphous phase films and 400ºC ≤ T_s ≤ 600ºC, 1.52 ≤ Y ≤ 1.58 polycrystalline (fcc) phase films were obtained. The crystalline fcc phase films grow with (111) and (200) crystallographic orientation of grains. The intensity of the (200) reflex gradually increases in comparison to intensity ratio of (111) with increasing T_s. The TEM analyses confirm the XRD findings. A comparison of mechanical properties shows that the

amorphous films deposited at T_s = 200ºC, exhibit maximum wear resistance (H/E_r ~ 0.22) and maximum resistance to fatigue fracture (H^3/E_r^2 ~ 1.1 GPa). Post annealing of films deposited at 200ºC have been carried out in air from 100º-600ºC (T_n). Annealing of the films at different T_n (100ºC ≤ T_n ≤ 600ºC) results in no change of its amorphous structure to crystalline up to T_n = 600ºC. The broadening of the hump is the only noticeable change in the XRD patterns with increasing T_n. The RMS roughness of the annealed films increases with increasing T_n. Oxygen starts to be incorporated in the films at 300ºC annealing temperature and its content increases with increasing T_n. No crystalline oxide phases are observed up to T_n = 600ºC. The hardness of the annealed films decreases with increasing oxygen incorporation. Indentation and scratch tests for as deposited and annealed films show that no cracks propagate in the films even at a high load of 50 mN and all the films exhibit high adhesion with the substrate. The amorphous phase $Zr_{19}W_{18}N_{63}$ film deposited at **T_s = 200ºC** shows the best mechanical performance.

The thermal stability and mechanical properties of crystalline fcc phase Zr-W-N thin films have been studied in detailed. Nanostructured Zr-W-N thin films have been deposited on Si (100) substrates by DC/RF reactive magnetron sputtering at varying substrate temperatures T_s (100º-600ºC). The atomic% of Zr, W and N elements was observed almost independent of T_s. The average elemental composition of the films is found to be $Zr_{22}W_{19}N_{58}$. For 100ºC ≤ T_s≤ 600ºC, XRD patterns of the films show a crystalline fcc phase grew with (111) and (200) preferred crystallographic orientations of grains. A close analysis of the diffraction pattern shows that for low T_s (< 400ºC) the coating structure is not simply fcc but probably contains some amorphous parts along with the fcc phase and the amorphous part is maximum for T_s = 100ºC, decreases with increasing T_s and disappears for T_s ≥ 400ºC. TEM analyses confirm the evolution of microstructure of films with increasing T_s. The microstrain was found to increase with increasing T_s. The thickness of the films varies non-monotonically with increasing T_s. Maximum wear resistance (H/E_r ~ 0.22) and maximum resistance to fatigue fracture (H^3/E_r^2 ~ 1.0 GPa) have been obtained for the film deposited at T_s = 400ºC. Post annealing of the films deposited at 400ºC have been carried out in air from 100º-600ºC (T_n). XRD patterns of the post annealed films show that the films retain the fcc structure up to T_n = 600ºC without forming any crystalline oxide phase. For T_n ≥ 400ºC, along with the peaks corresponding to crystalline zirconium tungsten nitride, an amorphous contribution can be clearly seen. This amorphous

contribution increases with increase in T_n and accounts for the large O% observed in the films annealed at $T_n \geq 400^oC$. Shifting (in $2\theta^o$) in peaks is the only noticeable change in the XRD patterns with increasing T_n. Oxygen starts to be incorporated at 300ºC resulting development of internal stress in the films and hence films begin to peel-off above 400ºC. The crystallite size increases with increasing T_n and reaches a maximum value of ~ 9 nm at T_n = 400ºC Hardness and elastic modulus of annealed films increase with increasing strain. For practical applicability, the fcc phase $Zr_{22}W_{19}N_{58}$ film deposited at **400ºC** and **pN_2 = 0.13 Pa** is found to be most suitable for application in the temperature range below 300ºC.

Mechanical response of amorphous phase Zr-W-N is found superior to crystalline fcc phase Zr-W-N coatings. But the amorphous phase Zr-W-N coatings exhibit lower crystallization temperature (≤ 300ºC) and as the crystallization occur, the properties of film degraded. As per the demand of tribological applications, the wear resistant coating should exhibit high hardness (H), low effective elastic modulus (E_r), high toughness, compressive macrostress (< 0), dense and voids-free microstructure (non-columnar microstructure). Such micro-structural growth is sensitive to two main factors which include high deposition temperature and negative bias applied. Hence for achieving mentioned properties, crystalline (fcc) phase Zr-W-N has been selected for further study in the present research work.

It has been noticed that the deposition of wear protective coatings at low temperature (≤ 200ºC) is more feasible for commercial aspects. But the crystalline (fcc) phase Zr-W-N coatings show sub-optimal mechanical properties at low substrate temperature (≤ 200ºC) in comparison to mechanical properties (H ~ 23 GPa, E_r ~ 118 GPa, W_e ~ 80%, H/E_r ~ 0.22, H^3/E_r^2 ~ 1.0) obtained at high substrate temperatures (≥ 400ºC) and also exhibit low thermal stability. These issues made the basis for further enhancement of physical and mechanical properties of crystalline phase Zr-W-N coatings either by varying other sputtering parameter such as negative biasing or by changing the architecture of coatings through substitution of amorphous non-metal nitride phases like boron nitride, silicon nitride into the film for achieving optimal performance of coatings.

7.3 Effect of microstructure features, altered by ions bombardment, on mechanical properties of magnetron sputtered nanocrystalline fcc phase Zr-W-N Coatings

Nanocrystalline fcc phase zirconium tungsten nitride (Zr-W-N) coatings have been deposited on Si (100) substrates by DC/RF magnetron sputtering at 200ºC substrate temperature. The effect of negative substrate bias (-20 V $\leq V_s \leq$ -120 V) on microstructure and hence on mechanical properties of deposited coatings has been studied in details. The deposition rate (a_D) and substrate ion current density (i_s) vary non-monotonically with increasing V_s. For -20 V $\leq V_s \leq$ -60 V, the a_D and i_s increased from ~ 19 nm/min to ~ 22 nm/min and 5.1E-5 A/cm^2 to 8.5E-5 A/cm^2 respectively. With further increase in V_s, a_D decreased up to ~ 17 nm/min and i_s became constant at 8.5E-5 A/cm^2 for V_s > -60 V. The kinetic energy of the bombarding ions increases with increasing V_s and maximum (~ 99 J/cm^3) kinetic energy was obtained at V_s = -120 V. The atomic percentages of Zr, W and N in Zr-W-N coating have not been affected significantly with increasing V_s. The average elemental composition of the films is found to be $Zr_{21}W_{19}N_{60}$. XRD patterns revel that the Zr-W-N coatings form a single solid-solution nitride phase rather than the co-existence of separated nitrides. The broadening and shifting are also observed in XRD patterns. The microstrain increases with increasing negative substrate bias V_s. Maximum microstrain (0.017) were obtained at V_s = -100 V. The TEM analyses confirm that any secondary phases have not grown except fcc phase Zr-W-N during deposition at higher negative bias voltage. The lattice parameter and thickness of Zr-W-N films varied non-monotonically with increasing negative substrate bias. The energetic ions bombardment on the film during deposition induced stress in the film which was found compressive in nature and increases from -1.7 GPa to -8 GPa with increasing kinetic energy of the ions. Nanoindentation hardness H and effective elastic modulus E_r of the coating increases as the negative substrate bias goes up. The film deposited at V_s = -100 V exhibit (i) high wear resistance H/E_r > 0.1 (ii) high elastic recovery W_e > 60% (iii) compressive macrostress (σ < 0) and (iv) dense, voids-free microstructure. Owing to synergetic contributions of dense structure, preferred orientation, crystallite size and compressive stress, a maximum wear resistance 0.23 and maximum fracture toughness 2.25 MPa.m$^{1/2}$ was obtained at V_s = -100 V. This indicates that the simultaneous increment of wear resistance and toughness

is achievable if the negative bias voltage is properly controlled. Therefore, for the deposition of Zr-W-N system done at low substrate temperature (**200ºC**) and at **-100 V** bias voltage, pronounced mechanical properties (H ~ 34 GPa, $H/E_r > 0.1$, $W_e > 60\%$, $H^3/E_r^2 > 0.1$, $K_{IC} \sim 2.25$ $MPa.m^{1/2}$) has been achieved.

7.4 The effect of microstructure on thermal stability and mechanical properties of co-sputtered deposited Zr-W-B-N coatings of varying boron concentration

The effect of microstructure on thermal stability and mechanical properties of co-sputtered deposited Zr-W-B-N films by DC/RF reactive magnetron sputtering technique on Si (100) substrates have been studied in detail. The power density of boron target has been varied from 0.1 to 7.5 watt/cm^2 to obtained films of varying microstructure. The B content in the coatings was varied by varying the power density (0.1 to 7.5 watt/cm^2) to the B target. The influence of the B content on the microstructure and mechanical properties of the Zr-W-B-N coatings was investigated. Post annealing of the Zr-W-B(7.5 at.%)-N film has been carried out in vacuum and air up to 900ºC to comment on its thermal stability. It has been observed that films with boron content < 2.3 at.% exhibited (200) preferred crystallographic orientation of grains and columnar structure. While the films of boron content ≥ 7.5 at.% are columnarless with crystal phase grain size less than 7 nm and of amorphous-crystalline structure. The contribution of amorphous phase in microstructure is increases with increasing B content. Owing to synergetic contribution of microstructure, solid solution strengthening and grain boundary hardening film with boron concentration ~ 7.5 at.% exhibits maximum hardness (~ 37 GPa), wear resistance (H/E_r ~ 0.24) and fracture toughness (2.9 $MPa.m^{1/2}$). Zr-W-B(7.5 at.%)-N film retains the fcc (NaCl-B1type) structure after vacuum annealing at T_v = 900ºC. However, film retains the fcc structure during air annealing at $T_n \leq 700$ºC and at T_n = 900ºC, full degradation of the Zr-W-B(7.5 at.%)-N film in crystalline monoclinic ZrO_2 and WO_3 phases was observed. The oxygen starts to be incorporated in the film at T_n = 500ºC and its

content increases substantially with increasing T_n. The film got completely peeled off at T_n = 900ºC. The hardness (H) and elastic modulus (E_r) of Zr-W-B(7.5 at.%)-N film were gradually affected in vacuum annealing, while a continuous increase in H and E_r values was observed in air annealing.

Hence Zr-W-B(7.5 at.%)-N film deposited at pN2 = 0.13 Pa, T_s = 200ºC, V_s = -100 V exhibit high hardness and high toughness with high thermal stability

7.5 Suggestions for future work

The hard and tough Zr-W-N nitride system is a noble system and hence offering many research activities on this system. With the key processing-structure-property relationships for Zr-W-N and Zr-W-B-N nitride system developed in the present research thus far, there are several directions which can be followed to further expand upon this work:

(1) The effect of sputtering process parameters such as various gas compositions of Ar and $N_{2,}$ substrate temperature, post annealing temperature, bias voltage and power density on the various properties of Zr-W-N and Zr-W-B-N coatings deposited on Si substrate has been studied thoroughly. However, it is very essential to study the influence of these parameters on properties of Zr-W-N and Zr-W-B-N coatings deposited on industrial material, i.e. deposited on AISI M2 steel or WC substrates using DC/RF magnetron sputtering technique.

(2) The nature of bonding of these transition metal nitride films can be analyzed in detail using XPS technique as it is important to correlate nature of bonding to elastic modulus of the films, which enable to develop coatings of optimal performance for tribological applications.

(3) The influence of different concentrations of boron as well as other light elements like silicon, carbon and aluminum on physical and chemical properties of Zr-W-N coatings needs to be study.

(4) The wear resistance of Zr-W-N and Zr-W-B-N coatings such as cavitaion erosion resistance and silt erosion resistance need to be study to understand the failure mechanisms.

(5) The coating design space can be expanded to include multilayer architecture of transition metal nitride films like ZrWN/BN or ZrWN/Si_3N_4 and its effect on various properties can be studied.

(6) Other properties of Zr-W-N coatings like optical, electrical and magnetic properties can be examined.

REFERENCES

[1] A. Inoue, T. Zhang, T. Masumoto, “Glass-forming ability of alloys”, Journal of Non-Crystalline Solids 156-158 473-480 (1993).

[2] Abadias G., “Stress and preferred orientation in nitride-based PVD coatings,” Surface and Coatings Technology 202 2223–2235 (2008).

[3] Abadias G., Dub S., Shmegra R., “Nanoindentation hardness and structure of ion beam sputtered TiN_x, W and TiN/W multilayer hard coatings”, Surface and Coating Technology 200 6538–6543 (2006A).

[4] Abadias G., Koutsokeras L.E., Siozios A., Patsalas P., “Stress, phase stability and oxidation resistance of ternary Ti–Me–N (Me = Zr, Ta) hard coatings”, Thin Solid Films, 538 56–70 (2013).

[5] Abadias G., Tse Y. Y., Guérin Ph., Pelosin V., “Interdependence between stress, preferred orientation, and surface morphology of nanocrystalline TiN thin films deposited by dual ion beam sputtering”, Journal of Applied Physics 99 113519 (2006A).

[6] Ajayan P. M., Schadler L.S., and Braun P.V., “Nanocomposite Science and Technology”, Wiley-VCH-Verlag GmbH, Weinheim, Germany (2003).

[7] An T., Wen M., Wang L.L., Hu C.Q., Tian H.W., Zheng W.T., “Structures, mechanical properties and thermal stability of TiN/SiN_x multilayer coatings deposited by magnetron sputtering”, Journal of Alloys and Compounds 486 (1–2) 515-520 (2009).

[8] Argon A.S., Veprek S., “Mechanical properties of superhard nanocomposites”, Surface and Coating Technology 146-147 175-182 (2001).

[9] Ashrafizadeh F., “Adhesion evaluation of PVD coatings to aluminum substrate”, Surface & Coating Technology 130 186-194 (2000).

[10] Asthana B.N., Mathur G.N., Gupta A.C., “Sediment Management in Water Resources Projects”, Central Board of Irrigation and Power (2007).

[11] Baker C.C., Shah S.I., "Reactive sputter deposition of tungsten nitride thin films", Journal of Vacuum Science and Technology A 20 (5) 1699–1703 (2002).

[12] Baker M.A., Monclus M.A., Rebholz C., Gibson P.N., Leyland A., Matthews A., " A study of the nanostructure and hardness of electron beam evaporated TiAlBN Coatings", Thin Solid Films 518 4273-4280 (2010).

[13] Banerjee R., Chandra R., Ayyub P., "Influence of the sputtering gas on the preferred orientation of nanocrystalline titanium nitride thin films", Thin Solid Films 405 64-72 (2002).

[14] Banerjee R., Jayakrishnan R., Ayyub A., "Effect of the size-induced structural transformation on the band gap in CdS nanoparticles", Journal of Physics: Condensed Matter 12 10647 (2000).

[15] Barin I., Knacke O., Kubaschewski O., "Thermochemical properties of inorganic substances", Springer-Verlag Berlin Heidelberg, New York (1973).

[16] Barnett S.A., and Madan A., "Hardness and stability of metal–nitride nanoscale multilayers", Scripta Materialia 50 739–744 (2004).

[17] Barshilia Harish C., Jain A., Rajam K.S., "Structure, hardness and thermal stability of nanolayered TiN/CrN multilayer coatings", Vacuum 72 241-248 (2004).

[18] Baudrand D.W., "Electroless Nickel Plating", ASM Handbook, ASM International, Surface Engineering 5 290-310 (1994).

[19] Beaks B.D., Vishnyakov V.M., Colligon J.S., "Nano-impact testing of TiFeN and TiFeMoN films for dynamic toughness evaluation", Journal of Physics D: Applied Physics 44 085301(2011).

[20] Benia H.M., Guemmaz M., Schmerber G., Mosser A., Parlebas J.C., "Investigations on non-stoichiometric zirconium nitrides", Applied Surface Science 200 231-238 (2003).

[21] Beyers R., Sinclair R., Thomas M.E., "Phase equilibria in thin-film metallizations" Journal of Vacuum Science and Technology B 781-784 (1984).

[22] Bhaduri Debajyoti, Ghosh Arnab, Gangopadhyay Soumya, Paul Soumitra, "Effect of target frequency, bias voltage and bias frequency on microstructure and mechanical properties of pulsed DC CFUBM sputtered TiN coating", Surface & Coating Technology 204 3684-3697 (2010).

[23] Boukhris L., Poitevin J.M., "Electrical resistivity, structure and composition of d.c. sputtered WN_x films", Thin Solid Films 310 222-227 (1997).

[24] Breake B.D., Vishnyakov V.M., Colligon J.S., “Nano-impact testing of TiFeN and TiFeMoN films for dynamic toughness evaluation”, Journal of Physics D: Applied Physics 44 085301 (2011).

[25] Browning M.E., “Plating and Electroplating”, ASM Handbook, ASM International, Section Edition, Surface Engineering 5 165-332 (1994).

[26] Brugnoni C., Lanza F., Macchi G., Muller R., Parnisari E., Stroosnijder M.F., Vinhas J., "Evaluation of the wear resistance of ZrN coatings using thin layer activation", Surface and Coatings Technology 100–101 23–26 (1998).

[27] Bull S J, “Correlation of microstructure and properties of hard coatings”, Vacuum 43 387-391 (1992).

[28] Cao G., "Nanostructures & Nanomaterials : Synthesis, Properties & Applications", Imperial College Press London (2004).

[29] Carpenter W.W., “Ceramic Coatings and Linings”, ASM Handbook, ASM International, Surface Engineering 5 469-481 (1994).

[30] Chandra R., Chawla A. K., Ayyub P., “Optical and structural properties of sputter-deposited nanocrystalline Cu_2O films: effect of sputtering gas”, Journal of Nanoscience and Nanotechnology 6 1119-1123 (2006).

[31] Chandra R., Chawla A.K., Kaur D., Ayyub P., "Structural, optical and electronic properties of nanocrystalline TiN films", Nanotechnology 16 3053-3056 (2005).

[32] Chandra R., Kaur D., Chawla A.K., Phinichka N., Barber Z.H., “Texture development in Ti–Si–N nanocomposite thin films”, Materials Science and Engineering A 423 111-115 (2006A).

[33] Chang Y.Y., Wang D.Y., Hung C.Y., "Structural and mechanical properties of nanolayered TiAlN/CrN coatings synthesized by a cathodic arc deposition process", Surface and Coatings Technology 200 1702-1708 (2005).

[34] Charitidis C.A., "Nanomechanical and nanotribological properties of carbon-based thin films:A review," International Journal Of Refractory Metals & Hard Materials 28 51-70 (2010).

[35] Chauhan A., Vaish R., “Hard coating material selection using multi-criteria decision making”, Materials and Design 44 240–245 (2013).

[36] Chawla A.K., Singhal S., Gupta H.O., Chandra R., "Study of the physical properties of PLD grown cobalt doped nanocrystalline $Zn_{0.9}Cd_{0.1}S$ thin films", Thin Solid Films **520** 1437-1441 (2011).

[37] Chawla V., Jayaganthan R., Chandra R., "A study of structural and mechanical properties of sputter deposited nanocomposite Ti–Si–N thin films", Surface & Coating Technology 204 1582–1589 (2010).

[38] Chawla V., Jayaganthan R., Chawla A. K., Chandra R., "Morphological study of Magnetron Sputtered Ti thin films on Silicon substrate", Materials Chemistry and Physics 111 414-418 (2008).

[39] Chen L., Du Y., Yin F., Li J., "Mechanical properties of (Ti, Al)N monolayer and TiN/(Ti, Al)N multilayer coatings", International Journal of Refractory Metals and Hard Materials 25 72-76 (2007).

[40] Chen L., Paulitsch J., Du Y., Mayrhofer P.H., "Thermal stability and oxidation resistance of Ti–Al–N coatings," Surface and Coatings Technology 206 2954–2960 (2010).

[41] Cheng Y., Zheng Y.F., "A Study of ZrN/Zr Coatings Deposited on NiTi Alloy by PVD Technique", IEEE Transactions On Plasma Science 34 (4) 1105-1108 (2006).

[42] Cheng Y.H., Browne T., Heckerman B., Bowman C., Gorokhovsky V., Meletis E.I., "Mechanical and tribological properties of TiN/Ti multilayer coating", Surface and Coatings Technology 205 146-151 (2010).

[43] Chhowalla Manish, Unalan H. Emrah, "Thin films of hard cubic Zr_3N_4 stabilized by stress", Nature Materials 1338 (2005).

[44] Chioncel M.F., Haycock P.W., "Cobalt Thin Films Deposited by Photoassisted MOCVD Exhibiting Inverted Magnetic Hysteresis", Chemical vapor deposition **12** 670–678 (2006).

[45] Chopra K. L., "Thin Film Phenomena", McGraw-Hill New York (1969).

[46] Chou W.J., Yu G.P., Huang J.H., "Bias effect of ion-plated zirconium nitride film on Si(100)", Thin Solid Films 405 162–169 (2002).

[47] Chu K., Shen Y.G., "Mechanical and tribological properties of nanostructured TiN/TiBN multilayer films", Wear 265 516–524 (2008).

[48] Chun , Bias S.Y., “Voltage effect on the properties of TiN films by reactive magnetron sputtering”, Journal of the Korean Physical Society 56 (4) 1134-1139 (2010).

[49] Chung Y-W., Sproul W.D., “Superhard coating materials”, MRS Bulletin 28 164–168 (2003).

[50] Claflin B., Binger M., Lucovsky G., “Interface studies of tungsten nitride and titanium nitride composite metal gate electrodes with thin dielectric layers”, Journal of Vacuum Science and Technology A 16 1757-1761 (1998).

[51] Coil B.F., Sathrum P., Fontana R., “Optimization of arc evaporated (Ti,Al)N film composition for cutting tool applications”, Surface and Coating Technology 52 57-64. (1992).

[52] Craciun D., Socol G., Stefan N., Dorcioman G., Hanna M.,Taylor C.R., Lambers E., Craciun V, “The effect of deposition atmosphere on the chemical composition of TiN and ZrN thin films grown by pulsed laser deposition”, Applied Surface Science 302 124–128 (2014).

[53] Cullity B.D., Stock S. R., “Elements of X-Ray Diffraction”, 3rd edition, Prentice Hall, New Jersey (2001).

[54] Daniel R., Musil J., Zeman P., Mitterer C ,“Thermal stability of magnetron sputtered Zr – Si– N films reference”, Surface and Coatings Technology 201 3368-3376 (2006).

[55] Dauchot J.P., Edart S., Wautelet M., Hecq M., “Synthesis of zirconium nitride films monitored by in situ soft X-ray spectrometry”, Vacuum 46 927-930 (1995).

[56] De M.M., Gupta D.K., “Protective coatings in the gas turbine engine”, Surface and Coating Technology 68-69 1-9 (1994).

[57] Dey S.P., Deevi S.C., “Single layer and multilayer wear resistant coatings of (Ti,Al)N: a review”, Materials Science and Engineering:A 34 258-79 (2003).

[58] Dubey P., Arya V., Srivastava S., Singh D., Chandra R. “Effect of nitrogen flow rate on structural and mechanical properties of Zirconium Tungsten Nitride (Zr–W–N) coatings deposited by magnetron sputtering," Surface and Coatings Technology 236 182-187 (2013A).

[59] Dubey P., Arya V., Srivastava S.K., Singh D., Chandra R., “Study of thermal stability and mechanical properties of fcc phase $Zr_{22}W_{19}N_{58}$ thin films deposited by reactive magnetron sputtering”, Surface & Coating Technology 245 34-39 (2014).

[60] Dubey P., Dave V., Srivastava S., Singh D., Chandra R., "Study of thermal stability and mechanical properties of amorphous $Zr_{19}W_{18}N_{63}$ coatings deposited by DC/RF reactive magnetron sputtering," Surface and Coatings Technology 237 205-211 (2013B).

[61] Dwivedi D.K., Sharma A., Rajan T.V., "Friction and wear behavior of cast hypereutectic Al-Si alloy (LM28) at low sliding velocities", Indian Institute of Metal 54 247-254 (2001).

[62] Edelberg E., Bergh S., Naone R., Hall M., Aydil E.S., "Visible luminescence from nanocrystalline silicon films produced by plasma enhanced chemical vapor deposition", Applied Physics Letters 68 1415 (1996).

[63] Eichler J., Lesniak C., "Boron nitride (BN) and BN composites for high-temperature applications", Journal of the European Ceramic Society 28 1105–1109 (2008).

[64] Ensinger W., Volz K., Kiuchi M., "Ion beam-assisted deposition of nitrides of the 4th group of transition metals", Surface and Coating Technology 128-129 81-84 (2000).

[65] Farkas N., Zhang G., Donnelly K.M., Evans E.A., Ramsier R.D., Dagata J.A., "The role of subsurface oxygen in the local oxidation of zirconium and zirconium nitride thin films", Thin Solid Films 447–448 468-473 (2004).

[66] Fischer-Cripps A.C., "Nanoindentation, mechanical engineering series", Springer-Verlag, New York (2001).

[67] Frank F.C., Van der Merwe J.H., "One-Dimensional Dislocations. I. Static Theory", Proceedings of the Royal Society of London. Series A: Mathematical and physical sciences 198 205-216 (1949).

[68] Fultz B., Howe J., "Transmission Electron Microscopy and Diffractometry of Materials", 2nd Edition Springer New York (2002).

[69] Funken J., Kreutz E.W., Krösche M., Sung H., Voss A., Erkens G., Lemmer O., Leyendecker T., "Laser-assisted physical vapour deposition of ceramics', Surface and Coatings Technology 52 221-227 (1992).

[70] Gadhikar Aniruddha A., Sharma A., Goel D.B., Sharma C.P., "Effect of carbides on erosion resistance of 23-8-N steel", Bulletin of Materials Science 37 315-319 (2014).

[71] Gao W., Liu Z., Li Z., "Nano and Microcrystal Coatings and Their High-Temperature Applications", Advanced Materials 13 12-13 (2001).

[72] Gonzales M., Chessa J.F., Ramana C.V., “An ab initio study of the elastic behavior of single crystal group (IV) diborides at elevated temperatures”, Applied Physics Letters 97 211908 (2010).

[73] Gossner J.P., Tator K.B., “Painting”, ASM Handbook, ASM International, Surface Engineering 5 421-447 (1994).

[74] Gray D.M., Anand K., Nelson W.A., Aunemo H., Demers A., Rommetveit O., “Erosion resistant coatings and methods thereof”, United State patent US7431566 B2 (2008).

[75] Grimberg I., Zhitomirsky V.N., Boxman R.L., Goldsmith S., Weiss B.Z., “Multicomponent Ti–Zr–N and Ti–Nb–N coatings deposited by vacuum arc”, Surface and Coatings Technology 108–109 154–159 (1998).

[76] Gu B., Tu J.P., Zheng X.H., Yang Y.Z., Peng S.M., "Comparison in mechanical and tribological properties of Cr–W –N and Cr–Mo–N multilayer films deposited by DC reactive magnetron sputtering", Surface and Coatings Technology 202 2189–2193 (2008).

[77] Gu Q., Krauss G., Steurer W., “Transition metal borides: Superhard versus ultra-incompressihle”, Advanced Materials 20:3 620 –6 (2008A).

[78] Gulbinski W., Suszko T., Sienicki W., and Warcholinski B., “Tribological properties of silver-and copper-doped transition metal oxide coatings”, Wear 254 129–135 (2003).

[79] Gupta R., Rathi P., Mandawat P., Sharma A., “Mechanism of grain refinement of aluminum melt-A Review”, Indian Foundry Journal 60 41-48 (2014).

[80] Gupta S., Tiwari M., Prakash R., “Gold nanoparticles incorporated 3-(trimethoxysilyl) propyl methacrylate modified electrode for non-enzymatic electro-sensing of urea”, Journal of Nanoscience and Nanotechnology 14(4) 2786-2791 (2014A).

[81] Hadian F., Rahmati A., Movla H., Khaksar M., “Reactive DC magnetron sputter deposited copper nitride nanocrystalline thin films: Growth and characterization”, Vacuum 86 1067–1072 (2012).

[82] Hall E.O., “The deformation and ageing of mild steel: III Discussion of Results”, Proceedings of the Physical Society A Section B 64 747 (1951).

[83] Han S.M., Shah R., Banerjee R., Viswanathan G.B., Clemens B.M. and Nix W.D., "Combinatorial studies of mechanical properties of Ti–Al thin films using Nanoindentation", Acta Materialia 53 2059-2067 (2005).

[84] Hasegawa H., Kimura A., Suzuki T., "Microhardness and structural analysis of (Ti,Al)N, (Ti,Cr)N, (Ti,Zr)N and (Ti,V)N films", Journal of Vacuum Science and Technology A 18 1038-1040 (2000).

[85] Hauert R., Patscheider J., Knoblauch L., and Diserens M., "New coatings by nanostructuring", Advanced Materials 11 175–177 (1999).

[86] Hay J.L., Pharr G.M., "Instrumented Indentation testing", ASM Handbook, Materials Testing and Evaluation 8 232-243 (2000).

[87] Hedenqvist P., Olsson M., "Solid particle erosion of titanium nitride coated high speed steel", Tribology Internation 23 (3) 173-181 (1990).

[88] Herr W., Broszeit E., "The influence of a heat treatment on the microstructure and mechanical properties of sputtered coatings", Surface and Coatings Technology 97 335–340 (1997).

[89] Hertzberg R.W., "Deformation and fracture mechanics of engineering materials", 3rd edition New York Wiley (1989).

[90] Hirai T., Hayashi S., "Preparation and some properties of chemically vapour-deposited Si_3N_4-TiN composite", Journal of Materials Science 17 1320-1328 (1982).

[91] Holleck H., "Material selection for hard coatings", Journal of Vacuum Science and Technology A 4 (6) 2661-2669 (1986).

[92] Holubar P., Jilek M., Sima M., "Present and possible future applications of superhard nanocomposite coatings", Surface and Coating Technology 133–134 145–151 (2000).

[93] Hones P., Consiglio R., Randall N., Le´vy F., "Mechanical properties of hard chromium tungsten nitride coatings", Surface and Coatings Technology 125 179–184 (2000).

[94] Hones P., Martin N., Regula M., Lévy F., "Structural and mechanical properties of chromium nitride, molybdenum nitride and tungsten nitride thin films", Journal of Physics D: Applied Physics 36 1023–1029 (2003).

[95] Hsu C.H., Lin C.K., Huang K.H., Ou K.L., "Improvement on hardness and corrosion resistance of ferritic stainless steel via PVD-(Ti,Cr)N coatings", Journal of Surface and Coating Technology 31 380-384 (2013).

[96] Hultman L ,"Review Paper: Thermal stability of nitride thin films," Vacuum 57 1-30 (2000).

[97] Hultman L., Engström C., Odén M., "Mechanical and thermal stability of TiN/NbN super-lattice thin films", Surface and Coating Technology 133–134 227–233 (2000A).

[98] Hutchings I.M., "A model for the erosion of metals by spherical particles at normal incidence", Wear 70 (3) 269-281 (1981).

[99] Ivanovskii A.L., Medvedeva N.I., Okatov S.V., "Effect of Vacancies on the Electronic Structure and Bonding of Zirconium Nitride", Inorganic Materials 37 459-465 (2001).

[100] Jehn H.A., "Multicomponent and multiphase hard coatings for tribological applications", Surface and Coatings Technology 131 433-440 (2000).

[101] Jiang P.C., Lai Y.S., Chen J.S., "Dependence of crystal structure and work function of WN_x films on the nitrogen content", Applied Physics Letters 89 122107 (2006).

[102] Jimenez H., Restrepo E., Devia A., "Effect of the substrate temperature in ZrN coatings grown by the pulsed arc technique studied by XRD," Surface and Coatings Technology 201 1594–1601 (2006).

[103] John A., "Thornton, the microstructure of sputter deposited coatings", Journal of Vacuum Science & Technology A 4(6) 3059–3065 (1986).

[104] Johnson W.L., "Bulk Amorphous Metal-An Emerging Engineering Material", Journal of Minerals, Metallurgy and Materials Society (JOM) 54 40-43 (2002).

[105] Kanakia M., Owens M.E., Ling F.F., "Proceedings of Workshop on Fundamentals of High Temperature Friction and Wear with Emphasis on Solid Lubrication for Heat Engines", Industrial Tribology Institute, Troy, NY 19–38 (1984).

[106] Kanakia M.D., Peterson M.B., "Literature Review of the Solid Lubrication Mechanisms", Interim Report, BFLRF #213, Southwest Research Institute, San Antonio, TX 6–18 (1987).

[107] Kaner R.B., Gilman J.J., Tolbert S.H., "Materials science-designing superhard materials", Science 308:1 268–9 (2005).

[108] Karimi A., Verdon C., Barbezat G., "Microstructure and hydroabrasive wear behaviour of high velocity oxy-fuel thermally sprayed WC-Co(Cr) coatings", Surface and Coating Technology 57 81-89 (1993).

[109] Karuna P.R.P., Chakraborti P.C., Mishra S.K., “Structure and indentation behavior of nanocomposite Ti–B–N films”, Thin Solid Films 564 160-169 (2014).

[110] Karvankova P., Veprek-Heijman M.G.J., Zindulka O., Veprek S., “Superhard nc-TiN/a-BN and nc-TiN/a-TiB_x/a-BN coatings prepared by plasma CVD and PVD: a comparative study of their properties”, Surface and Coatings Technology 163/164 149-156 (2003).

[111] Kataria S., Srivastava S.K., Kumar P., Srinivas G., Siju, Khan J., Sridhar Rao D.V., Barshilia Harish C., “Nanocrystalline TiN coatings with improved toughness deposited by pulsing the nitrogen flow rate”, Surface and Coatings Technology 206 4279-4286 (2012).

[112] Kaufmann E.N., "Characterization of Materials" John Wiley and Sons Inc. New Jersey (2003).

[113] Khamseh S., “A study of the oxidation behavior of multilayered tungsten nitride/amorphous tungsten oxide film prepared in a planar magnetron sputtering system,” Ceramics international 40 465-470 (2014).

[114] Khanna A., Bhat D.G, “Effects of substrates on the crystal structure, texturing and optical properties of AlN coatings deposited by inverted cylindrical magnetron sputtering”, European Physical Journal of Applied Physics 9 30301 (2012).

[115] Khanna A., Bhat D.G., “Effects of deposition parameters on the structure of AlN films grown by reactive magnetron sputtering”, Journal of Vacuum Science and Technology A 25 557 (2007).

[116] Kim G.S., Kim Y.S., Kim S.M., Lee S.Y., Lee K.R. “Tribological and Corrosion Properties of Cr-Zr-N Coatings”, Journal of Korean Physical Society, 54 (4) 1569-1573 (2009A).

[117] Kim K.H., Choi S.R., Yoon S.Y., “Superhard Ti–Si–N coatings by a hybrid system of arc ion plating and sputtering techniques”, Surface and Coatings Technology 161 243–248 (2002).

[118] Kim S.H., Kim J.K., Kim K.H., “Influence of deposition conditions on the microstructure and mechanical properties of Ti–Si-N film by DC reactive magnetron sputtering”, Thin Solid Films 420-421 360-365 (2002A).

[119] Kim Sun Kyu, Le Vinh Van, “Cathodic arc plasma deposition of nano-multilayered ZrN/AlSiN thin films”, Surface and Coatings Technology 206 1507-1510 (2011).

[120] Kim Y.S., Kim G.S., Lee S.Y., “Thermal stability and electrochemical properties of CrZr–Si –N films synthesized by closed field unbalanced magnetron sputtering,” Surface and Coatings Technology 204 978-982 (2009).

[121] Kim Y.T., Min S.K., “New method to suppress encroachment by plasma-deposited β-phase tungsten nitride thin films”, Applied Physics Letters 59 929–931(1991).

[122] Klostermann H., Fietzke F., Modes T., Zywitzki O., “Zr-Al-N nanocomposite coatings deposited by pulse magnetron sputtering”, Reviews on Advanced Material Science 15 33-37 (2007).

[123] Knotek O., Barimani A., “On spinodal decomposition in magnetron sputtered (Ti, Zr) nitride and carbide thin films”, Thin Solid Films 174 51-56 (1989).

[124] Korotaev A.D., Borisov D.P., Moshkov V.Yu., Vchinnikov S.V.O, Oskomov K.V., Pinzhin Yu.P., Savostikov V.M., Tymentsev A.N., “Nanocomposite and nanostructured superhard Ti–Si–B–N coatings”, Russian Physics Journal 50 (10) 969-979 (2007).

[125] Koutsokeras L.E., Abadias G., Patsalas P., “Texture and microstructure evolution in single-phase Ti $_x$Ta$_{1-x}$N alloys of rocksalt structure”, Journal of Applied Physics 110 043535 (2011).

[126] Laegried N., Wehner G.K., “Sputtering Yields of metals for Ar^+ and Ne^+ Ions with energies from 50 to 600 eV”, Journal of Applied Physics **32** 365-369 (1961).

[127] Lahav A., Grim K.A.,"Measurement of thermal expansion coefficients of W, WSi, WN, and WSiN thin film metallizations”, Journal of Applied Physics 67 (2) 734-738 (1990).

[128] Lai Chia-Han, Lin Su-Jien, Yeh Jien-Wei, Davison Andrew, “Effect of substrate bias on the structure and properties of multi-element (AlCrTaTiZr)N coatings”, Journal of Physics D: Applied Physics 39 4628–4633 (2006).

[129] Lamni R., Sanjinés R., Parlinska-Wojtan M., Karimi A., Lévy F., “Microstructure and nanohardness properties of Zr–Al–N and Zr–Cr–N thin films”, Journal of Vacuum Science and Technology A 23 593-598 (2005).

[130] Larijani M.M., Norouzian S., Afzalzadeh R., Balashabadi P., Dibaji H., “Effects of post annealing on micro and nanostructural properties of ZrN films prepared by ion beam sputtering technique on SS304”, Surface and Coatings Technology 203 2486 – 2489 (2009).

[131] Lawn B.R., Evans A.G., Marshall D.B., “Elastic/Plastic Indentation Damage in Ceramics: The Median/Radial Crack System”, Journal of the American Ceramic Society 63 574–581 (1980).

[132] Le´vy F., Hones P., Schmid P.E., Sanjine´s R., Diserens M., Wiemer C., “Electronic states and mechanical properties in transition metal nitrides”, Surface and Coatings Technology 120–121 284–290 (1999).

[133] Lee C.W., Kim Y.T., “High temperature thermal stability of plasma-deposited tungsten nitride Schottky contacts to GaAs”, Solid State Electron 38 679-682 (1995).

[134] Lee Dong Bok, Dinh Thuan Nguyen, Kim Sun Kyu, “Air-oxidation of nano-multilayered CrAlSiN thin films between 800 and 1000ºC”, Surface and Coatings Technology 203 1199-1204 (2009).

[135] Lee Dong-Bok, Kim Sun-Kyu, “Oxidation of Ti-B-C-N Film Deposited on Steel”, Metals and Materials International, 13(6) 469-473 (2007).

[136] Lejeune M., Benlahsen M., Lemoine P., “Effect of air post contamination on mechanical properties of amorphous carbon nitride thin films”, Solid State Communications 135 434–439 (2005).

[137] Lemine O.M., “Microstructural characterization of α-Fe_2O_3 nanoparticle using, XRD line profiles analysis,” FE-SEM and FT-IR, Superlattices and Microstructures 45 576-582 (2009).

[138] Leyendecker T., Lemmer O., Esser S., Ebberink J., “The development of the PVD coating TiAlN as a commercial coating for cutting tools”, Surface and Coatings Technology 48 175-178 (1991).

[139] Leyland A., Matthews A., “On the significance of the H /E ratio in wear control: a nanocomposite coating approach to optimized tribological behavior”, Wear 246 1-11 (2000).

[140] Lin J., Moore J.J., Mishra B., Pinkas M., Sproul W.D., “Structure, Mechanical and Tribological Properties of TiBCN Nanocomposite Coatings”, Acta Metallurgica 58 1554-1564 (2010).

[141] Linus Pauling, “Nature of the Chemical Bond”, Cornell Univ. Press, Ithaca, Ch. 2 28-61 (1939).

[142] Liu C.P., Yang H.G., "Systematic study of the evolution of texture and electrical properties of ZrN_x thin films by reactive DC magnetron sputtering", Thin Solid Films 444 111-119 (2003).

[143] Liu F., Yu J., Bai X., "Crystallinity improvement of hexagonal boron nitride films by molybdenum catalysts during microwave plasma chemical vapor deposition and post-annealing", Applied Surface Science 258 10191-10194 (2012).

[144] Ljungerantz H., Oden M., Huttman L., Greene J.E., Sundgren J.E., "Nanoindentation studies of single-crystal (001), (011), and (111) oriented TiN layers on MgO", Journal of Applied Physics 80 6725-6733 (1996).

[145] Löffler F.H.W., "Systematic approach to improve the performance of PVD coatings for tool applications", Surface and Coatings Technology 68-69 729-740 (1994).

[146] Logothetidis S., "Haemocompatibility of carbon based thin films," Diamond and Related Materials 16 (10) 1847-1857 (2007).

[147] Louro C., Lamni T.R., Le´vy F., "W-B-N sputter-deposited thin films for mechanical application", Surface & Coatings Technology 200 753–759 (2005).

[148] Lugscheider E., Knotek O., Barwulf S., and Bobzin K., "Characteristic curves of voltage and current, and phase generation and properties of tungsten- and vanadium-oxides deposited by reactive d.c.-MSIP-PVD-process for self-lubricating applications", Surface and Coating Technology 142-144 137-142 (2001).

[149] Mallia B., Stüber M., Dearnley P.A., "Character and chemical-wear response of high alloy austenitic stainless steel (Ortron 90) surface engineered with magnetron sputtered Cr–B–N ternary alloy coatings", Thin Solid Films 549 216–223 (2013).

[150] Manivannan A., Seehra M.S., Majumder S.B. and Katiyar R.S., "Magnetism of cobalt doped titania thin films prepared by spray pyrolysis", Applied Physics Letters **83** 111-113 (2003).

[151] Mannling H.D., Patil D.S., Moto K., Jilek M., Veprek S., "Thermal stability of superhard nanocomposite coatings consisting of immiscible nitrides", Surface and Coatings Technology 146 – 147 263–267 (2001).

[152] Marques A.P., Cavaleiro A., "Structural and mechanical properties of amorphous W–Si–N sputtered films after thermal annealing", Thin Solid Films 441 150-160 (2003).

[153] Martin P.M., "Handbook of Deposition Technologies for Films and Coatings", Science, Applications and Technology, Elsevier 3rd (2010).

[154] Mawella K.J.A., Sheward J.A., “Sputtered alloy coatings by codeposition: effects of bias voltage”, Thin Solid Films 193/194 27-33 (1990).

[155] Mayrhofer P. H., Mitterer C., Hultman L., Clemens H., "Microstructural design of hard coatings", Progress in Materials Science 51 1032-1114 (2006).

[156] Mayrhofer P.H., Horling A., Karlsson L., Sjolen J., Mitterer C., Hultman L., “Self-organized nanostructures in the Ti–Al–N system”, Applied Physics Letter 83 (10) 2049–2051 (2003).

[157] Mayrhofer P.H., Hovsepian P.E., Mitterer C., and Münz W.D., “Calorimetric evidence for frictional self-adaptation of TiAlN/VN superlattice coatings”, Surface and Coating Technology 177 341–347 (2004).

[158] Mayrhofer P.H., Stoiber M., “Thermal stability of superhard Ti–B–N coatings”, Surface and Coatings Technology 201 6148–6153 (2007).

[159] Mayrhofer Paul H., Geier M., Löcker C., Chen L., “Influence of deposition conditions on texture development and mechanical properties of TiN coatings”, International Journal of Materials Research 100(8) 1052-1058 (2009).

[160] Mei F., Shao N., Hu X., Li G., Gu M., “Microstructure and mechanical properties of reactively sputtered Ti–Si–N nanocomposite films”, Materials Letters 59 2442–2445 (2005).

[161] Meng L.J., Andritschky M., Santos M.P., “The effect of substrate temperature on the properties of DC reactive magnetron sputtering titanium oxide films,” Thin Solid Films 223 242-249 (1993).

[162] Meng Q.N., Wen M., Qu C.Q., Hu C.Q., Zheng W.T., “Preferred orientation, phase transition and hardness for sputtered zirconium nitride films grown at different substrate biases,” Surface and Coatings Technology 205 2865 -2870 (2011).

[163] Michalski J., Lunarska E., Wierzchon T., AlGhanem S., “Wear and corrosion properties of TiN layers deposited on nitrided high speed steel”, Surface and Coatings Technology 72 (3) 189–195 (1995).

[164] Migita T., Kamei R., Tanaka T., Kawabata K., “Effect of dc bias on the compositional ratio of WNx thin films prepared by rf–dc coupled magnetron sputtering”, Applied Surface Science 169–170 362–365 (2001).

[165] Mitterer C., Mayrhofer P.H., “Design of nanostructured hard coatings for optimum performance”, Key Engineering Materials 264–268 453–458 (2004).

[166] Mitterer C., Mayrhofer P.H., “Some materials science aspects of PVD hard coatings”, Advances in Solid State Physics 41 263-274 (2001).

[167] Mitterer C., Ubleis A., Ebner R., “Sputter deposition of wear-resistant coatings within the system Zr-B-N”, Materials Science and Engineering A140 670-675 (1991).

[168] Mohallem N.D.S., Seara L.M., Novak M.A., Sinnecker E.H.C.P., “Magnetic Nanocomposite Thin Films Prepared by Sol-Gel Process”, Brazilian Journal of Physics **36** 210-215 (2010).

[169] Mohamed S.H., “Thermal stability of tungsten nitride films deposited by reactive magnetron sputtering”, Surface and Coatings Technology 202 2169–2175 (2008).

[170] Mollart T.P., Baker M., Haupt J., Steiner A., Hammer P., Gissler W., “Nanostructured titanium boron nitride coatings of very high hardness”, Surface and Coatings Technology 74-75 491-496 (1995).

[171] Moriwaki M.,Yamada T., Harada Y., Fujii S., “Improved Metal Gate Process by Simultaneous Gate-Oxide Nitridation during W/WN_x Gate Formation”, Japanese Journal of Applied Physics 39 2177-2180 (2000).

[172] Moser J.H., Tian F., Haller O., Bergstrom D.B., Petrov I., Greene J.E., Wiemer C., “Single-phase polycrystalline $Ti_{l\_x}W_xN$ alloys ($0 \leq x \leq 0.7$) grown by UHV reactive magnetron sputtering: microstructure and physical properties”, Thin Solid Films 253 445-450 (1994).

[173] Münz W.D., “Super lattice structured hard coatings in trends and applications of thin films”, Vides, Nancy 12–16 (2000).

[174] Murthy J.K.N., Venkataraman B., “Abrasive wear behaviour of WC–CoCr and Cr_3C_2–20(NiCr) deposited by HVOF and detonation spray processes”, Surface and Coating Technology 200 2642-2652 (2006).

[175] Musil J., “Hard and superhard nanocomposite coatings”, Surface and Coating Technology 125 322–330 (2000).

[176] Musil J., “Hard nanocomposite coating: Thermal stability, oxidation resistance and toughness”, Surface and Coatings Technology 207 50–65 (2012).

[177] Musil J., “Physical and Mechanical Properties of Hard Nanocomposite Films Prepared by Magnetron Sputtering”, Nanostructured Hard Coatings, Kluwer Academic, New York, (2005).

[178] Musil J., Daniel R., Solda´n J., Zeman P., "Properties of reactively sputtered W–Si–N films", Surface and Coatings Technology 200 3886–3895 (2006).

[179] Musil J., Daniel R., Zeman P., Takai O. "Structure and properties of magnetron sputtered Zr–Si–N films with a high (≥ 25 at.%) Si content", Thin Solid Films 478 238–247 (2005).

[180] Musil J., Jílek R., Meissner M., Tolg T., Čerstvý R., "Two-phase single layer Al-O-N nanocomposite films with enhanced resistance to cracking", Surface and Coating Technology 206 4230-4234 (2012A).

[181] Musil J., Kunc F., Zeman H., Polakova H., "Relationships between hardness, Young's modulus and elastic recovery in hard nanocomposite coatings", Surface & Coating Technology 154 304 -313 (2002).

[182] Musil J., Polakova H., "Hard nanocomposite Zr-Y-N coatings: correlation between hardness and structure" Surface and Coatings Technology 127 99-106 (2000).

[183] Musil J., Šícha J., Heřman D., Čerstvý R., "Role of energy in low-temperature high-rate formation of hydrophilic TiO_2 thin films using pulsed magnetron sputtering", Journal of Vacuum Science and Technology A 25 (4) 666-674 (2007).

[184] Musil J., Vlcek J., "Magnetron sputtering of hard nanocomposite coatings and their properties", Surface and Coatings Technology 142-144 557-566 (2001).

[185] Nagao M., Fujimori Y., Gotoh Y., Tsuji H., Ishikawa J., "Emission characteristics of ZrN thin film field emitter array fabricated by ion beam assisted deposition technique", Journal of Vacuum Science and Technology B 16 829-832 (1998).

[186] Naidu B S K., Indian Scenario of Renewable Energy for Sustainable Development, Energy Policy 24 575-581 (1996).

[187] Naim M., Bahadur S., "Effect of microstructure and mechanical properties on the erosion of 18 Ni (250) maraging steel", Wear 112 (2) 217–234 (1986).

[188] Nalwa H.S., Handbook of Organic-Inorganic Hybrid Materials and Nanocomposites, Stevenson Ranch, CA, USA, American Scientific 1–2 (2003).

[189] Nayar P., Khanna A., Kabiraj D., Abhliash S.R., Beake B., Losset Y., Chen B., "Structural, optical and mechanical properties of amorphous and crystalline alumina thin films", Thin Solid Films 568 19-24 (2014).

[190] Nes E., Ryum N., Hunderi O., "On the Zener drag", Acta Metallurgica 33 11–22 (1985).

[191] Ni J., Li Z.C., Zhang Z.J., "Influence of deposition temperature on the structure and optical properties of HfO2 thin films," Frontiers of Materials Science in China 2(4) 381- 385 (2008).

[192] Nicolet M.A., Giauque P.H., "Highly metastable amorphous or near-amorphous ternary films (mictamict alloys)", Microelectronic Engineering, 55 357–367 (2001).

[193] Niyomsoan S., Grant W., Olson D.L., Mishra B., "Variation of color in titanium and zirconium nitride decorative thin films", Thin Solid Films 415 187-194 (2002).

[194] Oberle T.L., "Properties influencing wear of metals", Journal of Metals 3 438 (1951).

[195] Oh U.C., Je J.H., "Effects of strain energy on the preferred orientation of TiN thin films," Journal of Applied Physics 74 (3) 1692-1696 (1993).

[196] Ohring M., "The Materials Science of Thin Films", Academic Press Inc, San Diego (1992).

[197] Oliveira J.C., Manaia A., Cavaleiro A., Vieira M.T "Structure, hardness and thermal stability of Ti(Al, N) coatings, Surface and Coatings Technology 201 4073–4077 (2006).

[198] Oliver W.C., Pharr G.M., "Measurement of hardness and elastic modulus by instrumented indentation: advances in understanding and refinements to methodology", Journal of Materials Research 19 3-20 (2004).

[199] Otani Y., Hofmann S., "High temperature oxidation behaviour of $(Ti_{1-x}Cr_x)N$ coatings", Thin Solid Films 287 188-192 (1996).

[200] Panjan P., Navinsek B., Cvelbar A., Zalar A., Milosev I., "Oxidation of TiN, ZrN, TiZrN, CrN, TiCrN and TiN/CrN multilayer hard coatings reactively sputtered at low temperature", Thin solid Films 281-282 298-301 (1996).

[201] Park J.K., Park H.J., Ahn J.H., Baik Y.J., "Effect of Ti to Al ratio on the crystalline structure and hardening of a $Ti_{1-x}Al_xN$/CrN nanoscale multilayered coating", Surface and Coatings Technology 203 3099–3103 (2009).

[202] Patsalas P., Charitidis C., Logothetidis S., "The effect of substrate temperature and biasing on the mechanical properties and structure of sputtered titanium nitride thin films," Surface and Coatings Technology 125 335–340 (2000).

[203] Pelleg J., Bibi A., Sinder, M., "Contact characterizations of ZrN thin films obtained by reactive sputtering", Physica B 393 292-297 (2007).

[204] Perevislov S.N.,Panteleev I.B., Ordan'yan S.S., "Synthesis of Complex Tungsten Zirconium Carbonitrides", Russian Journal of Applied Chemistry 78 1767-1771 (2005).

[205] Periasamy C., Prakash R., Chakrabarti P., "Effect of post annealing on structural and optical properties of ZnO thin films deposited by vacuum coating technique", Journal of Materials Science: Materials in Electronics 21(3) 309-315 (2010).

[206] Petrov I., Barna *P.B.*, Hultman *L.*, Greene *J.E.*, "Microstructural evolution during film growth", Journal of Vacuum Science and Technology A 21 S117-S128 (2003).

[207] Pichon L., Girardeau T., Straboni A., Lignou F., Guérin P., Perrière J., "Zirconium nitrides deposited by dual ion beam sputtering: physical properties and growth modeling", Applied Surface Science 150 115-124 (1999).

[208] Pierson H.O., "Chemical Vapor Deposition of Semiconductor Materials", ASM Handbook, ASM International, Surface Engineering 5 510-516 (1994).

[209] Pilloud D., Dehlinger A.S., Pierson J.F., Roman A., Pichon L., "Reactively sputtered zirconium nitride coatings: structural, mechanical, optical and electrical characteristics", Surface and Coatings Technology 174–175 338–344 (2003).

[210] Pinheiro D., Vieira M.T., Djouadi M.A., "Advantages of depositing multilayer coatings for cutting wood-based products", Surface and Coatings Technology 203 3197-3205 (2009).

[211] Polaki S.R., Ramaseshan R., Jose F., Dash S., Tyagi A.K., "Evolution of Structural and Mechanical Properties of TiN Films on SS 304LN", Intenational Journal of Applied Ceramics Technology 10 (1) 45-50 (2013).

[212] Polcar T., Kubart T., Novák R., Kopecky L.´, Široky P., "Comparison of tribological behaviour of TiN, TiCN and CrN at elevated temperatures", Surface and Coating Technology 193 192-199 (2005).

[213] Polcar T., Parreira N.M.G., Calveiro A., "Tribological characterization of tungsten nitride coatings deposited by reactive magnetron sputtering", Wear 262 655–665 (2007).

[214] Polcar T., Parreira N.M.G., Cavaleiro A., "Structural and tribological characterization of tungsten nitride coatings at elevated temperature", Wear 265 319–326 (2008).

[215] Pollock H.M., "Nanoindentation", ASM Handbook, Friction, Lubrication and Wear Technology 18 419-429 (1992).

[216] Polychronopoulou K., Neidhardt J., Rebholz C., Baker M.A., O'Sullivan M., Reiter A.E., Gunnaes A.E., Giannakopoulos K., Mitterer C., "Synthesis and characterization of Cr-B-N coatings deposited by reactive arc-evaporation", Journal of Materials Research 23 3048-3055 (2008).

[217] Purushotham K.P., Ward L.P., Brack N., Pigram P.J., Evans P., Noorman H., Manory R.R., "Corrosion behavior of Zr modified CrN coatings using metal vapor vacuum arc ion implantation", Journal of Vacuum Science & Technology A 25 110-116 (2007).

[218] Purwanto A., Widiyandari H., Ogi T., Okuyama K., "Role of particle size for platinum-loaded tungsten oxide nanoparticles during dye photodegradation under solar-simulated irradiation" Catalysis Communications 12 525 –529 (2011).

[219] Pyper O., Schöllhorn R., Donkers J.J.T.M., Krings L.H.M., "Nanocrystalline structure of WO_3 thin films prepared by the sol-gel technique", Materials Research Bulletin **33** 1095–1101 (1998).

[220] Ramadoss R., Kumar N., Pandian R., Dash S., Ravindran T.R., Arivuoli D., Tyagi A.K., "Tribological properties and deformation mechanism of TiAlN coating sliding with various counter bodies", Tribology International 66 143-149 (2013).

[221] Ramana C.V., Utsunomiya S., Ewing R.C., Julien C.M., Becker U., "Structural stability and phase transitions in WO_3 thin films", Journal of the Physical Chemistry B 110 10430 (2006).

[222] Ramana J.V., Kumar S., David C., Ray A.K., Raju V.S., "Characterization of zirconium nitride coatings prepared by DC magnetron sputtering", Materials Letters 43 73-76 (2000).

[223] Raveh A., Zukerman I., Shneck R., Avni R., Fried I., "Thermal stability of nanostructured superhard coatings: A review", Surface and Coatings Technology 201 6136-6142 (2007).

[224] Reddy G.L.N., Ramana J.V., Kumar S., Kumar S.V., Raju V.S., "Investigations on the oxidation of zirconium nitride films in air by nuclear reaction analysis and back scattering spectrometry," Applied Surface Science 253 7230-7237 (2007).

[225] Regent F., Musil J., "Magnetron sputtered Cr- Ni- N and Ti-Mo- N films: comparison of mechanical properties", Journal of Surface and Coating Technology142- 144 146-151 (2001).

[226] Reid J.S., Kolawa E., Ruiz R.P., Nicolet M.A., “Evaluation of amorphous (Mo, Ta, W)-Si-N diffusion barriers for 〈Si〉|Cu metallizations”, Thin Solid Films 236 319–324 (1993).

[227] Reid J.S., Liu R.Y., Smith P.M., Ruiz R.P., Nicolet M.A., “W-B-N diffusion barriers for Si/ Cu metallizations”, Thin Solid Films 262 218-223 (1995).

[228] Reimer L., “Transmission electron microscopy: Physics of image formation and microanalysis”, 3rd Edition Springer-Verlag, Berlin (1993).

[229] Reinhold E., Faber J., “Large area electron beam physical vapor deposition (EB-PVD) and plasma activated electron beam (EB) evaporation - Status and prospects”, Surface & Coatings Technology 206 1653–1659 (2011).

[230] Rhode S.L., “Sputter Deposition”, ASM Handbook, ASM International, Surface Engineering, 5 573-581 (1994).

[231] Rhys-Jones T.N., “Thermally sprayed coating systems for surface protection and clearance control applications in aero engines”, Surface and Coating Technology 43-44 402-415 (1990).

[232] Rizzo A., Signore M.A., Mirenghi L., Dimaio D., “Deposition and properties of ZrN_x films produced by radio frequency reactive magnetron sputtering”, Thin Solid Films 515 1486- 1493 (2006).

[233] Rizzo A., Signore M.A., Valerini D., Altamura D., Cappello A., Tapfer L., “A study of suppression effect of oxygen contamination by bias voltage in reactively sputtered ZrN films”, Surface & Coatings Technology 206 2711–2718 (2012).

[234] Rosenberg D., Wehner G.K., “Sputtering Yields for low-energy He^+, Kr^+ and Xe^+ ion bombardment”, Journal of Applied Physics **33** 1842-1845 (1962).

[235] Rossnagel S.M., Cuomo J.J., Westwood W.D., "Reactive Sputter Deposition Handbook of Plasma Processing, Technology: Fundamentals, Etching, Deposition and Surface Interactions", Noyes Publications New Jersey (1990).

[236] Ruan J.L., Lii D.F., Chen J.S., Huang J.L., “Investigation of substrate bias effects on the reactively sputtered ZrN diffusion barrier films”, Ceramics International 35 1999–2005 (2009).

[237] Rupa P.K.P., Chakraborti P.C., Mishra S.K., “Structure and indentation behavior of nanocomposite Ti–B–N films”, Thin Solid Films 564 160–169 (2014).

[238] Ryan N.E., “An appraisal of possible scavenger elements for chromium and chromium alloys”, Journal of the Less-Common Metals 6 21-35 (1964).

[239] Sakai M., “Energy principle of the indentation-induced inelastic surface deformation and hardness of brittle materials”, Acta Metallurgica et Materialia 41(6) 1751–1758 (1993).

[240] Sandu C.S., Cusnir N., Oezer D., Sanjinés R., Patscheider J., “Influence of bias voltage on the microstructure and physical properties of magnetron sputtered Zr–Si–N nanocomposite thin films”, Surface & Coating Technology 204 969-972 (2009).

[241] Sankaran K.J., Kumar N., Dash S., Chen H.C., Tyagi A.K., Tai N.H., Lin I.N., “Significance of grain and grain boundary characteristics of ultra nanocrystalline diamond films and tribological properties”, Surface and Coatings Technology 232 75-87 (2013).

[242] Schuster J.S., Bauer J., “The ternary system titanium-aluminum-nitrogen”, Journal of Solid State Chemistry 53 260-265 (1984).

[243] Schwarz K., Yee D.S., Cuomo J.J., Harper J.M.E., “Zr-Mo-N as a high-T_c, superconductor”, Physical Review B 32 8 (1985).

[244] Segrnuller A., Noyan I.C., Speriosu V.S., "X-ray diffraction studies of thin films and multilayer structures", Progress in Crystal Growth and Characterization 18 21-66 (1989).

[245] Selvakumar N., Barshilia Harish C., “Review of physical vapor deposited (PVD) spectrally selective coatings for mid- and high-temperature solar thermal applications”, Solar Energy Materials and Solar Cells 98 1-23 (2012).

[246] Shar P.L., “Refractory metal gate processes for VLSI applications”, IEEE Trans Electron Devices ED-26 631–640 (1979).

[247] Sharma A.K. , Rajaram P., “Nanocrystalline thin films of $CuInS_2$ grown by spray pyrolysis”, Materials Science and Engineering: B 172 37–42 (2010).

[248] Shen Y.G., Mai Y.W., “Microstructure and structure characteristics of cubic WN_x compounds”, Materials Science and Engineering A 288 47–53 (2000A).

[249] Shen Y.G., Mai Y.W., McBride W.E., Zhang Q.C., McKenzie D.R., “Structural properties and nitrogen-loss characteristics in sputtered tungsten nitride films”, Thin Solid Films 372 257–264 (2000).

[250] Shi Y., Pan F., Bao M., Yang Z., Wang L., "Effect of N_2 flow rate on structure and property of $ZrNbAlN_x$ multilayer films deposited by magnetron sputtering", Journal of Alloys & Compounds 559 196-202 (2013).

[251] Shi Yongjing, Long Siyuan, Yang Shicai, Pan Fusheng, "Deposition of nano-scaled CrTiAlN multilayer coatings with different negative bias voltage on Mg alloy by unbalanced magnetron sputtering", Vacuum 84 962-968 (2010).

[252] Shin J. H. , Choi K.S., Wang T.G., Kim K.H., Nowak R., "Microstructure evolution and mechanical properties of Ti−B−N coatings deposited by plasma-enhanced chemical vapor deposition", Transactions of Nonferrous Metals Society of China 22 722−728 (2012).

[253] Shizhi L., Yulong S., Hongrui P., "Ti-Si-N films prepared by plasma-enhanced chemical vapor deposition", Plasma Chemistry and Plasma Processing 21/3 287-297 (1992).

[254] Shtansky D.V., Lobova T.A., Fominski V.Y., Kulinich S.A., Lyasotsky I.V., Petrzhik M.I., Levashov E.A., Moore J.J., "Structure and tribological properties of WSe_x, WSe_x/TiN, WSe_x/TiCN and WSe_x/TiSiN coatings", Surface and Coatings Technology 183 328–336 (2004).

[255] Shtansky D.V., Tsuda O., Ikuhara Y., Yoshida T., "Crystallography and structural evolution of cubic boron nitride films during bias sputter deposition", Acta materialia 48 3745–3759 (2000).

[256] Singh P., Sharma A., Rajan T.V., "Effect of grain refinement and modification on mechanical and wear properties of Al-9% Si-4% Cu-0.5%Mg alloys", Indian Foundry Journal 52 23-34 (2006).

[257] Singh S., Srivastava V.K., Prakash R., "Mechanical properties and morphological studies of C/C–SiC composites", Materials Science and Engineering A 534 707-710 (2012).

[258] Sneddon I.N., "The relation between load and penetration in the axisymmetric boussinesq problem for a punch of arbitrary profile", International Journal of Engineering Science 3 47-57 (1965).

[259] So F.C.T., Kolawa E., Zhao X.A., Nicolet M.A., "W_xN_{1-x} alloys as diffusion barriers between Al and Si", Journal of Applied Physics 64 2787- 2789 (1988).

[260] Soderberg H., Oden M., Aldareguia J.M., Hultman L., “Nanostructure formation during deposition of TiN/SiN_x nanomultilayer films by reactive dual magnetron sputtering”, Journal of Applied Physcis 97 114327 (2005).

[261] Som T., Ghosh S., Tripathi J.K, Grotzschel R., Mader M., Ganesan V., Gupta A., Kanjilal D., “Copper-based nanocluster composite silica films by rf-sputtering deposition”, Materials Science and Engineering: C 26 1092–1096 (2006).

[262] Song D.H., Yang G.S., Lee J.K., “Effect of Heat Treatment on Characterizations of TiCrN Coated Layer by R.F Magnetron Sputtering”, Solid State Phenomena 124-126 1513-1516 (2007).

[263] Soto G., Cruz W.D.L., Castillón F.F., Díaz J.A., Machorro R., Farías M.H., “Tungsten nitride films grown via pulsed laser deposition studied in situ by electron spectroscopies”, Applied Surface Science 214 58–67 (2003).

[264] Spalvins T., “Coatings for wear and lubrication”, Thin Solid Films 53 285-300 (1978).

[265] Spillmann H., Willmott P.R., Morstein M., Uggowitzer P.J., “ZrN, Zr_xAl_yN and Zr_xGa_yN thin films–novel materials for hard coatings grown using pulsed laser deposition”, Applied Physics A: Materials Science and Processing 73 441-450 (2001).

[266] Sproul W.D., “New routes in the preparation of mechanically hard films,” Science 273 (5277) 889-892 (1996).

[267] Sproul W.D., Christie D.J., Carter D.C., "Control of reactive sputtering processes", Thin Solid Films 491 1-17 (2005).

[268] Stappen M.V., Stals L.M., Kerkhofs M., Quaeyhaegens C., “State of the art for the industrial use of ceramic PVD coatings”, Surface and Coatings Technology 74-75 629-633 (1995).

[269] Stranski N.I., Krastanov S.L., “Theory of orientation separation of ionic crystals”, Akad. Wiss. Wien, Math.-naturw. Klasse, Abt. IIb , 146 797-810 (1938).

[270] Styazhkin V.A., Kopylov A.A., Paleeva S.Y., Veksler Y.G., and Paderov A.N., “Certain, Peculiarities of Zr-Cr-N Coatings on Steel Blades of a Gas-Turbine Engine Compressor”, Protection of Metals. 36 5 466-469 (2000).

[271] Subramanian C., Strafford K.N., “Review of multicomponent and multilayer coatings for tribological application”, wear 165 85-95 (1993).

[272] Sue J.A., Chang T.P., “Friction and wear behavior of titanium nitride, zirconium nitride and chromium nitride coatings a elevated temperatures”, Surface & Coating Technology 76-77 61-69 (1995).

[273] Sue J.A., Troue H.H., “Influence of crystallographic orientation, residual strains, crystallite size and microhardness on erosion in ZrN coating”, Surface and Coatings Technology, 39/40 421-434 (1989).

[274] Sue J.A., Tucker R.C., Jr., “High temperature erosion behavior tungsten- and chromium-carbide-based coatings”, Surface and Coatings Technology 32 237–248 (1987).

[275] Suetin D.V., Shein I.R., and Ivanovskii A.L., “Electronic structure of cubic tungsten subnitride W_2N in comparison to hexagonal and cubic tungsten mononitrides WN”, Journal of Structural Chemistry 51 199-203 (2010).

[276] Sumi H., Inoue H., Taguchi M., Sugano Y., Masuya H., Ito N., Kishida S., Tokutaka H., "Characteristics of TiN films sputtered under optimized conditions of metallic mode deposition", Japanese Journal of Applied Physics 36 595-600 (1997).

[277] Sun X., Reid J.S., Kolawa E., Nicolet M.A., “Reactively sputtered Ti-Si-N films I. Physical properties”, Journal of Applied Physcis 81 (2) 656–663 (1997).

[278] Takeyama M.B., Itoi T., Aoyagi E., Noya A., “High performance of thin nano-crystalline ZrN diffusion barriers in Cu/Si contact systems”, Applied Surface Science 190 450-454 (2002).

[279] Tang Z.Z., “Effect of nitrogen concentration to the structural, chemical and electrical properties of tantalum zirconium nitride films”, Ceramics International 38 2997–3000 (2012).

[280] Tian Y., Xu B., Zhao Z., “Microscopic theory of hardness and design of novel superhard crystals”, International Journal of Refractory Metals and Hard Materials 33 93-106 (2012).

[281] Tillmann Wolfgang, Sprute Tobias, Hoffmann Fabian, Chang Yin-Yu, Tsai Ching-Yu, “Influence of bias voltage on residual stresses and tribological properties of TiAlVN-coatings at elevated temperatures”, Surface & Coating Technology 231 122-125 (2013).

[282] Tjong S.C., Chen H. “Nanocrystalline materials and coatings”, Materials Science and Engineering R 45 1–88 (2004).

[283] Toru Ogawa, “Structural stability and thermodynamic properties of Zr-N alloys”, Journal of Alloys and Compounds 203 221-227 (1994).

[284] Toth L., “Transition Metal Carbides and Nitrides”, Academic, New York (1971).

[285] Tsotsos C., Baker M.A., Polychronopoulou K., Gibson P.N., Giannakopoulos A., Polycarpou A.A., Böbel K., Rebholz C., “Structure and mechanical properties of low temperature magnetron sputtered nanocrystalline (nc-)Ti(N,C)/amorphous diamond like carbon (a-C:H) coatings”, Thin Solid Films 519 24-30 (2010A).

[286] Tsotsos C., Polychronopoulou K., Demas N.G., Constantinides G., Gravani S., Böbel K., Baker M.A., Polycarpou A.A., Rebholz C., “Mechanical and high pressure tribological properties of nanocrystalline Ti(N,C) and amorphous C:H nanocomposite coatings”, Diamond and Related Materials 19 960-963 (2010).

[287] Tucker R.C., Jr., “Thermal Spray Coatings”, ASM Handbook, ASM International, Surface Engineering 5 497-509 (1994).

[288] Tung H.M., Huang J.H., Tsai D.G., Ai C.F., Ping Y.G., “Hardness and residual stress in nanocrystalline ZrN films: Effect of bias voltage and heat treatment”, Materials Science Engineering A 500 104-108 (2009A).

[289] Tung Hsiao-Ming, Huang Jia-Hong, Tsai Ding-Guey, Ai Chi-Fong, Yu Ge-Ping, “Hardness and residual stress in nanocrystalline ZrN films: Effect of bias voltage and heat treatment”, Materials Science and Engineering A 500 104–108 (2009).

[290] Uglov V.V., Anishchik V.M., Zlotski S.V., Abadias G., Dub S.N., “Structural and mechanical stability upon annealing of arc-deposited Ti–Zr–N coatings,” Surface and Coatings Technology 202 2394-2398 (2008).

[291] Urgen M., Caklr A.F., Eryllmaz O.L., Mitterer C., “Corrosion of zirconium boride and zirconium boron nitride coated steels”, Surface and Coatings Technology 71 60-66 (1995).

[292] Vemuri R.S., Noor-A-Alam M., Gullapalli S.K., Engelhard M.H., Ramana C.V., “Nitrogen-incorporation induced changes in the microstructure of nanocrystalline WO_3 thin films”, Thin Solid Films 520 1446-1450 (2011).

[293] Venables J.A., Spiller G.D.T., Hanbucken M., “Nucleation and growth of thin films, Search Results”, Reports on Progress in Physics 47 399-459 (1984).

[294] Veprek S., “Superhard nanocomposites: design concept, properties, present and future industrial applications”, The European Physical Journal Applied Physics 28 313–317 (2004).

[295] Veprek S., “Ultra Hard Nanocomposite Coatings with Hardness of 80 to 105 GPa”, Societe Francaise du Vide 185–192 (2000).

[296] Veprek S., Heijman M.G.J.V., Karvankova P., Prochazka J., “Different approaches to superhard coatings and nanocomposites”, Thin Solid Films 476 1–29 (2005).

[297] Veprek S., Jilek M., “Super and ultrahard nanacomposite coatings: generic concept for their preparation, properties and industrial applications”, Vacuum 67 443–449 (2002).

[298] Veprek S., Reiprich S., “A concept for the design of novel superhard coatings”, Thin Solid Films 268 64-71 (1995).

[299] Veprek S., Reiprich S., Shizhi L., “Superhard nanocrystalline composite materials: The TiN/Si_3N_4 system”, Applied Physics Letters 66 (20) 2640 (1995A).

[300] Vetter J., Rochotzki R., “Tribological behaviour and mechanical properties of physical-vapour-deposited hard coatings: TiN_x, ZrN_x, TiC_x, TiC_x/i-C”, Thin Solid Films 192 253-261 (1990).

[301] Voevodin A.A., O’Neill J.P., Zabinski J.S., “Nanocomposite tribological coatings for aerospace applications”, Surface and Coating Technology 119 36–45 (1999).

[302] Voevodin A.A., Shtansky D.V., Levashov E.A., Moore J.J., “Nanostructured Thin Films and Nanodispersion Strengthened Coatings”, KLUWER ACADEMIC PUBLISHERS NEW YORK, BOSTON, DORDRECHT, LONDON, MOSCOW (2004).

[303] WahlstroKm U., Hultman L., Sundgren J.E., Adibi F., Petrov I., Greene J.E., “Crystal growth and microstructure of polycrystalline $Ti_{1-x}Al_xN$ alloy films deposited by ultra-high-vacuum dual-target magnetron sputtering”, Thin Solid Films 62 235 (1993).

[304] Wang Huili, Zhang Sam, Li Yibin, Sun Deen, “Bias effect on microstructure and mechanical properties of magnetron sputtered nanocrystalline titanium carbide thin films”, Thin Solid Films 516 5419-5423 (2008).

[305] Wang L.L., Wang X., Zheng W.T., Ma N., Li H.B., Guan Q.F., Jin D.J., Zong Z.G., “Structural and magnetic properties of nanocrystalline Fe–N thin films and their thermal stability”, Journal of Alloys and Compounds 443 43–47 (2007).

[306] Wang M.X., Zhang J.J., Yang J., Wang L.Q., Li D.J., “Synthesis of nanoscale multilayered ZrN/W_2N multilayered coatings by magnetron sputtering”, Surface and Coatings Technology 201 6800–6803 (2007A).

[307] Wang Yu Xi, Zhang Sam, Lee Jyh-Wei, Lew Wen Siang, Li Bo, “Influence of bias voltage on the hardness and toughness of CrAlN coatings via magnetron sputtering”, Surface & Coating Technology 206 5103-5107 (2012).

[308] Wasa K., Hayakawa H., “Handbook of sputter deposition technology: Principles, Technology and Applications,” Noyes Publication pp. 1-296 (1992).

[309] Wasa K., Kitabatake M., Adachi H., “Thin film materials technology: sputtering of compound materials”, William Andrew, USA, 71-111 (2004).

[310] Wehner G.K., Rosenberg D., “Mercury ion beam sputtering of metals at energies 4-115 keV”, Journal of Applied Physics 32 887-890 (1961).

[311] Wei Jian, “Synthesis of nanoporous silicon carbide ceramics by thermal evaporation process”, Applied Surface Science 256 6626-6629 (2010).

[312] Wen M., Meng Q.N., Yu W.X., Zheng W.T., Mao S.X., Hua M.J., “Growth, stress and hardness of reactively sputtered tungsten nitride thin films”, Surface & Coating Technology 205 1953-1961 (2010).

[313] Wiedemann R., Weihnacht V., Oettel H., "Structure and mechanical properties of amorphous Ti–B–N coatings", Surface and Coatings Technology 116–119 302–309 (1999).

[314] Williams D.B., Carter C.B.,“Transmission Electron Microscopy: A text book for material science”, Springer New York 291 (2009).

[315] Wu D., Zhang Z., Fu W., Fan X., Guo H., “Structure, electrical and chemical properties of zirconium nitride films deposited by dc reactive magnetron sputtering”, Applied Physics A 64 593-595 (1997).

[316] Wuhrer R., Yeung W.Y., Philips M.R., McCredie G., “Study on d.c. magnetron sputter deposition of titanium aluminium nitride thin films: effect of aluminium content on coating”, Thin Solid Films 290–291 15 339–342 (1996).

[317] Xiao Z., Cheng X., Yan X., “Effect of post-deposition annealing on ZrW_2O_8 thin films prepared by radio frequency magnetron sputtering,” Surface and Coatings Technology 201 5560-5563 (2007).

[318] Xin Y., Liu C., Huo K., Tang G., Tian X., Chu P.K., "Corrosion behavior of ZrN/Zr coated biomedical AZ91 magnesium alloy", Surface and Coatings Technology 203 2554–2557 (2009).

[319] Yacobi B. G., Holt D. B, "Cathodoluminescence scanning electron microscopy of semiconductors", Journal of Applied Physics 59(4) R1–R24 (1986).

[320] Yamamoto Kenji, "Hard films and sputtering targets for the deposition there of, United States patent", US 7648781 B2 (2010).

[321] Yamamoto T., Kawate M., Hasegawa H., Suzuki T., "Effects of nitrogen concentration on microstructures of WN_X films synthesized by cathodic arc method", Surface Coating Technology 193 372-374 (2005).

[322] Yamamura Y., Matasunami N., Itoh N., "Theoretical studies on an empirical formula for sputtering yields at normal incidence", Radiation Effects 71 65-86 (1983).

[323] Yang B., Chen L., Chang K.K., Pan W., Peng Y.B., Du Y., Liu Y., "Thermal and thermo-mechanical properties of Ti–Al–N and Cr–Al–N coatings", International Journal of Refractory Metals and Hard Materials 35 235–240 (2012).

[324] Yang Q., Zhao L.R., "Micro structure, mechanical and tribological properties of novel multi-component nanolayered nitride coatings", Journal of Surface and Coating Technology 200 1709 – 1713 (2005).

[325] Zadeh K.K., Fry B., "Nanotechnology-Enabled Sensors", Springer New York (2008).

[326] Zega B., "Hard decorative coatings by reactive physical vapor deposition", Surface and Coatings Technology 39-40 507-520 (1989).

[327] Zeman P., Cerstvy R., Mayrhofer P.H., Mitterer C., Musil J., "Structure and properties of hard and superhard Zr–Cu–N nanocomposite coatings", Materials Science and Engineering A 289 189 – 197 (2000).

[328] Zhang S., Sun D., Fu Y., Du H., "Recent advances of superhard nanocomposite coatings: a review", Surface and Coating Technology 167 113–119 (2003).

[329] Zhang S., Sun D., Fu Y., Du H., "Toughness measurement of thin films: a critical review", Surface and Coatings Technology 198 74–84 (2005).

[330] Zhang T.C., Kuznetsov A.Y., "Surface/strain energy balance controlling preferred orientation in CdZnO films", Journal of Applied Physics 110 053512 (2011).

[331] Zhao L.R., Chen K., Yang Q., Rodgers J.R., Chiou S.H., “Materials informatics for the design of novel coatings”, Surface and Coatings Technology 200 1595–1599 (2005).

[332] Zhitomirsky V.N., Grimberg I., Boxman R.L., Travitzky N.A., Goldsmith S., Weiss B.Z., “Vacuum arc deposition and microstructure of ZrN-based coatings”, Surface and Coating Technology 94–95 207-212 (1997).

[333] Zhou L., Holec D., Mayrhofer P.H., “First-principles study of elastic properties of cubic $Cr_{1-x}Al_xN$ alloys”, Journal of Applied Physics 113 043511 (2013).

[334] Zhou X., Gall D., Khare S.V., “Mechanical properties and electronic structure of anti-ReO_3 structured cubic nitrides, M_3N, of d block transition metals M: An ab initio study”, Journal of Alloys and Compounds 595 80–86 (2014).

[335] Zhou Z., Rainforth W.M., Rother B., Ehiasarian A.P., Hovsepian P.Eh., and Münz W.D., “Elemental distributions and substrate rotation in industrial TiAlN/VN superlattice hard PVD coatings”, Surface and Coating Technology 183 275–282 (2004).

[336] Zhu Y.T., Narayan J., Hirth J.P., Mahajan S., Wu X.L., Liao X.Z., “Formation of single and multiple deformation twins in nanocrystalline fcc metals”, Acta Materialia 57 3763-3770 (2009).